Etude des micro-contraintes dans les matériaux texturés hétérogènes par diffraction et modèles de comportement

Sebastian Wronski

N° : 2007-ENAM-0017

Ecole Nationale Supérieure d'Arts et Métiers

École doctorale n°432 : Science de Métiers de l'Ingénieur

THÈSE

Pour obtenir le grade de

Docteur
de
l'École Nationale Supérieure d'Arts et Métiers
et
l'Université de Sciences et Technologie AGH de Cracovie
Spécialité : Mécanique et Matériaux

Présentée et soutenue publiquement
par

Sebastian Wroński

le 29 septembre 2007 à Cracovie

Etude des micro-contraintes dans les matériaux texturés hétérogènes par diffraction et modèles de comportement

Direction de thèse:
Chedly BRAHAM et Krzysztof WIERZBANOWSKI

Jury:

Andrzej KOŁODZIEJCZYK, Professeur, AGH, UST, Cracovie.....	Président
Paul LIPIŃSKI, Professeur, ENIM, Metz.....	Rapporteur
Henryk FIGIEL, Professeur, AGH, UST, Cracovie.....	Rapporteur
Jan BONARSKI, MIMI, dr hab. PAN, Cracovie.....	Rapporteur
Alain LODINI, Professeur, LACM, Université de Reims.....	Examinteur
Antoni PAJA, Professeur, AGH, UST, Cracovie.....	Examinteur
Janusz WOLNY, Professeur, AGH, UST, Cracovie.....	Examinteur
Wiesława SIKORA, Professeur, AGH, UST, Cracovie.....	Examinteur

Laboratoire d'Ingénierie des Matériaux (LIM) ENSAM, CER de Paris
Department of Condensed Matter Physics AGH, UST de Cracovie

Acknowledgements

First of all I would like to thank my supervisors: Prof. Krzysztof Wierzbanowski and Dr Chedly Braham for their guidance and help. Thanks are also due to Dr Andrzej Baczmański and Dr Jacek Tarasiuk for discussions and to all colleagues from the Group of Condensed Matter Physics (Faculty of Physics and Applied Computer Sciences, AGH-UST, Kraków, Poland) for help and friendly atmosphere.

I would like to express my thanks to Dr Wilfrid Seiler for careful planning and assistance in carrying out many experiments using X-ray diffraction and to Dr Mirosław Wróbel for preparing many samples.

I am grateful to Dr Michael Fitzpatrick for enabling my visits in the Open University, Milton Keynnes, UK. I would also like to thank Dr Ed Oliver for his help during experiment using neutron diffraction at Rutherford Appleton Laboratory, ISIS, UK.

Finally, I would like to express my gratefulness for my family and especially Justyna Wojno for her patience and support.

Résumé

Etude des micro-contraintes dans les matériaux texturés hétérogènes par diffraction et modèles de comportement

L'objectif de ce travail est le développement d'une méthodologie d'analyse des contraintes utilisant des modèles théoriques pour décrire le comportement élasto-plastique des matériaux polycristallins. L'étude vise d'abord l'interprétation de résultats expérimentaux par des modèles de déformation qui décrivent la création des champs de contrainte dans les matériaux polycristallins déformés. Une attention particulière est portée à l'explication des phénomènes physiques à l'origine des contraintes résiduelles et à la prédiction de leur évolution et de leur influence sur les propriétés du matériau.

Dans le premier chapitre, la méthode classique, dite des $\sin^2\psi$, d'analyse des contraintes est présentée. Ensuite, la nouvelle méthode d'analyse, méthode de multi-réflexions, basée sur les mesures de déformation en utilisant plusieurs réflexions hkl est introduite. Dans cette méthode, tous les pics de diffraction sont analysés simultanément et la distance interréticulaire d_{hkl} est remplacée par une distance équivalente a. Aussi, sont présentées les méthodes de calcul des constantes élastiques radiocristallographiques qui jouent un rôle crucial dans la détermination des contraintes. La détermination de ces constantes est indispensable pour l'interprétation des différents résultats expérimentaux. De nouvelles méthodes de calculs des constantes élastiques radiocristallographiques utilisant le modèle autocohérent ont été développées et testées. Une attention particulière a été portée au calcul par ce nouveau modèle autocohérent dans le cas des couches superficielles (surface libre). Dans ce modèle, le calcul des forces et contraintes normales à la surface est effectué selon le modèle de Reuss et pour les deux autres directions, c'est le modèle auto-cohérent qui est utilisé. Cette méthode de calcul est particulièrement adaptée au cas de la diffraction des rayons X où seulement une couche superficielle du matériau est examinée (généralement de quelques μm d'épaisseur).

Dans le chapitre suivant, deux modèles de déformation ont été développés et utilisés pour déterminer l'évolution des contraintes et analyser les propriétés du matériau. Le premier modèle (LF) est basé sur les formulations de Leffers (Lefers 1968) qui ont été reprises et développées par Wierzbanowski (Wierzbanowski 1978, 1982). Le second est le modèle auto-cohérent (SC) (Hutchinson 1964, Berveiller et Zaoui 1979). Dans ce travail, le calcul est réalisé à partir de l'algotithme développé par Lipinski et Berveiller (Lipinski et Berveiller 1989). Dans cette approche, le tenseur de Green est utilisé pour décrire les interactions entre

les grains. Les grains du polycristal sont considérés comme des inclusions ellipsoïdales (en 3D) dans une matrice homogène. Ces deux modèles de déformation elasto-plastique (LW et SC) sont des outils très utiles pour l'étude des propriétés mécaniques des matériaux polycristallins. Ils permettent la prédiction des propriétés macroscopiques du matériau (texture, courbes contrainte-déformation, surfaces d'écoulement plastique, densité des dislocations, état final des contraintes résiduelles, etc.) à partir de ses caractéristiques microsructurales (systèmes de glissement, loi d'écrouissage, texture initiale, état initial des contraintes résiduelles, etc.) (Wierzbanowski 1978). Des résultats typiques: de texture, écrouissage et énergie stockée, obtenus par ces modèles, ont été comparés aux résultats expérimentaux.

Le chapitre 3 est consacré principalement à l'explication des origines physiques des contraintes et de la prédiction de leur évolution, ainsi qu'à leur influence sur les propriétés du matériau. Les contraintes internes sont classées en trois types selon l'échelle : contraintes d'ordre I, II ou III. Une attention particulière est portée aux contraintes d'ordre I et II car ce sont les seules qui sont déterminées à partir de la position des pics de diffraction. Les modèles de déformation ont été utilisés pour l'analyse des contraintes à l'échelle des grains (contraintes du second ordre). L'évaluation quantitative de ce type de contraintes ne peut pas être effectuée directement par des mesures mais elle est possible grâce aux modèles. Les matériaux multi-phasés ont été également étudiés. Pour ces matériaux, l'interprétation des données expérimentales est plus complexe que celle du cas des matériaux monophasés en raison de la nécessité de prendre en compte l'interaction entre les phases. C'est pourquoi, une nouvelle méthode adaptée aux matériaux multi-phasés a été développée et appliquée au cas des aciers inoxydables austéno-ferritiques (aciers Duplex). Les paramètres de déformation plastique (τ_c^{ph} - scission critique résolu et H^{ph} - paramètre d'écrouissage) de chacune des phases ont pu être déterminés. Lors de la déformation plastique, l'évolution des contraintes dans les phases et la création de contraintes d'incompatibilité de second ordre, sont observées et l'influence de la texture cristallographique et de l'anisotropie élastique est étudiée. La méthodologie développée et utilisée dans ce travail a, donc, permis de déterminer quantitativement les contraintes du premier et du second ordre, pour chaque phase. Il a été montré qu'une bonne corrélation entre les déformations déterminées expérimentalement et les résultats théoriques, n'est obtenue que si l'influence des contraintes du second ordre est prise en compte. Aussi, le meilleur lissage des courbes expérimentales est obtenu quand les calculs intègrent les constantes d'élasticité anisotropiques et la texture réelle initiale de l'échantillon.

Les méthodes de détermination des contraintes du premier et du second ordre, présentées au troisième chapitre, sont employées pour l'étude des contraintes résiduelles dans des alliages écrouis par laminage croisé (Chapitre 4). Le laminage croisé a été retenu pour ajouter une symétrie de la texture cristallographique et, donc, de réduire l'anisotropie de la pièce (comparé au laminage uniaxial). Les résultats sont présentés pour des séries d'éprouvettes en acier et en alliage de cuivre. Dans le cas de l'alliage de cuivre, les résultats montrent de très faibles niveaux de contraintes d'incompatibilité de second ordre qui peuvent être négligées. Par contre, dans le cas de la ferrite, il faut en tenir compte car leur niveau s'avère important. Les oscillations observées sur les courbes des $\sin^2\psi$ peuvent être expliquées, dans ce cas, principalement par la présence de contraintes du second ordre.

Enfin, au chapitre 5, une nouvelle méthode d'analyse des contraintes utilisant un faisceau de rayons X avec un angle d'incidence faible et constant (méthode de diffraction en incidence rasante GID-$\sin^2\psi$). Cette méthode présente l'avantage d'une profondeur de pénétration des rayons X constante, contrairement à la méthode des $\sin^2\psi$ classique qui présente l'inconvénient d'une forte variation de la pénétration avec l'angle ψ. C'est pour cette raison que la méthode classique des $\sin^2\psi$ est mal adaptée pour l'étude des matériaux à forts gradients de contraintes. Moyennant un choix optimisé des angles d'incidence et du type de rayonnement, la nouvelle méthode s'avère efficace pour l'étude des matériaux à forts gradients de contraintes, en permettant des mesures dans différentes couches proches de la surface. L'incertitude des mesures a été évaluée et le rôle de l'absorption, de l'indice de réfraction et des facteurs de Lorentz-polarisation et de diffusion atomique ont été étudiés.

A partir de mesures sur des poudres de référence, l'influence de chacun de ces paramètres a été évaluée et prise en compte dans la détermination de la position des pics de diffraction. Les analyses effectuées ont confirmé la faible influence de l'absorption et des facteurs de Lorentz-polarisation et de diffusion atomique sur la contrainte déterminée. Par contre, ils ont révélé un effet important de l'indice de réfraction, en particulier aux petits angles d'incidence. Pour des angles d'incidence $\alpha \leq 10^0$, les corrections sont importantes et modifient les résultats des contraintes d'une manière significative (la correction peut atteindre 70 MPa dans le cas de la poudre). Cet effet et, donc, la correction nécessaire décroît quand l'angle d'incidence augmente.

Table of Contents

Summary

The aim of this work is to develop the methodology of stress measurement using theoretical models describing elasto-plastic behaviour of polycrystalline materials. The main purpose is to interpret experimental results on the basis of the self-consistent model which describes the mechanisms of stress field generation in deformed polycrystalline materials. Special attention has been paid to the explanation of the physical origins of stresses and to the prediction of their evolution and influence on material properties.

In Chapter 1 the classical method of stress measurement called $\sin^2\psi$ was described. The new stress analysis – multi-reflection method - based on strain measurements using a few reflections *hkl* is introduced (in this method all peaks are analysed simultaneously). Also the methods of calculation of the diffraction elastic constants, which play a crucial role in the stress analysis, were presented. The determination of these constants is essential in explanation of many experimental results. New methods for the calculation of diffraction elastic constants using the self-consistent model have been elaborated and tested. These methods were used for textured samples.

In Chapter 2 two models (self-consistent and Leffers-Wierzbanowski models) were presented. They enable the prediction of macroscopic material properties (e.g., texture, stress-strain curves, plastic flow surfaces, dislocation density, final state of residual stress, etc.) basing on the micro-structural characteristics (crystallography of slip systems, hardening law, initial texture, initial residual stress state, etc.).

In Chapter 3 a special attention has been paid to the explanation of physical origins of the stresses and to the prediction of the stress evolution and their influence on material properties. The internal stresses were divided into three types in function of the scale. The deformation models were used to analyse the stresses present in grains (the second order stresses). Quantitave estimation of this kind of stresses is possible only by means of models; they cannot be measured directly. Interpretation of experimental data for multiphase material is more complex than for a single phase one, because it is necessary to consider interaction between phases. For this reason, the new method of investigation of multiphase materials was developed and applied for duplex stainless steel.

The methods of estimation of the first and the second order stresses which were presented in the third chapter are used to study the residual stresses in materials after cross rolling (Chapter 4). The cross-rolling is applied in order to symmetrize the crystallographic texture and consequently, to decrease the sample anisotropy. The results for series of copper and steel samples are presented.

Finally, in Chapter 5 a new method of stress estimation using a constant and low incident beam angle (grazing angle incidence X-ray diffraction technique) was presented. In this method, the penetration depth is almost constant on the contrary to classical method. For this reason, the grazing incidence diffraction technique can be used to investigate materials with a significant stress gradient. Measurement uncertainties in this method were considered; especially the influence of absorption, Lorentz-polarization, atomic scattering factor and refractive index were studied.

Chapter 1

Determining of stresses in polycrystalline materials

1.1. Introduction

The internal stresses are generated by applying external loads to the sample. They appear after deformation of the material as a result of a change of the shape and volume. In most cases the stress field is homogeneous and anisotropic. During plastic deformation the sample is deformed irreversibly and stresses remain in the sample even if external forces are unloaded. The stresses which can be found in unloaded samples are called the residual stresses. Residual stresses affect the mechanical properties of materials and they are responsible for such processes like fracture, cracks growth, fatigue, creep, recrystallisation and many others. However in some cases the residual stresses improve selected properties of materials. For example the presence of the compression stress field can improve endurance for cracking.

There are several techniques for determination of residual stresses, such as the destructive mechanical methods (layers removal), the methods based on the measurements of material properties affected by stresses (ultrasonic methods, measurement of Barkhausen magnetic noise, Raman spectroscopy) and the diffraction method based on the measurement of strain of the crystallographic lattice. The advantage of the diffraction method is its non-destructive character and the possibility of macro and microstress analysis in multiphase and anisotropic materials. This method is frequently used in industry, material science, electronics and biomaterial technology. Because of high absorption of X-ray radiation this method can be applied to study residual stresses to the depth of few μm below the surface of sample. In order to get deeper penetration, synchrotron or neutron radiation has to be applied. The use of synchrotron or neutron radiation enables to study stresses up to a few cm below the surface and sometimes in the entire sample volume.

In the case of synchrotron or neutron radiation the sampling volume can be well defined by special slits forming the incidence and the diffracted beams. In this way the measurement

from small selected parts of the sample can be done. The stress measurement is possible with high spatial resolution (less than 20μm). In this work, the classical X-ray and the neutron diffraction methods are used to study the stress fields in polycrystalline materials. The influence of various types of stress on the results of a diffraction experiment is discussed.

1.2. Measurements of macrostresses using diffraction method.

When internal stresses are present in a material a systematic change of the lattice parameter in each grain is observed. The interplanar spacing is described by Bragg's law:

$$2d_{\{hkl\}} \sin\theta = n\lambda \qquad (1.1)$$

The increase of interplanar spacing $d_{\{hkl\}}$ causes a decrease of θ angle. In typical cases the shift of a peak is: $0{,}001^0$ - $0{,}1^0$. It seems to be a small value, however a good fitting procedure of the diffraction peak (using Gauss or Lorentz function) enables to observe and measure this effect. The presence of internal stresses causes not only a shift of a diffraction peak ($\Delta(2\theta)= 2\theta - 2\theta_0$) but also a change of its intensity and width (this latter is expressed as FWHM, i.e., full width at half maximum).

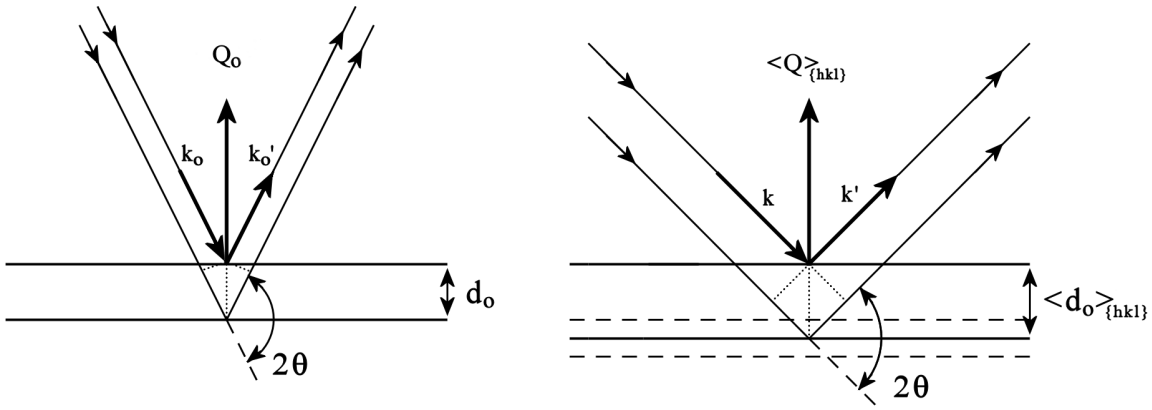

a. b.

Fig. 1.1. *Diffraction on a stress free lattice (a) and on a deformed lattice (b). A range of interplanar spacings in different diffracting crystallites is shown by dashed lines, while the continuous line is used to mark the average distance between reflecting planes.*

The lattice parameter can be determined using diffraction method. The measured value is the average over the group of diffracting grains. This kind of average will be marked as <...>. Hence, the Bragg law can be written as:

$$2 < d_{\{hkl\}} > \sin < \theta_{\{hkl\}} >= n\lambda \qquad (1.2)$$

An important condition concerning the sensitivity of the method can be derived from Bragg law. A small change of interplanar spacing ($\Delta < d >_{\{hkl\}}$) is related with a shift of the peak position ($\Delta < 2\theta >_{\{hkl\}}$) by equation:

$$\Delta < 2\theta >_{\{hkl\}} = -2\left[\frac{\Delta < d >_{\{hkl\}}}{< d >_{\{hkl\}}}\right] tg < \theta >_{\{hkl\}} = -2 < \varepsilon >_{\{hkl\}} tg < \theta >_{\{hkl\}} \qquad (1.3)$$

where: $< \varepsilon >_{\{hkl\}} = \dfrac{\Delta < d >_{\{hkl\}}}{< d >_{\{hkl\}}}$

It is visible that for the same value of $\dfrac{\Delta < d >_{\{hkl\}}}{d_{\{hkl\}}}$, bigger shift of $\Delta < 2\theta >_{\{hkl\}}$ is observed for higher 2θ scattering angle. For this reason usually the peaks with 2θ angle higher than 90^0 are used for the stress measurement. In the case of diffraction peaks with 2θ smaller than 90^0 the precision of measurement is generally not good enough (let us remark that the detector position is usually set with the precision of $0{,}01^0$). This is why the measurements for angles smaller than 90^0 are not reliable (Bojarski, 1995)

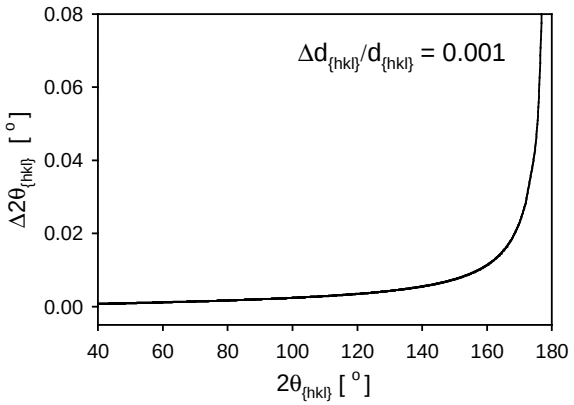

Fig. 1.2. *$\Delta 2\theta_{\{hkl\}}$ vs. $2\theta_{\{hkl\}}$ for $\Delta d_{\{hkl\}} / d_{\{hkl\}} = 0.001$. It should be noticed that shift of the peak 211 for steel under pressure 200MPa equals $0{,}1^0$.*

Let us describe now the measurement geometry. The experiment consists of the sample rotation around the scattering vector **Q** for a fixed 2θ angle. Two types of the coordinate system should be considered: sample system (X) and the measurement coordinate system (L). The definition of these coordinate systems is presented in Fig. 1.3. L_3 axis is parallel to the scattering vector **Q**. During the measurement a sample is rotated and the position of the vector $\mathbf{L_3} \| \mathbf{Q}$ is described by ϕ and ψ angles (Wolfstieg, 1976) (with respect to X coordinate system).

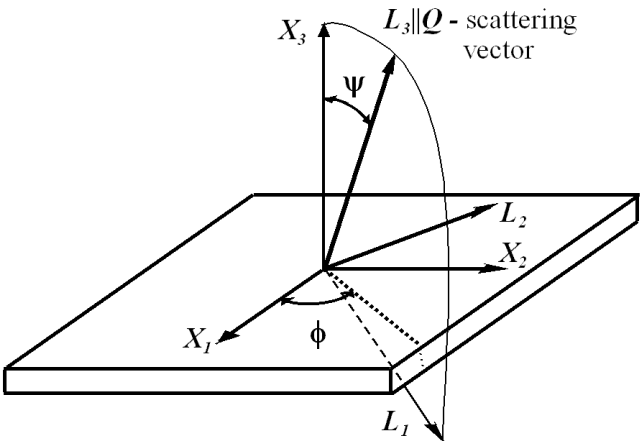

Fig. 1.3. *Orientation of the scattering vector with respect to the sample system X. The ψ and ϕ angles define the orientation of the L system (L_2 axis lies in the plane of the sample surface). The laboratory system, L, defines the measurement of the interplanar spacings $\langle d(\psi,\phi)\rangle_{\{hkl\}}$ along the L_3 axis.*

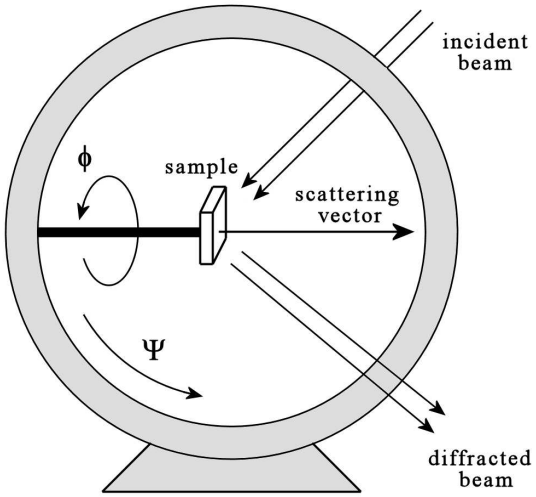

Fig. 1.4. *Eulerian cradle used to change the relative sample orientation.*

Bragg's law enables to measure interplanar spacing $d=d_{\{hkl\}}$. So for each orientation of vector $\mathbf{L_3} \| \mathbf{Q}$ it is possible to measure interplanar spacing $d(\psi,\phi)_{\{hkl\}}$ for crystallographic planes {hkl} perpendicular to the scattering vector **Q**. In all relations expressed in L coordinate system the index (') will be used (e.g., the measured deformation along L_3 axis is marked as ε_{33}'). The diffraction method enables to measure the mean interplanar spacing $\langle d(\psi, \phi)\rangle_{\{hkl\}}$, averaged over reflecting crystallites. The mean lattice strain $\langle \varepsilon(\psi, \phi)\rangle_{\{hkl\}}$ in L_3 direction (Fig. 1.3) is defined as:

$$< \varepsilon_{33}'(\psi,\phi) >_{\{hkl\}} = \frac{< d(\psi,\phi) >_{\{hkl\}} - d^{\,0}_{\{hkl\}}}{d^{\,0}_{\{hkl\}}} \tag{1.4}$$

The lattice strain $\varepsilon_{33}'(\psi,\phi)_{\{hkl\}}$ for a given grain can be calculated from Hook's law:

$$\varepsilon_{33}'(\psi,\phi)_{\{hkl\}} = s_{33ij}'(\psi,\phi)\sigma_{ij}' \tag{1.5}$$

where ε'_{ij}, σ'_{mn} and s'_{ijmn} are the elastic strain, stress and elastic compliance tensor of a grain. In the above equation the convention of repeated index summation is applied (Einstein convention). This convention will be used in the whole present work and it will concern always lower indices.

For a given orientation of the scattering vector (**Q**) and for a given Bragg's angle (2θ) only those crystallites diffract which have one of the {hkl} planes perpendicular to $\mathbf{Q} \| \mathbf{L_3}$. This group of crystallites is called *diffracting group*. Average measured deformation is:

$$< \varepsilon_{33}'(\psi,\phi) >_{\{hkl\}} = < s_{33ij}'(\psi,\phi)\sigma_{ij}' > \tag{1.6}$$

It is next assumed that an effective tensor S_{ijkl}' exists for the diffracting group which simplifies the above relation to:

$$< \varepsilon_{33}'(\psi,\phi) >_{\{hkl\}} = S_{33ij}'(\psi,\phi)\sigma_{ij}^{M\,\prime} \tag{1.7}$$

where σ_{ij}^{M} is the average macroscopic stress, constant in a big part of a sample (i.e., in the measurement volume).

Let us note that even if a sample has the quasi-isotropic symmetry (random texture), the diffracting group has a lower symmetry. Orientation of the crystallites belonging to this group can differ one from another by rotation γ around $\mathbf{Q} \| \mathbf{L_3} \| \mathbf{N_{hkl}}$ vector – Fig. 1.5. Consequently, the average elastic matrix S_{mn} for diffracting group has the same structure as a body with axial symmetry. It is defined by five independent parameters and has a form (see e.g., Reid, 1974):

$$S_{mn}' = \begin{bmatrix} S'_{11} & S'_{12} & S'_{13} & & & \\ S'_{12} & S'_{11} & S'_{13} & & 0 & \\ S'_{13} & S'_{13} & S'_{33} & & & \\ & & & S'_{44} & & \\ & 0 & & & S'_{44} & \\ & & & & & S'_{66} \end{bmatrix} \tag{1.8}$$

In the above equation the matrix notation (S_{mn}) was used for tensor components (S_{ijkl}). The rules for the reduction of indices are following:

Tensor indices	Reduced matrix indices
11	→ 1
22	→ 2
33	→ 3
23, 32	→ 4
13, 31	→ 5
12, 21	→ 6

(1.9)

e.g., the tensor component S_{1123} becomes the matrix component S_{14}. In the present work the elastic constant tensors will be used both in matrix and tensor convention, depending on the case in order to simplify equations.
It is evident, that the symmetry axis for the assembly of diffracting grains is $\mathbf{Q} \| \mathbf{L_3}$.
Using the elastic constants matrix, equation 1.7 can be written as:

$$< \varepsilon_{33}'(\psi,\phi) >_{hkl} = S_{31}'\sigma_{11}^{M}' + S_{32}'\sigma_{22}^{M}' + S_{33}'\sigma_{33}^{M}' \tag{1.10}$$

On the right hand there are only three components, because $S'_{34}=S'_{35}=S'_{36}= 0$ (see. Eq. 1.8).

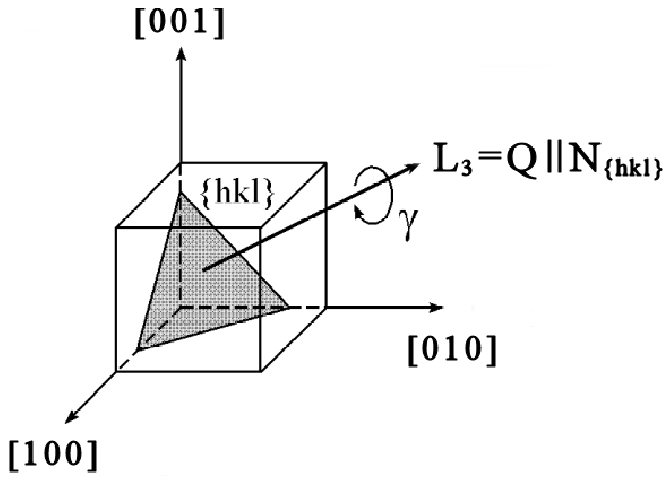

Fig. 1.5. *Definition of lattice rotation around the scattering vector* $\mathbf{L_3}=\mathbf{N_{\{hkl\}}} \| \mathbf{Q}$

Taking into account the structure of the S'_{mn} matrix (Eq. 1.8), the above equation can be rewritten as:

$$< \varepsilon_{33}'(\psi,\phi) >_{\{hkl\}} = S_{13}'\sigma_{11}^{M}' + S_{13}'\sigma_{22}^{M}' + S_{33}'\sigma_{33}^{M}' \tag{1.11}$$

Let us note that all quantities in the above equation are expressed in L coordinate system. Our goal is to relate the measured deformation ε_{33}' (expressed in L coordinate system) in function of stress components σ_{ij} (expressed in X coordinate system). To transform stress tensor σ_{ij} to L coordinate system, the transformation matrix has to be defined. This matrix is (see Fig.1.3):

$$a_{ij} = \begin{bmatrix} \cos\phi\cos\psi & \sin\phi\cos\psi & -\sin\psi \\ -\sin\phi & \cos\phi & 0 \\ \cos\phi\sin\psi & \sin\phi\sin\psi & \cos\psi \end{bmatrix} \tag{1.12}$$

The transformation law for four stress rank tensors is:

$$\sigma_{ij}' = a_{ik} a_{jl} \sigma_{kl} \tag{1.13}$$

According to the above, three needed components σ_{ii}' are:

$$\begin{aligned}
&\sigma_{11}^{M}{}' = \sigma_{11}^{M} \cos^2\phi\cos^2\psi + \sigma_{22}^{M} \sin^2\phi\cos^2\psi + \sin^2\psi\sigma_{33}^{M} + \sin 2\phi\cos^2\psi\sigma_{12}^{M} \\
&-\cos\phi\sin 2\psi\sigma_{13}^{M} - \sin\phi\sin 2\psi\sigma_{23}^{M} \\
&\sigma_{22}^{M}{}' = \sigma_{11}^{M} \sin^2\phi + \sigma_{22}^{M} \cos^2\phi - 2\cos\phi\sin\psi\sigma_{12}^{M} \\
&\sigma_{33}^{M}{}' = \sigma_{11}^{M} \cos^2\phi\sin^2\psi + \sigma_{22}^{M} \sin^2\phi\sin^2\psi + \cos^2\psi\sigma_{33}^{M} + \sin 2\phi\sin^2\psi\sigma_{12}^{M} \\
&+\cos\phi\sin 2\psi\sigma_{13}^{M} + \sin\phi\sin 2\psi\sigma_{23}^{M}
\end{aligned} \tag{1.14}$$

After substituting the stress components from Eq. 1.14 to Eq. 1.11 we obtain:

$$\begin{aligned}
<\varepsilon_{33}'(\psi,\phi)>_{\{hkl\}} = {} & \frac{1}{2} s_2 (\sigma_{11}^{M} \cos^2\phi + \sigma_{12}^{M} \sin 2\phi + \sigma_{22}^{M} \sin^2\phi)\sin^2\psi + \\
& + \frac{1}{2} s_2 \sigma_{33}^{M} \cos^2\psi + s_1(\sigma_{11} + \sigma_{22} + \sigma_{33}) + \\
& + \frac{1}{2} s_2 (\sigma_{13}^{M} \cos\phi + \sigma_{23} \sin\phi)\sin 2\psi
\end{aligned} \tag{1.15}$$

where:

$$\frac{1}{2} s_2 = (S'_{33} - S'_{31}), \qquad s_1 = S'_{31} \tag{1.16}$$

The quantities s_1 and ½ s_2 are so called diffraction elastic constants for a quasi-isotropic material. Eq. 1.15 can be also expressed by interplanar spacings $d_{\{hkl\}}$ (see Eq. 1.4):

$$\begin{aligned}
<d(\psi,\phi)>_{\{hkl\}} = {} & \left[\frac{1}{2} s_2 (\sigma_{11}^{M} \cos^2\phi + \sigma_{12}^{M} \sin 2\phi + \sigma_{22}^{M} \sin^2\phi)\sin^2\psi + \frac{1}{2} s_2 \sigma_{33}^{M} \cos^2\psi + \right. \\
& \left. + s_1(\sigma_{11}^{M} + \sigma_{22}^{M} + \sigma_{33}^{M}) + \frac{1}{2} s_2 (\sigma_{13}^{M} \cos\phi + \sigma_{23}^{M} \sin\phi)\sin 2\psi \right] \; d_{\{hkl\}}^{0} + d_{\{hkl\}}^{0}
\end{aligned} \tag{1.17}$$

Using obvious trigonometric identities the above equation can be converted to:

$$< d(\psi,\phi) >_{\{hkl\}} = \left\{ \frac{1}{2} s_2 \left[\left(\sigma_{11}^M - \sigma_{33}^M \right) cos^2\phi + \left(\sigma_{22}^M - \sigma_{33}^M \right) sin^2\phi + \sigma_{12}^M sin2\phi \right] sin^2\psi \right.$$
$$\left. + s_1 \left[\sigma_{11}^M + \sigma_{22}^M + \sigma_{33}^M \right] + \frac{1}{2} s_2 \sigma_{33}^M + \frac{1}{2} s_2 \left[\left(\sigma_{13}^M cos\phi + \sigma_{23}^M sin\phi \right) sin2\psi \right] \right\} d_{\{hkl\}}^0 + d_{\{hkl\}}^0 \quad (1.18)$$

An important simplification is obtained if one assumes a particular plane state of stress, which occurs usually on the surface of rolled samples. In such the case:

$$\sigma_{11}{}^M \neq 0, \qquad \sigma_{22}{}^M \neq 0, \qquad \sigma_{33}{}^M = \sigma_{12}{}^M = \sigma_{13}{}^M = \sigma_{23}{}^M = 0 \quad (1.19)$$

The rolled samples have orthorhombic symmetry and for this reason only the main stress components - $\sigma_{ii}{}^M$ - occur (symmetry axes are determined by the edges of the sample). Moreover, the static equilibrium condition on the surface involves: $\sigma_{33}{}^M=0$. During X-ray diffraction measurement only a thin layer of a material near the surface is examined. (see for example: Noyan and Cohen, 1987; Dolle, 1979; Hauk, 1986; Brakman, 1987, Major et al., 1999; Bochnowski et al., 2003) Consequently, the approximation of the plane state of stress is correct in such the case. However, the assumption of $\sigma_{33}{}^M=0$ can not valid in the case of the neutron diffraction technique, because due to very low absorption the neutron beam penetrates up to several centimetres inside the sample. (Allen et al. 1981; Daymond and Priesmeyer, 2002; Fitzpatrick and Lodini, 2003)
Assuming the approach of plane state of stress, Eq. 1.18 takes the form:

$$< d(\psi,\phi) >_{\{hkl\}} = \left[\frac{1}{2} s_2 (\sigma_{11}{}^M \cos^2\phi + \sigma_{22}{}^M \sin^2\phi) \sin^2\psi + s_1 (\sigma_{11}{}^M + \sigma_{22}{}^M) \right] d_{\{hkl\}}{}^0 + d_{\{hkl\}}{}^0 \quad (1.20)$$

We can conclude that in the case of a quasi-isotropic sample and plane stress state the linear relation of $<d(\psi,\phi)>_{\{hkl\}}$ versus $\sin^2\psi$ occurs (for a fixed ϕ value) - Fig. 1.6.

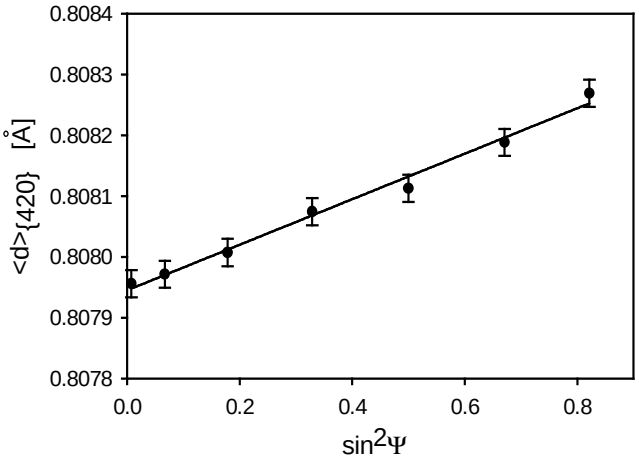

Fig. 1.6. *The lattice parameter $<d>_{\{420\}}$ in function of $sin^2\psi$ for copper. The slope of the curve equals ½ s_2 σ_{11}^M when $\varphi=0$.*

Information about stress components is contained in the slope of the curve (Eq. 1.20). For example, if $\phi=0^0$ we can determine the value of σ_{11}^M component from the slope of the diagram. Similarly, if $\phi=90^0$, it is possible to determine the stress components σ_{22}^M. Generally, to obtain a good precision of determined stress components σ_{11}^M and σ_{22}^M, the experiment is repeated for different φ angles and the least squares procedure is applied.

In the case of neutron or synchrotron diffraction Eq. 1.18. cannot be simplified. The both techniques give the information from the whole sample volume and the assumption $\sigma_{33}^M = 0$ is no more valid. In general the value of $d_{\{hkl\}}^0$ is unknown, hence for orthorhombic and quasi-isotropic sample the values of $(\sigma_{11}^M - \sigma_{33}^M)$ and $(\sigma_{11}^M - \sigma_{22}^M)$ instead of σ_{11}^M and σ_{22}^M are determined.

1.3. Diffraction elastic constants

The important step in residual stress measurement is the determination of so called diffraction elastic constants. A general definition of diffraction elastic constants is obtained from Eq. 1.7:

$$< \varepsilon_{33}'(\psi,\phi) >_{\{hkl\}} = R_{ij}^M{}'(\psi,\phi)\sigma_{ij}^M{}' \tag{1.21}$$

with :

$$R_{ij}^M{}' = S_{33ij}{}' \tag{1.22}$$

$R_{ij}^M{}'$ are macroscopic diffraction elastic constants and $\sigma_{ij}^M{}'$ is the macro-stress, i.e., the average stress in a big macroscopic part of a material. They depend not only on ψ and ϕ angles but also on diffracting plane {hkl}. These constants are essential for interpretation of the results of residual stress measurement. The diffraction elastic constants can be calculated (Baczmański et al., 1993) and also determined experimentally.

Combining Eq. 1.6: $<\varepsilon_{33}'(\psi,\phi)>_{\{hkl\}}=<s_{33ij}'(\psi,\phi)\sigma_{ij}'>$ and Eq. 1.21 we can write:

$$R_{ij}^{M}'(\psi,\phi)\sigma_{ij}^{M}'=<s_{33ij}'(\psi,\phi)\sigma_{ij}'> \tag{1.23}$$

In general $R'_{ij}(\psi,\phi)$ cannot be calculated in a direct way, because elastic interactions between grains in polycrystalline sample are quite compliex. For these reason we use some simplifying assumptions or models. Eq. 1.18 can be rewritten in terms of $R_{33}^{M'}$ and $R_{11}^{M'}$ (using Eqs. 1.16 and 1.22) as:

$$\begin{aligned}<d(\psi,\phi)>_{\{hkl\}} &= \left\{\left(R_{33}^{M}'-R_{11}^{M}'\right)\left[\left(\sigma_{11}^{M}-\sigma_{33}^{M}\right)\cos^2\phi+\left(\sigma_{22}^{M}-\sigma_{33}^{M}\right)\sin^2\phi+\sigma_{12}^{M}\sin 2\phi\right]\sin^2\psi\right. \\ &\left.+R_{11}^{M}'\left[\sigma_{11}^{M}+\sigma_{22}^{M}+\sigma_{33}^{M}\right]+\left(R_{33}^{M}'-R_{11}^{M}'\right)\sigma_{33}^{M}+\left(R_{33}^{M}'-R_{11}^{M}'\right)\left[\left(\sigma_{13}^{M}\cos\phi+\sigma_{23}^{M}\sin\phi\right)\sin 2\psi\right]\right\}d_{\{hkl\}}^{0}+d_{\{hkl\}}^{0}\end{aligned} \tag{1.24}$$

In general, the aim of experiment is to find residual stresses expressed in X coordinates system (σ_{ij}). Hence, it is convenient to establish the relation between ($<\varepsilon_{33}'(\psi,\phi)>_{\{hkl\}}$) and σ_{ij} (while Eq. 1.21 contain stresses in L coordinate system). This aim is achieved by introducing modified elastic diffraction constants F_{ij} and instead of Eq. 1.21 we have:

$$<\varepsilon_{33}'(\psi,\phi)>_{\{hkl\}}=F_{ij}^{M}(R_{ij}^{M},\psi,\phi)\sigma_{ij}^{M} \tag{1.25}$$

where σ_{ij}^{M} are the macrostresses expressed in X coordinate system. The F_{ij}^{M} coefficients are not tensor components because they relate the stress tensor σ_{ij}^{M} expressed in the sample coordinate system **X** to the elastic strain $<\varepsilon_{33}'^{g(el)}>_{\{hkl\}}$ defined along L_3 axis of the L system. Using the appropriate transformation of stress tensor (Eq. 1.13), the F_{ij}^{M} diffraction elastic constants can be calculated from R_{ij} ones:

$$F_{ij}^{M}(\{hkl\},\psi,\phi)=a_{ki}a_{lj}\,R_{kl}^{M}(\{hkl\},\psi,\phi) \tag{1.26}$$

For example:

$$\begin{aligned}F_{11}^{M} &= R_{11}^{M}\cos^2\phi\cos^2\psi+R_{22}^{M}\sin^2\phi+R_{33}^{M}\cos^2\phi\sin^2\psi \\ &-R_{12}^{M}\sin 2\phi\cos\psi+R_{13}^{M}\cos^2\phi\sin 2\psi-R_{23}^{M}\sin 2\phi\sin\psi\end{aligned} \tag{1.27}$$

It should be emphasised that the R_{ij}^{M} constants, as noted in Eq. 1.21, depend on the orientation of L system with respect to X one if the sample is textured. However, in the case of a polycrystalline with random grain orientations (quasi-isotropic sample), the R'_{ij} constants do not vary with the ϕ and ψ angles because the sample is isotropic.

1.4. Calculation of diffraction elastic constants

As it was already mentioned, diffraction elastic constants are the main parameters used in the analysis of residual stresses by diffraction method. In general it is not possible to find equation expressing $R'_{ij}(\psi,\phi)$ due to a complex character of elastic interactions. For this reason some simplifying assumptions and models are used.

1.4.1. Diffraction elastic constants for quasi-isotropic material

The quasi-isotropic polycrystalline material is defined as a material having isotropic macroscopic properties in spite of the anisotropy of particular grains (Bunge, 1982). For a quasi-isotopic material the following relation occurs:

$$R_{12}^M = R_{13}^M = R_{23}^M = 0 \quad \text{and} \quad R_{11}^M = R_{22}^M \tag{1.28}$$

Consequently, only two independent diffraction elastic constants, i.e.: $R_{11}^M = R_{22}^M$ and R_{33}^M exist. These diffraction elastic constants are defined with respect to the L coordinates system and they do not depend on its orientation characterized by the angles ϕ and ψ (Fig.1. 3).
For quasi-isotropic materials the s_1 and s_2 diffraction elastic constants are commonly used instead of the more general R_{ij}^M constants. In this case the following relations are fulfilled (compare Eq. 1.16):

$$s_1 = R_{11}^M = R_{22}^M \quad \text{and} \quad \frac{1}{2}s_2 = (R_{33}^M - R_{11}^M) \tag{1.29}$$

Hence, the exemplary equation for F_{11} constant (Eq. 1.27) for quasi-isotropic material can be simplified to:

$$F_{11}^{\ M} = s_1 + \frac{1}{2}s_2 \cos^2\phi \sin^2\psi \tag{1.30}$$

The s_1 and s_2 constants can be also expressed by the Young's modulus (E') and Poisson's ratio (ν') defined for a group of diffracting grains, interacting with the surrounding matrix (E' and ν' are expressed in L system, i.e., for example the Young's modulus is taken along L_3 axis). The s_1 and s_2 constants are equal to:

$$s_1 = -\frac{\nu'}{E'} \quad \text{and} \quad s_2 = 2\left(\frac{1+\nu'}{E'}\right) \tag{1.31}$$

where: $E' = \frac{1}{R_{33}^M}$ and $\nu' = -\frac{R_{11}^M}{R_{33}^M} = -\frac{R_{22}^M}{R_{33}^M}$.

We can conclude that for a quasi-isotropic polycrystalline material only two independent diffraction elastic constants are defined (i.e., s_1 and s_2 or $R_{11}^M = R_{22}^M$ and R_{33}^M) with respect to L system. These elastic constants depend on the single crystal constants, grain-matrix interaction and *hkl* reflection, but they do not depend on ϕ and ψ angles. A linear relation of F_{11}^M versus $sin^2\psi$ (for a fixed ϕ value) can be easily seen from Eq. 1.30.

In further considerations the effects of crystal anisotropy (existing also in a quasi-isotropic sample) will be characterized by the factor $\Gamma_{\{hkl\}}$ (Dölle, 1979).:

$$\Gamma_{\{hkl\}} = \frac{\left(h^2k^2 + h^2l^2 + k^2l^2\right)}{\left(h^2 + k^2 + l^2\right)^2} \tag{1.32}$$

The $\Gamma_{\{hkl\}}$ factor depends only on Miller indices of reflecting planes and it varies in the range (0,1/3). It has the minimum and the maximum for {100} and {111} crystal planes, respectively. We will calculate now the diffraction elastic constants for a quasi-isotropic material using two limiting models of elasticity.

Voigt model

In this approach (Voigt, 1928) the constant elastic deformation in each grain "g" is assumed: $\varepsilon'^{g(el)}_{ij} = \varepsilon'^{M(el)}_{ij}$ (Fig 1.9). It means that

$$< \varepsilon'^{g(el)}_{33} >_{\{hkl\}} = \varepsilon'^{M(el)}_{33} = [c'^{g}\ ]^{-1}_{33ij}\ \sigma'^{M}_{ij} \tag{1.33}$$

$$R^{M(V)}_{ij} = [c'^{g}\ ]^{-1}_{33ij} \tag{1.34}$$

where […] means the average over the volume sample.
Diffraction elastic constants s_1^V and ½ s_2^V for quasi-isotropic material with regular lattice are (Noyan and Cohen, 1987):

$$s^V_{1,\{hkl\}} = \frac{S_{11}\left(2S_{11} + S_{12}\right) + S_{12}\left(S_{11} - 4S_{12}\right) - S_{44}\left(S_{11} - 3S_{12}\right)}{2S_{44} + 6\left(S_{11} - S_{12}\right)}$$

$$\frac{1}{2}s^V_{2,\{hkl\}} = \frac{5S_{44}\left(2S_{11} + S_{12}\right)}{2S_{44} + 6\left(S_{11} - S_{12}\right)} \tag{1.35}$$

Diffraction elastic constants in this model do not depend on reflecting plane indices {hkl} and on the Γ_{hkl} factor.

Reuss model

In this case a constant stress is assumed in all grains: $\sigma'^{g(er)}_{ij} = \sigma'^{M}_{ij}$ (Fig. 1.8); the superscript "er" means: "elastic reaction" (of a grain). Elastic constants for the group of diffracting grains can be expressed by single crystal compliance constants (Noyan and Cohen, 1987):

$$E_{\{hkl\}}{}^{R}{}' = \left(S_{11} - \left(2S_{11} - 2S_{12} - S_{44}\right)\Gamma_{\{hkl\}}\right)^{-1}$$
$$\nu^{R}_{\{hkl\}}{}' = -\frac{S_{12} + \left(S_{11} - S_{12} - 0.5S_{44}\right)\Gamma_{\{hkl\}}}{S_{11} - 2\left(S_{11} - S_{12} - 0.5S_{44}\right)\Gamma_{\{hkl\}}} \tag{1.36}$$

After substitution of the above equation to Eq.1.31, anisotropic elastic constants are:

$$s^{R}_{1,\{hkl\}} = S_{12} + \left(S_{11} - S_{12} - 0.5S_{44}\right)\Gamma_{\{hkl\}}$$
$$\frac{1}{2}s^{R}_{2,\{hkl\}} = S_{11} - S_{12} - 3\left(S_{11} - S_{12} - 0.5S_{44}\right)\Gamma_{\{hkl\}} \tag{1.37}$$

In this case diffraction constants depend on the refelecting plane {hkl}. Diffraction elastic constants for Reuss and Voigt models for ferrite and austenic steel are presented in Fig 1.7. They were calculated using stiffness elastic tensor presented in Table 1.1. The compliance tensor presented in equations is an inverse of the stiffness tensor.

Table 1.1. *Single crystal elastic constants used for the calculation of diffraction elastic constants (Simoms and Wang, 1971; Ceretti, 1993).*

Material	C_{11} [GPa]	C_{12} [GPa]	C_{44} [GPa]
Fe-austenite	197	122	124
Fe-ferrite	231	134.4	116.4
TiN	497	105	168
Cu	170	124	64.5
Al	106.8	60.4	28.3
SiC	350	140.4	233

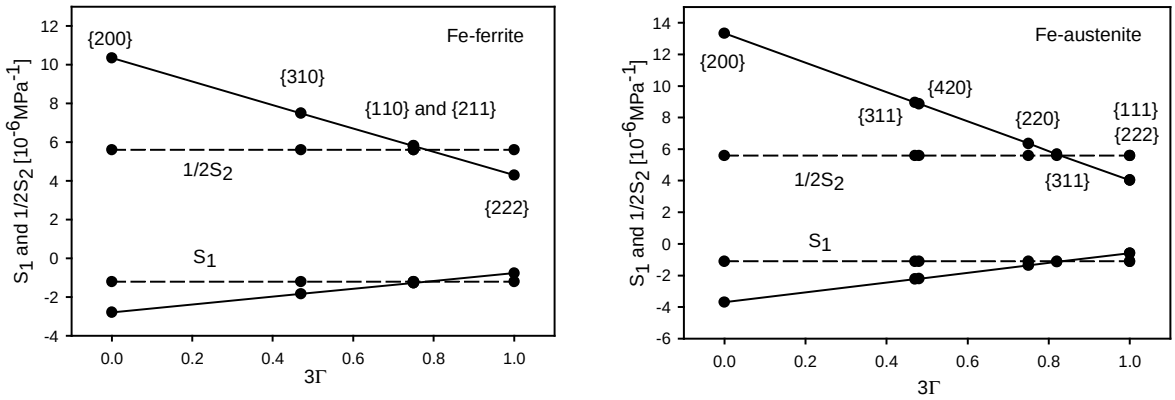

Fig. 1.7. *The s_1 and ½ s_2 constants versus orientation factor 3Γ calculated from the single crystal data using Reuss (solid line) and Voigt (dotted line) models.*

1.4.2. Diffraction elastic constants for anisotropic material (textured)

In many cases we cannot assume isotropic interaction between grains, then we talk about anisotropic material. Anisotropic interaction is a result of texture, anisotropic properties of the grains and shapes of the grains. Because of sample anisotropy, the six independent elastic constants R_{ij}^M vary with orientation of the scattering vector. The values of F_{ij}^M must be known for each orientation of the scattering vector for which the interplanar spacings are measured. The anisotropy of the sample can be observed as nonlinearities of the F_{11}^M versus $sin^2\psi$ *plot*. To calculate diffraction elastic constants we have to use appropriate model of interactions between grains. We will consider the following models:

Reuss model

In this approach the stress is assumed to be uniform across the sample (Barral et al., 1987; Brakman, 1987; Reuss, 1929) for all polycrystalline grains, i.e., $\sigma'^{g(er)}_{ij} = \sigma'^{M}_{ij}$ (Fig. 1.8). The grain elastic strain in the L_3 direction (Fig.1.3) can be written as:

$$\varepsilon'^{g(el)}_{33} = s'^{g}_{33ij}\,\sigma'^{g(er)}_{ij} = s'^{g}_{33ij}\,\sigma'^{M}_{ij} \quad \text{and} \quad <\varepsilon'^{g(el)}_{33}>_{\{hkl\}} = <s'^{g}_{33ij}>_{\{hkl\}}\,\sigma'^{M}_{ij} \tag{1.38}$$

where s'^{g}_{33ij} are the single crystal compliances of a grain and all quantities are expressed in L system.

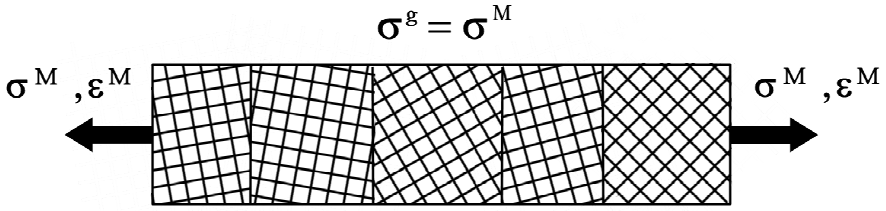

Fig. 1.8. *Scheme of interaction between grains for Reuss model - homogeneous stress.*

Consequently, using the Reuss model, the diffraction elastic constants can be calculated as the average value of single crystal compliances:

$$R_{ij}^{M(R)} = < s'^{g}_{33ij} >_{\{hkl\}} = \frac{\sum_{\{h\,k\,l\}} \left\{ \int_0^{2\pi} s'^{g}_{33ij}(\boldsymbol{g})\, f(\boldsymbol{g})\, d\gamma \right\}_{(h\,k\,l)}}{\sum_{\{h\,k\,l\}} \left\{ \int_0^{2\pi} f(\boldsymbol{g})\, d\gamma \right\}_{(h\,k\,l)}} \tag{1.39}$$

The integration is carried over all $\boldsymbol{g}$ orientations representing reflecting grains only (these orientations are inter-related by the rotation γ around the scattering vector, see Fig. 1.5. Moreover, the averaging over all equivalent {hkl} planes is done.

Voigt model

The uniform grain elastic strain is assumed to be equal to the elastic macro-strain value $\varepsilon'^{g(el)}_{ij} = \varepsilon'^{M(el)}_{ij}$ in the Voigt model (Voigt 1928) - Fig. 1.9.

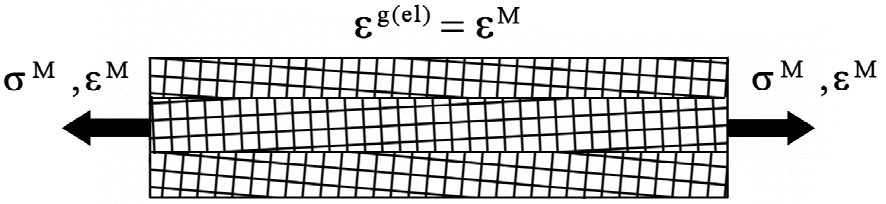

Fig. 1.9. *Scheme of interaction between grains for Voigt model - homogeneous strain.*

In this case the grain elastic strain in the L_3 direction can be written as:

$$< \varepsilon'^{g(el)}_{33} >_{\{hkl\}} = \varepsilon'^{g(el)}_{33\ \{hkl\}} = \varepsilon'^{\,M(el)}_{33} = [c'^{g}\,]^{-1}_{33ij}\, \sigma'^{\,M}_{ij} \tag{1.40}$$

where $\boldsymbol{c}'^{g}$ is the single crystal stiffness tensor defined with respect to L frame. The average, marked by *[…]*, is calculated over the whole considered volume. Finally, the $R_{ij}^{M(V)}$ constants are equal to:

$$R_{ij}^{M(V)} = [c'^{g}\ ]_{33ij}^{-1} \tag{1.41}$$

The texture function $f(\mathbf{g})$ is again used in the calculation of $R_{ij}^{M(V)}$ constants; however in this model *all grains* from the studied volume contribute to the average:

$$[c'^{g}_{ijkl}\ ] = \frac{1}{8\pi^2}\int_E c'^{g}_{ijkl}(\boldsymbol{g})\, f(\boldsymbol{g})\, d\boldsymbol{g} \tag{1.42}$$

In the above equation the single crystal stiffnesses $c'^{g}_{ijkl}(\boldsymbol{g})$ (considered in L system) is integrated over the whole orientation Euler space (E). Because the integration is over the whole Euler space the elastic constants do not depend on {hkl} plane.

Self-consistent model

In the self-consistent model (Baczmański et al., 1997b and 2003c; Kröner 1961; Lipiński and Berveiller 1989) a polycrystalline grain is considered as an ellipsoidal inclusion inside a homogeneous continuous medium (Fig. 1.10).

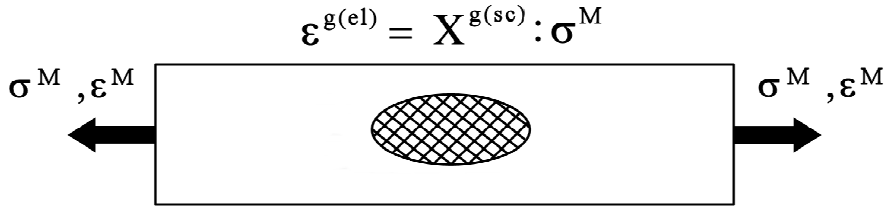

Fig. 1.10. *Scheme of interaction between grains for self-consistent model. Ellipsoidal inclusion is embedded in a homogeneous medium.*

According to this formalism, the elastic strain $\varepsilon'^{g(el)}_{nm}$ (or stress $\sigma'^{g(er)}_{nm}$), in the *g-th* grain, is related to the macrostrain $\varepsilon'^{M(el)}_{kl}$ (or macrostress σ'^{M}_{kl}) by the concentration tensor $\boldsymbol{A}'^{g(sc)}$ (or $\boldsymbol{B}'^{g(sc)}$), i.e.:

$$\varepsilon'^{g(el)}_{nm} = A'^{g(sc)}_{mnkl}\ \varepsilon'^{M(el)}_{kl} \quad \text{and} \quad \sigma'^{g(er)}_{nm} = B'^{g(sc)}_{mnkl}\ \sigma'^{M}_{kl} \tag{1.43}$$

where $\boldsymbol{A}'^{g(sc)}$ and $\boldsymbol{B}'^{g(sc)} = \boldsymbol{c}'^{g}\,\boldsymbol{A}'^{g(sc)}\,\boldsymbol{S}'^{eff}$ are the strain and stress concentration tensors calculated for a purely elastic interaction using the self-consistent method, $\boldsymbol{S}'^{eff}$ is the macroscopic compliance tensor ($\boldsymbol{S}'^{eff}$ will be described in Chapter 2) and $\boldsymbol{c}'^{g}$ is the grain stiffness tensor expressed in L system.
Substituting the Hook's law in macro and micro scales ($\varepsilon'^{M(el)}_{ij} = S'^{eff}_{ijkl}\sigma'^{M}_{kl}$ and $\varepsilon'^{g(el)}_{ij} = s'_{ijkl}\,\sigma'^{g(er)}_{kl}$) in the above equations, the grain elastic strain can be related to the macro-stress, i.e.:

$$\varepsilon'^{g(el)}_{nm} = X'^{g(sc)}_{33kl}\ \sigma'^{M}_{kl} \tag{1.44}$$

where: $X'^{g(sc)}_{33kl} = A'^{g(sc)}_{33mn}\ S'^{eff}_{mnkl}$ or $X'^{g(sc)}_{33kl} = s'^{g}_{33mn}\ B'^{g(sc)}_{mnkl}$.
Finally, the diffraction elastic constants $R_{ij}^{(sc)}$ for a textured sample are defined as:

$$R_{ij}^{M(sc)} = < X'^{g(sc)}_{33ij} >_{\{hkl\}} = \frac{\sum_{\{h\,k\,l\}} \left\{ \int_0^{2\pi} X'^{g(sc)}_{33ij}(\boldsymbol{g})\ f(\boldsymbol{g})\, d\gamma \right\}_{(h\,k\,l)}}{\sum_{\{h\,k\,l\}} \left\{ \int_0^{2\pi} f(\boldsymbol{g})\, d\gamma \right\}_{(h\,k\,l)}} \tag{1.45}$$

where the integration is carried over all $\boldsymbol{g}$ orientations representing reflecting grains.
For the calculation of the $\boldsymbol{X}'^{g(sc)}$ tensor, the macro-compliance tensor $\boldsymbol{S}'^{eff}$ for a polycrystalline aggregate must be known. To do this, the self-consistent algorithm is applied for the elastic range of deformation. For textured material the macroscopic stiffness tensor can be written as:

$$C'^{eff}_{ijkl} = \int_E c'^{g}_{ijmn} A'^{g(sc)}_{mnkl}(\boldsymbol{g})\ f(\boldsymbol{g})\, d\boldsymbol{g} \tag{1.46}$$

The macroscopic stiffness tensor $\boldsymbol{C}'^{eff}$, as well as the strain concentration tensor $\boldsymbol{A}'^{g(sc)}$ can be calculated using the self-consistent scheme described in Chapter 2 and assuming the ellipsoidal shape of inclusion, representing a polycrystalline grain.

Self-consistent model for free surface conditions

In this part the idea of directional dependence of grain interaction is proposed for any symmetry of the textured sample. To do this, the influence of a free surface (grains on the surface can freely deform in normal direction) and of the shape of grains is considered. (Van Leeuwen et al., 1999, Welzel et al., 2003) In general, the deformed grains are elongated and flat (for example, after cold rolling). Moreover, in X-ray diffraction the information volume of the sample is defined by absorption, causing unequal contribution of different crystallites to the intensity of the measured peak (the surface grains participate more effectively in diffraction than the grains which are deeper in the sample (see Fig 1.11). The following scheme for flat and elongated grains in the near surface volume (Fig. 1.12) is proposed: the forces and stresses normal to the surface propagate similarly as in the Reuss model, while a two dimensional elastic coupling between grains occurs in the plane parallel to the sample surface (it is calculated by the self-consistent model).

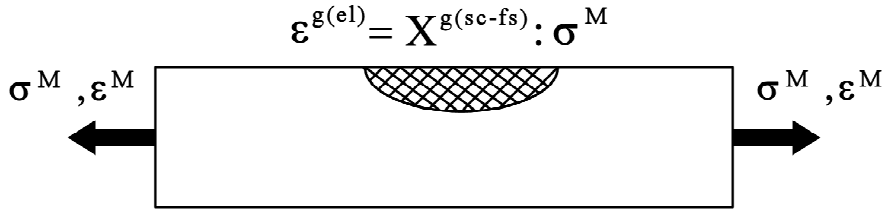

Fig. 1.11. *Scheme of interaction between grains for self-consistent free-surface. Ellipsoidal inclusion is placed near the surface of the homogeneous medium.*

Similarly as in Eq. 1.43, the grain stresses $\sigma_{ij}^{g(er)}$ are related to the macrostress by the concentration $\boldsymbol{B}^{g(sc-fs)}$ tensor, (see chapter 2.6) i.e.,:

$$\sigma_{ij}^{g(er)} = B_{ijkl}^{g(sc-fs)} \sigma_{kl}^{M} \tag{1.47}$$

where $\mathrm{B}^{\mathrm{g(sc-fs)}} = \mathrm{c}^{\mathrm{g}}\mathrm{A}^{\mathrm{g(sc)}}\mathrm{S}^{\mathrm{eff}}$ tensor must be calculated for inclusion in the surface volume of the sample and all quantities are expressed in X system (see Fig. 1.11).

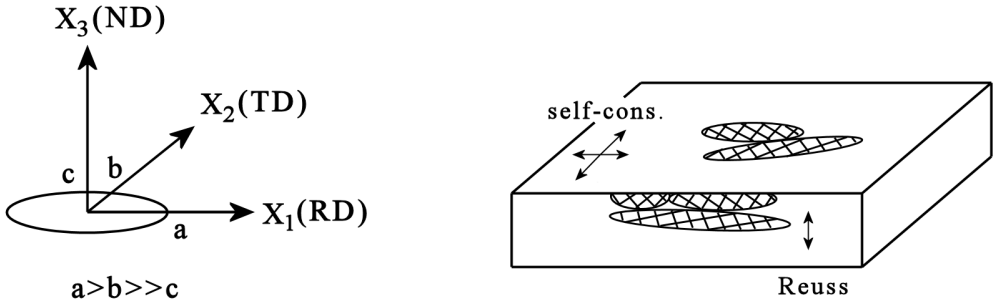

Fig.1.12. *Scheme of interaction between elongated and flat grains in the near surface volume for cold rolled sample, i.e., Reuss model in x_3 direction and self-consistent model in the plane (x_2, x_3). The sample axes are defined by: RD - rolling direction, TD - transverse direction and ND - normal direction. The orientation and the main axis of ellipsoidal inclusion are defined.*

The main difficulty is to calculate the $B_{ijkl}^{g(sc-fs)}$, which differs from that defined for inclusion completely embedded in the material. To realize the conditions of flat grains with a free surface, a special construction of stress concentration tensor is proposed, i.e.:

$$B_{ijkl}^{g(sc-fs)} = \begin{cases} I_{ijkl} & \text{for } i = 3 \text{ or } j = 3 \;\Rightarrow \textit{as in Reuss model} \\ B_{ijkl}^{g(sc)} & \text{for } i \neq 3 \text{ and } j \neq 3 \;\Rightarrow \textit{as in self-consistent bulk model} \end{cases} \tag{1.48}$$

where $\boldsymbol{I}$ is the identity tensor, and $\boldsymbol{B}^{g(sc)}$ is the concentration tensor calculated for inclusion completely embedded in the material.

Using Eqs. 1.47 and 1.48, the planar components of grain stress ($\sigma_{ij}^{g(er)}$ for $i \neq 3$ and $j \neq 3$) are calculated assuming the same interaction between grains as for inclusion completely embedded in the material. However, the grain stress components in which appear forces normal to the sample surface ($\sigma_{ij}^{g(er)}$ for $i = 3$ or $j = 3$), are taken as equal to the corresponding macrostresses (σ_{ij}^{M}). This means that elastic interaction between grains is neglected in the direction normal to the surface.

To calculate diffraction elastic constants, the stress concentration tensor is transformed to L system, i.e., $B'^{g(sc-fs)}_{ijkl} = a_{im}a_{jn}a_{ko}a_{lp}B^{g(sc-fs)}_{mnop}$ and $X'^{g(sc-fs)}_{33kl} = s'^{g}_{33mn}\, B'^{g(sc-fs)}_{mnkl}$ tensor components are computed. Finally, $R_{ij}^{M(sc-fs)}$ diffraction elastic constants are equal to (cf., Eq. 1.45):

$$R_{ij}^{M(sc-fs)} = < X'^{g(sc-fs)}_{33kl} >_{\{hkl\}} = \frac{\sum_{\{h\,k\,l\}} \left\{ \int_0^{2\pi} X'^{g(sc-fs)}_{33ij}(\boldsymbol{g})\, f(\boldsymbol{g})\, d\gamma \right\}_{(h\,k\,l)}}{\sum_{\{h\,k\,l\}} \left\{ \int_0^{2\pi} f(\boldsymbol{g})\, d\gamma \right\}_{(h\,k\,l)}} \tag{1.49}$$

Experimental verification

Each of the models described above is based on different assumptions and consequently the calculated diffraction elastic constants are different. The calculated elastic constants F_{ij}^{M} (see Eq. 1.26) which are expressed by the R_{ij}^{M}, can be verified experimentally. In the first step, the measurement of $< d^{\Sigma=0}(\psi,\phi) >_{\{hkl\}}$ in the non-loaded sample is done; the residual strain $< \varepsilon(\psi,\phi) >^{res}_{\{hkl\}}$ present in a material is:

$$< \varepsilon(\psi,\phi) >^{res}_{\{hkl\}} = \frac{< d^{\Sigma=0}(\psi,\phi) >_{\{hkl\}} - d^{0}_{\{hkl\}}}{d^{0}_{\{hkl\}}} \tag{1.50}$$

Next, the interplanar spacings $< d^{\Sigma}(\psi,\phi) >_{\{hkl\}}$ for the same sample but under unaxial stress Σ_{11} (applied along the rolling direction) are measured. Due to the superposition of strains for purely elastic deformation, the total lattice strain $< \varepsilon(\psi,\phi) >^{tot}_{\{hkl\}}$ in the loaded sample is:

$$< \varepsilon(\psi,\phi) >^{tot}_{\{hkl\}} = \frac{< d^{\Sigma}(\psi,\phi) >_{\{hkl\}} - d^{0}_{\{hkl\}}}{d^{0}_{\{hkl\}}} = < \varepsilon(\psi,\phi) >^{res}_{\{hkl\}} + F_{11}^{M}(\psi,\phi)\Sigma_{11} \tag{1.51}$$

where: $F_{11}^{M}(\psi,\phi)$ are the diffraction elastic constants for *{hkl}* reflection.
The value $d^{0}_{\{hkl\}}$ used in Eq. 1.51 can be approximated by the mean value of lattice spacings measured at different directions of the scattering vector in the non-loaded sample. Finally, the values of $F_{11}^{M}(\psi,\phi)$ can be experimentally determined for different orientations of the scattering

vector:

$$F_{11}^{M}(\psi,\phi)=\frac{<\varepsilon^{\Sigma}(\psi,\phi)>_{\{211\}}}{\Sigma_{11}} \tag{1.52}$$

where $<\varepsilon^{\Sigma}(\psi,\phi)>_{\{hkl\}}=<\varepsilon(\psi,\phi)>_{\{hkl\}}^{tot}-<\varepsilon(\psi,\phi)>_{\{hkl\}}^{res}$ and Σ_{11} stress component is calculated as the ratio of the applied force and the cross-section of the sample.

The results of the elastic constants calculations made by Baczmański (Baczmański, Habilitation Thesis, 2005) are presented here. The cold rolled ferrite steel sample (reduction of 95%) was studied. The *{110}, {100}* and *{211}* pole figures have been determined and the orientation distribution function was calculated. Next, the interplanar spacings *{211}* have been measured using Cr X-ray radiation (λ=2.291 Å). The measurements were repeated for three values of the applied stresses, i.e., Σ_{11} = *200, 400* and *500* MPa. As shown in Fig. 1.13, the determined diffraction elastic constants are almost the same for different values of applied stress Σ_{11}.

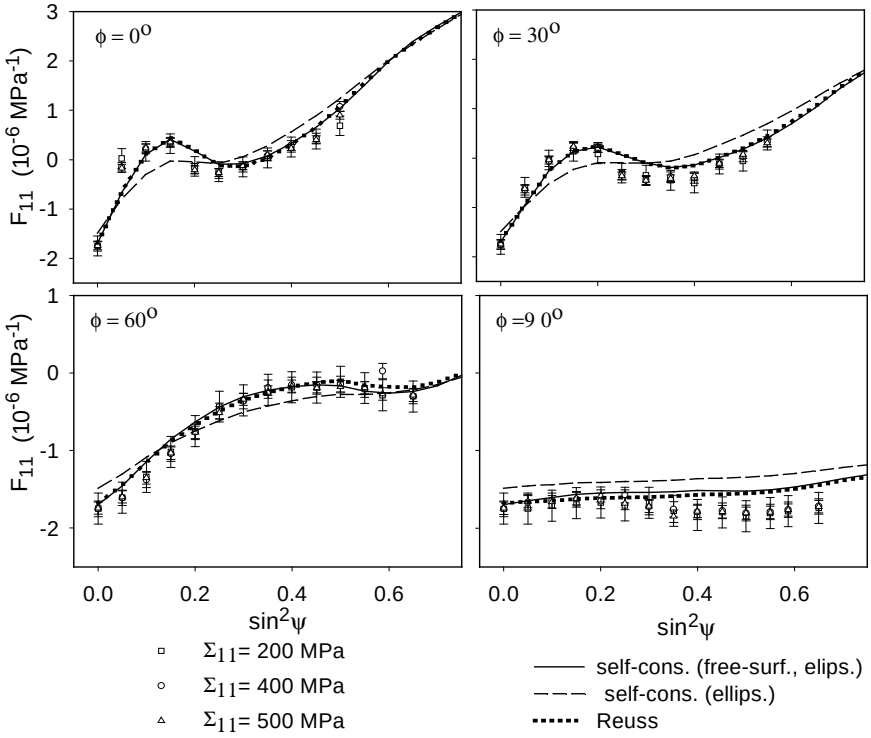

Fig.1.13. *Experimental and theoretical F_{11}^{M} versus $\sin^2\psi$ for cold rolled ferritic steel (reduction of 95%). Single crystal elastic constants given in Table 1.1 and orientation distribution function were used in calculations. (Baczmański, Habilitation Thesis, 2005)*

The best agreement between experimental and calculated diffraction elastic constants was obtained using the Reuss and self-consistent (free surface) models. Similar conclusions were reported by other authors (for example, Hauk, 1986, Pintschovius et al. 1987) for plastically deformed steels.

1.5. Multi-reflection method for stress determination

The standard $sin^2\psi$ method of stress determining is based on the measurement of interplanar spacing for various directions of the scattering vector (Noyan and Cohen, 1987). These directions are defined by ϕ and ψ angles (Fig. 1.3). In diffraction method, the mean interplanar spacing $<d(\psi,\phi)>_{\{hkl\}}$, averaged for grains from the reflecting group (scattering vector normal to the reflecting *{hkl}* planes), is measured. Using the standard X-ray diffraction method, interplanar spacings are measured as a function of $sin^2\psi$ for constant *hkl* reflection and ϕ angle. The measured interplanar spacings are expressed as (cf. Eq. 1.25):

$$< d(\psi,\phi)>_{\{hkl\}} = [\ F_{ij}^{M}\ (\{hkl\},\psi,\phi)\ \sigma_{ij}^{M}\ ]\ d_{\{hkl\}}^{0} + d_{\{hkl\}}^{0} \tag{1.53}$$

where: $F_{ij}^{M}\ (\{hkl\},\psi,\phi)$ are anisotropic diffraction elastic constants.

In classical $\sin^2\psi$ method the residual stresses are determined using a selected diffraction peak. In the new method elaborated by Baczmański and Skrzypek (Skrzypek and Baczmański; 2001a 2001b) a few diffraction peaks are analysed simultaneously (multi-reflection method). In this procedure, the *equivalent lattice parameters* $<a(\psi,\phi)>_{\{hkl\}}$:

$$< a(\psi,\phi) >_{\{hkl\}} =< d(\psi,\phi) >_{\{hkl\}} \sqrt{h^2+k^2+l^2} \tag{1.54}$$

are calculated from the measured interplanar spacings for different *hkl* reflections and for various orientations of the scattering vector characterized by the ϕ and ψ angles; (the above relation is valid in the case of the cubic crystal symmetry). Consequently, the σ_{ij}^{M} residual macrostresses are determined from the following formula:

$$< a(\psi,\phi)>_{\{hkl\}} = [\ F_{ij}^{M}\ (\{hkl\},\psi,\phi)\,\sigma_{ij}^{M}\ ]\ a^0 + a^0 \tag{1.55}$$

where the a^0 is the reference length equal to the lattice parameter for a stress free sample.

Due to transformation expressed by Eq. 1.54 only one a^0 value instead of many $d_{\{hkl\}}^{0}$ values is used when equivalent $<a(\psi,\phi)>_{\{hkl\}}$ parameters are fitted to the experimental points. The reference length (a^0) and macrostresses σ_{ij}^{M} can be found using the fitting procedure and previously calculated $F_{ij}^{M}\ (\{hkl\},\psi,\phi)$ constants. The main advantage of the multi-reflection method is that experimental data obtained for various *hkl* reflections are treated simultaneously and only one stress-free lattice parameter is to be determined.

Chapter 2

Deformation models for polycrystalline materials

2.1. Introduction

In order to perform correct interpretation of many experimental data it is necessary to apply deformation models. Roughly, there are two types of deformation models: these using the finite elements method and micro-macro crystallographic models. In the first case the material is treated as a continuous medium and the crystalline character of grains was not taken into account. The finite element method is suitable for the prediction of deformation of samples with complex shapes subjected to various loads. On the other hand, the crystallographic deformation models are better adapted to the study of the internal microstructure evolution of a polycrystalline material.

In this work crystallographic deformation models will be used. These models can predict many parameters and characteristics which are essential for experimental data analysis, e.g.: crystallographic texture, hardening curves (stress-strain curves), residual stresses, plastic flow surfaces, dislocation density, stored energy and many others.

In the present chapter two elastoplastic deformation models will be discussed. The first one - LW model - is based on original formulations due to Leffers (Lefers, 1968a 1968b) and on further developments done by Wierzbanowski (Wierzbanowski, 1978, 1982, 1987). The second one is the self-consistent (SC) model. The first applications of SC scheme were performed by Hutchinson (Hutchinson, 1964a, 1964b) and Berveiller and Zaoui (Berveiller and Zaoui, 1979) in the range of the small elasto-plastic strain. A more systematic and general approach, based on the kinematic integral equation, was developed by Lipinski and Berveiller (Lipinski and Berveiller, 1989) and successfully applied for the three-dimensional representative volume element under large deformation (Lipiński, 1993). In this chapter the SC model developed by A. Baczmański (Baczmański et al. 1994a and 2004) will be presented. The results predicted by both models for typical fcc, bcc and hcp structure will be discussed.

2.2. Mechanisms of plastic deformation

Contrary to the elastic deformation, which involves reversible atom displacements, the plastic deformation undergoes by non-reversible mechanisms such as crystallographic slip or (and) mechanical twinning. The both mechanisms are non-reversible, which means that after the release of external forces some permanent deformation stays in the material. Both during the slip and twinning, two parts of crystal (or grain) are sheared one with respect to another. The crystallographic slip is schematically presented in Fig.2.1. Neighboring blocs of crystal are relatively displaced. This movement (i.e. slip) occurs on a slip plane (hkl) and along a slip direction [uvw]. Consequently, one defines a slip system [uvw](hkl) and also a family of crystallographically equivalent slip systems <uvw>{hkl}. The slip phenomenon occurs due to a movement of a huge number of dislocations on a slip plane. The dislocation movement, and hence the slip itself, appears in relatively narrow volume of material, called the slip band (with an average width *h*); on the other hand, displaced blocs of crystal (with an average width *H*) are "inactive" in their volume (Fig. 2.1). The slip usually appears on planes for which the density of atoms is the highest (due to the lowest energy necessary to shift atoms from one stable position to another). The slip occurs if the shear stress acting in a slip system exceeds some critical value.

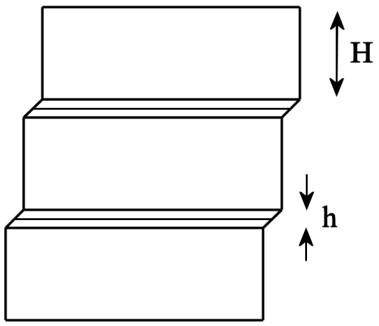

Fig. 2.1. *Slip in a single crystal: blocs of a crystal of an average width H are relatively displaced along the slip plane and slip direction. Regions of an average width h, where slip intensively occurs – are called slip bands. Dislocation density is of a few orders of magnitude higher inside slip bands than in other parts of a crystal. Typical ratio of H/h is between* 10^3 *and* 10^4.

Mechanical twinning consists of the shearing movements of atomic planes, which leads to the formation of a crystal region with a crystal lattice being a mirror image (with respect to the boundary plane) of the original crystal – Fig. 2.2. This newly created crystal region is called *twin*. Let us notice that during a twin formation, all subsequent atom layers of the twin are displaced (by shear movement) with respect to neighboring ones. "Non-active blocs" do not exit in this case and consequently the shear deformation is high. By activation of many slip (or twinning) systems one can obtain any imposed deformation of a crystal. It can be shown that at least five independent shear systems (slip or twinning) are necessary to produce an imposed deformation. We will see later that besides deformation also crystal lattice rotation is induced by slip or twinning.

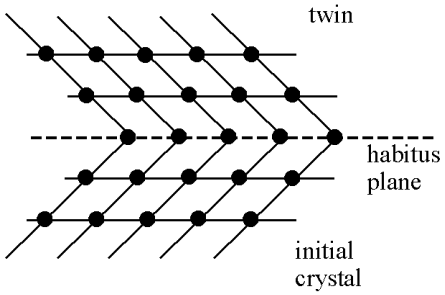

Fig. 2.2. *A twin is created from an original crystal by shearing movements of consecutive atomic layers. In analogy to slip, one defines the twinning direction and plane (the latter being parallel to the boundary plane and is called habitus plane).*

Among two described mechanisms of plastic deformation, generally the slip is dominating. Twinning can appear in materials in which a number of independent slip systems in not sufficient to produce an imposed deformation (e.g., in h.c.p. metals or in f.c.c. metals deformed in low temperatures). However, if one considers f.c.c. or b.c.c. metals deformed in room temperature, it is generally sufficient to take into account only slip phenomenon.

2.3. Macroscopic description

The aim of elastoplastic models is to describe processes occurring in polycrystalline materials during deformation. In such models, the behaviour of a crystal grain inside the polycrystalline material under applied stresses Σ_{ij} is studied. The calculations are performed on two different scales: the macro-scale, where the average elastic $E_{ij}^{(el)}$ and plastic $E_{ij}^{(pl)}$ macrostrains are defined, and the grain scale, in which the behaviour of each crystallite under stresses σ_{ij}^{g} is analyzed (Fig 2.3).

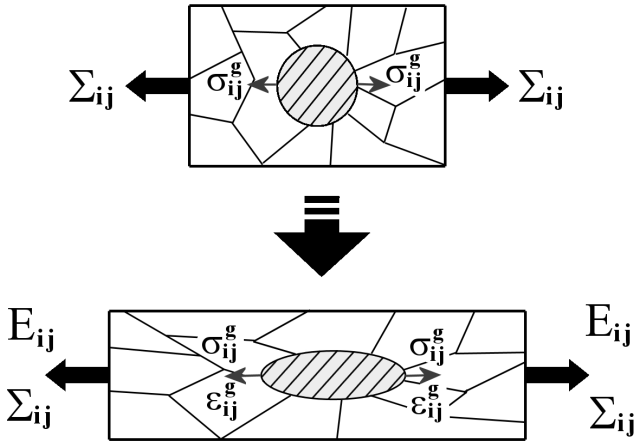

Fig. 2.3. *Elastoplastic deformation of a polycrystalline material under applied stress* Σ_{ij} .

The scheme of elastoplastic behaviour of a polycrystalline material during unaxial tensile test is presented in Fig. 2.4, where two characteristic regions of deformation are indicated. The linear part of Σ_{11} vs. E_{11} curve represents the elasticity described by average elastic constants tensors, which relate the applied stresses (Σ_{ij}) with the elastic strains of the sample (E_{kl}). In this range Hook law is used. In the elasto-plastic deformation range we use similar relations, but concerning the stress and strain increments. Increments $\Delta\Sigma_{ij}$ and ΔE_{kl} are related by *tangent moduli*. They can be calculated if active slip systems and corresponding glide shears are known in all grains. In the elasto-plastic range tangent moduli change with deformation and their values have to be calculated continuously.

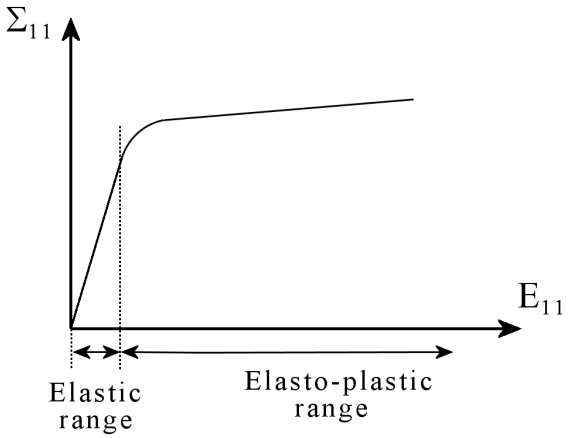

Fig. 2.4. Σ_{11} *vs.* E_{11} *curve for unaxial tensile test.*

2.4. Behaviour of a grain

2.4.1. Slip system

To predict the plastic deformation on a grain scale it is necessary to study the modification of grain parameters occurring during the slip and twinning phenomena. In the models used in this work only the first one, i.e. the slip, is taken into account.

Slip is the elementary mechanism of plastic deformation. It occurs on a crystal plane (hkl) and along a [uvw] direction (situated in this plane). The slip plane is defined by the unit vector **n** (perpendicular to the plane), and slip direction – by the unit vector **m**. A slip system {**m**, **n**} is usually denoted its crystal indices as: *[uvw](hkl).* It is very useful to introduce the reference frame connected with the slip system: $\boldsymbol{x_1^g=m}$, $\boldsymbol{x_3^g=n}$ (Fig. 2.5 and Fig 2.7). The resolved shear stress, decisive for a slip system activation, is easily expressed in this coordinates system: $\tau = \sigma_{13}^g$. In a similar way, the glide shear $\Delta\gamma$ produced by a single slip is characterized by only one non-zero component $\Delta e_{13}^{pl(g)} = \Delta\gamma$ of the plastic displacement gradient tensor ($\Delta e_{ij}^{pl(g)}$) (compare Figs. 2.5 and 2.6).

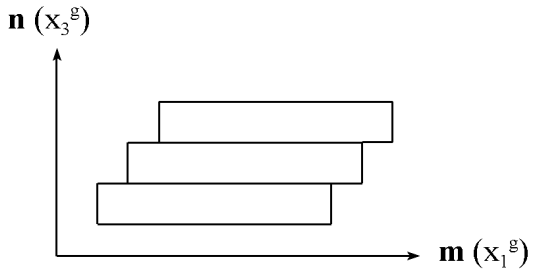

Fig. 2.5. *Displacement of the material during a single slip. The first axis of the* ***g*** *system is defined by* ***m*** *vector and the third axis – by* ***n*** *vector.*

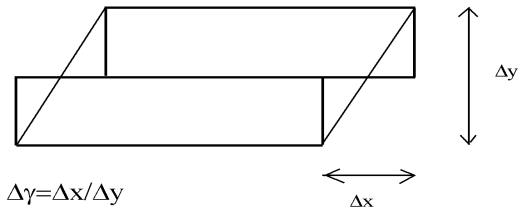

Fig. 2.6. *Definition of the glide shear γ caused by a single slip ($\Delta\gamma = \Delta e_{13}^{pl(g)}$).*

The condition for the slip occurrence is:

$$\tau = \tau_{cr} \tag{2.1}$$

i.e., the resolved shear stress ($\tau = \sigma_{13}^{g}$) has to exceed a critical value τ_{cr} (Schmid law). The resolved shear stress $\tau = \sigma_{13}^{g}$ on the slip system {**m**, **n**} is calculated as:

$$\tau = \sigma_{13}^{g} = a_{1i} a_{3j} \sigma_{ij} = m_i n_j \sigma_{ij} \tag{2.2}$$

where σ_{ij} is the local stress tensor expressed in the sample reference frame - **S** (defined by main symmetry axes of the sample - e.g., rolling, transverse and normal directions in the case of rolling). In the above equation - and in the whole text of this thesis - the convention of summation on repeated lower indices is applied (for upper indices we apply a classical summation symbol). The coefficients a_{ij} define the transition from the system **S** to **g**. It is practical to define the following quantity:

$$R_{ij} = m_i n_j \tag{2.3}$$

characterizing the orientation of **g** system with respect to **S** (Fig. 2.7.). Finally, shear stress τ on the slip system can be expressed as:

$$\tau = R_{ij} \sigma_{ij} \tag{2.4}$$

Both coordinate systems **S** and **g** are schematically shown in Fig. 2.7.

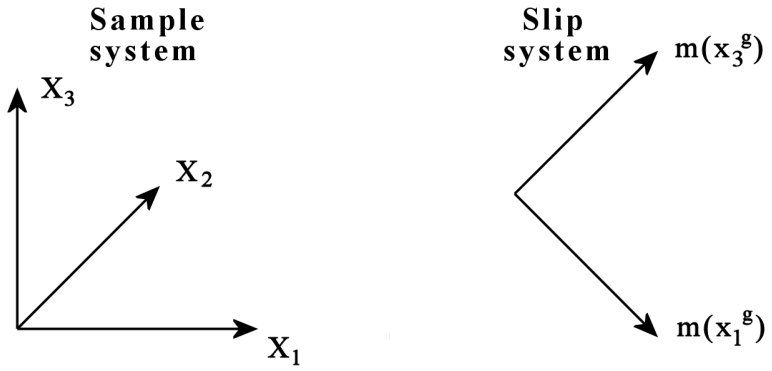

Fig. 2.7. *The coordinates systems of: sample (**S**) and slip (**g**)*

2.4.2. Hardening of slip systems

The slip systems are hardened during deformation, which is reflected in the shape of the stress-strain curve (Fig. 2.8a). In many cases the hardening can be described by linear approach. Consequently a linear range is observed on the stress-strain curve. On the other hand, if one considers a given slip system ("i"), its critical resolved shear stress for slip is linearly dependent on a shear glide of any other active slip system ("j") in a relatively wide range of deformation - Fig. 2.8b. The physical reason of the hardening is an intensive multiplication of dislocations during plastic deformation. The dislocations are necessary for crystal glide, but if they are in an

excessive number – they block each other and this leads to the increasing of critical stress for slip (Franciosi, 1980).

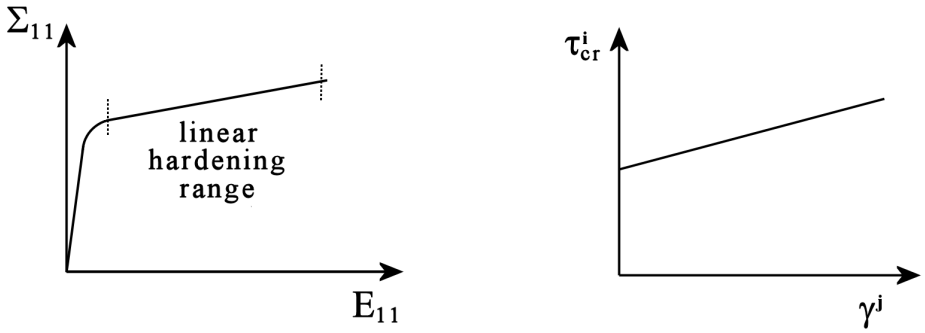

a b

Fig. 2.8. *Hardening curves: a) linear range of stress-strain curve, b) τ_{cr} versus γ according to linear hardening.*

Generally, a multiple slip is observed and in such the case the hardening of the system („*i*") depends on shear glides on all other active slip systems („*j*"):

$$\Delta\tau_{cr}^{i} = \sum_{j} H^{ij}\Delta\gamma^{j} \tag{2.5}$$

or also:

$$\tau_{cr}^{i} = \tau_{0} + \sum_{j} H^{ij}\gamma^{j} \tag{2.6}$$

H^{ij} is called the hardening matrix; obviously it is symmetrical. Both theoretical and experimental study show that in the first approximation this matrix contains two types of terms: strong (h_2) and weak (h_1) ones. Their ratio $A=h_2/h_1$ is called the hardening anisotropy coefficient. The terms located on the matrix diagonal (weak terms) describe the self-hardening of slip systems. An example of a strong term corresponds to a pair of slip systems with perpendicular system directions. For the f.c.c. metals (twelve slip systems <110>{111}) the following hardening matrix was found (Franciosi et al., 1980) :

$$H^{ij} = h_1 \begin{bmatrix} 1 & 1 & 1 & 1 & A & A & 1 & A & A & 1 & A & A \\ 1 & 1 & 1 & A & 1 & A & A & 1 & A & A & 1 & A \\ 1 & 1 & 1 & A & A & 1 & A & A & 1 & A & A & 1 \\ 1 & A & A & 1 & 1 & 1 & 1 & A & A & 1 & A & A \\ A & 1 & A & 1 & 1 & 1 & A & 1 & A & A & 1 & A \\ A & A & 1 & 1 & 1 & 1 & A & A & 1 & A & A & 1 \\ 1 & A & A & 1 & A & A & 1 & 1 & 1 & 1 & A & A \\ A & 1 & A & A & 1 & A & 1 & 1 & 1 & A & 1 & A \\ A & A & 1 & A & A & 1 & 1 & 1 & 1 & A & A & 1 \\ 1 & A & A & 1 & A & A & 1 & A & A & 1 & 1 & 1 \\ A & 1 & A & A & 1 & A & A & 1 & A & 1 & 1 & 1 \\ A & A & 1 & A & A & 1 & A & A & 1 & 1 & 1 & 1 \end{bmatrix} \tag{2.7}$$

2.4.3. Grain deformation and lattice rotation

Every elementary act of the slip causes the deformation $\Delta\varepsilon_{ij}^{pl}$ and the rotation $\Delta\omega_{ij}^{pl}$ of a grain. The lattice rotation is not only a result of the slip. After elementary act of slip the grain is rotated (as a rigid body) - Fig. 2.9, but the lattice itself does not change the orientation. The rotation of lattice is introduced by the orientation preservation of selected sample axes or planes. In the case of tensile test (Fig. 2.9) it is the preservation of the tensile axis orientation.

Let us calculate the deformation and rotation ($\Delta\varepsilon_{ij}^{pl}$ and $\Delta\omega_{ij}^{pl}$), resulting from a glide on one slip system with the shear glide $\Delta\gamma$. In the slip system reference frame (***g***) the displacement gradient tensor has only one non-zero component: $\Delta e_{13}^{pl(g)} = \Delta\gamma$. This tensor after transformation to the sample reference frame (**S**) has the form: $\Delta e_{ij}^{pl} = a_{i1}^{'} a_{j3}^{'} \Delta e_{13}^{pl(g)}$. Taking into account the definition of **S** and **g** systems (Fig. 2.7) we see that: $a_{i1}^{'} = m_i$ and $a_{j3}^{'} = n_j$ ($a_{ij}^{'}$ define the transformation from ***g*** do ***S***, while a_{ij} – from **S** do **g**; obviously: $a_{ij} = a_{ji}^{'}$). Finally: $\Delta e_{ij}^{pl} = m_i n_j \Delta\gamma$, or also:

$$\Delta e_{ij}^{pl} = R_{ij} \Delta\gamma \tag{2.8}$$

If a multiple slip is occurring, then:

$$\Delta e_{ij}^{pl} = \sum_s R_{ij}^s \Delta\gamma^s \tag{2.9}$$

where *s* numbers all active slip systems.
Having Δe_{ij}^{pl}, one finds easily grain deformation and rotation: $\Delta\varepsilon_{ij}^{pl}$ and $\Delta\omega_{ij}^{pl}$ (they are symmetric and anti-symmetric parts of Δe_{ij}^{pl}, respectively):

$$\Delta\varepsilon_{ij}^{pl} = \frac{1}{2}\sum_s (R_{ij}^s + R_{ji}^s)\Delta\gamma^s = \sum_s R_{(ij)}^s \Delta\gamma^s \tag{2.10}$$

$$\Delta\omega_{ij}^{pl} = \frac{1}{2}\sum_s (R_{ij}^s - R_{ji}^s)\Delta\gamma^s = \sum_s R_{)ij(}^s \Delta\gamma^s \tag{2.11}$$

where: $R_{(ij)}^s = \frac{1}{2}(R_{ij}^s + R_{ji}^s)$ and $R_{)ij(}^s = \frac{1}{2}(R_{ij}^s - R_{ji}^s)$. Let us underline that $\Delta\omega_{ij}^{pl}$ is a rigid body grain rotation produced by slip. If there was not interaction between a grain and the matrix – *crystal lattice* orientation would not change (see Fig. 2.9 a,b). However, in general a grain does not rotate as a rigid body, because of the constraints imposed by the neighboring material and the deformation device. As a consequence, some compensating rotation occurs ($\Delta\omega_{ij}^{latt}$) and it changes the grain lattice orientation:

$$\Delta\omega_{ij}^{latt} = -\Delta\omega_{ij}^{pl} \tag{2.12}$$

As it was stated above, in the tensile test of a single crystal (Fig. 2.9), the direction defined by a tensile force has to be preserved. This condition imposes a compensating rotation of a crystal, $\Delta\omega_{ij}^{latt}$, which causes the rotation of a lattice.

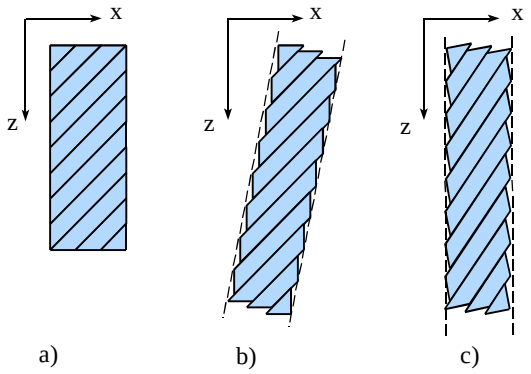

Fig. 2.9. *Tensile test of a crystal along* ***z*** *direction: a) before slip, b) after slip, c) after fulfilment of the condition of* ***z*** *axis orientation preservation (parallel to applied force).*

2.4.4. Mascroscopic deformation

The deformation of the sample is the average of grain deformations:

$$E_{ij}^{pl} = <\varepsilon_{ij}^{pl}> = \frac{1}{V_0}\sum_I \varepsilon_{ij}^{pl(I)} V^I \tag{2.13}$$

where V^I is the volume of the I-th grain and V_0 is the sample volume.

2.5. Leffers-Wierzbanowski plastic deformation model (LW)

The basic question, which has to be answered in any model, is: what is the relation between macroscopic variables of the sample (Σ_{ij}, E_{ij}) and analogical microscopic ones (σ_{ij}, ε_{ij}) on the level of a polycrystalline grain – Fig. 2.10. Unfortunately, generally it is not possible to find the unknown quantities in an analytical way. This is the reason why we use models.

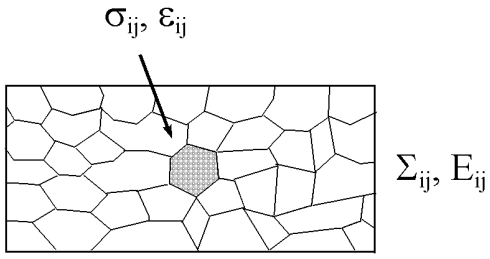

Fig. 2.10. *Macroscopic load Σ_{ij} is applied to a material and as a result a local stress σ_{ij} is induced on a grain level. The sample deformation is E_{ij}, but a local grain deformation is ε_{ij}.*

It was shown by Hill (Hill, 1965) that a general relation between local and global variables could be written in the form:

$$\dot{\sigma}_{ij} = \dot{\Sigma}_{ij} + L_{ijkl}^{*}(\dot{E}_{kl} - \dot{\varepsilon}_{kl}) \tag{2.14}$$

where L_{ijkl}^{*} is an interaction tensor and *dot* means the time derivative. Let us repeat that in the present work we use the convention of the summation on the repeated *lower* indices.
A strict calculation of L_{ijkl}^{*} tensor is not possible in general; hence some simplifying assumptions have to be done. A considerable progress was done by so-called self-consistent models (a model of this type will be described in the next chapter). Nevertheless, it was found that in many interesting cases the assumption of the isotropic grain-matrix interaction leads to surprisingly good predictions of material properties. In such the case the L_{ijkl}^{*} tensor is replaced by a scalar L:

$$\dot{\sigma}_{ij} = \dot{\Sigma}_{ij} + L(\dot{E}_{ij}^{pl} - \dot{\varepsilon}_{ij}^{pl}) \tag{2.15}$$

where “pl” denotes the plastic part of total deformation.
The above equation can be rewritten in the incremental form, useful in model calculations:

$$\Delta\sigma_{ij} = \Delta\Sigma_{ij} + L(\Delta E_{ij}^{pl} - \Delta\varepsilon_{ij}^{pl}) \tag{2.16}$$

Some of classical models can be reduced to Eq. 2.15 or 2.16 if L has a suitable value. For example:

Sachs model
L=0 leads to the Sachs model (Sachs, 1928). It is assumed in this model that no interactions between grains appear and consequently a homogeneous stress state results: $\sigma_{ij} = \Sigma_{ij}$. This model neglects sizes of grains and surface phenomena.

Taylor model

$L \rightarrow \infty$ leads to the Taylor model (Taylor, 1938). The basic assumption of the model is a homogeneous plastic deformation of the sample: $\varepsilon_{ij}^{pl} = E_{ij}^{pl}$.

Kröner model

$L = \frac{2(7-5\nu)}{15(1-\nu)}\mu$ is obtained under the assumption of a purely elastic interaction between a grain and the matrix (Kröner, 1961); in the above formula ν is the Poisson coefficient and μ is the shear modulus. One finds $L \cong \mu$ for typical value of $\nu \cong 0.3$. In this model each grain is treated as a spherical inclusion inside a homogenous, infinite continuous medium. This sphere is deformed during interaction with neighboring material.

Lin model

$L=2\mu$ is obtained for Lin model (Lin, 1957), which is a generalized Taylor model. In this model the basic assumption is that the total deformation is homogeneous: $E_{ij}^{e} + E_{ij}^{pl} = \varepsilon_{ij}^{e} + \varepsilon_{ij}^{pl}$ (*e* denotes elastic deformation and *pl* – plastic one) and that elasticity is isotropic.

LW model (with compromise interaction)

$L=\alpha\mu$ leads to a compromise description, very close to a real interaction (μ is the shear modulus and α is called *the elasto-plastic accommodation factor*). This is isotropic model with elasto-plastic interaction (Berveiller and Zaoui 1979, Wierzbanowski 1982, 1987). The estimated values of α factor are in the range (0.1 – 0.001). This parameter takes into account a partial plastic relaxation (by local slips near grain boundary region) of the interaction stresses between grains. Consequently, realistic interaction stresses are taken into account; they are much lower than purely elastic ones. For metals with low stacking energy (e.g., brass, silver) the estimated value of α is close to 0.001, while for metals with high stacking energy (aluminium, copper) α is in the range 0.01-0.1. The advantage of LW model is its flexibility in modelling the inter-granular interactions. LW model describes in general very well the plastic deformation, while the elastic part of the stress-strain curve can be only approximately taken into account.

Calculation mode using LW model

The initial orientation distribution of grains taken to model calculations is often random, but a distribution according to a given initial texture can also be used. The model calculations are continued till a preset final sample deformation. The calculations are done in incremental way (each increment corresponds to an increase of external load) and in each increment all crystallites are considered consecutively. At the beginning the external (applied) stress tensor amplitude has a value close to that necessary for activation of the best oriented slip systems. Next, the applied stress tensor is increased with an established step. The applied stress is transformed to slip system coordinate frames (e.g., there are 12 slip systems for f.c.c. structure and 12, 24 or 48 for b.c.c. one). If the resolved shear stress in a considered slip system exceeds the critical value – the slip system becomes active (Schmid law). Hence, a series of consecutive slips on different systems occurs, as long as the Schmid law is fulfilled. However, with progressing slip, the critical stress values are increasing due to the hardening law. And finally, we find the situation when no more slip systems can be activated. In such the moment the external stress tensor amplitude is increased of a preset $\Delta\Sigma$ value. The calculations are continued in such a way until the final sample deformation is obtained.

If we take an example of the tensile test (in z direction), the applied stress tensor can be presented as:

$$\Sigma_{ij} = \Sigma \begin{bmatrix} 0 & 0 & 0 \\ 0 & 0 & 0 \\ 0 & 0 & 1 \end{bmatrix} \tag{2.17}$$

where Σ is the stress tensor amplitude. In the *k-th* increment the applied stress tensor is: $\Sigma = \Sigma^0 + (k-1)\Delta\Sigma$.

The sequence of calculations in the first increment (k=1) is presented below:

Step 1:

- The initial local stress is: $\sigma_{ij} = \Sigma_{ij}^0$, where Σ_{ij}^0 is very close to fulfill the Schmid condition.: $\tau = \tau_{cr}$. We find "the most active" slip system: $\left|\tau^{Ig} - \tau_{cr}^{Ig}\right| = \max$ (where *I* numbers grains and *g* – slip systems),
- We attribute to this active slip system the elementary glide shear amplitude $\Delta\gamma^{Ig}$ and we calculate the resulting deformation and lattice rotation: $\Delta\varepsilon_{ij}^I$ and $\Delta\omega_{ij}^I$ (one of possibilities is to take a constant value of glide shear for all active slip system, e.g., $\Delta\gamma$=0.05),
- The local stresses are modified according to equation: $\Delta\sigma_{ij}^I = \Delta\Sigma_{ij} + L(\Delta E_{ij}^{\ pl} - \Delta\varepsilon_{ij}^{I\,pl})$,

Step 2:

- Another most active slip system is searched, taking into consideration local stress modified in previous step,
- next the same calculations as in step1 are performed,

Following steps ... (we examine all slip systems in all grains)).

.

.

If no more slip systems can become active, the external load is increased, i.e., we start the second increment (k=2) and we repeat the same operations as above,

And so on with next increments...

We stop the calculations if the calculated sample deformation has attained a preset final value.

2.6. Self-consistent model (SC)

The basic assumption of the used self-consistent model is the representation of an individual grain as a three dimensional ellipsoidal inclusion embedded in an equivalent homogeneous material.

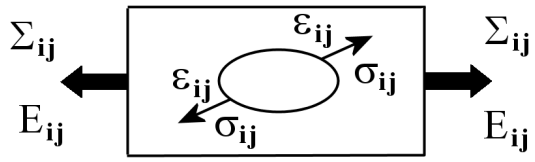

Fig 2.11. *Polycrystalline grain as an ellipsoidal inclusion*

The basic problem in deformation models is to find a relation between local (σ_{ij}, ε_{ij}) and global characteristics (Σ_{ij} and E_{ij}). This relation is less direct in SC model than in LW model. In the following text we present the calculation mode used in the elasto-plastic SC model, based on the scheme developed by Lipiński and Berveiller (Lipiński and Berveiller, 1989). In the elastic range a general form of the Hook's law is used:

$$\Sigma_{ij} = C_{ijkl} E_{kl} \text{ and } \sigma_{ij}^{I} = c_{ijkl}^{I} \varepsilon_{kl}^{I} \tag{2.18}$$

where C_{ijkl} and c_{ijkl}^{I} are stiffness tensors of the sample and the I-th grain, respectively, and E_{kl} and ε_{kl}^{I} are corresponding deformation tensors. In the elasto-plastic deformation range we use analogical relations, but concerning the stress and strain increments:

$$\Delta\Sigma_{ij} = L_{ijkl} \Delta E_{kl} \text{ and } \Delta\sigma_{ij}^{I} = l_{ijkl}^{I} \Delta\varepsilon_{kl}^{I} \tag{2.19}$$

where L_{ijkl} and l_{ijkl}^{I} are so called tangent moduli of the sample and the I-th grain. The tangent modulus tensor of a grain, l_{ijkl}^{I}, can be calculated if its active slip systems and corresponding glide shears are known. The sample tangent modulus, L_{ijkl}, is obtained by appropriate averaging of grain tangent moduli. If the elastic deformation range is considered then: $L_{ijkl} = C_{ijkl}$ and $l_{ijkl}^{I} = c_{ijkl}^{I}$. The single crystal elastic properties are known in general and the sample elastic properties can be calculated using some hypothesis concerning grain-grain interactions (e.g., Kröner 1961; Reuss, 1929; Voigt, 1928). In the elasto-plastic range tangent moduli change with deformation and their values have to be continuously calculated. Some components of the L_{ijkl} tensor have a direct experimental interpretation. For example the $(L^{-1})_{1111}$ component can be determined from the stress-strain curve - Fig. 2.12.

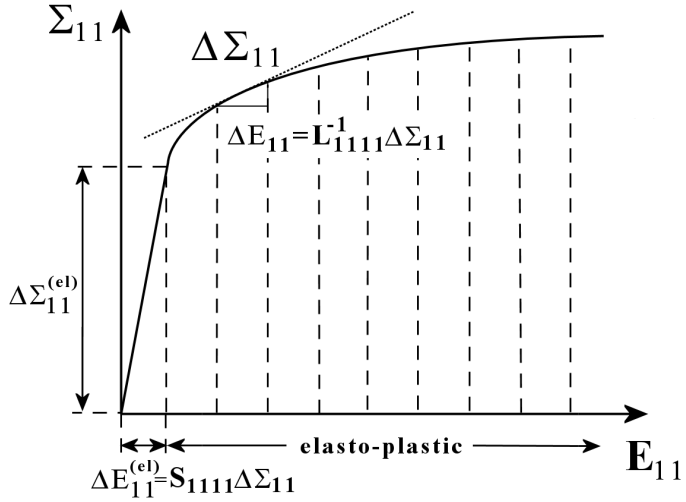

Fig. 2.12. *Determination of* $(L^{-1})_{1111}$ *from the stress-strain curve.*

Interaction between a grain and its environment

Interaction between a grain and the matrix can be directly calculated using the Eshelby theory (Eshelby, 1957). However, in the present work the calculation scheme developed by Lipinski and Berveiller (Lipiński and Berveiler, 1989) is used. According to Eq. 2.19, the local stress in the elasto-plastic range is:

$$\dot{\sigma}_{ij}(\mathbf{r}) = l_{ijkl}\,\dot{\varepsilon}_{kl}(\mathbf{r}) \tag{2.20}$$

where $l_{ijkl}(\mathbf{r})$ is the local tangent modulus tensor(„*I*" grain index is omitted here). This tensor can be also written as:

$$l_{ijkl}(\mathbf{r}) = L_{ijkl} + \delta\, l_{ijkl}(\mathbf{r}) \tag{2.21}$$

where $\delta\, l_{ijkl}(\mathbf{r})$ is its variable part depending on the position in a material (let us note that it is simply the difference between the local and global tangent moduli: $\delta\, l_{ijkl}(\mathbf{r}) = l_{ijkl}(\mathbf{r}) - L_{ijkl}$). Introducing the modified Green tensor, $\Gamma_{ijkl}(\mathbf{r}\text{-}\mathbf{r'})$, the local deformation can be expressed as (Lipiński and Berveiller, 1989; Baczmański, 2005):

$$\dot{\varepsilon}_{ij}(\mathbf{r}) = \dot{E}_{ij} + \int_V \Gamma_{ijkl}(\mathbf{r}-\mathbf{r'})\,\delta l_{klmn}(\mathbf{r'})\,\dot{\varepsilon}_{mn}(\mathbf{r'})\,dV' \tag{2.22}$$

The physical sense of the above equation is explained in Fig.2.13a. The local deformation in the point **r** depends on deformation $\dot{\varepsilon}_{mn}(\mathbf{r'})$ and $\delta\, l_{klmn}(\mathbf{r'})$ tensors in any other point **r';** these quantities are linked by the $\Gamma_{ijkl}(\mathbf{r}\text{-}\mathbf{r'})$ tensor.

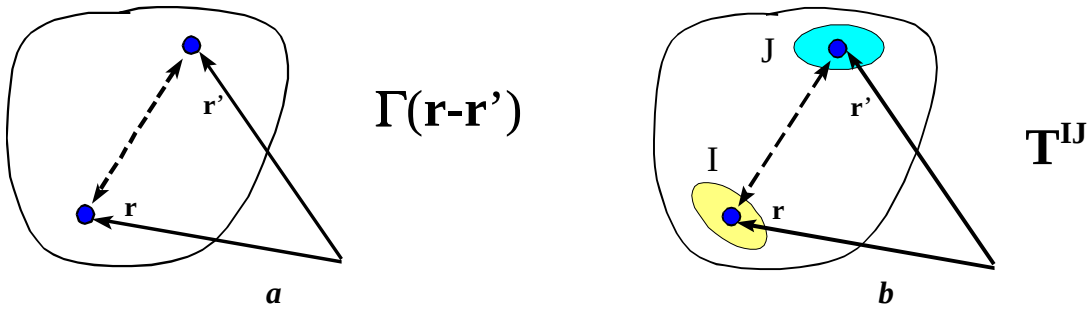

Fig. 2.13. *a) Deformation in the point* ***r*** *depends on deformation in any other point* ***r'*** and is described by the *Green's tensor, b) interaction between inclusions "I" and "J " is described by* $\boldsymbol{T^{IJ}}$ *tensor.*

Deformation in the inclusion (grain) „I" can be expressed as (Lipiński and Berveiler, 1989):

$$\dot{\varepsilon}_{ij}^{I} = \dot{E}_{ij} + \sum_{J=1}^{N} T_{ijkl}^{I\,J}\, \delta l_{klmn}^{J}\, \dot{\varepsilon}_{mn}^{J} \tag{2.23}$$

where $T_{ijkl}^{I\,J}$ tensor describes the interaction between inclusions „*I*" and „*J*" and *N* is the total number of them. Let us note that the above relation is a correct discretized form of Eq. 2.22, if:

$$T_{ijkl}^{I\,J} = \frac{1}{V_I} \int_{V_I} \int_{V_J} \Gamma_{ijkl}(\mathbf{r} - \mathbf{r}')\, dV dV' \tag{2.24}$$

We assume that δl_{klmn}^{J} and ε_{mn}^{J} are homogeneous inside each inclusion (grain). The interaction between inclusions "*I*" and "*J*" is schematically shown in Fig. 2.13b. We will see later that the tensor $T_{ijkl}^{I\,I}$ is a very important quantity, because it describes the interaction of the *I-th* inclusion with its environment. This tensor is also used in one-site approach, which is applied in the present work.

Concentration tensors

In the self-consistent models the idea of scale transition theory is based on the hypothesis of the existence of a concentration tensor A_{ijkl}^{I} relating the macro-strain rate $\dot{E}_{kl}$ with the grain strain rate $\dot{\varepsilon}_{ij}^{I}$ and another concentration tensor B_{ijkl}^{I} relating the macro-stress rate $\dot{\Sigma}_{kl}$ with the grain stress rate $\dot{\sigma}_{ij}^{I}$ (dot denotes the time derivative $\frac{\partial}{\partial t}$). Consequently, we can write:

$$\dot{\varepsilon}_{ij}^{I} = A_{ijkl}^{I}\, \dot{E}_{kl} \tag{2.25}$$

$$\dot{\sigma}_{ij}^{I} = B_{ijkl}^{I}\, \dot{\Sigma}_{kl} \tag{2.26}$$

We will describe now separately the elastic and elasto-plastic ranges of deformation.

Elastic deformation range:

It can be shown (Baczmański, 2005) that using the $T_{ijkl}^{I\,I}$ tensor (one-site approach) and the Hooke's law (Eq. 2.18) one obtains from Eq. 2.23 the concentration relation :

$$[(A^I)^{-1}]_{ijkl} = I_{ijkl} - T_{ijmn}^{II}(c_{mnkl}^I - C_{mnkl}) \tag{2.27}$$

where I_{ijkl} is the unit tensor. The macroscopic (sample) stiffness tensor, C_{ijkl}, appearing in the above equation is expressed as:

$$C_{ijkl} = \sum_{I=1}^{N} f^I c_{ijmn}^I A_{mnkl}^I \tag{2.28}$$

where f^I is the volume share of the grain „I".
If the A_{ijkl}^I tensor is known for each grain, the stiffness tensor, C_{ijkl}, can be calculated using above equation. However, the solution of Eq. 2.27 is not direct, because to calculate the A_{ijkl}^I tensor the C_{ijkl} tensor has to be known, while the C_{ijkl} tensor is obtained from the A_{ijkl}^I (Eq. 2.28). This is the reason, why A_{ijkl}^I and C_{ijkl} tensors have to be calculated simultaneously, using an iterative procedure. Once the A_{ijkl}^I tensor is calculated, the second concentration tensor can be found using the Hooke's law:

$$B_{ijkl}^I = c_{ijmn}^I A_{mnop}^I (C^{-1})_{opkl} \tag{2.29}$$

Elasto-plastic deformation range:

We obtain analogous results as above if C_{ijkl} tensor is replaced by L_{ijkl} and c_{ijmn}^I - by l_{ijmn}^I one. Moreover, Eqs. 2.19 or their equivalent forms:

$$\dot{\Sigma}_{ij} = L_{ijkl}\dot{E}_{kl} \quad \text{and} \quad \dot{\sigma}_{ij}^I = l_{ijkl}^I \dot{\varepsilon}_{kl}^I \tag{2.30}$$

have to be used instead of the Hooke's law.

As a result, the concentration tensor is:

$$[(A^I)^{-1}]_{ijkl} = I_{ijkl} - T_{ijmn}^{II}(l_{mnkl}^I - L_{mnkl}) \tag{2.31}$$

with the sample tangent modulus tensor defined as:

$$L_{ijkl} = \sum_{I=1}^{N} f^I l_{ijmn}^I A_{mnkl}^I \tag{2.32}$$

The concentration tensor for stress is:

$$B^I_{ijkl} = l^I_{ijmn} A^I_{mnop} (L^{-1})_{opkl} \tag{2.33}$$

The L_{ijkl} tensor can be calculated if the values of the tensor A^I_{ijkl} are known for every grain *I*. In turn, the concentration tensors are determined for the known L_{ijkl} tensor. To solve this problem the iteration procedure is used, i.e., starting from the initial value of the L_{ijkl} tensor, the A^I_{ijkl} tensors are calculated and the new L_{ijkl} tensor is determined from Eq. 2.32. The latter tensor is the initial one for the next iteration. The procedure is completed when the calculated L_{ijkl} tensor does not change significantly after consecutive iterations.

2.7. Calculations for hexagonal structure

Many metals crystallize in hexagonal structure, hence our calculations were adapted for this case. The elementary cell of a hexagonal system is defined by two vectors of equal length $\mathbf{a_1}$ and $\mathbf{a_2}$, forming 120^0 one with another, and the third vector **c** perpendicular to them (Fig. 2.14). In our calculations, however, an artificial orthogonal coordinate system for crystallographic cell was used. Two versors of the new coordinate system (X_2 and X_3) are defined by the vectors of the elementary cell (i.e., $\mathbf{a_2}$ and **c**) - Fig. 2.14 - and X_1 is perpendicular to them. The indices of a plane and a direction in the hexagonal system are often referred to four axes (the fourth axis $\mathbf{a_3}$ lays in the basal plane and is inclined 120^0 with respect to $\mathbf{a_1}$ and $\mathbf{a_2}$**)** and they are written as (*hkil)* and *[prst]*. It can be shown that:

$$h + k = -i \tag{2.34a}$$

and

$$p + r = -s \tag{2.34b}$$

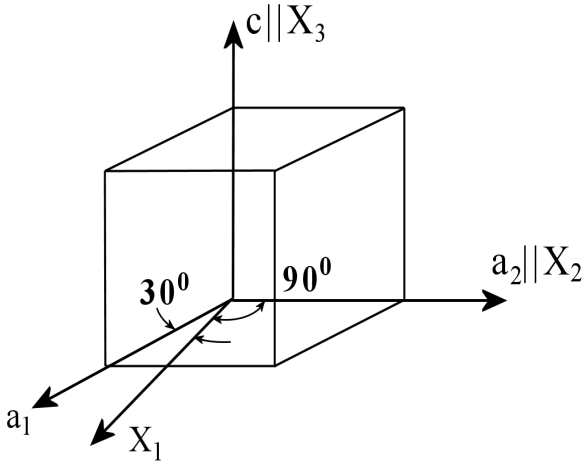

Fig. 2.14. *Hexagonal elementary cell defined by {**a₁**, **a₂**, **c**} and orthogonal coordinates system represented by { **X₁**, **X₂**, **X₃**}.*

Typical crystallographic planes in hexagonal structure are presented on Fig. 2.15.

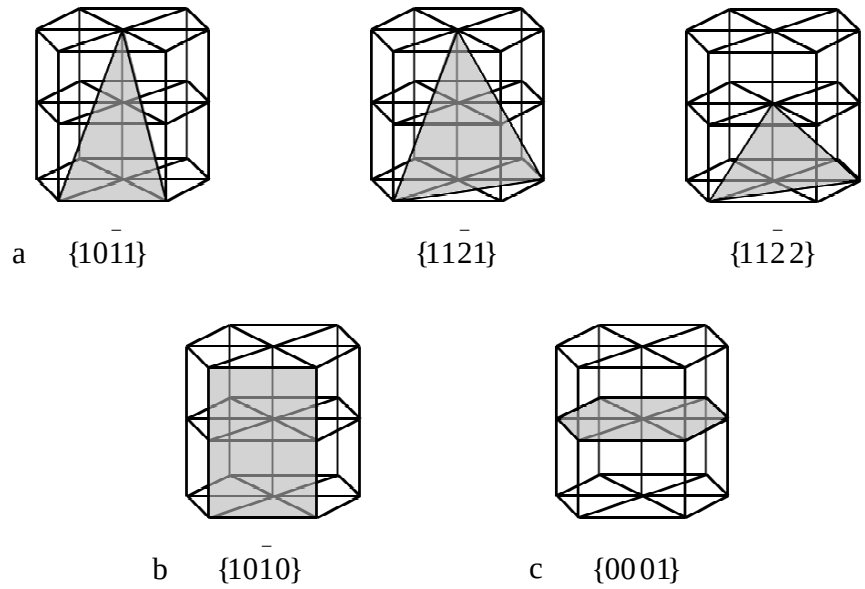

Fig 2.15. *The main planes in hcp structure: (a) pyramidal planes (b) prismatic planes (c) basal plane*

As it was mentioned, the artificial orthogonal coordinates system was used in our calculations. Hence, it is necessary to transform plane and direction indices to this new reference frame (four indices have to be reduced to three). This transformation can be found by simple geometrical relations (Wierzbanowski, 1978):

$$\begin{aligned} &\text{for plane:} \quad (hkil) \rightarrow (h'k'l') = \left(\frac{2h+k}{\sqrt{3}}, k, l, \frac{a}{c} \right) \\ &\text{for direction:} \quad [prst] \rightarrow [u'v'w'] = \left[\frac{\sqrt{3}}{2}(p-s), -\frac{3}{2}(p+s), t\frac{c}{a} \right] \end{aligned} \tag{2.35}$$

where: *h'k'l'* are plane indices in new (orthogonal) coordinates system and *u'v'w'* are new direction indices; *c* and *a* – are lattice parameters of hexagonal cell. After this transformation - the model calculations are done in an analogical way as for the cubic crystal structure.

2.8. Results obtained with the models

The models can be used for prediction of important material characteristics, e.g.:

- crystallographic texture
- hardening curves (e.g., stress-strain curves),
- residual stresses,
- plastic flow surfaces,
- dislocation density and stored energy,
- etc.

In this chapter the results obtained using LW and SC models for fcc, bcc and hcp structures will be presented. Essentially, there are two types of rolling texture of fcc metals: the copper type texture (e.g., in: Cu, Al, Ni) and brass texture (e.g., in: Cu-Zn, Ag). In general, the copper type texture is observed in materials with high stacking fault energy, whereas brass type texture - in materials with low stacking fault energy. The above classification can be still modified, because the type of texture depends also on deformation rate and on temperature.

The rolling textures presented in this chapter were predicted by LW model (this model gives very good results in the plastic deformation range; moreover, calculations are much faster with LW model than with SC model). In each case a model sample was represented by 5000 grains having equal volumes and initial random crystal orientation distribution. Typical values of model parameters (τ_o, τ_{cr}, H, L) were used (Table 2.1). Values of these parameters are close to the experimental ones. It was found that for a weak grain-matrix interaction (situation close to Sachs model) - the brass type texture is predicted, while for a strong interaction (close to Taylor model) - the copper type one. Consequently, in the case of brass texture the interaction parameter L=100 MPa was assumed, while for copper one - L=800 MPa was used (value of $L=\mu\alpha$ depends on the shear modulus μ but also on the grain-matrix interaction, which is described by the elasto-plastic accommodation factor α). According to Leffers' argumentation (Leffers, 1975), the cross slip is observed near the boundary regions in metals with medium and high stacking fault energy (like in copper). This leads to relatively homogeneous deformation of grains (Taylor model) and as a result the copper type texture is formed.

To describe the deformation of ferritic steel, the typical slip systems for bcc structure: <111>{110} an <111> {112} were used (sometimes also <111> {123} is reported). In bcc metals, where many slip systems can operate, also rather homogeneous deformation occurs and this situation was described by a strong interaction in the model (L=1000 MPa).

The results of texture prediction for fcc and bcc metals are shown in Fig. 2.15 - 2.17.

Table 2.1. *The input parameters used for calculations*

Structure	Slip systems <direction>{plane} (total number)	τ_c^0 - initial critical shear stress [MPa]	Hardening parameters [MPa]	Grain elastic constants E -Young modulus [MPa] ν - Poisson ratio	L Interaction parameter [MPa]
bcc	<111> {110} <111> {112} <111> {123} (48 slip systems)	150	H = 80 A = 1	E = 208 ν = 0.29	1000
fcc	<110> {111} (12 slip systems)	80	H=60 A = 1	E = 122.5, ν = 0.34 (copper)	800
				E = 110, ν = 0.3 (brass)	100

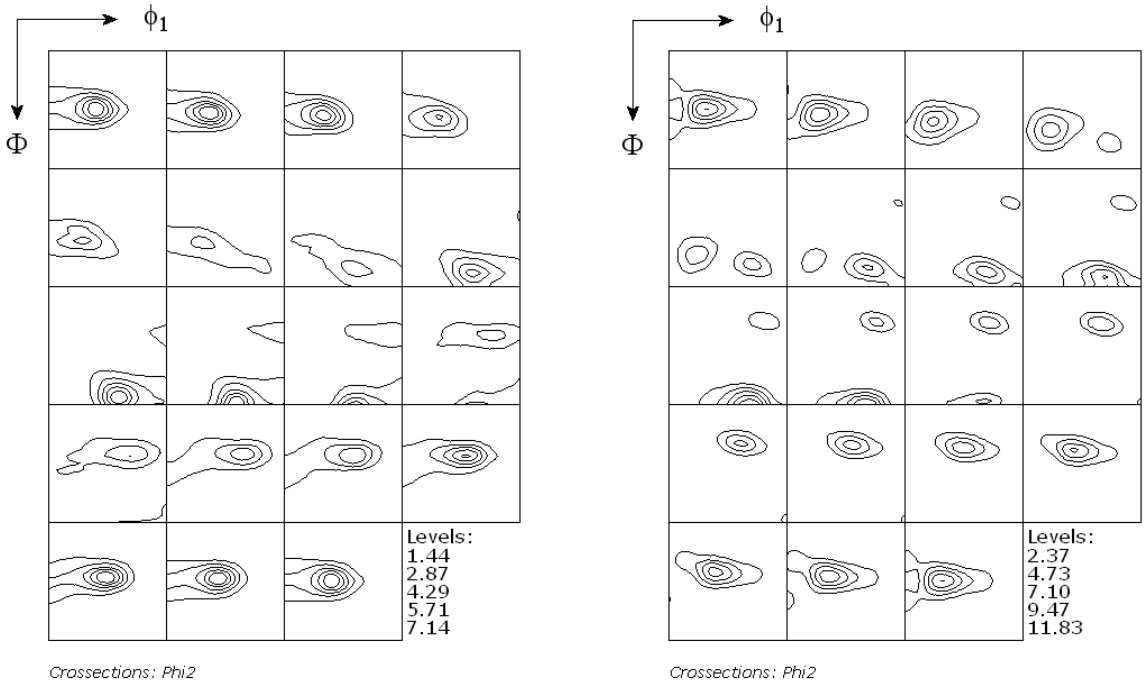

Fig. 2.15. *Measured (on the left) and predicted (on the right) ODFs of cold rolled brass (ϕ_2 sections are shown). Rolling reduction is 70%.*

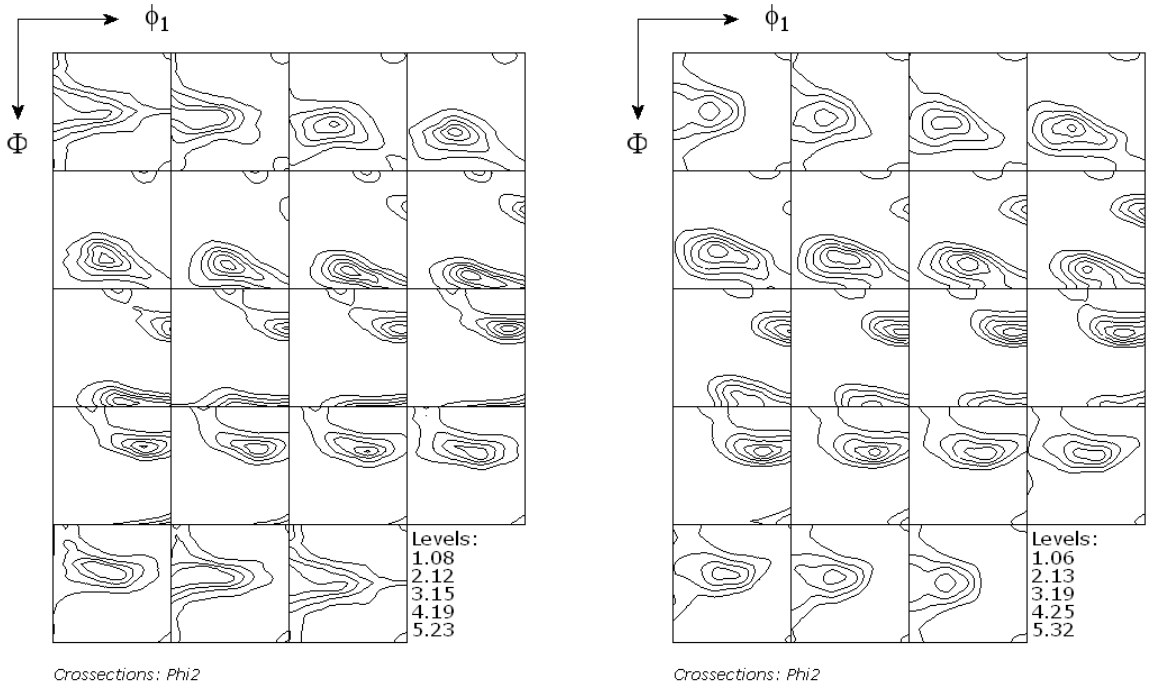

Fig. 2.16. . *Measured (on the leftt) and predicted (on the right) ODFs of cold rolled copper (ϕ_2 sections are shown). Rolling reduction is 70%.*

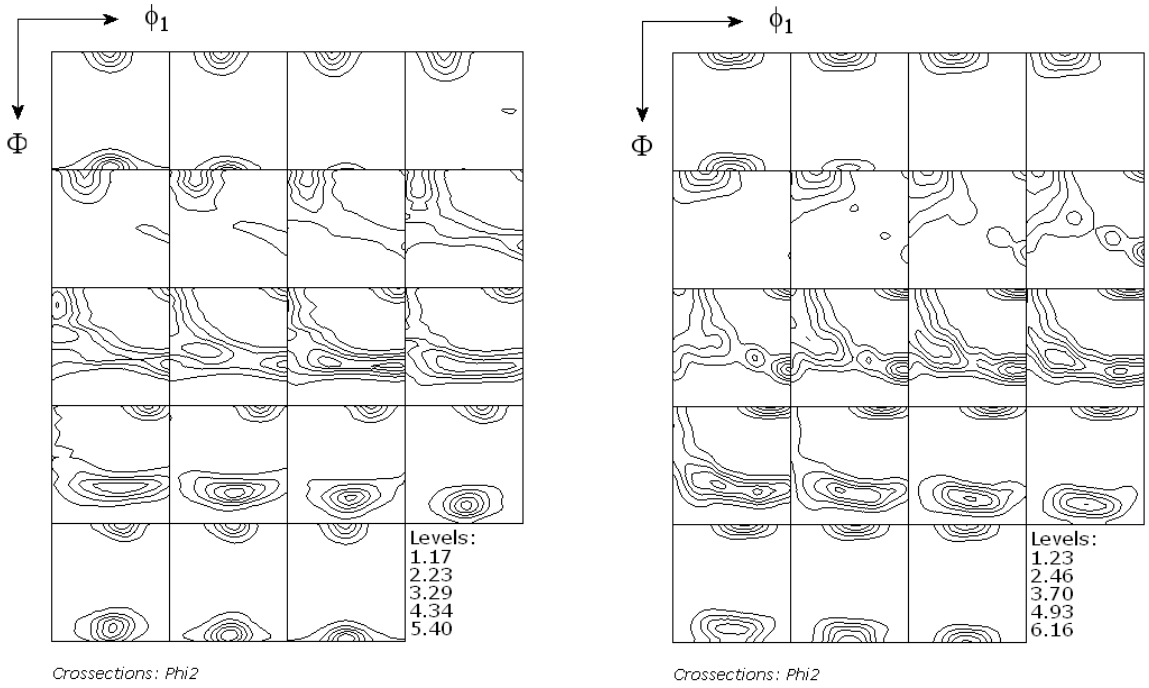

Fig. 2.17. *Measured (on the left) and predicted (on the right) ODFs of cold rolled ferritic steel (ϕ_2 sections are shown). Rolling reduction is 80%.*

The metals of hexagonal structure were also studied using LW model. In these metals besides of the slip also the twinning is often observed. Nevertheless, taking into account only deformation produced by slip we were able to predict the main texture features (Philippe, 1995) (however, in future the introduction of twinning to the model is also foreseen). In hexagonal materials some number of slip system families can be activated (their critical values τ_{cr} have different values in general). The data on τ_{cr}, which can be found in literature, is not always consistent. Moreover, these values strongly depend on purity of materials and conditions of deformation (Philippe, 1995). In Table 2.2 the c/a ratio as well as the most important slip systems for typical hcp materials (Be, Hf, Ti, Zr, Co, Mg, Zn and Cd) are listed. The textures of hexagonal metals and alloys can be classified into three groups, according to their *c*/*a* ratios, namely: materials with *c*/*a* ratio greater than, approximately equal to, and smaller than the theoretical value of 1.633. The rolling textures for these three groups of hcp metals were measured using X-ray diffraction. The examined materials were: magnesium (c/a =1.624), titanium (c/a =1.588) and zinc (c/a =1.856). The measured textures were compared next with those predicted by LW model - Figs. 2.18 - 2.20. The slip systems from Table 2.2 were used in calculations.

Table 2.2. *Typical slip systems observed in selected hcp metals (Wang et al., 2003; Philippe,* 1983*).*

Element	c/a	Deviation (%) from the ideal $c/a = 1.633$	Principal slip system	Secondary slip System	Other slip System
Cd	1.866	+15.5	$<11\bar{2}0>\{0001\}$	$<11\bar{2}3>\{11\bar{2}2\}$	$<11\bar{2}0>\{10\bar{1}0\}$ $<11\bar{2}0>\{10\bar{1}1\}$
Zn	1.856	+13.6	$<11\bar{2}0>\{0001\}$	$<11\bar{2}3>\{11\bar{2}2\}$	$<11\bar{2}0>\{10\bar{1}0\}$
Mg	1.624	-0.6	$<11\bar{2}0>\{0001\}$	$<11\bar{2}0>\{10\bar{1}0\}$	$<11\bar{2}0>\{10\bar{1}1\}$ $<11\bar{2}3>\{11\bar{2}2\}$
Co	1.623	-0.6	$<11\bar{2}0>\{0001\}$	None	None
Zr	1.593	-2.4	$<11\bar{2}0>\{10\bar{1}0\}$	$<11\bar{2}0>\{0001\}$	$<11\bar{2}0>\{10\bar{1}1\}$ $<11\bar{2}3>\{11\bar{2}2\}$
Ti	1.588	-2.8	$<11\bar{2}0>\{10\bar{1}0\}$	$<11\bar{2}0>\{0001\}$	$<11\bar{2}0>\{10\bar{1}1\}$ $<11\bar{2}3>\{11\bar{2}2\}$
Hf	1.581	-3.2	$<11\bar{2}0>\{10\bar{1}0\}$	$<11\bar{2}0>\{0001\}$	
Be	1.568	-4.0	$<11\bar{2}0>\{0001\}$	$<11\bar{2}0>\{10\bar{1}0\}$	$<11\bar{2}0>\{10\bar{1}1\}$ $<11\bar{2}3>\{11\bar{2}2\}$

Hcp metals and alloys with *c*/*a* ratio approximately equal to the theoretical value of 1.633, such as Mg, tend to form basal fiber textures during rolling (Fig. 2.18). The origin of such textures may be understood in terms of the slip systems operating in basal planes. Metals and alloys with *c*/*a* ratios above the ideal one, such as Zn (1.856) and Cd (1.885), tend to exhibit textures with basal poles tilted $\pm 15–25^0$ away from the normal direction towards the rolling direction. (Fig. 2.19.) Finally, the metals and alloys, having *c*/*a* ratio smaller than 1.633 such as Zr (1.589) and Ti (1.587), tend to form textures with basal poles tilted $\pm 20–40^0$ away from the normal direction towards the transverse direction (Fig. 2.20). The basal $<11\bar{2}0>\{0001\}$ slip produces the basal texture characteristic for Mg (*c*/*a* ≈ 1.633) – Fig.2.18. The combination of basal $<11\bar{2}0>\{0001\}$ slip, pyramidal $<11\bar{2}3>\{11\bar{2}2\}$ slip and prismatic $<11\bar{2}0>\{10\bar{1}0\}$ slip produces the characteristic textures with basal poles tilted away from the normal direction toward the rolling direction for Zn (*c*/*a* > 1.633) – Fig. 2.19. Finally, the combination of prismatic $<11\bar{2}0>\{10\bar{1}0\}$ slip and pyramidal $<11\bar{2}0>\{10\bar{1}1\}$ slip produces the characteristic textures with basal poles tilted away from the normal direction toward the transverse direction for Ti (*c*/*a* < 1.633) – Fig. 2.20 (Gloaugen, 2001). All the predicted textures agree well with corresponding experimental ones.

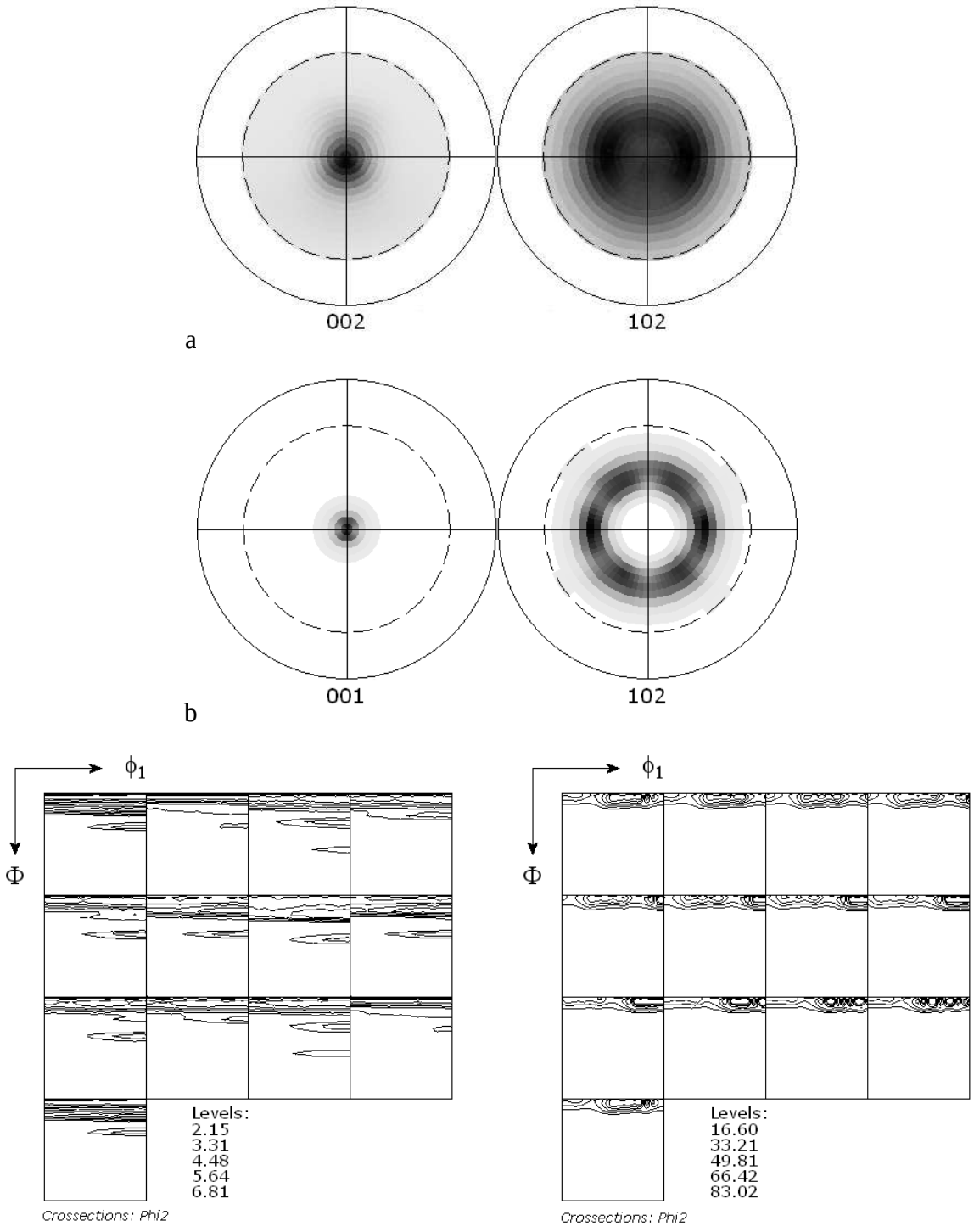

Fig. 2.18. *(001), (102) PFs and ODFs for polycrystalline magnesium rolled to 80% reduction: a) experimental PFs, b) predicted PFs, c) experimental ODF, d) predicted OD.* $<11\bar{2}0>\{0001\}$ *slip system was used for calculation.*

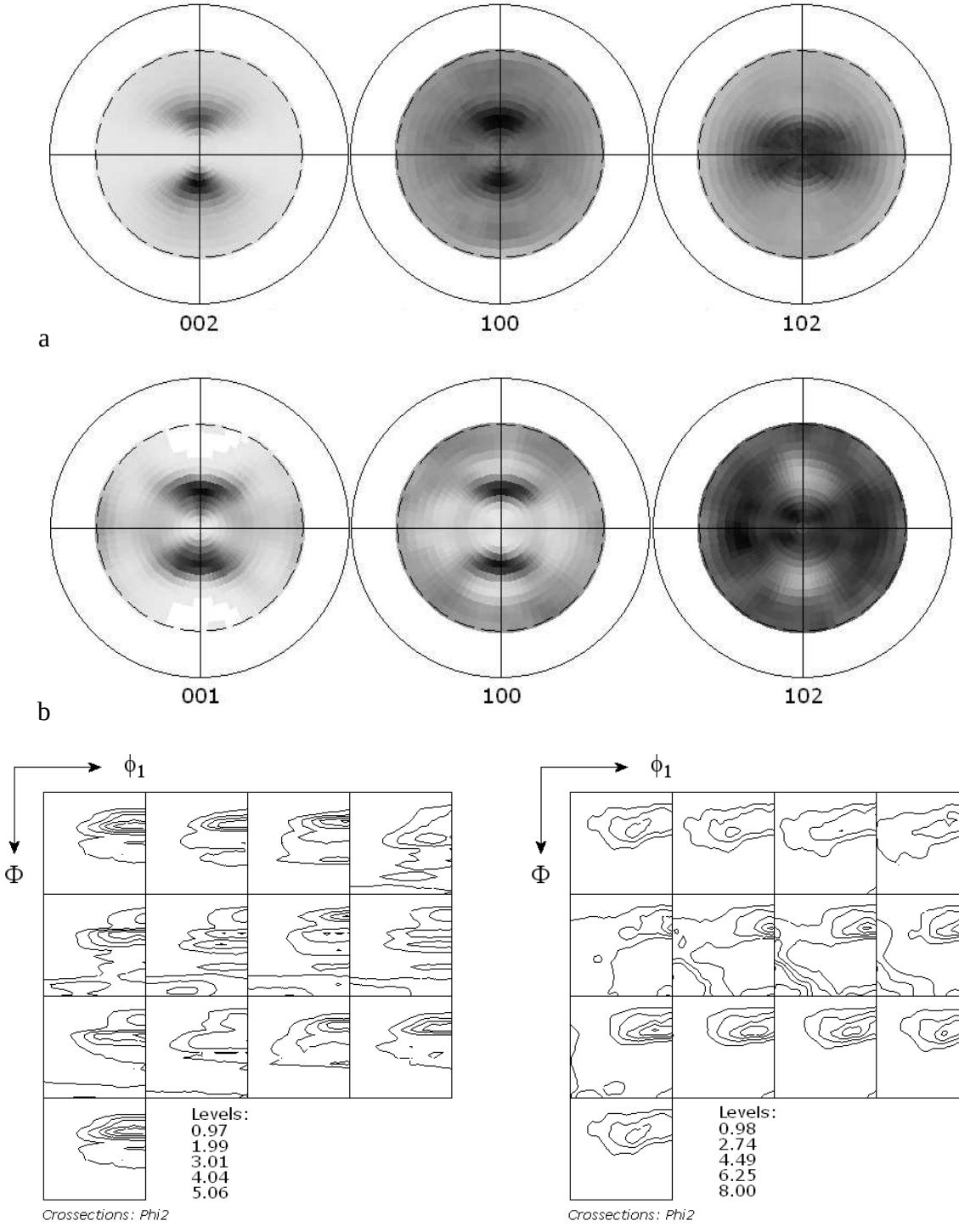

Fig. 2.19. *(001), (100), (102) PFs and ODFs for polycrystalline zinc rolled to 35% reduction: a) experimental PFs, b) predicted PFs,, c) experimental ODF, d) predicted ODF.* $<11\bar{2}0>\{0001\}$ $<11\bar{2}3>\{11\bar{2}2\}$ $<11\bar{2}0>\{10\bar{1}0\}$ *slip systems were used for calculation.*

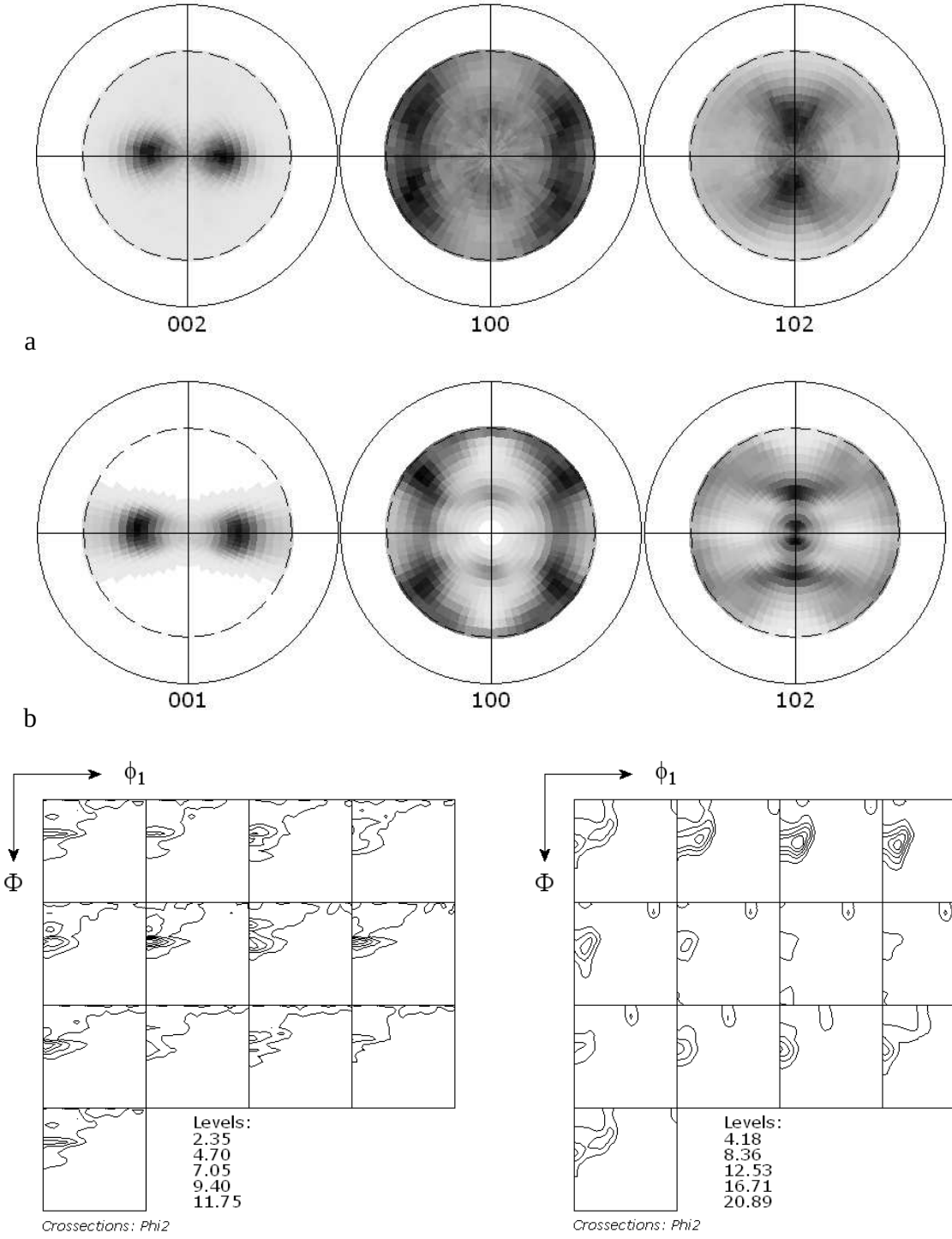

Fig. 2.20. *(001), (100), (102) PFs and ODFs for polycrystalline titanium rolled to 70% reduction: a) experimental PFs, b) predicted PFs, c) experimental ODF, d) predicted ODF.* $<11\bar{2}0>\{10\bar{1}0\}$ $<11\bar{2}0>\{10\bar{1}1\}$ *slip systems were used for calculation.*

The texture is not the only characteristics, which can be predicted by elasto-plastic deformation models. Another one is, e.g., the stored energy, which plays a crucial role in recrystallization process (Baczmański et al., 2007). One can distinguish two contributions to this energy. The first one is the elastic energy (E_{el}), connected with residual stresses, i.e., with grain-grain interactions. Another part of the stored energy (E_{disl}) is due to a huge increase of dislocation density inside grains, which occurs during plastic deformation. E_{disl} is about one order of magnitude higher than E_{el}, and, hence, is considered as the main driving force of recrystallization (Piękoś, 2006). Its value can be approximated as:

$$E_{disl} \cong Gb^2\rho \tag{2.36}$$

where G is the shear modulus, b – Burgers vector of dislocations and ρ is the dislocation density (Piękoś, 2006). This stored energy is decisive for kinetics of the recrystallization process. The dislocation density ρ is proportional to $<\tau_{cr}^2>$ and can be predicted by deformation models (τ_{cr} is the critical shear stress for slip and the average <..> is done over all active slip systems in a given grain). The exemplary prediction of E_{disl} by LW model is shown in Fig. 2.21 c. This distribution is compared with ODFs of rolled and recrystallized steel samples (Fig. 2.21 a, b).

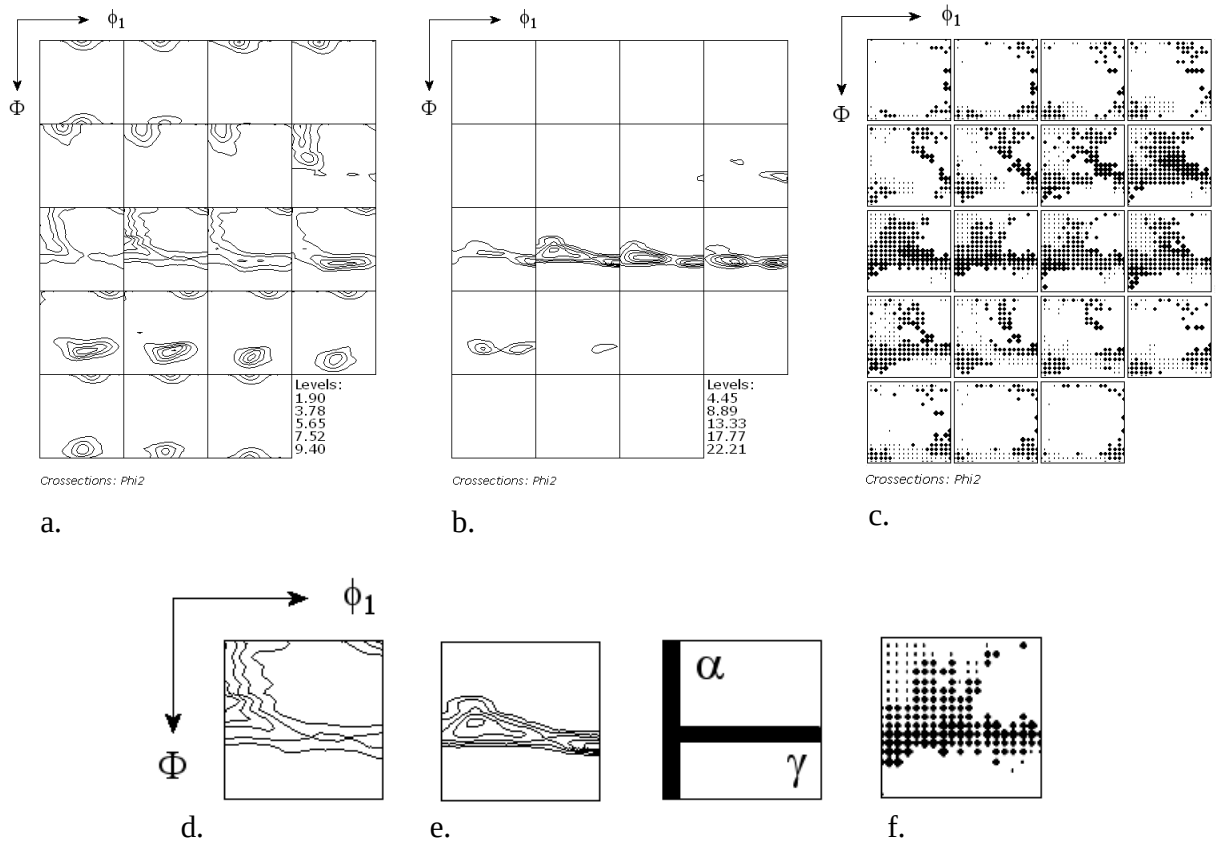

Fig. 2.21. *Texture of low carbon steel and its relation to the stored energy. a, d) rolling texture, b, e) recrystallization texture, c, f) stored energy predicted by model. For figs d, e and f only $\varphi_2=45^0$ were presented.*

It is visible (see section $\varphi_2=45^0$) that during recrystallization the series of orientations called γ fiber (horizontal one) is reinforced and, oppositely, the α fiber (vertical one) is reduced. On the other hand, high values of the stored energy also appear in γ fiber. The observed texture change can be explained by the fact that recrystallization nuclei appear preferentially in grains with high stored energy, i.e. in γ fiber in this case. Consequently, we can conclude that the obtained stored energy distribution explains qualitatively the main tendency of texture transformation during recrystallization.

The deformation model can predict also other properties of materials, for example hardening curves. The predicted stress-strain curve for polycrystalline copper is compared with the experimental one in Fig. 2.22.

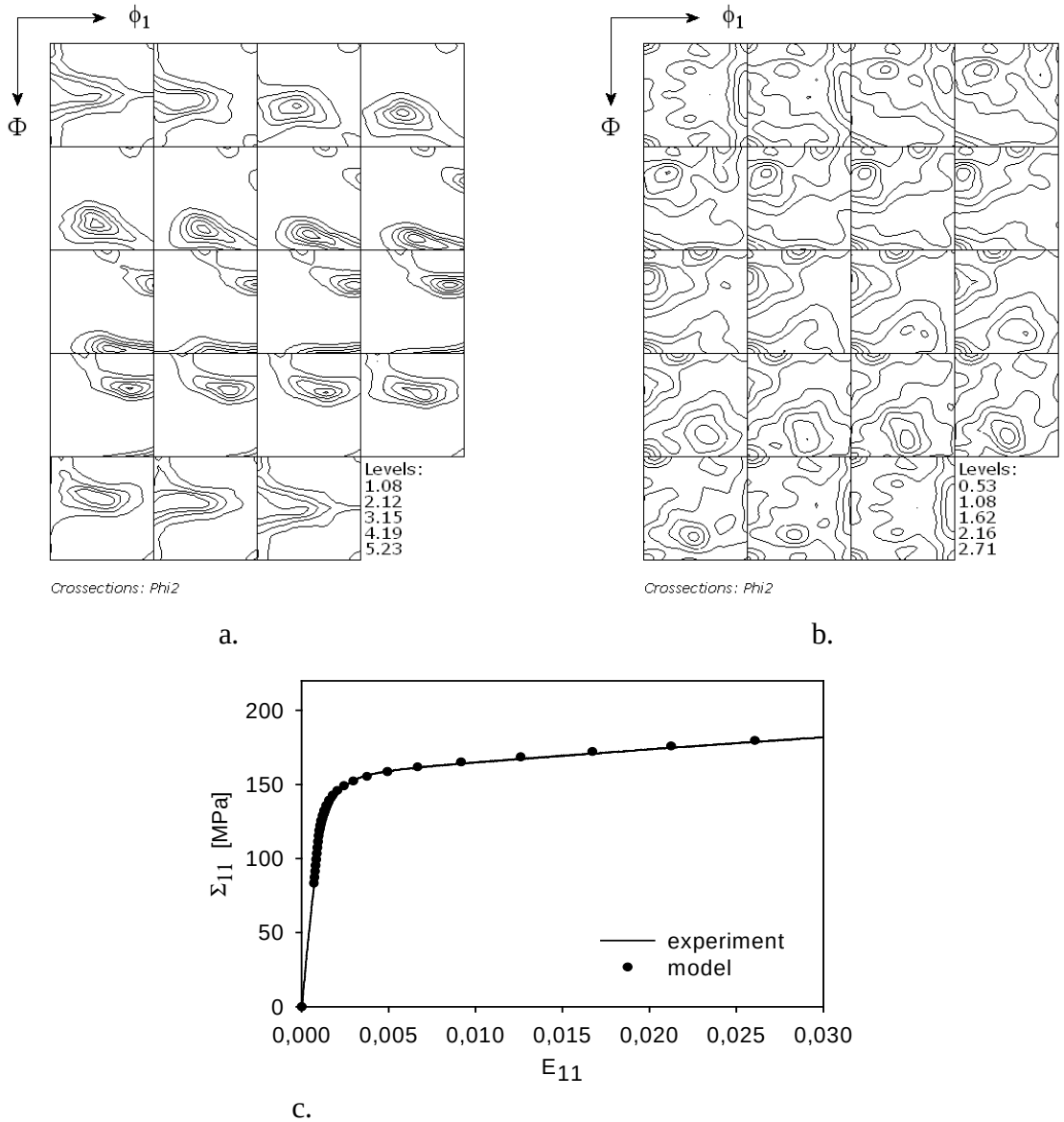

Fig. 2.22. *a) Initial texture of rolled copper (measured), b) texture of copper after tensile test in transverse direction (predicted starting from initial one), c) predicted and experimental stress-strain curves for tensile test. SC model was used for predictions.*

The SC model was used in this case. Its main advantage is that it gives precise results also in elastic range of deformation (LW model works very well only in plastic range). The agreement between experimental and predicted stress-strain curve is perfect. The change of texture of the studied copper sample during tensile test is also shown. The initial sample had a typical rolling texture (Fig. 2.22 a) and after the tensile test the texture changed very strongly (Fig. 2.22b).

2.9. Conclusions

The presented models of elasto-plastic deformation (LW and SC) are useful tools for the study of mechanical properties of polycrystalline materials. They enable prediction of macroscopic material properties (e.g., texture, stress-strain curves, plastic flow surfaces, dislocation density, final state of residual stress, etc.) basing on the micro-structural characteristics (crystallography of slip systems, hardening law, initial texture, initial residual stress state, etc.). Such the models are precious tools for technologists searching for optimal material properties.

In the following chapters these models (SC and LW) will be applied for the prediction of textures and analysis of residual stresses in polycrystalline one-phase and two-phase materials (e.g., in austeno-ferritic steel). The LW model will be used for the study of material properties after cross-rolling treatment.

Chapter 3

Residual stresses and elastoplastic behaviour of stainless duplex steel

3.1. Introduction

In the first chapter the methods of determining stresses by means of diffraction method were presented. The crucial problem in the stress analysis is the determination of diffraction elastic constants. These constants are essential for interpretation of residual stress measurement. They can be calculated by means of models (Reuss, Voigt, Kröner) and also determined experimentally.

In this chapter the sources of stresses will be explained. In the present work the total stress field is divided into three types in function of scale: first order stresses, second order stresses and third order stresses. *The first order stresses* are defined as the average stresses over a large volume of the sample. *The second order stress* is the difference between the grain stresses and the first order stresses. The last type is *the third order stress*; this stress field is a result of the heterogeneity within a single grain. As it is described in the first chapter, macroscopic stresses are determined from the slope of $\sin^2\psi$ graph. When the second ordered stresses are present in the sample, the relation $\langle d \rangle_{\{hkl\}}$ vs. $\sin^2\psi$ becomes non-linear. The variation of the second order stresses can be predicted by means of elasto-plastic deformation models and this is done in the present chapter. The results of residual stress examination will be presented for single and multi-phase materials.

3.2. Classification of stresses

Internal stresses can be generated by plastic deformation. The part of total stress field which remains in material when external load is released is called the residual stress. It can arise in a two-phase material (e.g., in a composite) due to different plastic flow of grains or due to different thermal expansion coefficients of both phases. A polycrystalline material consists of grains having different lattice orientations. Macroscopic material properties depend on single grain properties, their lattice orientations and interactions between neighboring grains.
As it was mentioned, we divide the stresses into three types in function of scale (Fig. 3.1) (Baczmanski et al., 1994b; Fitzpatrick, 1995; Meander et al., 1981; Bojarski 1970):

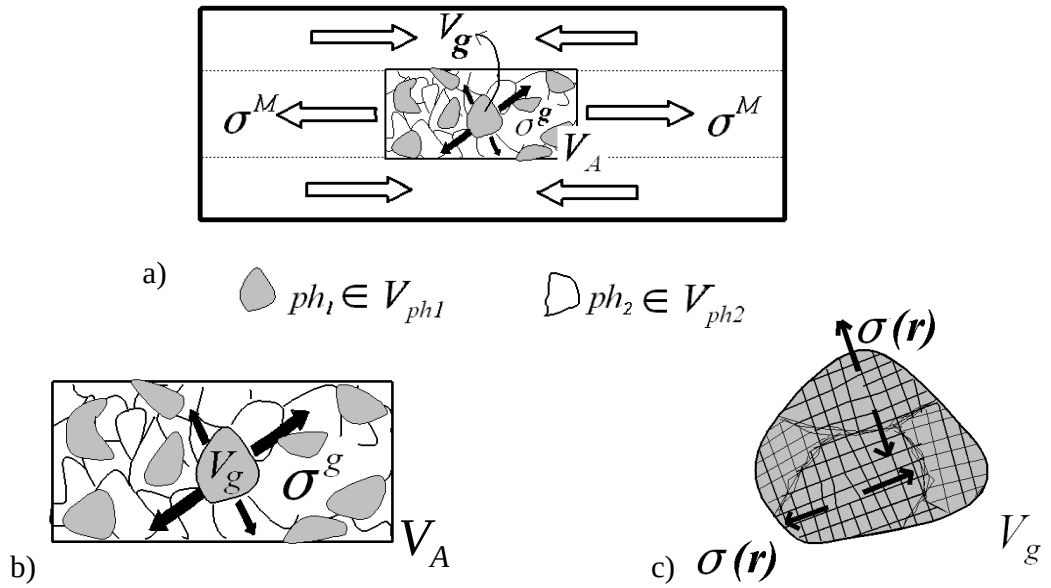

Fig. 3.1. *Definition of different types of stresses at various spatial scales of a polycrystalline material. a) First order stresses, b) second order stresses, c) third order stresses.*

The first order stresses σ^{I}_{ij} are defined as the average stresses over a large volume of the sample. For a single phase material they are equal to the macrostress ($\sigma^I_{ij} = \sigma^M_{ij}$),

$$\sigma^M_{ij} = \frac{1}{V_A} \int_{V_A} \sigma_{ij}(\mathbf{r})\, dV \tag{3.1}$$

where: σ^M_{ij} is the macrostress and V_A is volume of the sample

In multiphase material different physical properties of individual phases lead to different stresses in each phase. In order to separate those stresses it is convenient to introduce the phase stresses σ^{ph}_{ij}. They are defined as the average over the volume of grains from a given phase:

$$\sigma_{ij}^{ph} = \frac{1}{V_{ph}} \int_{V_{ph}} \sigma_{ij}(\mathbf{r})\, dV \tag{3.2}$$

where σ_{ij}^{ph} is the phase stress, V_{ph} – volume of the phase.
There is an obvious relation between the phase stresses and the macro-stresses:

$$\sigma_{ij}^{M} = \sum_{ph}^{N_{ph}} f^{ph} \sigma_{ij}^{ph} \tag{3.3}$$

where $f^{ph} = \frac{V_{ph}}{V_A}$ is the volume fraction of the *ph* phase and N_{ph} is the number of phases

In polycrystalline materials also the grain stresses (σ_{ij}^{g}) are interesting. The grain stresses represent average stress values inside individual grains ($\sigma_{ij}^{g} = \int_{V_g} \sigma_{ij}(\vec{r})dV$). They are a result of different plastic behaviour of crystallites having various lattice orientations with respect to the sample. They can also arise due to the anisotropy of thermal expansion and elastic constants.
The second order stress is defined as a difference between the grain stress and the first order stress. For a single phase material it is:

$$\sigma_{ij}^{IIg} = \sigma_{ij}^{g} - \sigma_{ij}^{I} \tag{3.4}$$

where $\sigma_{ij}^{I} = \sigma_{ij}^{M}$ for single phase and $\sigma_{ij}^{I} = \sigma_{ij}^{ph}$ for multiphase materials. The grain and the second order stresses have constant values inside a given grain. The average of the second order stress over the sample volume is zero.

The last type of stress is the *third order stress:* $\sigma^{III}(\boldsymbol{r})$. It results from the heterogeneity within single grains. This heterogeneity is caused by vacancies, insertions, substitutions, dislocations, sub-grain boundaries, etc. The third order stresses $\sigma^{III}(\boldsymbol{r})$ are defined as:

$$\sigma_{ij}^{III}(\boldsymbol{r}) = \sigma_{ij}(\boldsymbol{r}) - \sigma_{ij}^{g} \tag{3.5}$$

Their average of over the volume of an individual grain is zero.

3.3. Origin of stresses

A polycrystalline material consists of a big amount of grains having different orientations. Elastic deformation of each grain is determined by its elastic constants, which are generally anisotropic. Consequently, we define grain stresses, $\sigma_{ij}^{g(er)}$, resulting from *elastic responses*. They are a result of elastic responses of grains at the external load (macroscopic stresses). Using linear elasticity, the elastic response grain stress, $\sigma_{ij}^{g(er)}$, can be related to the macrostress, i.e.:

$$\sigma_{ij}^{g(er)} = B_{ijmn}^{g} \sigma_{mn}^{M} \tag{3.6}$$

where B_{ijmn}^{g} is the stress concentration tensor and the summing over repeated indices is applied. The stress concentration tensor, B_{ijmn}^{g}, is calculated for each grain using different models (Mura 1993; Lipiński and Berveiller, 1989; Clyne and Withers, 1993) (see chapter 2). In general, the B_{ijmn}^{g} tensor depends on the internal structure of the sample such as the elastic anisotropy of grain and of the sample, elastic coupling between grains and the presence of different phases.
In a real material after mechanical and thermal treatment, the situation is slightly more complicated, because there are other reasons for existence of residual stresses. One of them is the anisotropy of thermal expansion coefficient. This effect is responsible for generation of thermal origin stresses. Another important reason of residual stress appearance is the anisotropy of plastic deformation. It is known that basic mechanism of plasticity is the slip on crystallographic system. Moreover, in different grains (having different orientation), different slip systems are activated. This leads to different plastic deformations in different grains. The misfit (incompatibility) of plastic deformations between neighboring grains is the source of additional stresses in material. They are *incompatibility* stresses, $\sigma_{ij}^{g(ic)}$, remaining in a material even if the external forces are removed, i.e., when $\sigma_{mn}^{M} \to 0$. Finally the total grain stress is:

$$\sigma_{ij}^{g} = \sigma_{ij}^{g(er)} + \sigma_{ij}^{g(ic)} \tag{3.7}$$

Using Eq.3.6 the above relation can be written as:

$$\sigma_{ij}^{g} = B_{ijmn}^{g} \sigma_{mn}^{M} + \sigma_{ij}^{g(ic)} \tag{3.8}$$

In a single phase polycrystalline material the second order incompatibility stresses are equal to the grain stresses (see Fig. 3.2):

$$\sigma_{ij}^{IIg(ic)} = \sigma_{ij}^{g(ic)} \tag{3.9}$$

if the external forces are absent, i.e., $\sigma_{ij}^{M} = 0$ (compare Eq. 3.4).

Introducing the same condition for multiphase material ($\sigma_{mn}^{M} = 0$), the phase stresses and the second order stresses are defined as (see Fig. 3.2):

$$\sigma_{ij}^{ph(ic)} = \sum_{g}^{N_{g,ph}} f^{g/ph} \sigma_{ij}^{g(ic)}$$
$$\sigma_{ij}^{IIg(ic)} = \sigma_{ij}^{g(ic)} - \sigma_{ij}^{ph(ic)} \tag{3.10}$$

where $N_{g,ph}$ is the total number of orientations in a given phase ("ph").

The mean value of incompatibility stresses calculated over the whole considered volume V_A (containing a large number of grains) equals zero. These stresses sum up to zero in the mixture law defined by Eq.3.3, which takes the following form for incompatibility stresses:

$$\sum_{ph}^{N_{ph}} f^{ph} \sigma_{ij}^{ph(ic)} = 0 \tag{3.11}$$

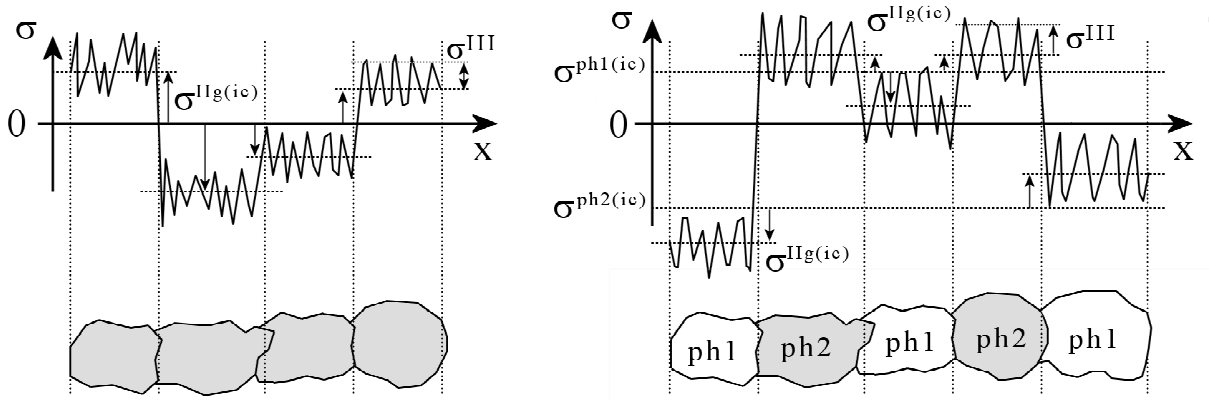

Fig. 3.2. *The first and the second order stresses induced by external loads or long-scale forces for single phase (a) and two phase (b). Also, the third order stresses,* σ^{III} *, characterizing local stress fields around lattice imperfections are indicated.*

The second order stresses are a result of (Baczmański, 2005)

- Plastic incompatibility stresses
- Thermal incompatibility stresses

Plastic incompatibility stresses are a result of anisotropic character of plastic deformation. Origin of these stresses in material is explained in Fig. 3.3. Initial grains are represented as spherical inclusions in a homogeneous matrix. After deformation and unloading of the applied forces - different grains have different deformations, depending on their orientations. Due to such misfit between grains, the second order stress ($\sigma_{ij}^{IIg(ic)} = \sigma_{ij}^{g(ic)}$, see Eq. 3.9) and the corresponding lattice strain arise, especially for strongly textured materials in which only a few preferred grain orientations are present.

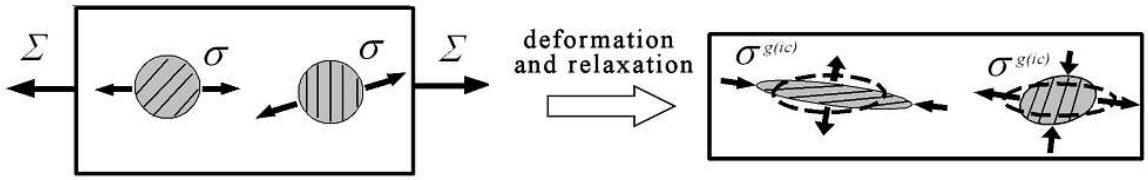

Fig. 3.3. *Scheme of plastic behavior of two exemplary grains having various orientations of slip systems with respect to the local stress* σ.

Thermal incompatibility stresses arise due to different thermal expansion coefficients of grains (Fig. 3.4). After thermal treatment the grain volume can significantly differ from those of the average matrix, due to difference between thermal expansion coefficients of the phases in multiphase material. If the expansion of grains belonging to particular phase is isotropic (for example in cubic structure), the misfit of their volumes leads to hydrostatic phase stress (first order stress). However, in some materials (e.g. in h.c.p. metals) the thermal expansion coefficient of crystal is anisotropic. This causes an additional incompatibility of the grain shape with the surrounding matrix after thermal treatment. Such the misfit generates the second order incompatibility stresses ($\sigma_{ij}^{IIg(ic)} = \sigma_{ij}^{g(ic)}$), even in single phase materials.

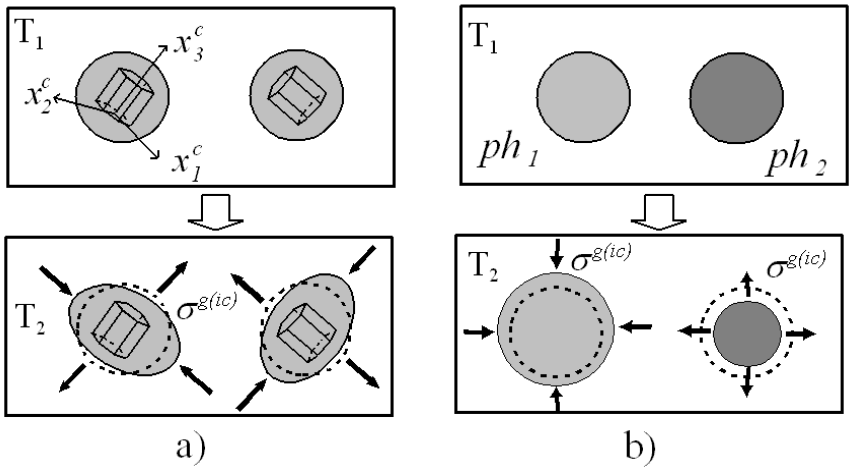

Fig. 3.4. *Scheme of thermal behaviour of two exemplary grains: a) having various orientations and anisotropic coefficients of thermal expansion, b) belonging to different phases with different coefficients of thermal expansion. The cooling process is presented* ($T_1 > T_2$).

3.4. Measurements of macrostresses using diffraction

The standard methods of stress determination (Culitty, 1978; Noyan and Cohen, 1987) are based on the measurement of interplanar spacing for various directions of the scattering vector. This method was described in Chapter 1. The mean lattice strain $<\varepsilon(\psi,\phi)>_{\{hkl\}}$ in L_3 direction (Fig. 1.3) is defined as:

$$<\varepsilon(\psi,\phi)>_{\{hkl\}} = \frac{<d(\psi,\phi)>_{\{hkl\}} - d^{0}_{\{hkl\}}}{d^{0}_{\{hkl\}}} \tag{3.12}$$

where: $d^{0}_{\{hkl\}}$ - the interplanar spacings for the *{hkl}* planes in a stress-free material,

$<d(\psi,\phi)>_{\{hkl\}}$ - the measured average interplanar spacings for the *{hkl}* planes,

$<\varepsilon(\psi,\phi)>_{\{hkl\}}$ - lattice strain averaged over the volume of diffracting grains.

$<\ldots>_{\{hkl\}}$ means the average for reflecting crystallites.

To relate the mean strain defined by the above equation to different types of stress, first the strain and stress for a diffracting grain have to be considered. In the case of linear elasticity the following relation can be written with respect to the ***L*** coordinate:

$$\varepsilon'^{g(el)}_{ij} = s'^{g}_{ijmn}\,\sigma'^{g}_{mn} \tag{3.13}$$

where $\varepsilon'^{g(el)}_{ij}$, σ'^{g}_{mn} and s'^{g}_{ijmn} are the elastic strain, stress and compliance for the grain *g*.

According to Eq. 3.8 the grain stress σ^{g}_{ij} is the superposition of the term depending on the macrostress $B^{g}_{ijkl}\sigma^{M}_{kl}$ and of the independent incompatibility stress $\sigma^{g(ic)}_{ij}$, i.e.:

$$\sigma^{g}_{ij} = B^{g}_{ijkl}\sigma^{M}_{kl} + \sigma^{g(ic)}_{ij} \tag{3.14}$$

For a multiphase material the incompatibility stresses can be split into the phase ($\sigma^{ph(ic)}_{ij}$) and the second order ($\sigma^{IIg(ic)}_{ij}$) stresses (see Eq. 3.10), i.e.:

$$\sigma^{g}_{ij} = B^{g}_{ijkl}\sigma^{M}_{kl} + \sigma^{ph(ic)}_{ij} + \sigma^{IIg(ic)}_{ij} \tag{3.15}$$

After transformation from ***X*** to ***L*** coordinate system the above equation takes the form:

$$\sigma'^{g}_{ij} = B'^{g}_{ijmn}\,\sigma'^{M}_{mn} + \sigma'^{ph(ic)}_{ij} + \sigma'^{IIg(ic)}_{ij} \tag{3.16}$$

where $\sigma'_{mn} = a_{mi}a_{nj}\,\sigma_{ij}$ for all types of stresses, $B'^{g}_{mnop} = a_{mi}a_{nj}\,a_{ok}a_{pl}B_{ijkl}$ and the transformation matrix a_{ij} is expressed by ϕ and ψ angles, i.e.:

$$\gamma_{ij} = \begin{bmatrix} \cos\phi\cos\psi & \sin\phi\cos\psi & -\sin\psi \\ -\sin\phi & \cos\phi & 0 \\ \cos\phi\sin\psi & \sin\phi\sin\psi & \cos\psi \end{bmatrix} \tag{3.17}$$

Substituting the grain stress given by Eq. 3.16 into Eq. 3.13, the elastic strain of a grain can be expressed through:

$$\varepsilon'^{g(el)}_{ij} = s'^{g}_{ijop}\,(B'^{g}_{opmn}\,\sigma'^{M}_{mn} + \sigma'^{ph(ic)}_{op} + \sigma'^{IIg(ic)}_{op}) \tag{3.18}$$

After calculation, the mean strain $<\varepsilon(\psi,\phi)>_{\{hkl\}}$ in L_3 direction can be expressed by:

$$\begin{aligned} <\varepsilon(\psi,\phi)>_{\{hkl\}} &= <\varepsilon'^{g(el)}_{33}>_{\{hkl\}} = <s'^{g}_{33op}\,B'^{g}_{opmn}\,\sigma'^{M}_{mn} + s'^{g}_{33mn}\,(\sigma'^{ph(ic)}_{mn} + \sigma'^{IIg(ic)}_{mn})>_{\{hkl\}} = \\ &= <s'^{g}_{33op}\,B'^{g}_{opmn}>_{\{hkl\}}\,\sigma'^{M}_{mn} + <s'^{g}_{33mn}>_{\{hkl\}}\,\sigma'^{ph(ic)}_{mn} + <s'^{g}_{33mn}\,\sigma'^{IIg(ic)}_{mn}>_{\{hkl\}} \end{aligned} \tag{3.19}$$

where the mean values $<\ldots>_{\{hkl\}}$ are calculated over the group of diffracting grains and the first order stresses σ'^{M}_{mn} and $\sigma'^{ph(ic)}_{mn}$ are excluded from the averaging operation (these values are independent of grain orientations).
Introducing the so-called diffraction elastic constants (Dolle, 1979; Barral, 1987; Brakman, 1987, Senczyk, 1995; Baczmański et al., 1993, 1997, 1997b), i.e.,

$$R^{M}_{mn}(\{hkl\},\psi,\phi) = <s'^{g}_{33op}\,B'^{g}_{opmn}>_{\{hkl\}} \text{ and } R^{ph(ic)}_{mn}(\{hkl\},\psi,\phi) = <s'^{g}_{33mn}>_{\{hkl\}} \tag{3.20}$$

Eq. 3.19 can be rewritten as:

$$<\varepsilon(\psi,\phi)>_{\{hkl\}} = R^{M}_{mn}(\{hkl\},\psi,\phi)\,\sigma'^{M}_{mn} + R^{ph(ic)}_{mn}(\{hkl\},\psi,\phi)\,\sigma'^{ph(ic)}_{mn} + <s'_{33mn}\,\sigma'^{IIg(ic)}_{mn}>_{\{hkl\}} \tag{3.21}$$

Finally, the above equation can be expressed in a more practical form if all the stresses are expressed in ***X*** coordinate system:

$$<\varepsilon(\psi,\phi)>_{\{hkl\}} = F^{M}_{mn}(\{hkl\},\psi,\phi)\,\sigma^{M}_{mn} + F^{ph(ic)}_{mn}(\{hkl\},\psi,\phi)\,\sigma^{ph(ic)}_{mn} + <a_{3m}a_{3n}s_{mnij}\,\sigma^{IIg(ic)}_{ij}>_{\{hkl\}} \tag{3.22}$$

where $F^{M}_{ij}(\{hkl\},\psi,\phi) = a_{mi}a_{nj}\,R^{M}_{mn}(\{hkl\},\psi,\phi)$ and $F^{ph(ic)}_{ij}(\{hkl\},\psi,\phi) = a_{mi}a_{nj}\,R^{ph(ic)}_{mn}(\{hkl\},\psi,\phi)$ are called the modified elastic constants. They join $<\varepsilon(\psi,\phi)>_{\{hkl\}}$ with the stresses σ_{ij} expressed in ***X*** coordinate system.

In a practical use of the multi-reflection method (see Chapter 1) the above equation is expressed as:

$$< a(\psi,\phi) >_{\{hkl\}} = \left\{ F_{mn}^{M}(\{hkl\},\psi,\phi)\,\sigma_{mn}^{M} + F_{mn}^{ph(ic)}(\{hkl\},\psi,\phi)\,\sigma_{mn}^{ph(ic)} + < a_{3m}a_{3n}s_{mnij}\sigma_{ij}^{IIg(ic)} >_{\{hkl\}} \right\} a^{0} + a^{0} \tag{3.23}$$

where $< a(\psi,\phi) >_{\{hkl\}}$ is the equivalent lattice parameter.

Eq. 3.23 constitutes the general relation between the stress field (the third order stresses σ_{ij}^{IIIg} are neglected) and strains which are determined using the diffraction method. As shown in Eq. 3.22, different types of stresses are differently conjugated with the $< \varepsilon(\psi,\phi) >_{\{hkl\}}$ strain. Simple linear relations occur for the mean stresses σ_{mn}^{M} and $\sigma_{mn}^{ph(ic)}$, which are multiplied by the diffraction elastic constants $F_{mn}^{M}(\{hkl\},\psi,\phi)$ and $F_{mn}^{ph(ic)}(\{hkl\},\psi,\phi)$, respectively. The difference between the diffraction elastic constants applied for the first order stresses and for the phase mean stresses becomes significant if the phases exhibit various elastic properties. The stresses σ_{mn}^{M} are imposed at the boundary of the volume penetrated by the used radiation, thus they must be localized at the diffracting grains using the concentration tensor $B_{ijkl}^{'g}$ (see $R_{mn}^{M}(\{hkl\},\psi,\phi)$ in Eq. 3.20). The $\sigma_{ij}^{ph(ic)}$ average incompatibility stresses do not depend on the values of the first order stresses and they represent the mean values over the grains of the considered phase. The third term of Eq. 3.23 is important if the second order stresses are present. The latter case is the most complicated one because the variation of the stresses between grains belonging to the same phase cannot be found directly from the experiment. The analysis of the second order stresses is possible only if the character of stress variation is known from a theoretical model. In the following chapter the prediction of the second order stresses by means of deformation models will be presented.

3.5. Multiphase materials

As mentioned in the beginning of this chapter, the residual plastic incompatibility stresses can be created by anisotropy of the plastic flow of different grains having slip systems oriented differently with respect to the local stress. After unloading of the external forces, the grains do not fit to the surrounding matrix. This gives rise to the second order stresses ($\sigma_{ij}^{IIg(ic)}$) and corresponding lattice strains, especially for strongly textured materials in which only a few preferred orientations of grains are present. In the case of a two-phase material, the deformation process is more complicated than in a single phase polycrystalline material, due to different properties of the phases. Additional incompatibility of grains occurs, leading to different values of mean phase stresses ($\sigma_{ij}^{ph(ic)}$).

Using the standard X-ray diffraction method, the lattice parameters are determined in function of $sin^2\psi$ for each phase independently. Interpretation of experimental data for multiphase materials is more complex than for a single phase material, because it is necessary to consider interaction between phases. The multireflection analysis is based on Eq. 3.23, written in a modified form for the ph_1 and ph_2 phases (Baczmański, 2005):

$$< a >^{ph1}_{\{hkl\}} = \left\{ F^{M}_{mn}\sigma^{M}_{mn} + F^{ph1(ic)}_{mn}\sigma^{ph1(ic)}_{mn} + q^{ph1} < a_{3m}a_{3n}s_{mnij}\sigma^{IIg(ic)}_{ij} >^{ph1}_{\{hkl\}} \right\} a^{0,ph1} + a^{0,ph1} \qquad (3.24a)$$

$$< a >^{ph2}_{\{hkl\}} = \left\{ F^{M}_{mn}\sigma^{M}_{mn} + F^{ph2(ic)}_{mn}\sigma^{ph2(ic)}_{mn} + q^{ph2} < a_{3m}a_{3n}s_{mnij}\sigma^{IIg(ic)}_{ij} >^{ph2}_{\{hkl\}} \right\} a^{0,ph2} + a^{0,ph2} \qquad (3.24b)$$

The incompatibility stresses sum up to zero in the mixture law defined by Eq. 3.11.

$$f^{ph1}\sigma^{ph1(ic)}_{mn} + f^{ph2}\sigma^{ph2(ic)}_{mn} = 0 \qquad (3.25)$$

where f^{ph1} and f^{ph2} are the volume fractions of the phases ph_1 and ph_2.
The unique solution of Eq. 3.24 can be found only when mixture law (Eq. 3.25) is taken into account. The solution of these equations can be found by the least square method in which all equations are used simultaneously in order to fit the theoretical $< a(\psi,\phi) >^{ph}_{\{hkl\}}$ vs. $sin^2\psi$ curves to experimental data for both phases. In turn, knowing the value of the macrostresses (σ^{M}_{ij}) and the mean incompatibility stresses ($\sigma^{ph1(ic)}_{mn}$ and $\sigma^{ph2(ic)}_{mn}$), the phase stresses (σ^{ph1}_{mn} and σ^{ph2}_{mn}) for each phase can be found:

$$\sigma^{ph1}_{ij} = B^{ph1}_{mnij}\sigma^{M}_{ij} + \sigma^{ph1(ic)}_{mn} \qquad \text{and} \qquad \sigma^{ph2}_{ij} = B^{ph2}_{mnij}\sigma^{M}_{ij} + \sigma^{ph2(ic)}_{mn} \qquad (3.26)$$

where the mean stress concentration tensors B^{ph1}_{ijmn} and B^{ph2}_{ijmn} are calculated for ph_1 and ph_2 phases, respectively. According to Eq. 3.3, the first order macrostresses must fulfill the mixture law, i.e.:

$$\sigma^{M}_{ij} = f^{ph1}\sigma^{ph1}_{ij} + f^{ph2}\sigma^{ph2}_{ij} \qquad (3.27)$$

Due to the weak penetration of X-ray radiation only the near-surface volume of the sample is studied. Because no force perpendicular to the sample surface is present in the analyzed volume, the σ^{M}_{33} macrostress is equal to zero. However, in spite of zero value of σ^{M}_{33} macrostress, a non-zero $\sigma^{ph(ic)}_{33}$ phase incompatibility stress can be present in each phase of a multiphase material, even in the near-surface volume penetrated by X-ray radiation. In such a case, the values of ($\sigma^{ph(ic)}_{11}$ - $\sigma^{ph(ic)}_{33}$) and ($\sigma^{ph(ic)}_{22}$ - $\sigma^{ph(ic)}_{33}$) can be found instead of $\sigma^{ph(ic)}_{11}$ and $\sigma^{ph(ic)}_{22}$ (Baczmański et al. 1997a). In the case of measurements performed inside a sample volume (e.g., neutron or synchrotron radiation) the non-zero value of σ^{M}_{33} stress can be also expected.

3.6. Calculation of the second order incompatibility stresses

The plastic incompatibility stresses arise during plastic deformation as a result of anisotropy of plastic flow of different grains. Plastic incompatibility stresses remain in material even if external stress is unloaded ($\Sigma_{ij} \rightarrow 0$). These stresses can be predicted by elastoplastic deformation models. In the calculations, the sample is represented by a number of grains, having an orientation distribution which reproduces the initial experimental texture. The model sample is subjected to elasto-plastic deformation and next the external forces are unloaded. Finally, the theoretical values of the second order plastic incompatibility stresses $\overline{\sigma_{ij}^{IIg(ic)}}$ are calculated (the bar denotes the model-predicted quantities). These stresses characterize the anisotropy of elasto-plastic deformation and they are correlated with nonlinearity of the experimental $<\varepsilon(\psi,\phi)>_{\{hkl\}}$ versus $sin^2\psi$ plot. In a plastically deformed material, the lattice strains $<\varepsilon(\psi,\phi)>_{\{hkl\}}$ can be expressed as a superposition of strains induced by macrostresses and the second order incompatibility stresses. For a single phase material, Eq. 3.22 can be simplified to:

$$<\varepsilon(\psi,\phi)>_{\{hkl\}} = F_{ij}^{M}(\{hkl\},\psi,\phi)\sigma_{ij}^{M} + < a_{3m}a_{3n}s_{mnij}\,\sigma_{ij}^{IIg(ic)} >_{\{hkl\}} \qquad (3.28)$$

In comparison with Eq.3.22, the term $\sigma_{ij}^{ph(ic)}$ is absent, because according to equation 3.11 in a single face material the average $\sigma_{ij}^{ph(ic)}$ equals zero.

The $\sigma_{ij}^{IIg(ic)}$ stress remains after unloading of the macrostresses and it can be calculated by the self-consistent model ($\overline{\sigma_{ij}^{IIg(ic)}}$ correspond to $\Sigma_{ij} \rightarrow 0$). The anisotropy of the incompatibility stresses can be correctly predicted by the model if the experimental texture is used as the input data. However, the absolute values of the stresses depend on the hardening process occurring during plastic deformation, which has generally a complicated character. Hence, to relate the magnitude of theoretical incompatibility stresses to the real one, an unknown scaling factor q is introduced. This factor does not depend on the grain orientation $\boldsymbol{g}$ and it rescales the amplitude of the stress tensor, i.e. the second order incompatibility stress $\sigma_{ij}^{IIg(ic)}(\boldsymbol{g})$ in the real sample is:

$$\sigma_{ij}^{IIg(ic)}(\boldsymbol{g}) = q\ \overline{\sigma_{ij}^{IIg(ic)}(\boldsymbol{g})} \qquad (3.29)$$

where q is the scaling parameter and $\overline{\sigma_{ij}^{IIg(ic)}(\boldsymbol{g})}$ is the model predicted second order stress for a grain with $\boldsymbol{g}$ orientation. Finally, the experimental lattice parameters $<a(\psi,\phi)>_{\{hkl\}}$ obtained from the diffraction method can be expressed as (Wroński, 2006b):

$$<a(\psi,\phi)>_{\{hkl\}} = [F_{ij}^{M}(\{hkl\},\psi,\phi)\sigma_{ij}^{M} + q\ \overline{< a_{3m}a_{3n}s_{mnij}\sigma_{ij}^{IIg(ic)}(\boldsymbol{g}) >_{\{hkl\}}}\,]\,a^{o} + a^{o} \qquad (3.30)$$

where $\overline{< a_{3m}a_{3n}s_{mnij}\,\sigma_{ij}^{IIg(ic)}(\boldsymbol{g}) >_{\{hkl\}}}$ is the model predicted strain caused by the plastic incompatibility second order stress. This term, characterizing the nonlinearities of the $sin^2\psi$ plot

is adjusted to the experimental data. Only the amplitude of the theoretical function $\overline{< a_{3m} a_{3n} s_{mnij}\, \sigma_{ij}^{IIg(ic)}(\boldsymbol{g}) >_{\{hkl\}}}$ is rescaled by the q factor, while its dependence on the orientation of the scattering vector (i.e., on ϕ and ψ angles) is given by the model. When the value of q parameter is determined, the real values of the plastic incompatibility second order stresses $\sigma_{ij}^{IIg(ic)}(\boldsymbol{g})$ can be calculated for all grain orientations $\boldsymbol{g}$ using Eq.3.29. It should be noted that if the determined value of q is near *1*, the model predicts correctly the amplitude of the stress tensor, but if $q < 1$, the magnitude of theoretical stresses is overestimated. The latter case can be explained due to stress relaxation or decreasing of the hardening process, which is not taken into account in our calculations.
To show the level of the second order stresses for a statistical grain, the average equivalent residual stress $[\sigma_{eq}^{g(ic)}]$ is calculated:

$$[\sigma_{eq}^{IIg(ic)}] = \frac{1}{8\pi^2} \int_E \sigma_{eq}^{IIg(ic)}(\boldsymbol{g})\, f(\boldsymbol{g})\, d\boldsymbol{g} \tag{3.31}$$

where

$$\sigma_{eq}^{IIg(ic)} = \left[\frac{1}{2} \left\{ (\sigma_{11}^{IIg(ic)} - \sigma_{22}^{IIg(ic)})^2 + (\sigma_{11}^{IIg(ic)} - \sigma_{33}^{IIg(ic)})^2 + (\sigma_{22}^{IIg(ic)} - \sigma_{33}^{IIg(ic)})^2 \right\} + 3 \left\{ (\sigma_{12}^{IIg(ic)})^2 + (\sigma_{13}^{IIg(ic)})^2 + (\sigma_{23}^{IIg(ic)})^2 \right\} \right]^{\frac{1}{2}}$$

is the equivalent stress of a grain (with orientation $\boldsymbol{g}$) calculated according to von Mises formula and the integral is calculated over the whole orientation space E using $f(\boldsymbol{g})$ texture function as the weighting parameter.

3.7. Analysis of incompatibility stresses in single phase materials

In this paragraph the results for single phase materials will be presented. The multi-reflection method was applied in order to estimate the second order stresses in cold rolled ferrite steel (bcc structure; 95% reduction). The surface layer of about *200* μm was removed by electropolishing and the crystallographic texture was determined from pole figures measured using the K_{α} wavelength of Cr radiation. The orientation distribution function was calculated from the pole figures *{110}*, *{100}* and *{211}* (Bunge, 1982). Experimental texture was compared with the theoretical one predicted by the model (Fig. 3.5). The cold rolling process was simulated using the self-consistent model. The polycrystalline sample was represented by *10000* random grains and typical values of τ_c, H, A and elastic constant were used for calculations Table 3.1. (τ_c and H parameters can be determined from the hardening curve).

Table 3.1. *Parameters used for calculations for ferrite steel .*

Parameters for self-consistent model			Calculation with anisotropic elastic constant			Calculation with isotropic elastic constant	
τ_c [MPa]	H [MPa]	A	C_{11} [GPa]	C_{12} [GPa]	C_{44} [GPa]	Young modulus [GPa]	Poisson ratio
240	90	1	231	134	116	196	0.3

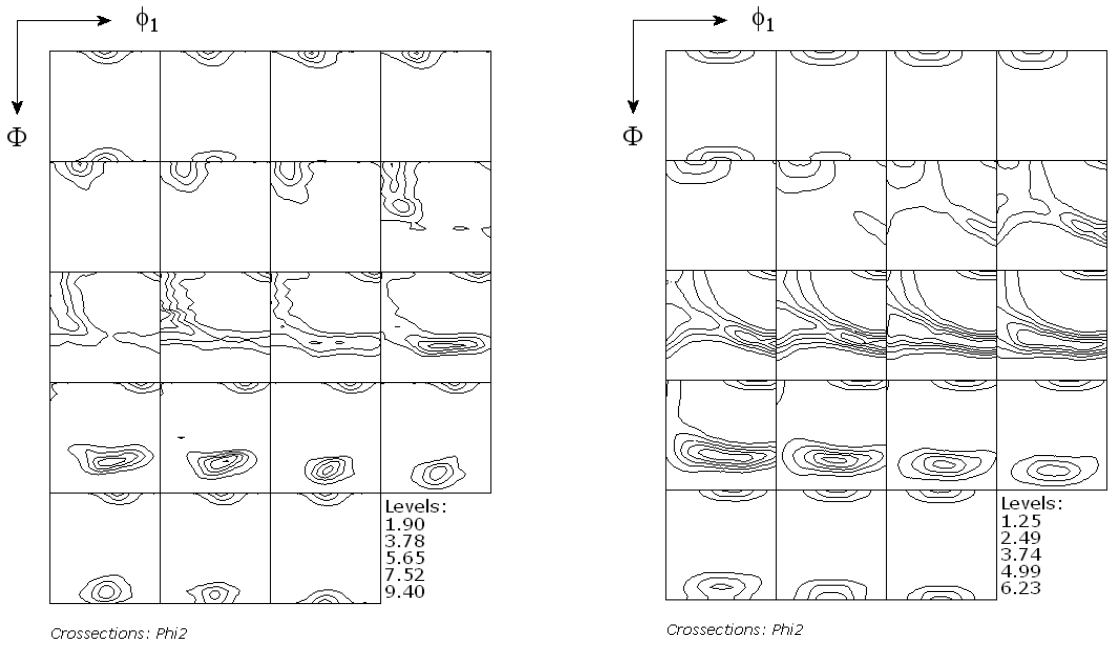

a. b.

Fig. 3.5. *Orientation distribution functions of cold rolled steel (80 % reduction): (a) experimental texture, (b) texture predicted by SC model; ϕ_2 sections are shown.*

Good agreement between experimental and theoretical texture was obtained. This proves that model works well. Before a proper experiment, the equipment alignment was checked with a stress free powder sample. A small pseudo stress (10 MPa) was found, which confirms that the equipment was correctly aligned. This value should be treated as a possible systematic error for all measurements. Interplanar spacings for {211}, {200}, {110} planes were measured and the $< a(\psi,\phi) >_{\{hkl\}}$ vs. $sin^2\psi$ plots were determined for many directions (i.e., $\phi=0^0$, 180^0, 30^0, 210^0, 90^0, 270^0). This enabled the estimation of shear stress components. In order to calculate the diffraction elastic constants, the Reuss, Voigt and SC (for interior and for surface) models were used. The obtained results are presented in table 3.2.

Table 3.2. *Results of the fitting procedure for ferrite sample. Calculations were performed taking into account plastic incompatibility stresses. The values of χ^2 parameter obtained neglecting plastic incompatibility stresses are given in brackets.*

Type of model	Type of diffraction elastic constants	Macrostresses [Mpa]					Scaling factor q	Average equival. plast. incomp. stress $\sigma_{eq}^{IIg(ic)}$ [MPa]	Stress free lattice param. a^0 [Å]	χ^2 $q\neq0$ (χ^2) $q=0$
		σ_{11}^M	σ_{22}^M	σ_{12}^M	σ_{13}^M	σ_{23}^M				
Self-cons. Aniso	Reuss	-52.6 ±3.2	-58.2 ±3.2	-2.6 ±2.3	2.6 ±1.2	-1.9 ±0.9	0.202 ±.01	48.6 ±2.2	2.86636 ±0.00001	5.1 (13.2)
	self-cons. (free surf.)	-53.6 ±3.1	-60.3 ±3.4	-2.8 ±2.2	2.5 ±1.5	-2.4 ±0.9	0.19 ±.01	47.7 ±2.2	2.86636 ±0.00001	5.03 (13.1)
	self-cons. (interior)	-56.8 ±3.2	-67.0 ±3.4	-2.7 ±2.3	2.7 ±1.3	-2.6 ±1.1	0.23 ±.01	56.1 ±2.0	2.86637 ±0.00001	4.6 (15.9)
	Voigt	-57.8 ±3.3	-70.3 ±3.8	-2.8 ± 2.7	2.8 ±1.3	-3.2 ±1.3	0.23 ±.01	55.2 ±2.0	2.86638 ±0.00001	4.96 (19.3)
Self-consistent isotropic		-79.4 ±3.1	-77.8 ±3.5	-3.1 ±2.7	2.5 ±1.1	-3.5 ±1.1	0.22 ±.01	74.7 ±2.2	2.86639 ±0.00001	4.9 (19.3)
Lefers-Wierzbanowski		-69.4 ±3.7	-66.8 ±3.9	0.7 ±2.8	1.3 ±1.1	-4.6 ±1.1	0.18 ±.05	68.1 ±2.2	2.86639 ±0.00001	4.67 (11.2)

The lattice parameters for different *hkl* are presented in Fig. 3.6. The strong oscillation of the $< a(\psi,\phi) >_{\{hkl\}}$ in function of $\sin^2\psi$ was observed due to the second order stresses. First, the multi-reflection method was used with the assumption that the second order stresses $\sigma_{ij}^{IIg(ic)}$ are absent ($q=0$ in Eq. 3.30); the results are presented by dashed lines in Fig. 3.6. In general, a poor convergence between the theoretical plots and experimental points was found for such an approach. Next, the procedure based on Eq. 3.30 was used and the value of q factor was determined. In this case, a very good agreement between the fitted curves and measured lattice parameters (continuous lines in Fig. 3.6) was obtained, because the nonlinearities caused by the plastic incompatibility stresses ($\sigma_{ij}^{IIg(ic)}$) were taken into account (χ^2 parameter decreased about 3-4 times, see Table 3.2).

A slightly asymmetrical behaviour of the $<a(\psi,\phi)>_{\{hkl\}}$ vs. $sin^2\psi$ curves was observed for the orientations ϕ and $\phi + 180^0$, which was not explained by the shear macrostresses σ_{13}^M , σ_{23}^M nor by texture asymmetry. This effect, probably caused by a non-symmetrical sample preparation, was not taken into account in the analysis of experimental data.

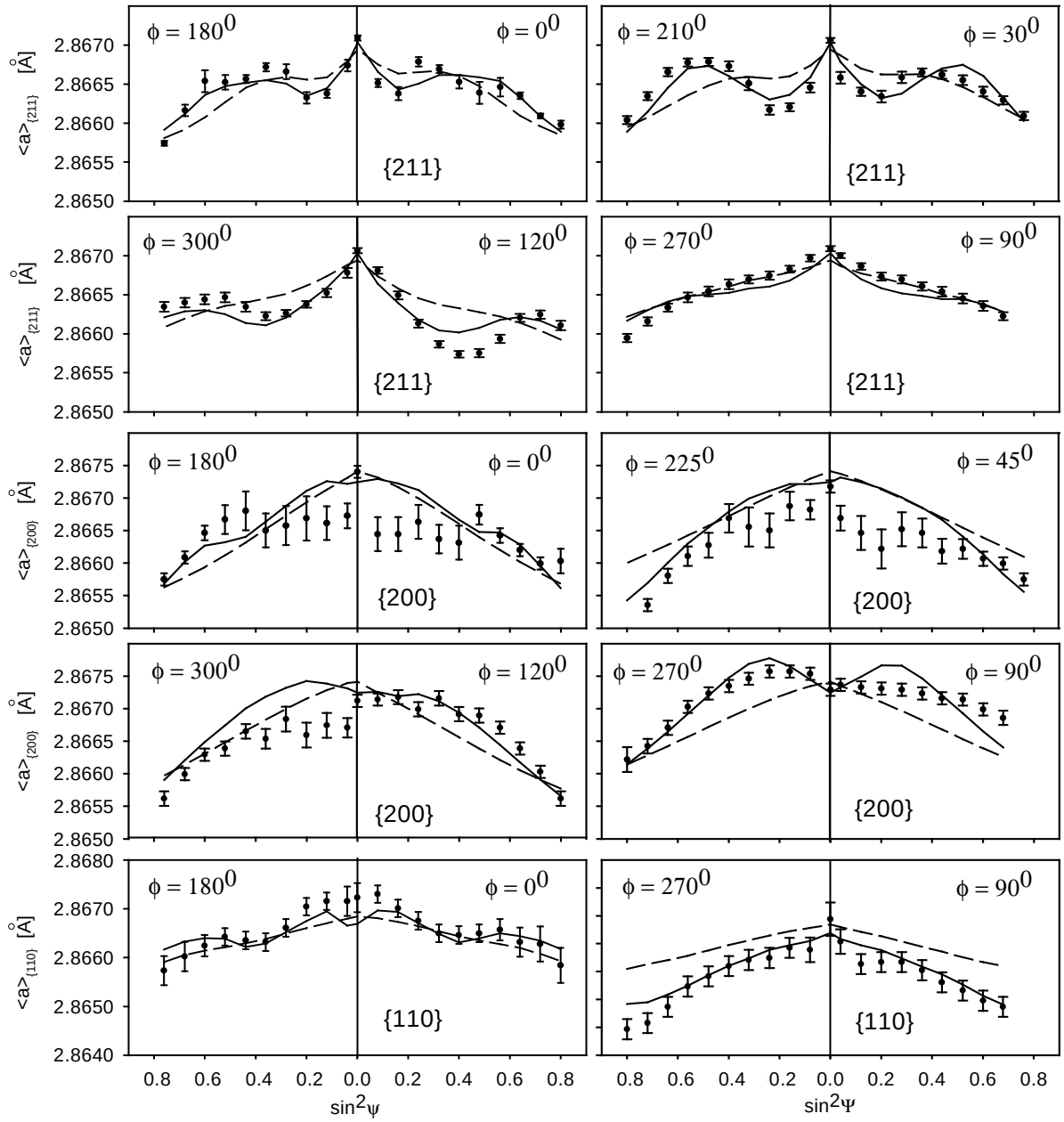

Fig. 3.6. *Measured lattice parameters (points) and theoretical results of fitting (continuous lines for $q \neq 0$ and dashed lines for $q = 0$) for cold rolled ferrite steel. The SC model for free surface was used to calculate the diffraction elastic constants.*

The $\langle a(\psi,\phi)\rangle_{\{hkl\}}$ vs. $sin^2\psi$ curves calculated for different models are shown in Fig. 3.7. The comparison of Reuss and Voigt models is presented in the left column, SC (interior) and SC (free surface) - in the right column. It should be noticed that the results for different models are quite similar and, consequently, the χ^2 is almost the same for all considered cases.

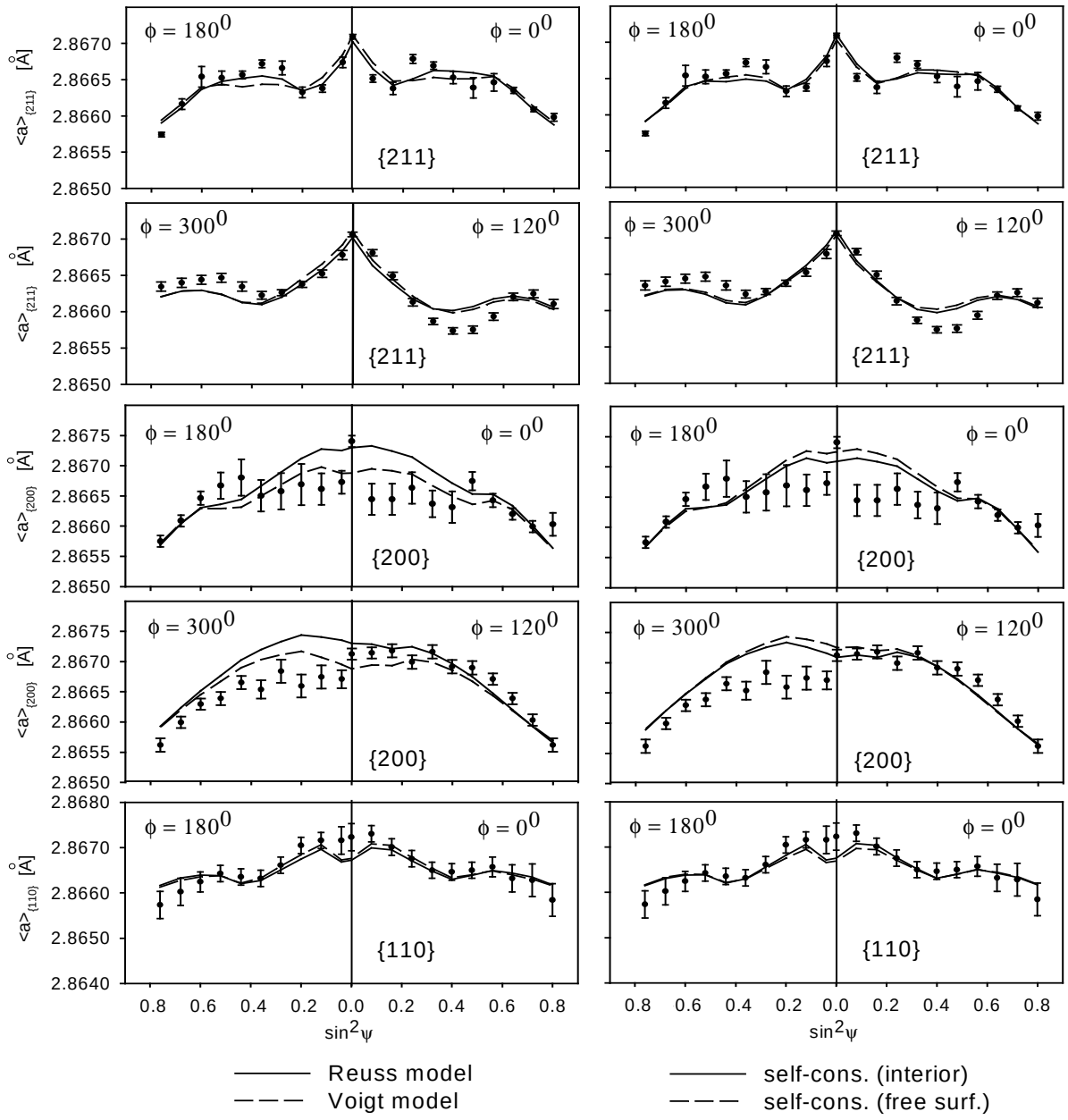

Fig. 3.7. *Measured lattice parameters (points) and theoretical results of fitting for cold rolled ferrite steel. The comparison of different models used for the calculation of diffraction elastic constants is done: the results corresponding to Reuss and Voigt models are shown in the left column, while those corresponding to SC (interior) and SC (free surface) models - in the right column.*

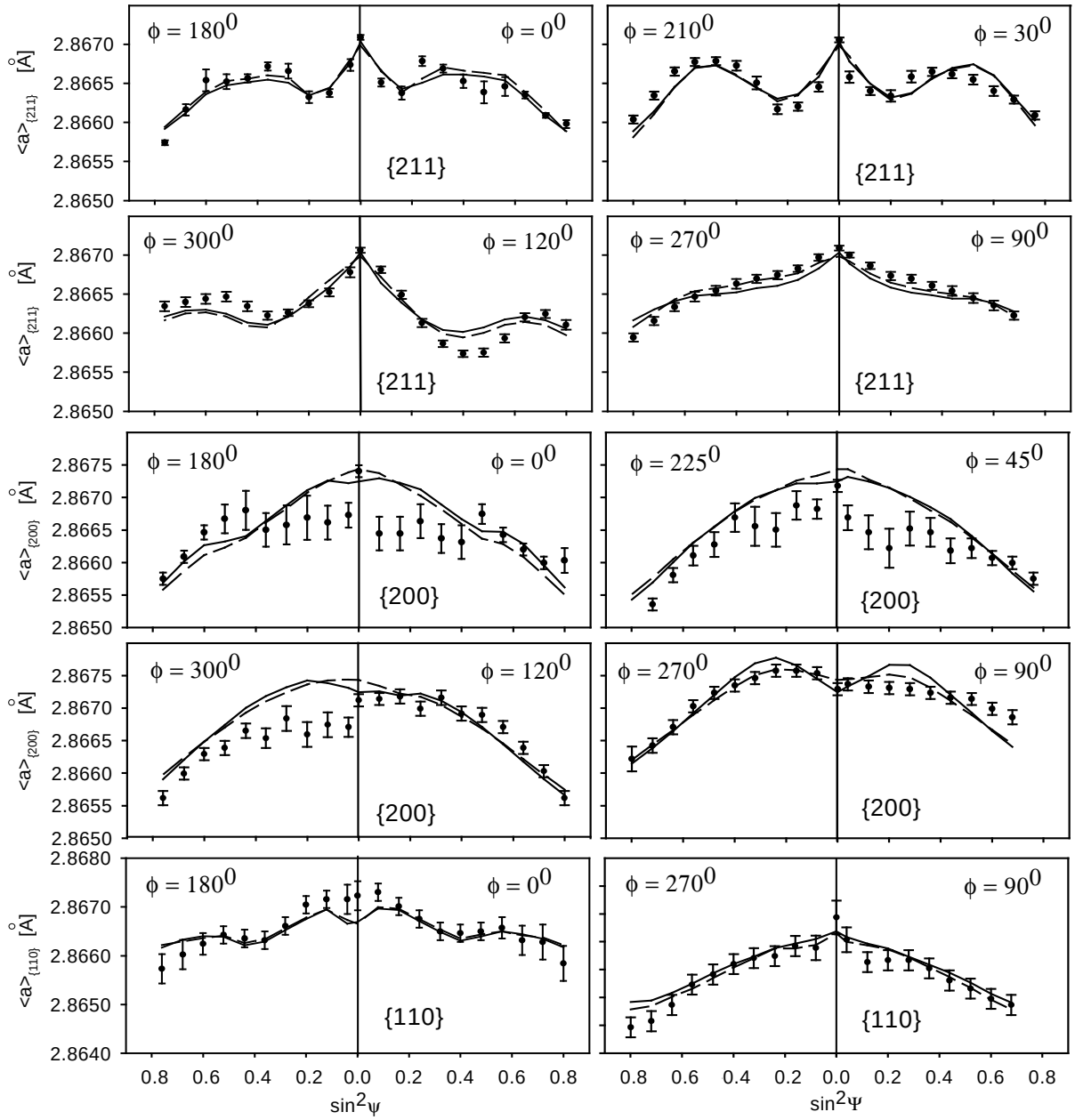

Fig. 3.8. *Measured lattice parameters (points) and theoretical results of fitting (continuous lines for anisotropic elastic constant and dashed lines for isotropic elastic constants) for cold rolled ferrite steel. The SC approach for free surface was used to calculate the diffraction elastic constants.*

The influence of elastic constants on the second order stresses was studied using the SC (self consistent) model. Both anisotropic and isotropic elastic constants were used. The data used for calculations are shown in Table 3.2. The results of SC model calculations with anisotropic or isotropic elastic constants are presented in Fig 3.8. In the case of ferrite a good agreement of experimental and predicted data is obtained both for isotropic and anisotropic elastic constants

(Wroński, 2004). However, different values of the second order stress level were predicted in the two cases: 74 MPa for isotropic elastic constants and 48 MPa for anisotropic ones.

The LW (Lefers-Wierzbanowski) model is also often used for the interpretation of experimental data. This model is based on isotropic interaction between grains. Hence, the comparison between the SC (isotropic case) and LW models was done. The results are shown in Table 3.2 and in Fig 3.9. Both models predict similar values of the second order stress level: 68 MPa (LW model) and 74 MPa (SC model -isotropic case) (Wroński, 2004; Wierzbanowski, Wroński et al. 2005). It should be noted, however, that the SC isotropic model predicts higher level of the second order stresses than the anisotropic one (Table 3.2).

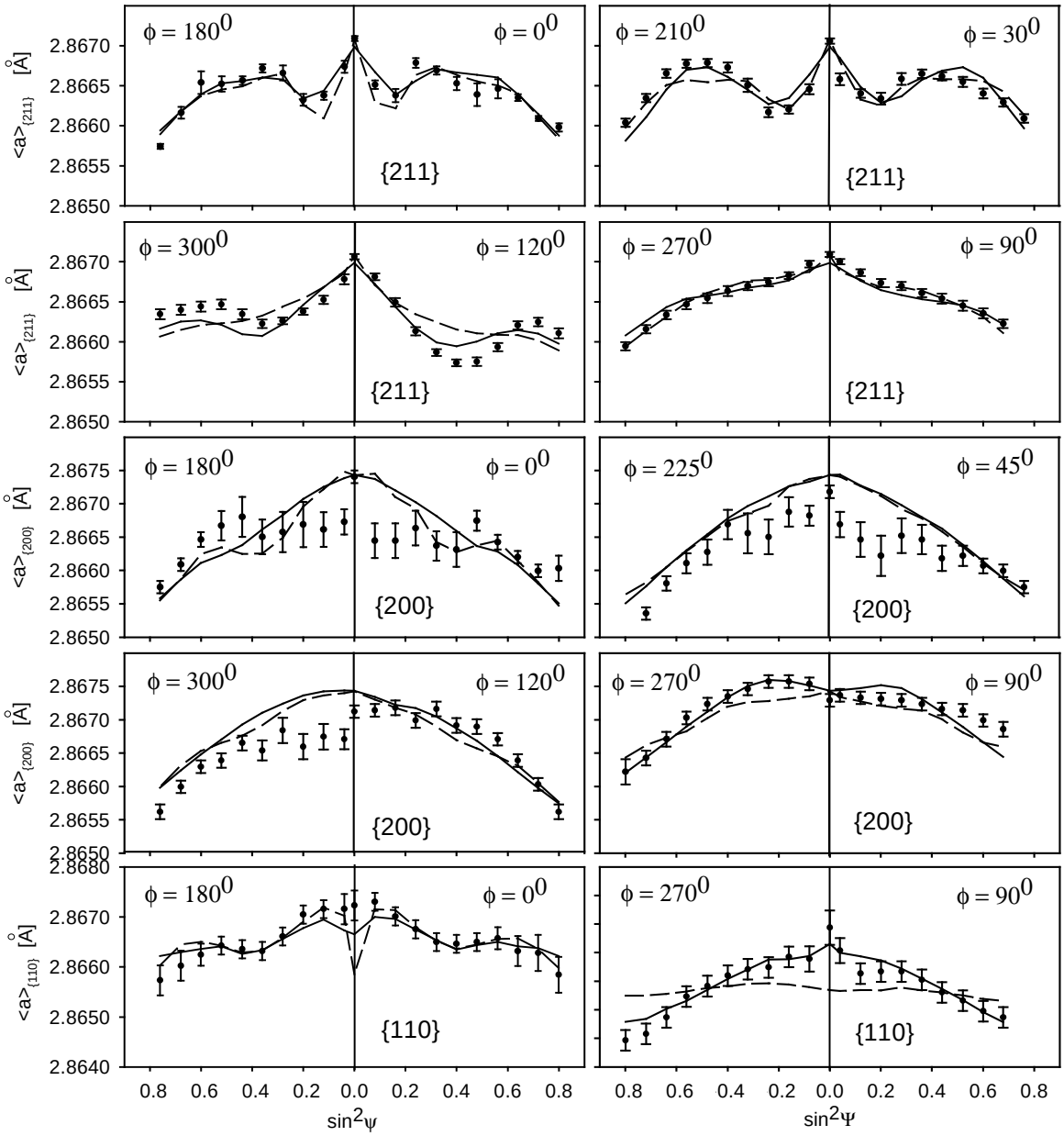

Fig. 3.9. *Measured lattice parameters (points) for cold rolled ferrite steel and predicted results: SC model (continuous lines) and LW model (dashed lines). Isotropic elastic constant were used.*

The next examined sample was the 316L austenite steel (fcc structure). This sample was cold rolled to the reduction of 50% and then stretched along the transverse direction (up to 20%). The classical $\sin^2\psi$ method was used. The ODF of the cold rolled sample was determined from *{111}*, *{100}* and *{220}* poles figures (determined using Cr radiation) (Bunge 1982). The determined ODF was compared with that predicted by SC model - Fig 3.10; the agreement is very good. The tensile test was studied using this model. The polycrystalline sample was represented by *10 000* grains and the cold rolling texture was the input data for calculations. Typical values of τ_c, *H*, *A* and elastic constants were used for calculations (see Table 3.3).

Table 3.3. *Parameters used in calculations for austenite steel.*

Parameters for self-consistent model			Calculation with anisotropic Elastic constant			Calculation with isotropic elastic constant	
τ_c [MPa]	*H* [MPa]	*A*	C_{11} [GPa]	C_{12} [GPa]	C_{44} [GPa]	Young modulus [GPa]	Poisson ratio
120	200	1	198	125	122	196	0.3

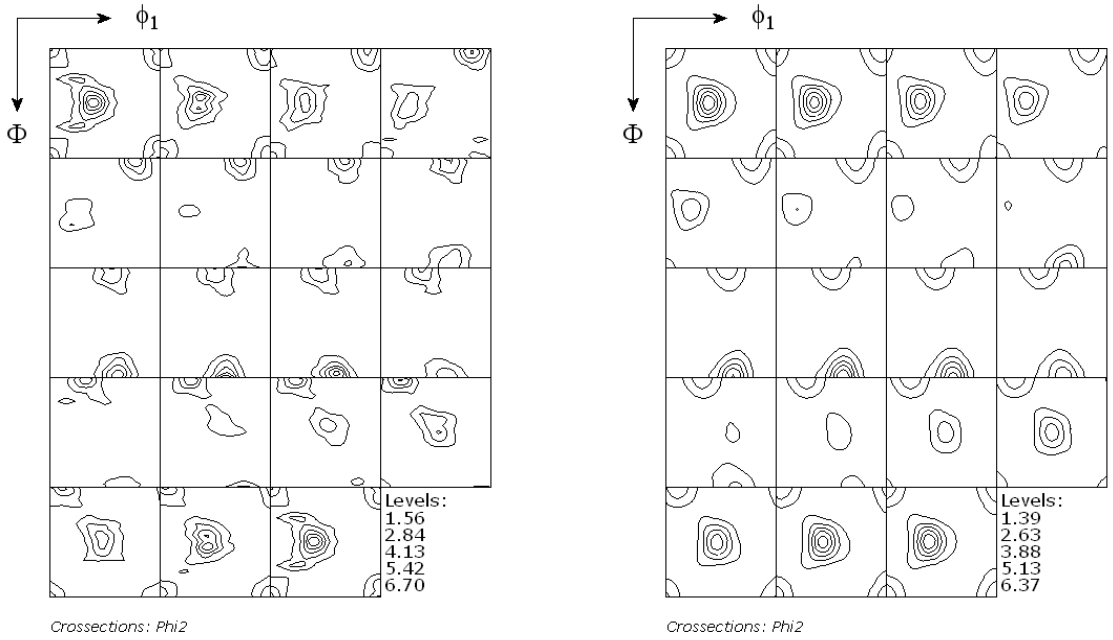

a. b.

Fig. 3.10. *ODF of cold rolled austenite steel 316L: (a) experimental texture, (b) texture predicted by SC model. The ϕ_2 sections are shown.*

Before the proper experiment, the equipment alignment was checked with a stress free powder sample. The small pseudo stress (12 MPa) was found, which confirmed a correct preparation of the equipment. The interplanar spacings for planes {200}, {220}, {311} were measured. In order

to estimate shear stress components the experiment was repeated for many values of φ angle (i.e., $\phi = 0^0, 45^0, 90^0, 180^0, 225^0, 270^0$). The multi-reflection method based on Eq. 3.23 was used. The diffraction elastic constants were calculated with Reuss, Voigt, SC (interior) and SC (free surface) models. In the case of SC model the anisotropic and isotropic elastic constants were used, while only isotropic case was considered in LW model. The results of calculation are listed in Table 3.4.

Table 3.4. *Results for 316L steel sample (errors correspond to uncertainties of the measured peak positions). Calculations were performed with (q≠0) and without (q=0) taking into account plastic incompatibility stresses. The values of* χ^2 *parameter in this second case are given in brackets.*

Type of model	Type of diffraction elastic constants	Macrostresses [MPa]					Scaling factor q	Average equival. plast. incomp. stress $[\sigma_{eq}^{IIg(ic)}]$ [MPa]	Stress free lattice param. a^0 [Å]	χ^2 $q\neq0$ (χ^2) $q=0$
		σ_{11}^M	σ_{22}^M	σ_{12}^M	σ_{13}^M	σ_{23}^M				
Self-cons. Aniso	Reuss	-84.8 ±4.4	-14.2 ±5.2	0.2 ±4.4	0.3 ±1.6	-1.2 ±1.6	0.46 ±.02	53.1 ±2.2	3.59349 ±0.00002	7.71 (10.3)
	self-cons. (free surf.)	-90.5 ±4.9	-9.9 ±6.1	1.8 ±5.2	0.2 ±2	-1.2 ±1.7	0.49 ±.02	57.4 ±2.2	3.59353 ±0.00002	8.74 (11.6)
	self-cons. (interior)	-108.1 ±6.1	-19.2 ±6.9	2.3 ±6.1	0.5 ±2.3	-1.7 ±2.3	0.45 ±.02	52.8 ±2.0	3.59356 ±0.00002	8.51 (11.2)
	Voigt	-127.2 ±7.7	-23.6 ±9	4.6 ± 8.4	0.8 ±3.1	-2.2 ±2.8	0.46 ±.02	53.2 ±2.0	3.59363 ±0.00001	9.72 (12.6)
Self-cons. ISO		-111.5 ±7.3	-28.6 ±7.9	-3.1 ± 7.6	1.0 ±2.6	-2.0 ±2.6	0.31 ±.03	57.1 ±2.0	3.59355 ±0.00001	11.4 (12.6)
LW		-111.1 ±7.2	-36.5 ±7.2	-8.8 ± 7.2	1. ±2.6	-2.1 ±2.6	0.36 ±.02	37.7 ±2.0	3.59357 ±0.00001	10.78 (12.6)

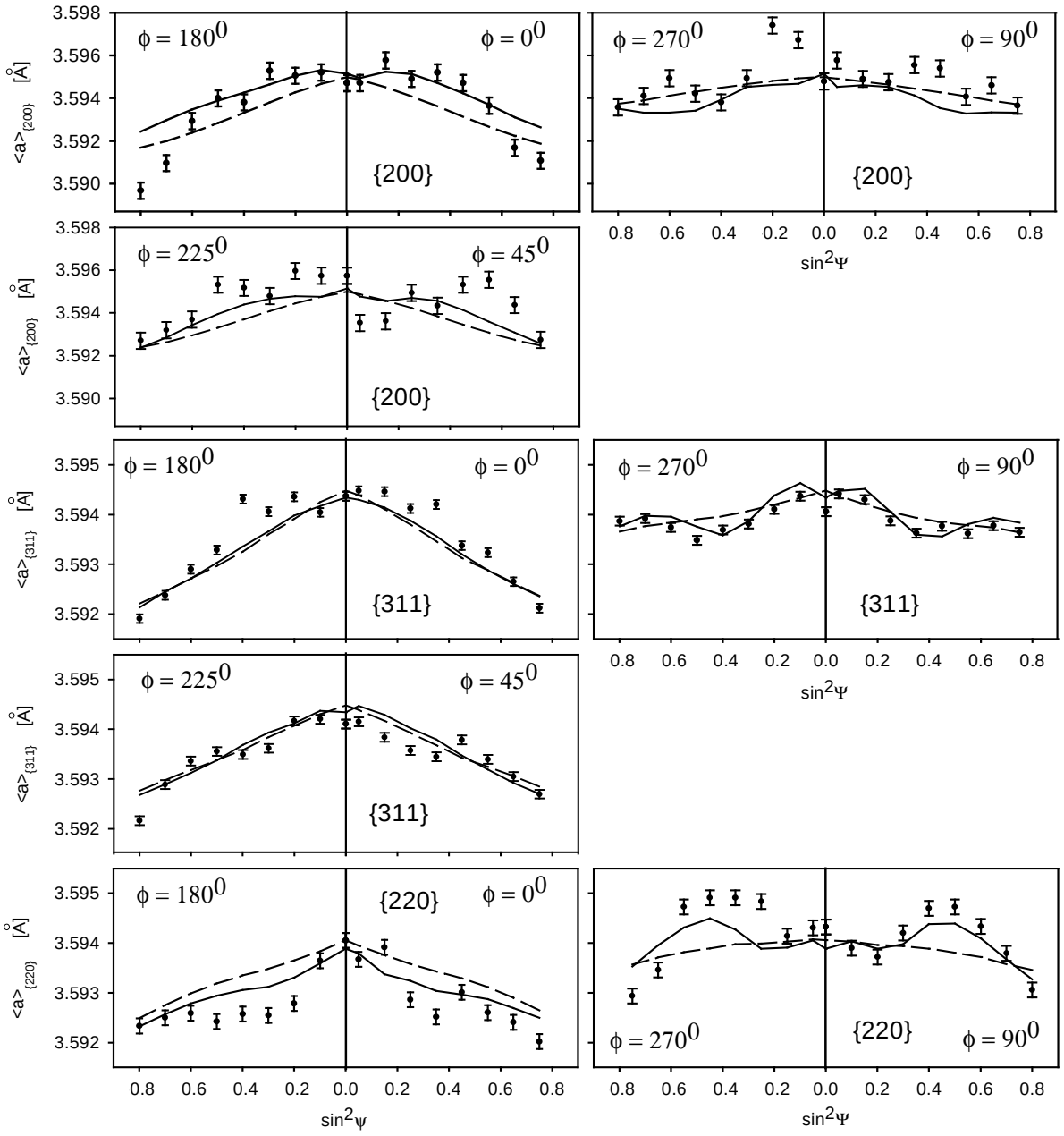

Fig. 3.11. *Measured lattice parameters (points) and theoretical results of fitting (continuous lines for $q \neq 0$ and dashed lines for $q = 0$) for 316L steel stretched in the tensile test. The multi-reflection method was used. The SC model (free surface) was used to calculate the diffraction elastic constants.*

The theoretical plots are presented for two assumptions, i.e., when the plastic incompatibility stresses are not assumed (dashed lines for $q=0$), and when the influence of $\overline{\sigma_{ij}^{g(ic)}(\boldsymbol{g})}$ stresses is taken into account and the q parameter is determined from Eq. 3.23 (continuous lines). As presented in Fig. 3.11, the quality of fitting is definitely better when the plastic incompatibility stresses are assumed (e.g., for SC free surface model: $\chi^2 = 8.74$ for $q \neq 0$, while $\chi^2 = 11.6$ for $q=0$).

The diffraction elastic constants were predicted by Reuss, Voigt, SC (interior) and SC (free surface) models. The results of calculations with these elastic constants are presented in Fig.3.12 and in Table 3.4. As it is seen, the considered models predict correctly the oscillations of $<a(\psi,\phi)>_{\{hkl\}}$ vs. $sin^2\psi$ graph. The second order stresses determined with all models have the values about 53 MPa.

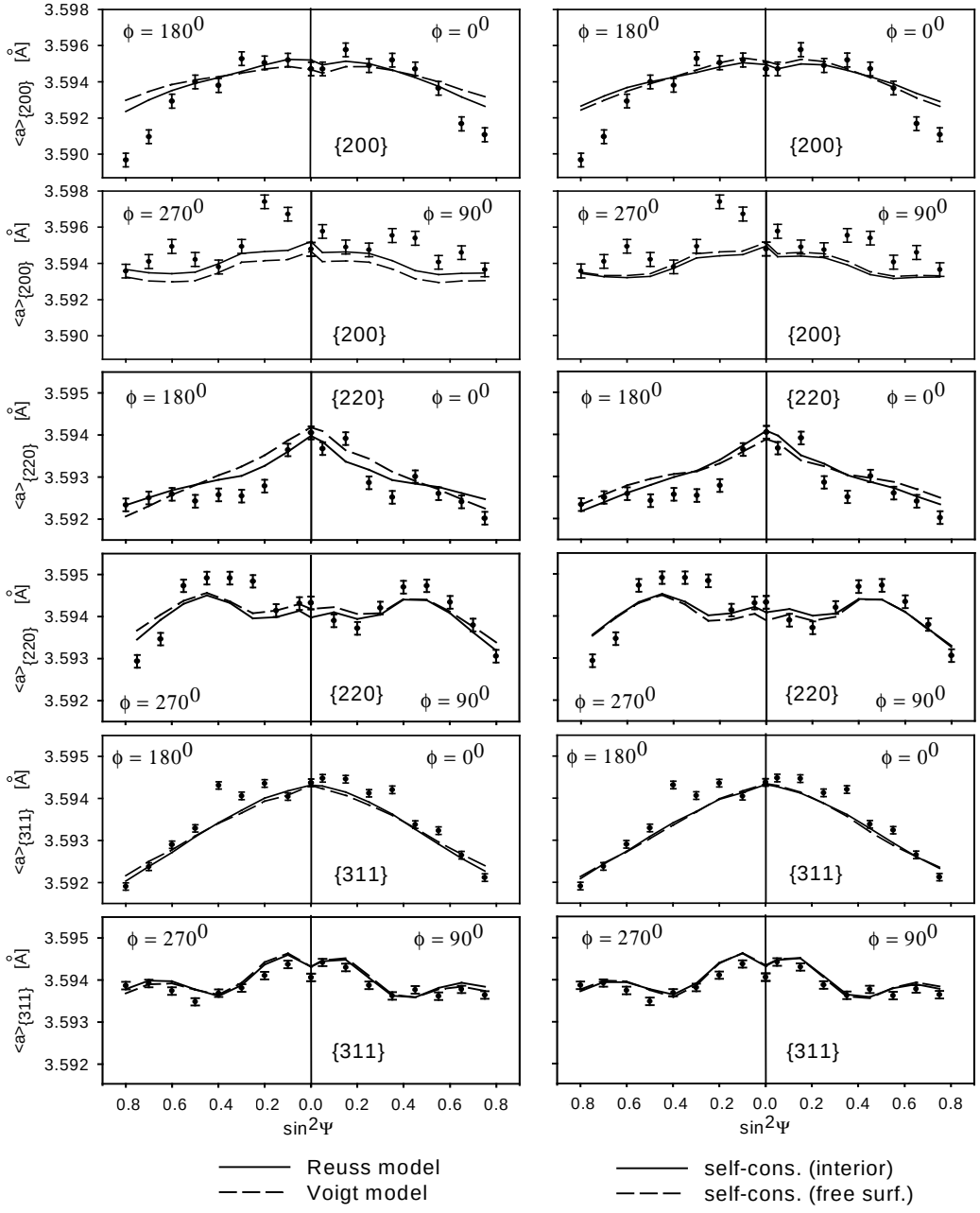

Fig. 3.12. *Measured lattice parameters (points) and predicted results for cold rolled austenite steel 316L. Different models were used for the calculation of diffraction elastic constants. Reuss and Voigt models are compared in the left column, SC (interior) and SC (free surface) - in the right column*

The influence of isotropic and anisotropic elastic constants on the obtained results was also checked for the 316L fcc steel - Fig 3.13. It should be noticed that, a worse convergence between the theoretical plots and experimental points was found when isotropic elastic constants were used in the case of austenitic phase. This effect can be easily observed for {220} planes. The χ^2 parameter increases when isotropic elastic constants are used (Table 3.4).

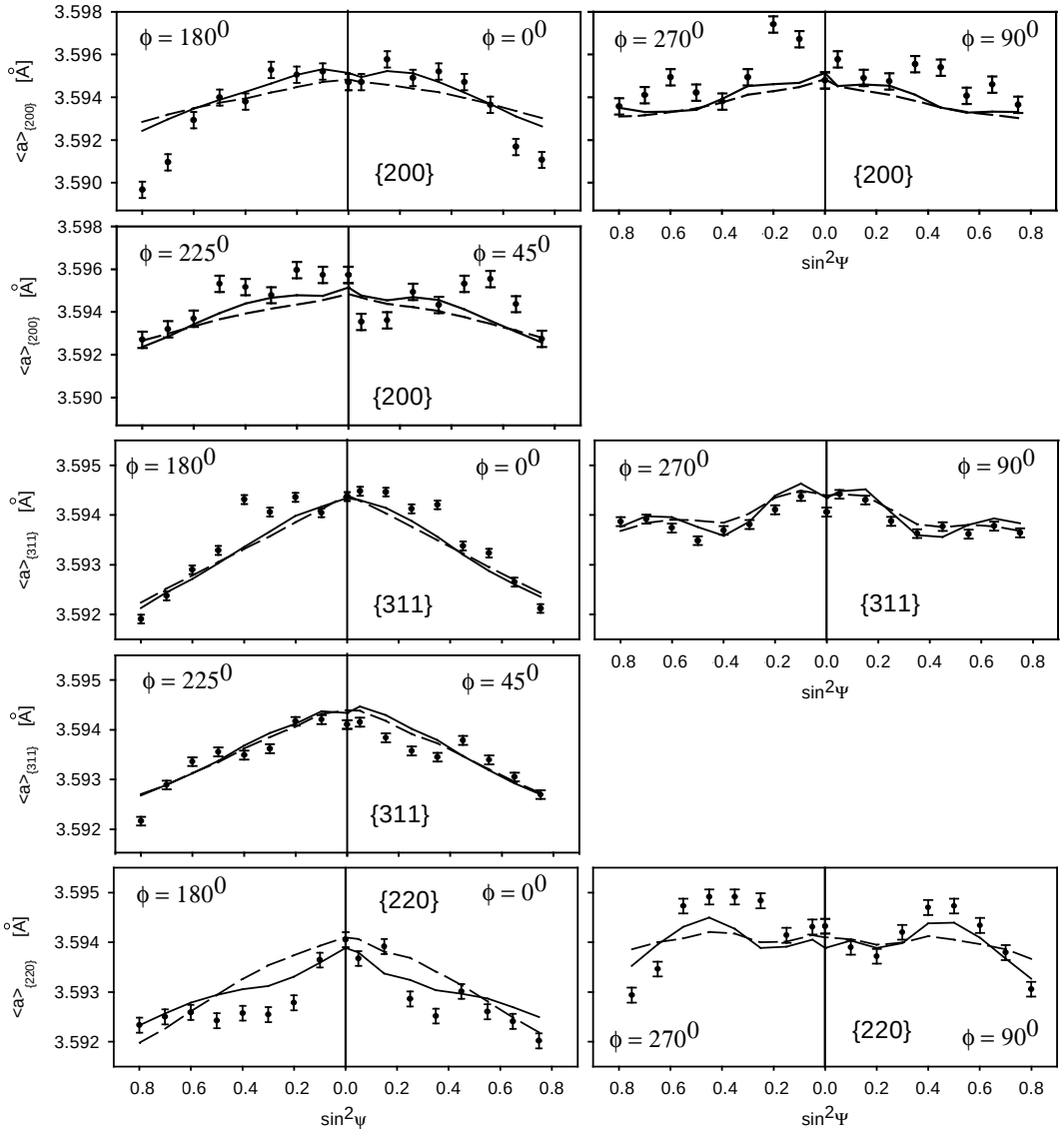

Fig. 3.13. *Measured lattice parameters (points) and theoretical results of fitting for the stretched 316L steel. Continuous lines are used for anisotropic elastic constant and dashed lines - for isotropic elastic constants. SC model was applied.*

Finally, the isotropic LW model was used for the calculations. The results are shown in Fig. 3.14 and in Table 3.4. It is visible that both LW model and SC model (with isotropic elastic constants) give similar results. However, the agreement between calculated and experimental data is not very good. We can conclude that models with isotropic interaction are not good enough to predict precisely the second ordered stresses in fcc materials. This stays in contrast with bcc ferrite phase, where the difference between use of isotropic and anisotropic elastic constant is not significant.

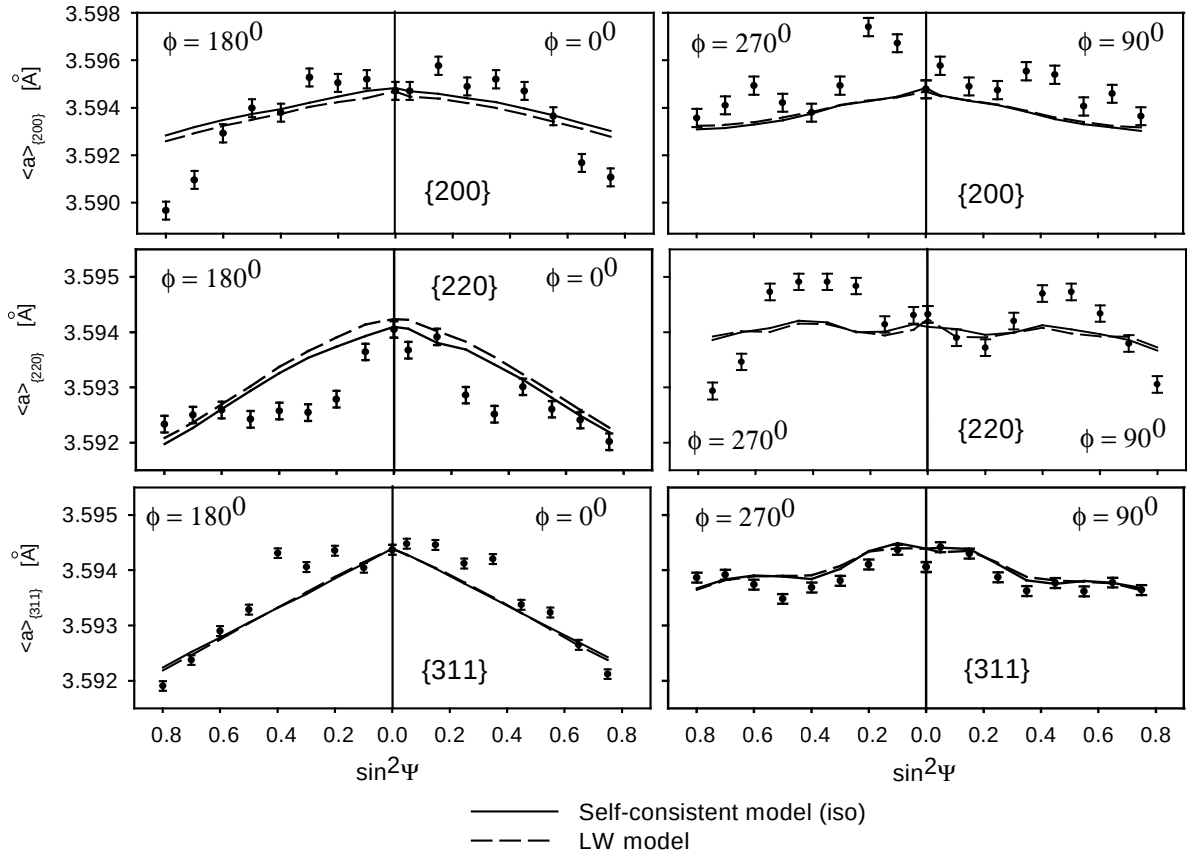

Fig. 3.14. *Measured lattice parameters (points) and theoretical results of fitting (lines) for austenitic 316L steel. Isotropic elastic constants were used in the frame of SC and LW model.*

3.8. Analysis of incompatibility stresses in multiphase materials

3.8.1. Material and experimental method

In this paragraph the results for duplex steel will be presented. This work is the second stage of the study started by Dakhlaoui (Dakhlaoui, Wroński, et al., 2006c) and it concerns the stresses remaining in the duplex steel after elasto-plastic deformation, when the sample is unloaded.

The studied material is the austeno-ferritic stainless steel, containing approximately 50% of each phase (the ferrite phase is called α and austenite - γ). It was obtained by continuous casting and then hot rolling down to 15 mm sheet thickness. A solution annealing heat treatment at 1050 ^{0}C was given, followed by quenching in water in order to avoid the precipitation of secondary phases. The chemical composition of the alloy are presented in Table 3.5. The characteristic microstructure of the steel consists of austenitic islands elongated along the rolling direction (RD) and embedded in a ferritic matrix (Fig. 3.15).

Table 3.5. *Chemical composition (wt. %) of duplex steel*

Material	C	Mn	Cr	Ni	Mo	Cu	S	N
X2 Cr Ni Mo 22.5.3 (UR45N)	0.015	1.6	22.4	5.4	2.9	0.12	0.001	0.17

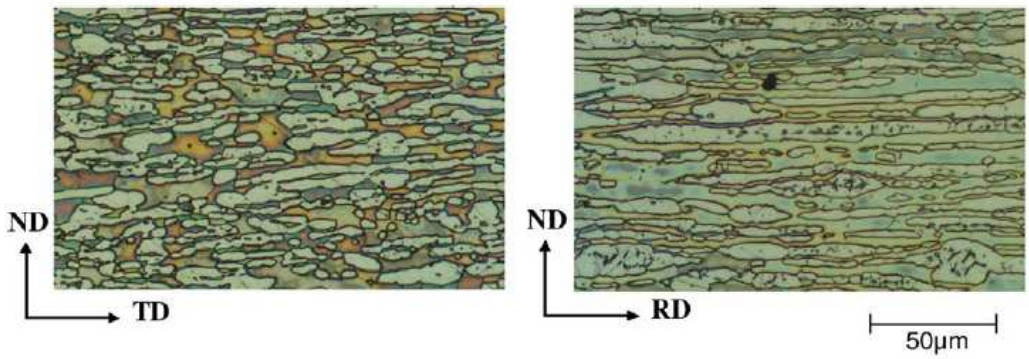

Fig. 3.15. *Microstructure of the studied duplex stainless steel for two different sections. The main directions of rolling are indicated: RD, rolling direction; TD, transverse direction; ND, normal direction.*

Two cylindrical samples (*8 mm* diameter and *10 mm* height, having axis aligned along transverse direction - TD) were machined from those measured previously using neutron diffraction during "in situ" tensile (14% of deformation) and compression (7% of deformation) tests. The third cylindrical sample having similar dimensions was cut from as-received non-loaded material.

The ENGIN-X diffractometer at the ISIS spallation neutron source, CCLRC Rutherford Appleton Laboratory (UK) (Dann, et al., 2003) was used to measure interplanar spacings $< d >_{\{hkl\}}$ applying the $sin^2\psi$ diffraction geometry (similar as usually for X-rays). The orientations of the scattering vector with respect to the applied load and to the directions of

rolling are shown in Fig. 3.16. As it is described in paragraph 3.5, the neutron radiation enables estimation of the values of $(\sigma_{11}^{ph(ic)} - \sigma_{33}^{ph(ic)})$, $(\sigma_{22}^{ph(ic)} - \sigma_{33}^{ph(ic)})$,$(\sigma_{11}^{M} - \sigma_{33}^{M})$ and $(\sigma_{22}^{M} - \sigma_{33}^{M})$. The configuration shown in Fig. 3.16a enabled the cylindrical sample to be rotated about an axis perpendicular to the positioning table, in order to change the ψ angle in the range from 0^0 to 90^0 for negative and positive ψ angles. The measurements were performed for two positions of the sample with respect to the table and the $sin^2\psi$ curves were determined for two different ϕ angles: $\phi = 0^0$ and $\phi = 90^0$ (Figs. 1.3 and 3.16b).

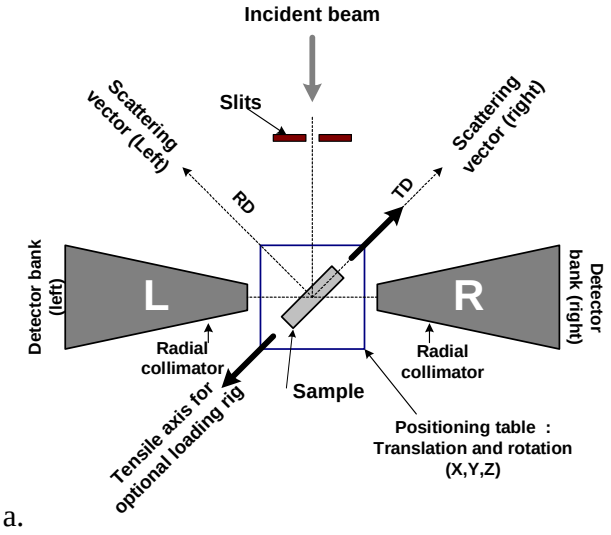

a.

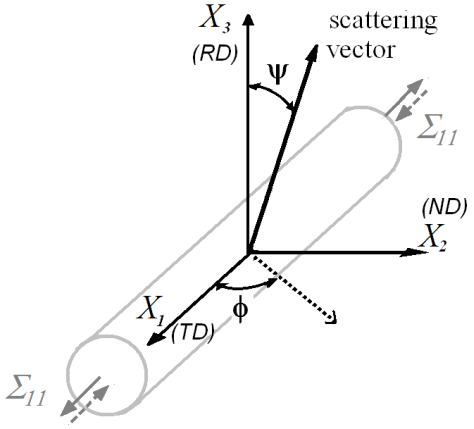

b.

Fig. 3.16. *Schematic of the ENGIN-X instrument with the sample subjected to the tensile (or compressive) loading along TD, overhead view (a). Orientation of the scattering vector with respect to the principal sample axes during tensile and compression tests (b). The main directions of rolling are indicated: RD - rolling direction, TD - transverse and ND – normal direction (the loads were applied along TD).*

The detectors measure time-resolved spectra, each Bragg peak being produced by reflection from a different family of {hkl} planes. The load axis was aligned horizontally at $+45^0$ to the incident beam, allowing simultaneous measurement of lattice strains in directions both parallel and perpendicular to the applied load. A boron carbide slit of dimensions 4 mm high, 4 mm wide was

used to define the incident beam. Radial collimators in front of each detector bank defined an exit aperture of approximately *4* mm. The experiments were performed using the time-of-flight diffraction method and the peak positions for many *hkl* reflections were determined independently for both phases using the GSAS software package (Larson and Von Dreele, 1994).

3.8.2. Modelling and experimental data

The stresses in the studied samples were determined from the $<a>_{\{hkl\}}$ parameters measured by TOF neutron diffraction for different *hkl* reflections (Oleś, 1998). Since a stress free sample was unavailable as a reference ($a^{0,ph}$ lattice parameters are unknown), hence only the differences between main stresses components: ($\sigma_{11}^{ph(ic)} - \sigma_{33}^{ph(ic)}$), ($\sigma_{22}^{ph(ic)} - \sigma_{33}^{ph(ic)}$), ($\sigma_{11}^{M} - \sigma_{33}^{M}$) and ($\sigma_{22}^{M} - \sigma_{33}^{M}$) were found using the least square fitting based on Eqs. 3.24, 3.25.
The orientation distribution functions (Fig. 3.17), characterizing crystallographic textures, were calculated from the experimental pole figures, which were measured using the neutron diffraction method on the 6T1 diffractometer at the LLB, Saclay, France (Bunge, 1982). The anisotropic single crystal elastic constants were used in the calculations (Table 3.6)

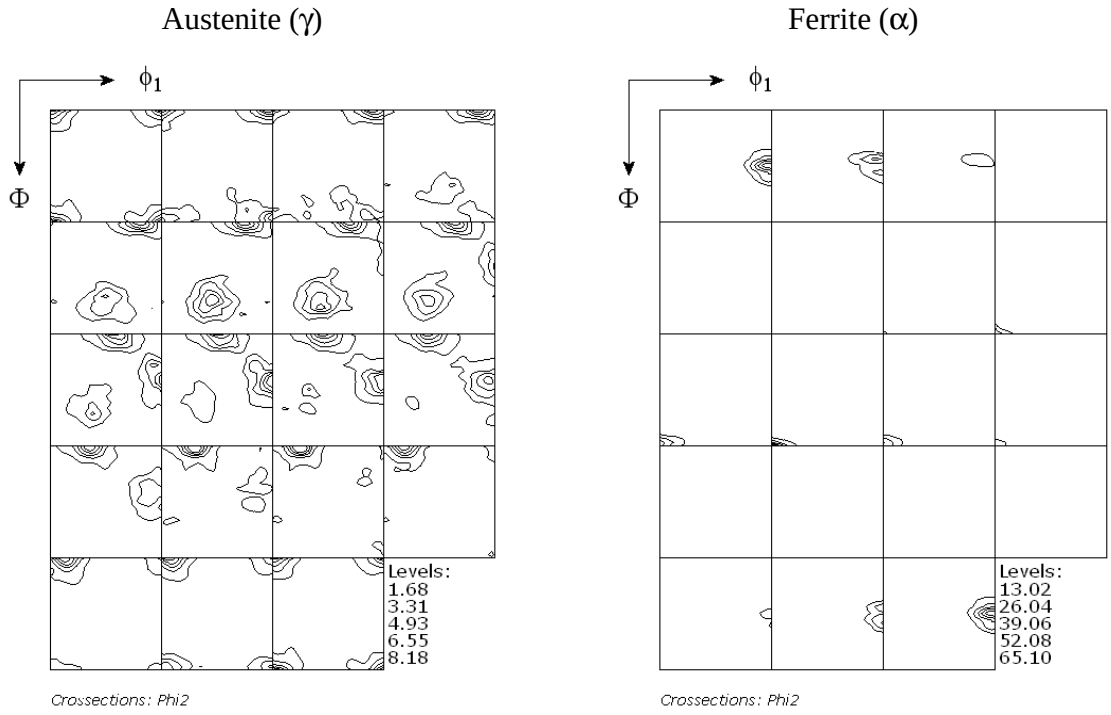

Fig. 3.17. *Orientation distribution functions (ODF) for both phases of duplex steel determined by neutron diffraction. The ϕ_2 sections through Euler space are presented for austenitic and ferritic phases. The sample axes are defined in Fig. 3.16b.*

The SC model was used for interpretation of the experimental data. The calculations were carried out for 20 000 spherical inclusions representing austenite (50%) and ferrite (50%) grains embedded in a homogeneous matrix having properties averaged over all crystallites belonging to both phases. Anisotropic single crystal elastic constants (Table 3.6) and experimental initial

stresses (see Table 3.7), equal for all grains within one phase, were assigned to the spherical inclusions. Crystal lattice orientations of individual grains were defined according to the orientation distribution functions of both phases (see Fig. 3.17). Two families of slip systems (i.e., <111>{110} and <111>{211}) were assumed for the ferritic phase, whereas only one was used for the austenitic phase (i.e., <110>{111}). The main goal is to find the effective model parameters (τ_c^{ph} - critical resolved stress and H^{ph} - work hardening parameter) characterizing both phases for which theoretical results agree with experimental data.

These parameters can be estimated from hardening curve and from lattice strains $<\varepsilon_{11}^{\Sigma}>_{\{hkl\}}^{ph}$ vs. applied external stress (Σ_{11}). Figs 3.18, 3.19 and 3.20 show the influence of initial critical shear stress and hardening parameter on the elastic strains and hardening curve.

The exemplary relation of $<\varepsilon_{11}^{\Sigma}>_{\{hkl\}}^{ph}$ vs. applied external stress (Σ_{11}) for duplex steel is shown in Figs. 3.18 and 3.19. At the beginning (up to $\Sigma_{11} \approx 250$ *MPa*) both phases are below the yield point and only linear elastic deformation occurs. Because of similar elastic constants (Table 3.6) the elastic response of ferrite is similar to austenite. After the yield point for the γ-phase (Γ points at $\Sigma_{11} \approx 250$ *MPa – Fig. 3.18)*, austenite is deformed plastically, while ferrite remains in the elastic range. Consequently, the created incompatibility stress leads to differences in lattice strains measured for both phases. The distance between two functions increases till the second characteristic point (Ω at $\Sigma_{11} \approx 450$ *MPa*), where the lines start to approach each other. This point (Ω in Fig. 3.18b) can be identified as the yield stress for α-phase and the opposite tendency of the evolution of mismatch strain (and stress) means that the work hardening is higher in gamma than in alpha phase. When the position of Γ and Ω is known it is possible to find the value of τ_c^{ph} for each phase.

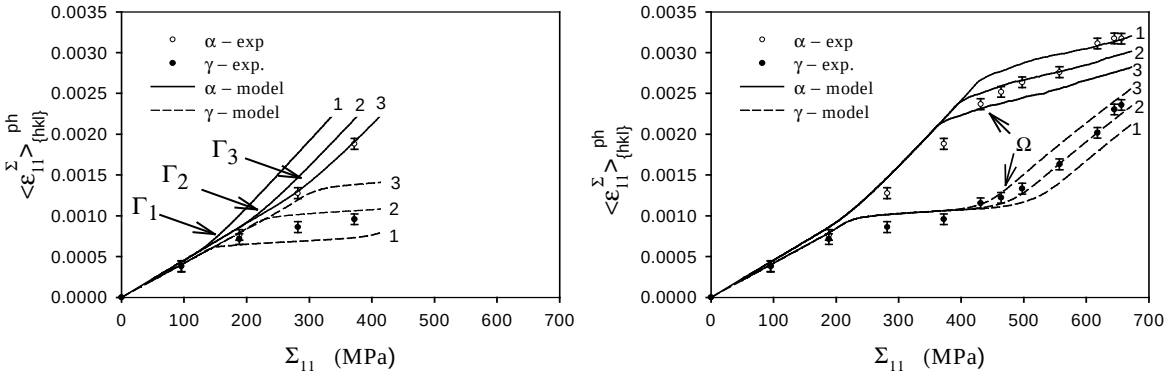

Fig. 3.18. *Influence of initial critical shear stress on the elastic strains measured "in situ" by neutron diffraction. The theoretical results are presented for: a)* $\tau_{eff}^{\gamma,0}$ *=50 MPa (1),* $\tau_{eff}^{\gamma,0}$ *=80 MPa (2) and* $\tau_{eff}^{\gamma,0}$ *=110 MPa (3); b)* $\tau_{eff}^{\alpha,0}$ *=230 MPa (1),* $\tau_{eff}^{\alpha,0}$ *=260 MPa (2) and* $\tau_{eff}^{\alpha,0}$ *=290 MPa (3).*

Another parameter, H^{ph}, can be found from $<\varepsilon_{11}^{\Sigma}>_{\{hkl\}}^{ph}$ vs. applied external stress Σ_{11} and from hardening curves. The last part of sample deformation (i.e., over $\Sigma_{11} \approx 450$ *MPa* in Figs. 3.19 and 3.20) shows the plastic behaviour of ferrite and austenite. In this range, the plots depend on the

relative hardening of both phases. From this range it is possible to estimate $H_{eff}^{\alpha} / H_{eff}^{\gamma}$ ratio. Also the slope of the hardening curve (Fig. 3.20) depends on the value of hardening parameter, but it depends on $H_{eff}^{\alpha} + H_{eff}^{\gamma}$ and does not depend on the ratio $H_{eff}^{\alpha} / H_{eff}^{\gamma}$. By means of these two graphs it is possible to estimate the values of hardening parameters of both phases. The influence of work hardening on the elastic strains and on the hardening curve is presented in Figs. 3.19 and 3.20.

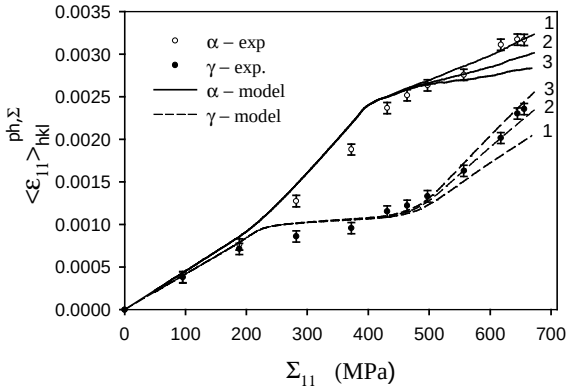

Fig. 3.19. *Influence of work hardening on the elastic strains measured "in situ" by neutron diffraction. The theoretical results are presented for: a)* $H_{eff}^{\alpha} / H_{eff}^{\gamma}$ *=1 (1),* $H_{eff}^{\alpha} / H_{eff}^{\gamma}$ *=0.35 (2) and* $H_{eff}^{\alpha} / H_{eff}^{\gamma}$ *=0.1 (3), while* $H_{eff}^{\alpha} + H_{eff}^{\gamma}$ *=270 MPa;*

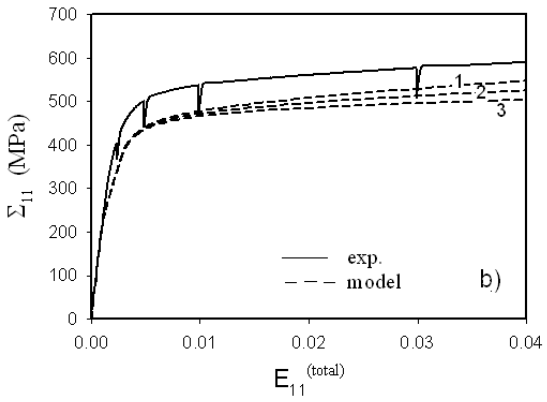

Fig. 3.20. *Results of the mechanical tensile test (solid line) compared with model prediction (dashed line). The deformation rate was stopped at the points corresponding to those for which neutron diffraction experiment was performed. The theoretical results are presented for* $H_{eff}^{\alpha} + H_{eff}^{\gamma}$ *=120 MPa (1),* $H_{eff}^{\alpha} + H_{eff}^{\gamma}$ *=270 MPa (2) and* $H_{eff}^{\alpha} + H_{eff}^{\gamma}$ *=420 MPa (3), while* $H_{eff}^{\alpha} / H_{eff}^{\gamma}$ *= 0.35.*

The final model parameters for which the theoretical curves are the closest to the experimental data were found by Rim Dakhlaoui and the present author (Dakhlaoui, Wroński et al., 2006c and Dakhlaoui,Wroński et al., 2007b) using SC model. The values of these parameters are given in

Table 3.6. They will be used in further calculations, performed in order to find the second order stresses and to investigate the anisotropy of internal stresses. The obtained results are presented in Fig. 3.21, 3.22 and 3.23.

Table 3.6*. Elastoplastic parameters of both phases*

phase	single crystal elastic constants (matrix notation) [GPa]			critical resolved shear stress τ_c^0 [MPa]	hardening parameter H [MPa]
	C_{11}	C_{12}	C_{44}		
austenite	198	125	122	135	200
ferrite	231	134	116	215	120

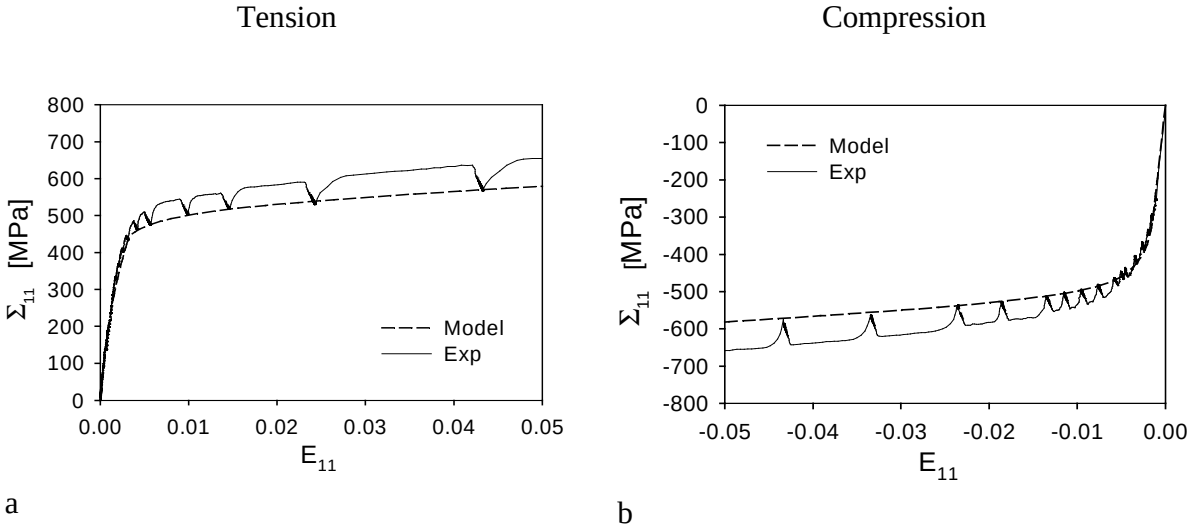

Fig. 3.21. *Macro-mechanical curves Σ_{11} vs. E_{11} are compared to model predictions for (a) tensile and (b) compressive tests. Initial crystallographic texture and initial residual stresses were used in the model calculations. The load was applied along TD. The deformation rate was stopped at the points corresponding to those for which neutron diffraction experiment was performed.*

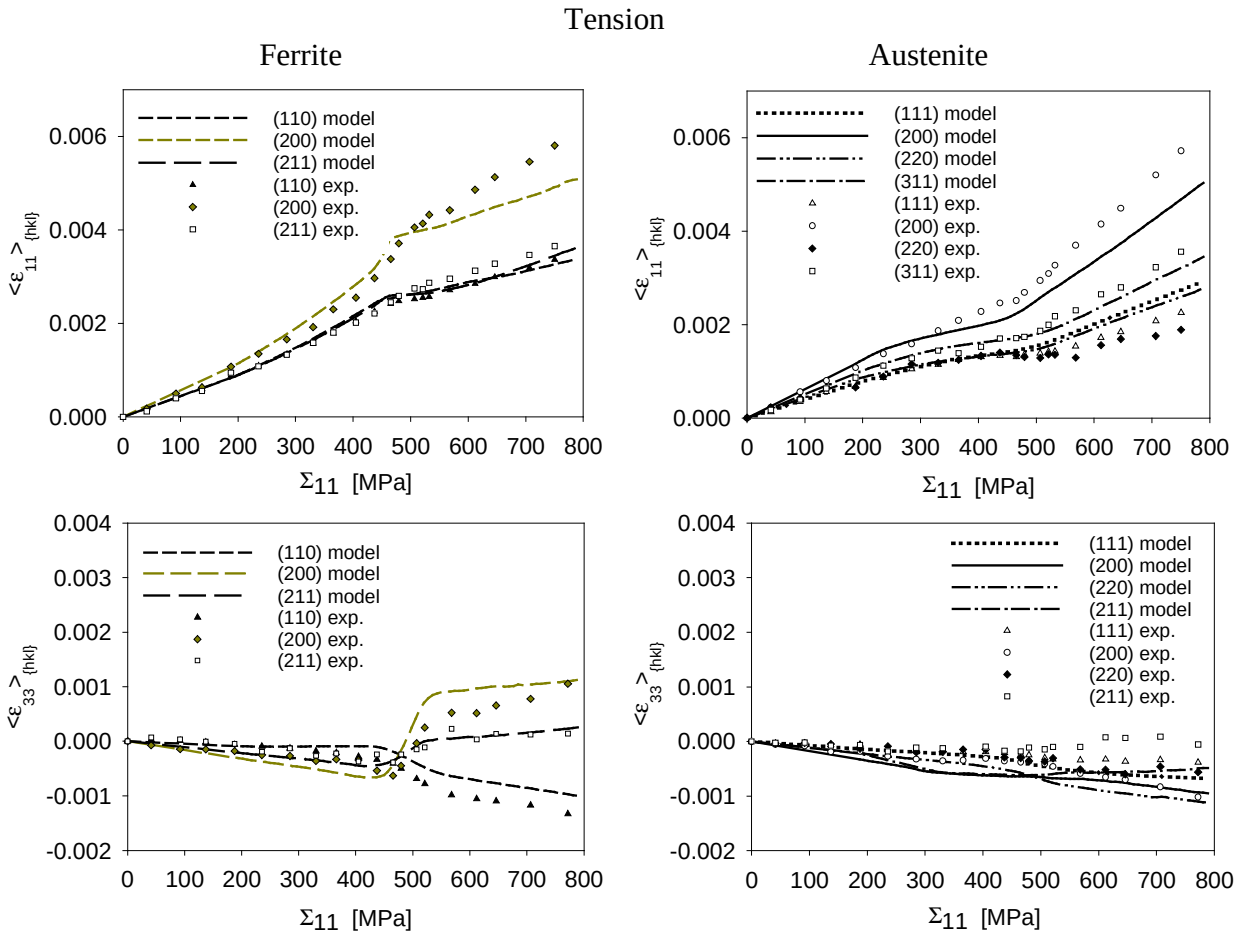

Fig. 3.22. *Elastic lattice strains* $<\varepsilon_{11}>_{\{hkl\}}$ *and* $<\varepsilon_{33}>_{\{hkl\}}$ *, versus to the applied stress* Σ_{11}*, measured by neutron diffraction (TOF). Strains measured "in situ" for several hkl reflections in both phases (points) are compared with SC model predictions (lines). Initial crystallographic texture measured by X-ray diffraction (Fig. 3.17) was used in the model calculations. The initial stresses (see Table 3.7) found in the sample were taken into account.*

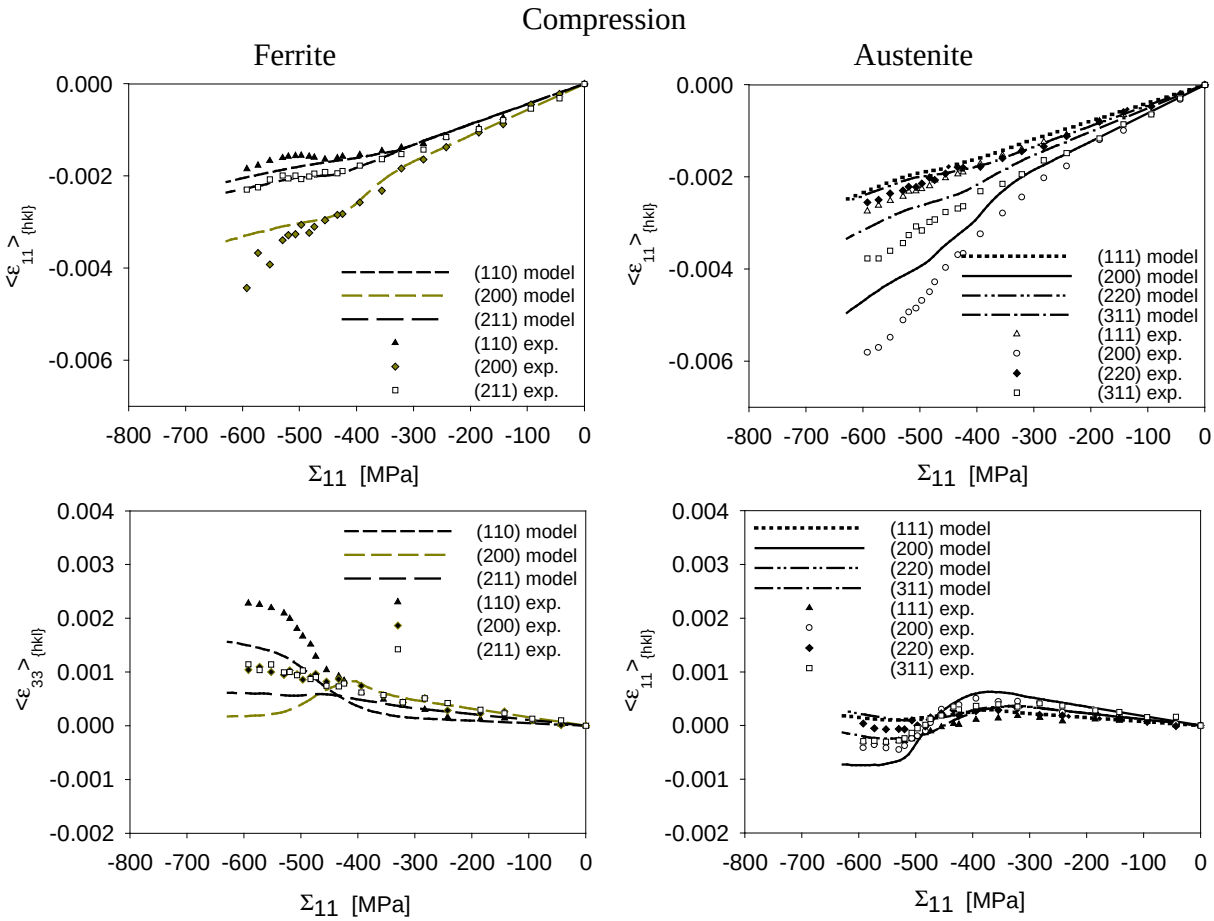

Fig. 3.23. *Similar comparison of experimental data with model results as presented in the preceding figure but for compression test.*

We focus on the estimation of the second order stresses and on investigation of internal stress anisotropy. In the case of the initial non-deformed sample a good fitting was obtained assuming q parameter equal to zero (in Eqs. 3.24a, 3.24b and 3.25). Thus the influence of the second order incompatibility stresses was not significant and the average stresses were determined (see Table 3.7 and Fig. 3.24). Contrary to the initial sample, the assumption of q=0 is not valid for the deformed samples and, as the consequence, the fitted curves are far from the experimental values (see dashed lines in Figs. 3.25 and 3.26 and χ^2 in Table 3.7). Thus the influence of the second order stresses has to be taken into account in the case of deformed samples. To do this, the theoretical stresses $\overline{\sigma_{ij}^{IIg(ic)}(\boldsymbol{g})}$ must be calculated by the elasto-plastic model. Using the theoretically calculated $\overline{\sigma_{ij}^{IIg(ic)}(\boldsymbol{g})}$ stresses, the least square fitting (based on Eqs. 3.24a 3.24b) was applied for the samples after tensile and compressive tests. In both cases an excellent fitting was obtained (χ^2 was about 3-4 times smaller than in the case when q=0 was assumed (see Table 3.6 and continuous lines in Figs. 3.25 and 3.26) and the values of average stresses as well as of the second order stresses were found. The fitting procedure was repeated using $\overline{\sigma_{ij}^{IIg(ic)}(\boldsymbol{g})}$ stresses predicted for different degrees of deformation and the values of q parameter were compared. In Table 3.7 the results obtained for q parameter close to 1 are presented (when q=1 the model second order stresses have the same magnitude as the experimental ones, see Eq. 3.29). It was found that theoretical stresses are almost equal to the experimental ones when the model calculations are performed to about twice lower deformation than that applied for a real sample. Using Eq. 3.29 and knowing the value of q parameter, the second order stresses $\sigma_{ij}^{IIg(ic)}(\boldsymbol{g})$ were determined for each grain orientation $\boldsymbol{g}$ (Fig. 3.27) (Wroński et al., 2006a 2006b). The average equivalent values $[\sigma_{eq}^{g(ic)}]$ (see Eq. 3.31) are given in Table 3.7 for each phase. Moreover, the total equivalent grain stress $\sigma_{eq}^{g}(\boldsymbol{g})$ (Eq. 3.15), calculated according to von Mises formula from σ_{ij}^{g}, was found for each orientation $\boldsymbol{g}$ and presented in Euler space in Fig 3.27.

Table 3.7. *Residual stresses determined using fitting procedure based on Eqs. 3.24 and 3.25. Relative values of χ^2 are shown, i.e.: $\chi^2/\chi^2_{initial}$ ($\chi^2_{initial}$ concerns the initial sample); the values obtained with assumption q = 0 are given in brackets.*

	macro-stresses [MPa]	mean phase incompatibility stresses [MPa]		mean equivalent second order stresses [MPa] $[\sigma_{eq}^{g(ic)}]$		q		χ^2/χ^2_{initil} (q=0)
		austenite	ferrite	austen.	ferrite	austen.	ferrite	
initial sample	$\sigma_{11}^M - \sigma_{33}^M =$ 18.6 ±5.9 $\sigma_{22}^M - \sigma_{33}^M =$ 34.8 ±5.0 $\sigma_{13}^M =$ -1.95 ±2.9 $\sigma_{23}^M =$ 2.7 ±3.9	$\sigma_{11}^{ph(ic)} - \sigma_{33}^{ph(ic)} =$ -19.8 ±4.5 $\sigma_{22}^{ph(ic)} - \sigma_{33}^{ph(ic)} =$ -67.7 ±4.5 $\sigma_{13}^{ph(ic)} =$ -0.3 ±2.2 $\sigma_{23}^{ph(ic)} =$ -4.7 ±3.3	$\sigma_{11}^{ph(ic)} - \sigma_{33}^{ph(ic)} =$ 19.8 ±7.2 $\sigma_{22}^{ph(ic)} - \sigma_{33}^{ph(ic)} =$ 67.7 ±5.4 $\sigma_{13}^{ph(ic)} =$ 0.3 ±3.6 $\sigma_{23}^{ph(ic)} =$ 4.7 ±4.5	not fitted	not fitted	not fitted	not fitted	(1)
tension to def. 15% (model calcul. to def. 7%)	$\sigma_{11}^M - \sigma_{33}^M =$ 47.7 ±13.8 $\sigma_{22}^M - \sigma_{33}^M =$ 21.1 ±10.1 $\sigma_{13}^M =$ 1.7 ±6.2 $\sigma_{23}^M =$ 2.3 ±8.6	$\sigma_{11}^{ph(ic)} - \sigma_{33}^{ph(ic)} =$ 14.2 ±8.2 $\sigma_{22}^{ph(ic)} - \sigma_{33}^{ph(ic)} =$ -89.6 ±7.2 $\sigma_{13}^{ph(ic)} =$ -0.4 ±4.5 $\sigma_{23}^{ph(ic)} =$ -0.5 ±5.4	$\sigma_{11}^{ph(ic)} - \sigma_{33}^{ph(ic)} =$ -14.2 ±19.6 $\sigma_{22}^{ph(ic)} - \sigma_{33}^{ph(ic)} =$ 89.6 ±13.0 $\sigma_{13}^{ph(ic)} =$ 0.4 ±7.8 $\sigma_{23}^{ph(ic)} =$ 0.5 ±11.7	128.3 ±1.3	250.5 ±1.3	0.85 ±0.01	1.1 ±0.01	1.14 (4.75)
compre-ssion to def. 5% (model calcul. to def. 2%)	$\sigma_{11}^M - \sigma_{33}^M =$ 15.5 ±12.1 $\sigma_{22}^M - \sigma_{33}^M =$ -8.8 ±9.2 $\sigma_{13}^M =$ 12.8 ±7.5 $\sigma_{23}^M =$ 0.8 ±7.2	$\sigma_{11}^{ph(ic)} - \sigma_{33}^{ph(ic)} =$ 17.0 ±6.9 $\sigma_{22}^{ph(ic)} - \sigma_{33}^{ph(ic)} =$ 55.9 ±6.8 $\sigma_{13}^{ph(ic)} =$ 1.4 ±4.6 $\sigma_{23}^{ph(ic)} =$ -2.5 ±4.6	$\sigma_{11}^{ph(ic)} - \sigma_{33}^{ph(ic)} =$ -17.0 ±17.2 $\sigma_{22}^{ph(ic)} - \sigma_{33}^{ph(ic)} =$ -55.9 ±11.5 $\sigma_{13}^{ph(ic)} =$ -1.4 ±8.4 $\sigma_{23}^{ph(ic)} =$ 2.6 ±9.8	118.5 ±1.0	154.5 ±1.0	1.0 ±0.01	0.85 ±0.01	1.51 (4.25)

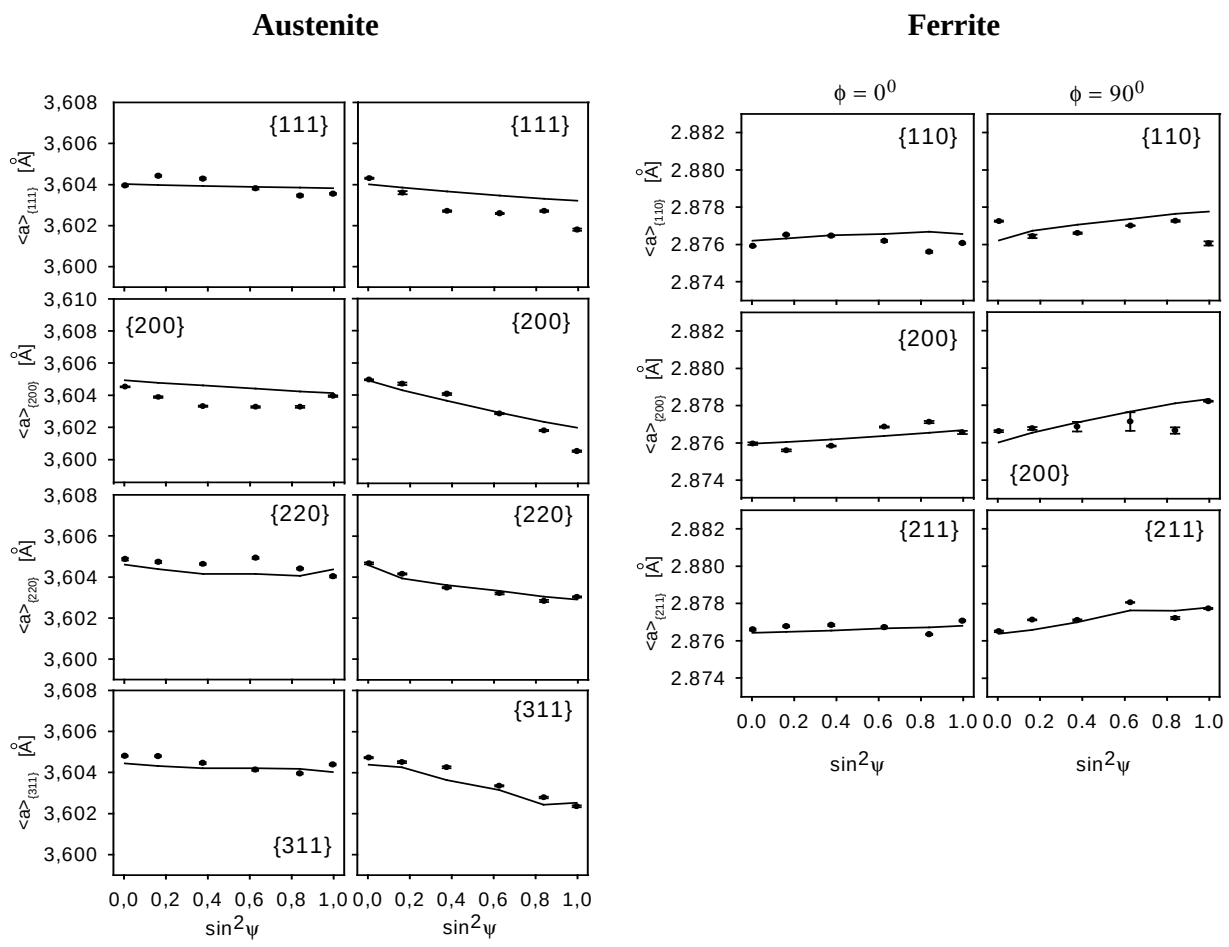

Fig. 3.24. *Measured lattice parameters (points) and theoretical results of fitting (continuous lines) for initial as-received sample (<a>$_{\{hkl\}}$ vs. sin$^2\psi$ curves for positive ψ are shown). The experimental data for various hkl reflections and both phases were simultaneously used in the fitting procedure assuming q = 0 (results are shown in Table 3.7).*

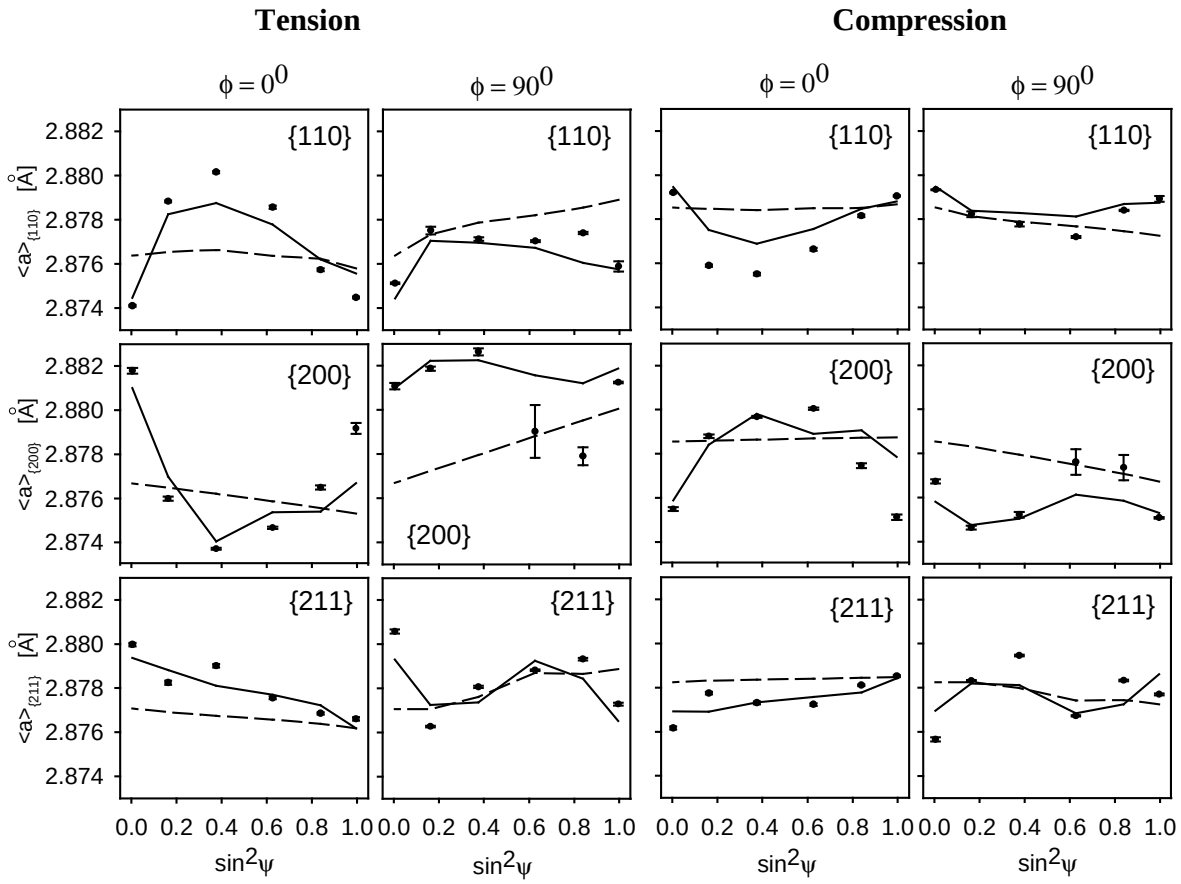

Fig. 3.25. *Measured lattice parameters and theoretical results of fitting for ferrite phase deformed in tensile and compression tests. The fitting procedure was applied for various hkl reflections and both phases for each sample, assuming: $q \neq 0$ (continuous lines) and $q = 0$ (dashed lines).*

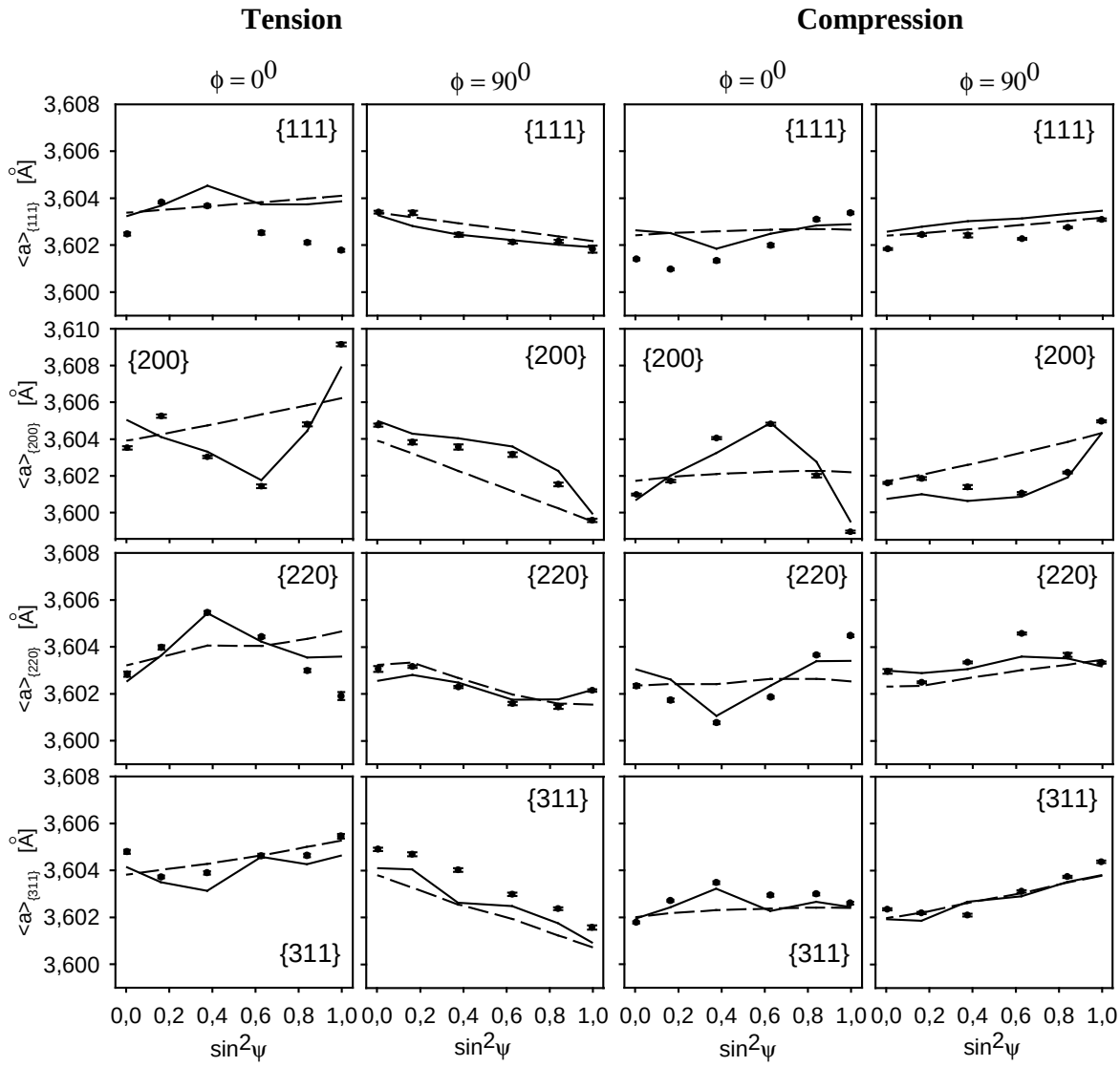

Fig. 3.26. *Measured lattice parameters and theoretical results of fitting for austenite phase deformed in tensile and compression tests. The fitting procedure was applied for various hkl reflections and both phases for each sample, assuming: $q \neq 0$ (continuous lines) and $q = 0$ (dashed lines).*

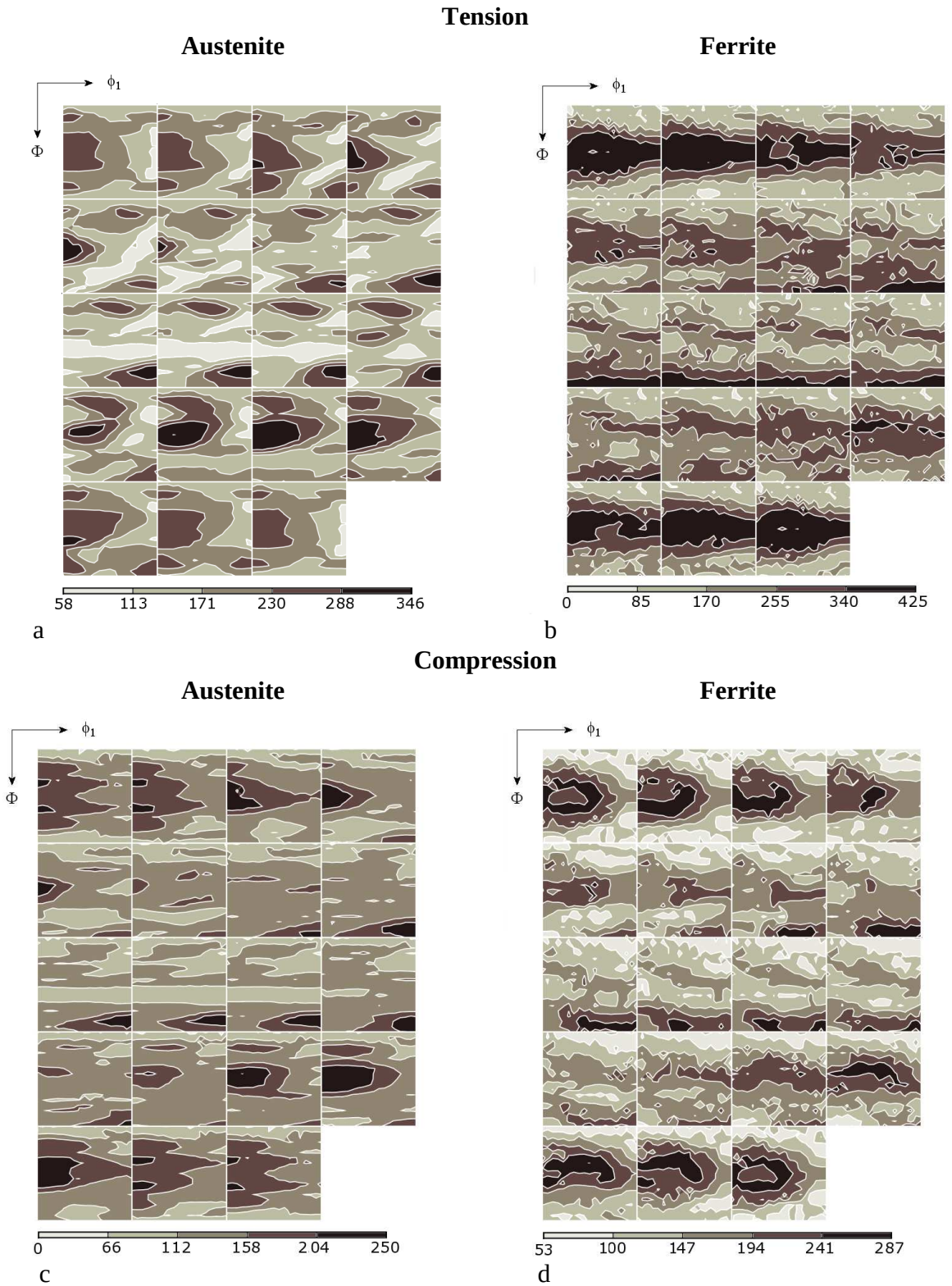

Fig. 3.27. *Total equivalent stress* $\sigma_{eq}^{g}(\boldsymbol{g})$ *for grains having various orientations* $\boldsymbol{g}$*, determined after tensile (a,b) and compressive (c,d) tests. The* ϕ_2 *sections are presented for both phases.*

Finally, the influence of elastic anisotropy and crystallographic texture on the creation of the second order incompatibility stresses was studied. (Wroński et al., 2006a) In this aim, the analysis of experimental data was performed with two different artificial assumptions. Firstly, isotropic single crystal elastic constants were used in modeling and in the calculation of the diffraction elastic constants. Secondly, the modeling was performed assuming random initial texture. In both cases the results of fitting procedure were definitively worse in comparison with those when anisotropic single crystal elastic constants and textured initial samples were considered in data analysis (see Figs. 3.28 – 3.31) (Wroński 2006b et al.). It should be noticed that agreement between experimental and calculated data is worse for austenite than ferrite were isotopic elastic constants were taken into account. This effect was observed as well for single as for multiphase materials.

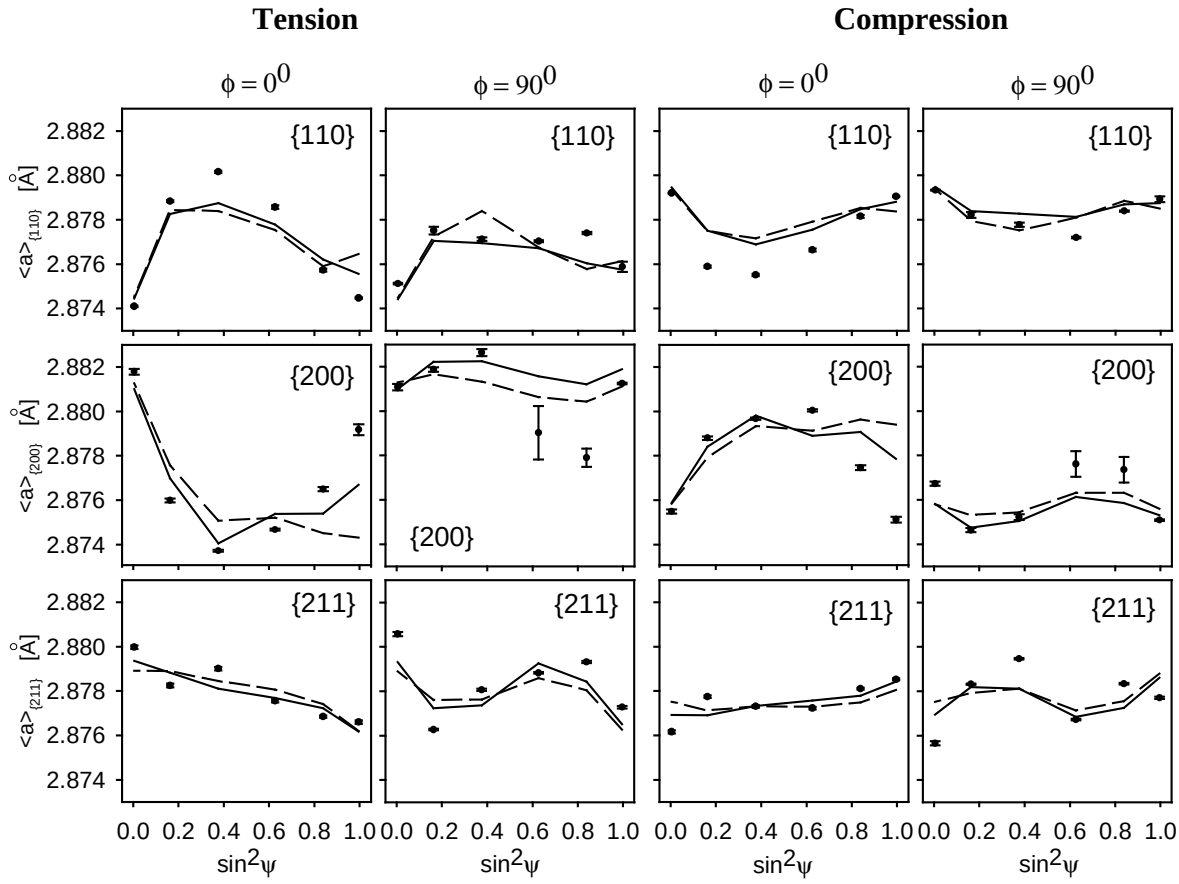

Fig. 3.28. *Measured and fitted $< a >_{\{hkl\}}$ vs. $\sin^2\psi$ curves for ferrite phase after tensile test ($q \neq 0$). The analysis was performed assuming: anisotropic (continuous lines) and isotropic single crystal elastic constants (dashed lines).*

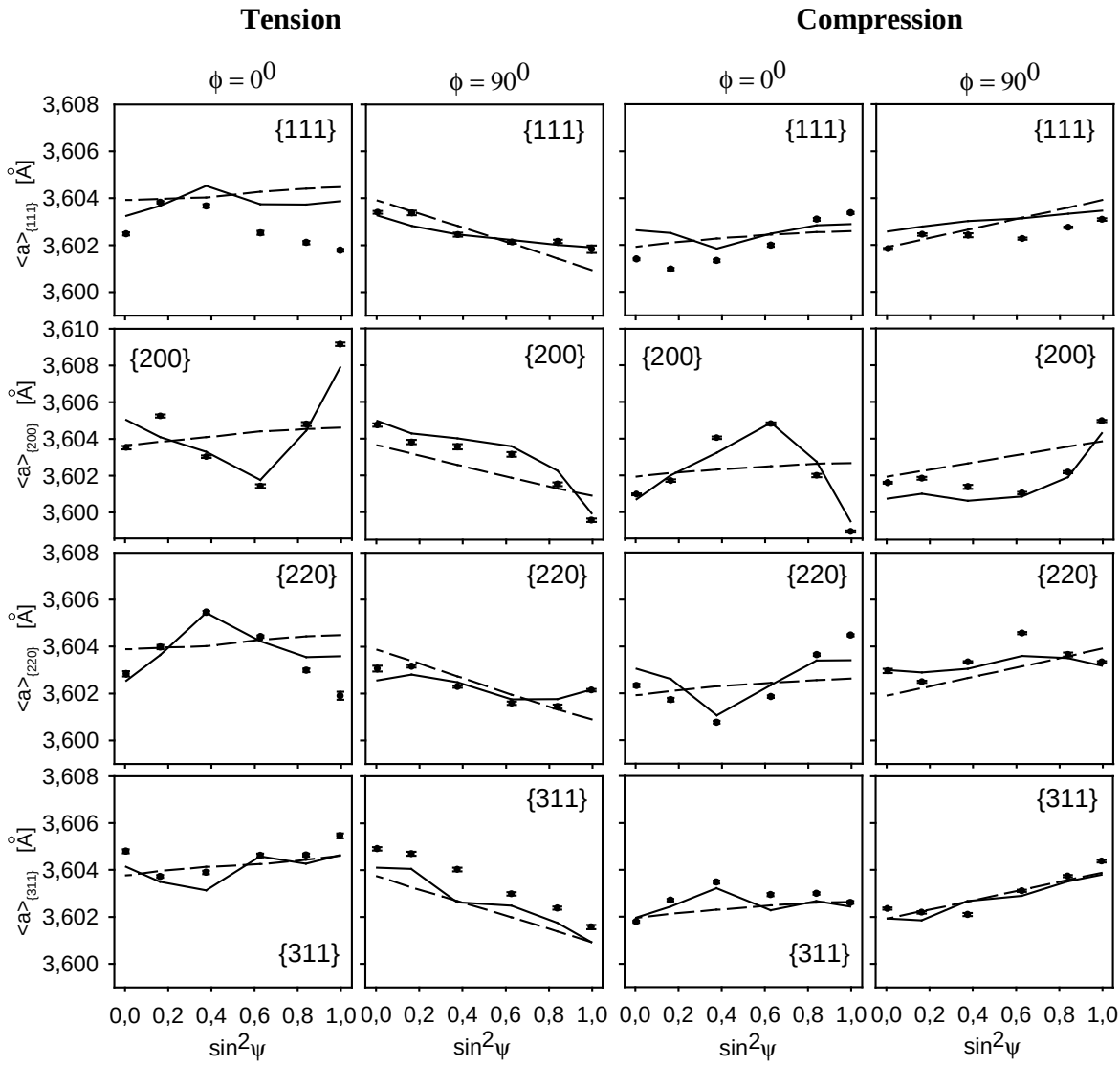

Fig. 3.29. *Measured and fitted* $< a >_{\{hkl\}}$ *vs.* $\sin^2\psi$ *curves for austenite phase after tensile test* ($q \neq 0$). *The analysis was performed assuming: anisotropic (continuous lines) and isotropic single crystal elastic constants (dashed lines).*

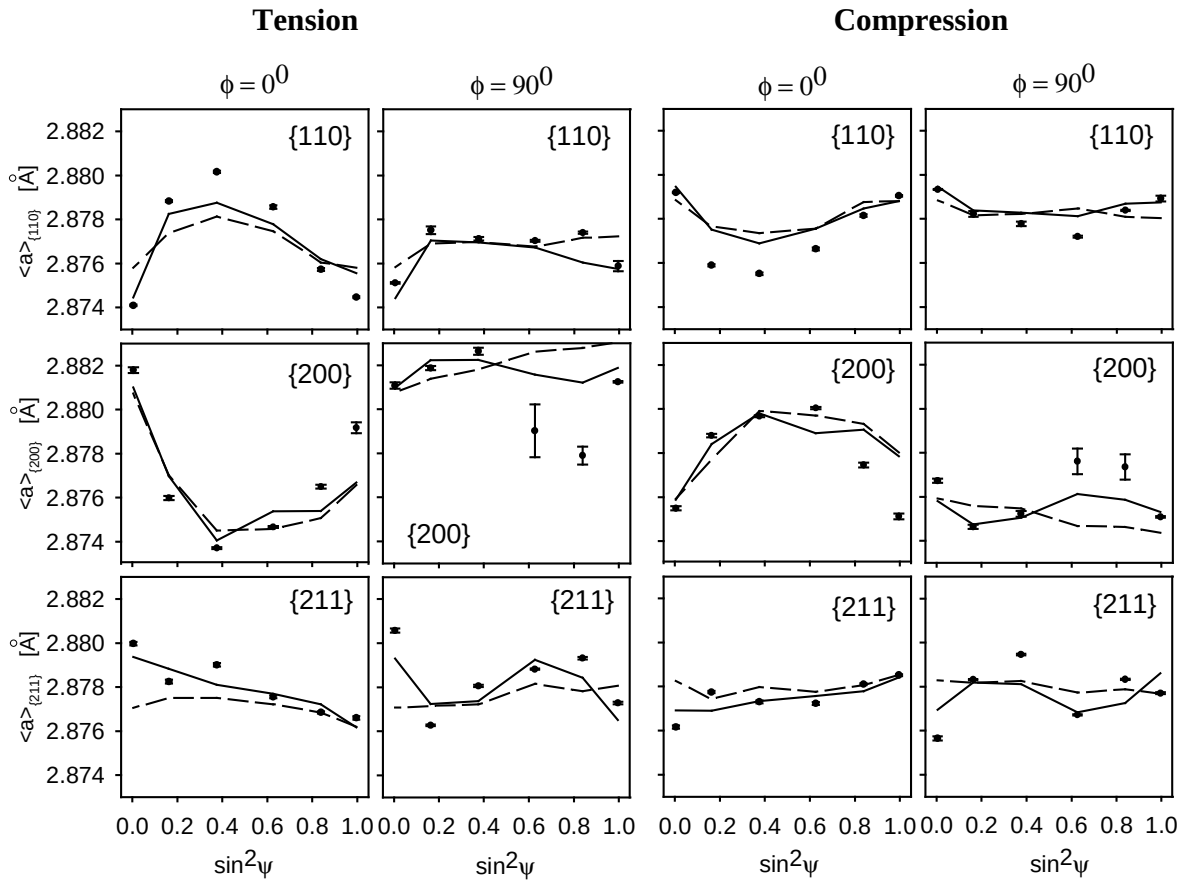

Fig. 3.30. *Measured and fitted* $< a >_{\{hkl\}}$ *vs.* $sin^2\psi$ *curves for ferrite phase after tensile test* ($q \neq 0$). *The analysis was performed assuming: textured sample (continuous lines) and randomly oriented grains in the initial sample (dashed lines).*

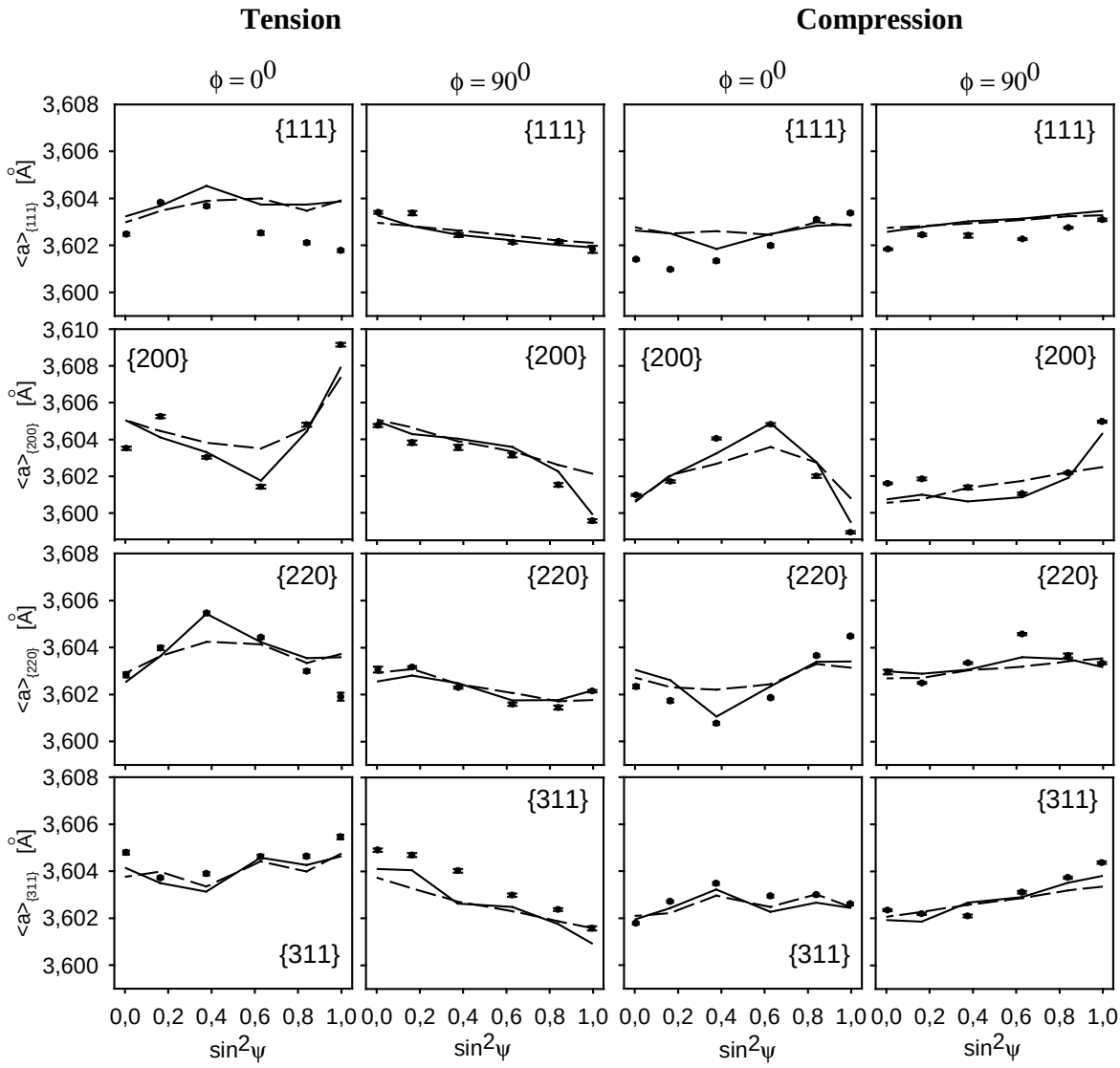

Fig. 3.31. *Measured and fitted* $< a >_{\{hkl\}}$ *vs.* $\sin^2\psi$ *curves for austenite phase after tensile test* ($q \neq 0$). *The analysis was performed assuming: textured sample (continuous lines) and randomly oriented grains in the initial sample (dashed lines).*

3.9. Conclusions

The residual stresses are generated by plastic deformation. They remain in a material even when external forces are unloaded. In this work we focus on the first order stresses (macroscopic stresses) and the second order stresses (stresses in grains). As it is described in the previous chapter, macroscopic stresses are determined from the slope of the $\sin^2\psi$ graph. When the second order stresses are present in the sample, the relation $<d>_{\{hkl\}}$ vs. $\sin^2\psi$ is non-linear. The second order stresses are a result of plastic incompatibility and thermal anisotropy, but in this work only

this first is taken into account. These stresses arise due to anisotropic plastic flow of grains. Different behaviour of grains is caused by various orientations of slip systems with respect to the local stress tensor. Thus the activation of slip systems depends strongly on the localization of the applied stress at a considered grain, intergranular stresses and grain lattice orientation. Finally, after plastic deformation some of the grains are more (or less) elongated in a given direction than the other and consequently they do not fit into the surrounding matrix. Due to such misfit, the second order stress and a corresponding lattice strain arise.

In the first part of this chapter the single phase materials (ferrite and austenite) were investigated. In both cases the first and the second order stresses were estimated. The second order stresses can be predicted by elasto-plastic models, and consequently the self–consistent and Lefers-Wierzbanowski model were applied. The calculations were done using anisotropic and isotropic elastic constants. A good agreement between experimental and theoretical data was observed when anisotropic elastic constants were taken into account.

The next investigated material was the duplex stainless steel (composed of ferrite and austenite phase). Similarly like in single phase materials, the first and the second order stresses were estimated. The stresses were determined for duplex steel after tensile and compressive tests using TOF neutron diffraction. It was found that in the as received non-deformed sample the second order stresses were small and consequently the $sin^2\psi$ plots were almost linear. After elasto-plastic deformation the second order incompatibility stresses were generated causing strong nonlinearities of the $sin^2\psi$ plots. The nonlinearities have opposite character after tension and compression (Figs. 3.25 and 3.26), i.e., the second order stresses of opposite sign are created during those modes of deformations. Also, the opposite average incompatibility stresses ($\sigma_{11}^{ph(ic)}$ - $\sigma_{33}^{ph(ic)}$, $\sigma_{22}^{ph(ic)}$ - $\sigma_{33}^{ph(ic)}$) were found after these tests. As expected, small values of macrostresses (σ_{11}^{M} - σ_{33}^{M}, σ_{22}^{M} - σ_{33}^{M}) were determined in the volumes studied by neutrons, while relatively high values of $[\sigma_{eq}^{g(ic)}]$ indicate that the second order incompatibility stresses are very significant in deformed duplex steel (see Table 3.7).

Similarly like in single phase materials, the influence of elastic anisotropy and texture on the second order incompatibility stress was studied in duplex steel. As seen in Figs. 3.28 and 3.29, the $sin^2\psi$ plots fit significantly worse when the isotropic elastic constants are used in data analysis. This effect is especially pronounced in the case of austenitic phase. In single phase materials this effect was also observed. Thus the anisotropy of elastic constants plays an important role in the creation of the second order incompatibility stresses. On the other hand, the initial texture is also important for proper determination of the second order stresses in ferritic phase (some of the $sin^2\psi$ plots fit worse when random texture is assumed in model prediction, Figs. 3.30 and 3.31). It can be concluded that creation of the second order stresses is a complex process and it depends on different parameters characterizing elasto-plastic deformation of polycrystalline material. The evolution of grain stresses can be qualitatively and even quantitatively predicted by the elasto-plastic models when elastic anisotropy, texture evolution and interaction between grains are taken into account. However, the magnitude of the theoretical stresses is often overestimated in comparison with experimental one. The correct theoretical magnitudes are obtained when the model $\overline{\sigma_{ij}^{IIg(ic)}(\boldsymbol{g})}$ stresses are calculated for smaller deformation than the real one.

Chapter 4

Variation of residual stresses during cross-rolling

4.1. Introduction

The cross-rolling is generally applied in order to symmetrize the crystallographic texture and consequently, to decrease the sample anisotropy. Such the operation involves also the modification of residual stresses.

The goal of the study was to follow the character of residual stresses in function of applied deformation in each of two rolling directions. The studied material was polycrystalline copper (fcc structure) and ferritic steel (bcc structure). The observed experimental results were studied using the model of elasto-plastic deformation. The variation of the first order stresses and non-linearity of the ε versus $\sin^2\psi$ plot were studied and explained. The diffraction elastic constants and the second order stress distributions were also determined using the self-consistent model.

4.2. Residual stresses and texture in cross-rolled polycrystalline metals

4.2.1 Copper

A plate of polycrystalline copper was rolled to the reduction Red1=62 % and next four samples were cut out, which were cross-rolled to the reduction Red2 of 10 %, 40 %, 62 % and 80 %, respectively (Red1 is rolling reduction in principal direction and Red2 is rolling reduction in perpendicular cross direction). The surface layer of 200 μm was removed by electropolishing

in each sample. Classical X-ray diffraction (Cu radiation) was used (Baczmański et al., 1994a; Baczmański et al., 1995) (see chapter 1). The texture and internal stress (ε_{33} vs. $sin^2\psi$ method) were measured on Brücker Advance D8 diffractometer at the Open University,Walton Hall, Milton Keynes, England. In the present study a general *multi-reflection method* (Baczmański et al., 2003c) of stress determination was applied (see chapter 1). The average equivalent inter-planar lattice distances, $< a(\psi,\phi) >_{\{hkl\}}$ were determined for 331 and 420 reflections. Before performing accurate measurements, the calibration of the apparatus was done by measuring the stress in powder sample. The measurement shows that the stress in the sample is on –10.5 MPa level, what proves a proper calibration of the apparatus.

The crystallographic textures (orientation distribution functions – ODFs and pole figures) of the considered samples were determined experimentally and also predicted by the LW model (Fig.4.1) (Wierzbanowski et al.,1979; Wierzbanowski et al.,1992). The cross-rolling texture (Fig. 4.1b) is strongly symmetrized compared with the simple rolling one (Fig. 4.1a). Two new symmetry axes of pole figures, inclined $\pm 45^0$ with respect to x axis, appear. The model predicted cross-rolling texture (Fig. 4.1c) is in perfect agreement with the experimental one. These results confirm the correct construction of the model.

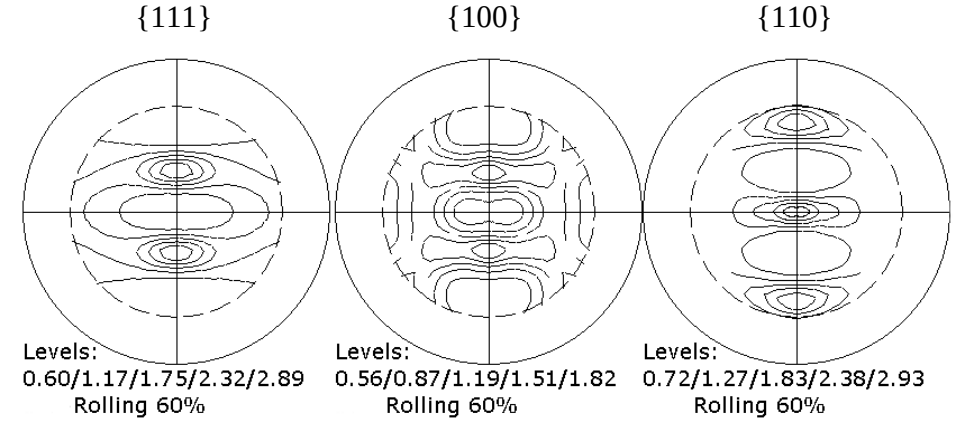

a

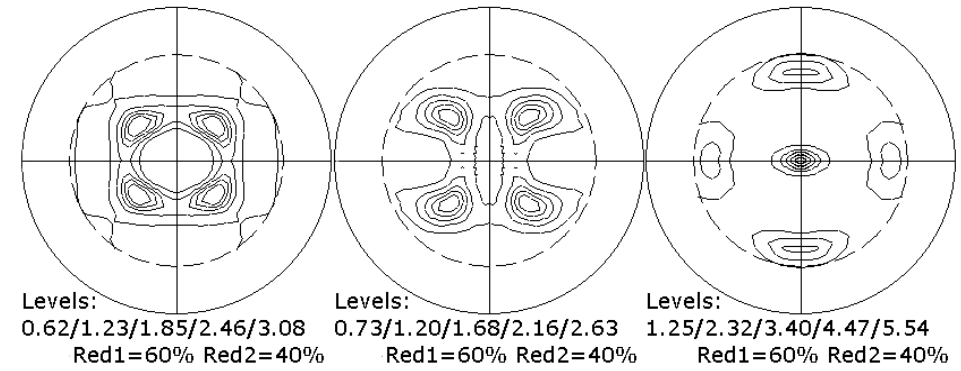

b

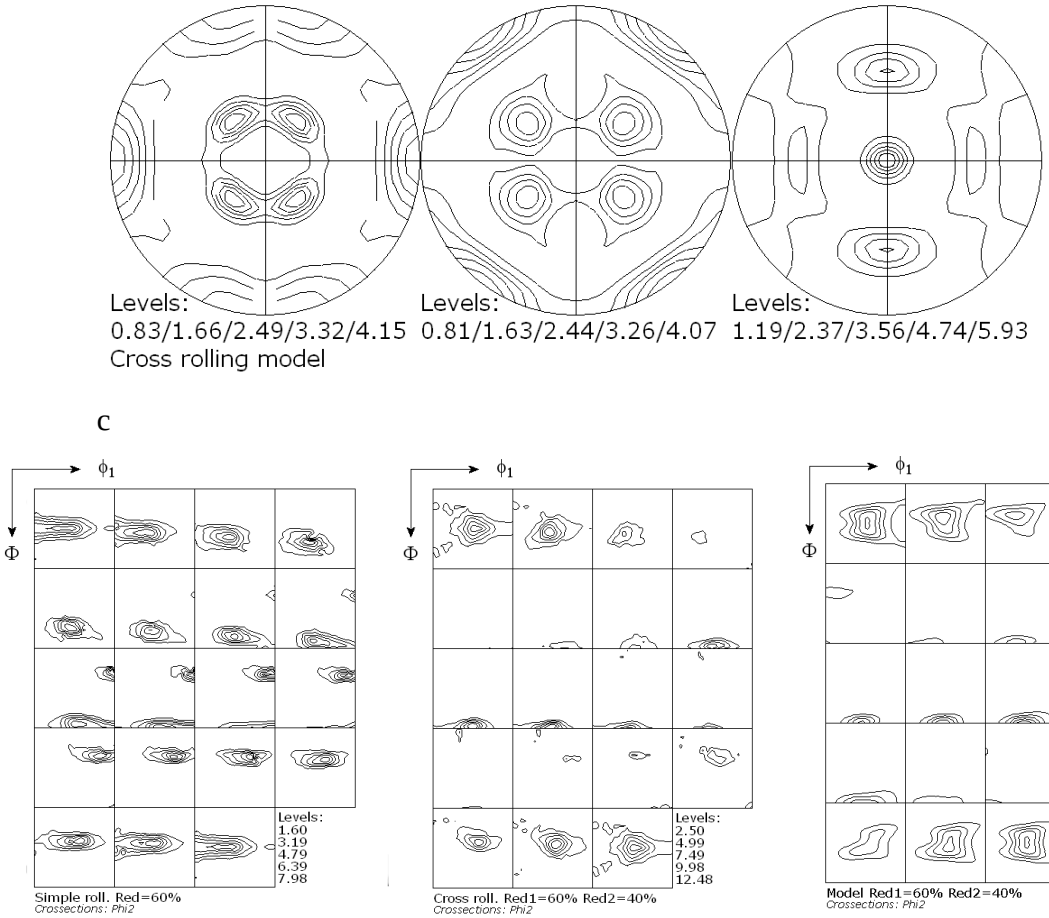

Fig. 4.1. *ODF and (111), (100), (110) pole figures for polycrystalline copper: a) after simple rolling (Red1=60%), b) cross- rolling (Red1=60% and Red2=40 %), c) as above but predicted by the elasto-plastic deformation model.*

To determine residual stresses, the calculation of diffraction elastic constants has to be done. The values were calculated using Reuss, self-consistent (free surface), self-consistent (interior) and Voigt model (see chapter 1). The results for all models are listed in Table 4.1.

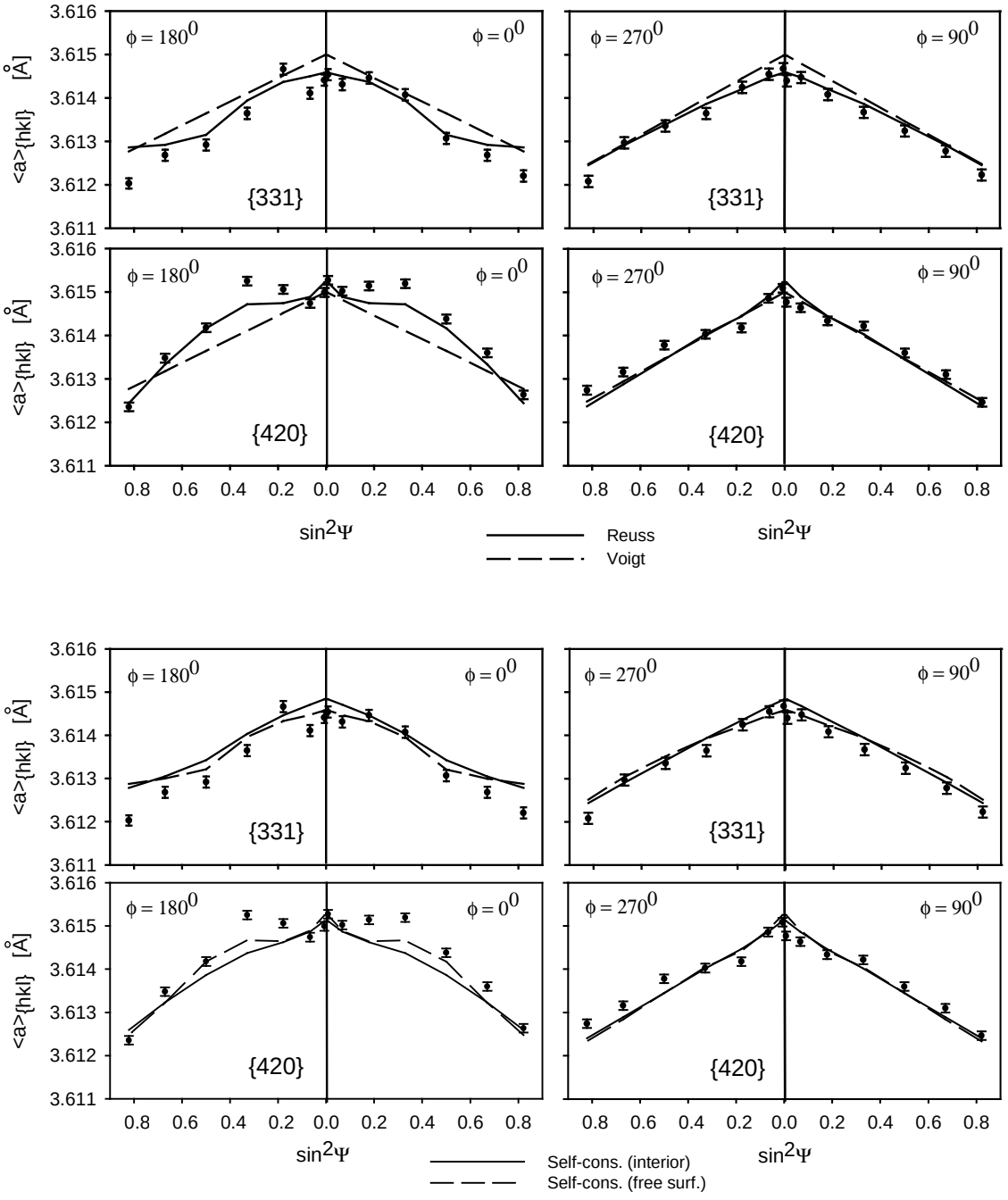

Fig. 4.2. *Plots of $\langle a(\psi,\phi)\rangle_{\{21l\}}$ vs. $\sin^2\psi$ for polycrystalline copper rolled to 62 %. Results for Reuss, self-consistent (interior), self-consistent (free surface) and Voigt model.*

Table 4.1. *Components of macroscopic residual stress σ_{11}^{M} and σ_{22}^{M} (in MPa) for Reuss, self-consistent (free surface), self-consistent (interior) and Voigt model. χ^2 parameter is also listed.*

Sample	Type of diffraction elastic constants	Macrostresses [MPa]		Stress free interpl. spacing d^o [Å]	χ^2
		σ_{11}^{M}	σ_{22}^{M}		
Red1=62%	Reuss	-57.4 ±2.9	-68.4 ±3.2	3.61339 ±0.00002	5.97
	self-cons. (free surf.)	-62.1 ±3.8	-72.5 ±3.8	3.61342 ±0.00002	7.43
	self-cons. (interior)	-68 ±4.7	-79.4 ±4.7	3.61346 ±0.00002	9.93
	Voigt	-73.2 ±6.7	-84.8 ±6.7	3.61353 ±0.00002	15.31
Red1=62% Red2=10%	Reuss	-42.4 ±3.5	-67.4 ±3.2	3.6134 ±0.00002	7.15
	self-cons. (free surf.)	-44.4 ±3.9	-73.6 ±3.9	3.61342 ±0.00002	7.75
	self-cons. (interior)	-50.6 ±4.1	-79.9 ±4.1	3.61344 ±0.00002	7.42
	Voigt	-55.6 ±5.4	-86.4 ±5.1	3.613489 ±0.00002	9.95
Red1=62% Red2=40%	Reuss	22.8 ±2.5	-23.9 ±2.5	3.61334 ±0.00002	4.09
	self-cons. (free surf.)	27.2 ±2.9	-26.1 ±3.1	3.61335 ± 0.00002	4.2
	self-cons. (interior)	28.2 ±3.1	-28.1 ±3.1	3.61334 ± 0.00002	4.23
	Voigt	31.9 ±3.8	-29.3 ±3.9	3.61334 ±0.000016	5.04
Red1=62% Red2=62%	Reuss	-2.2 ±2.3	-27.2 ±2.3	3.61337 ±0.00002	3.56
	self-cons. (free surf.)	-1.7 ±2.8	-28.9 ±2.7	3.61337 ±0.00002	4.1
	self-cons. (interior)	-3.2 ±3	-31.6 ±3	3.61338 ±0.00002	4.1
	Voigt	-3.8 ±3.7	-34.1 ±3.5	3.6134 ±0.00002	4.75
Red1=62% Red2=80%	Reuss	-14.8 ±7	-41.9 ±7	3.61344 ±0.00003	5.85
	self-cons. (free surf.)	-14.5 ±3.5	-45 ±3.3	3.61346 ±0.00002	6.35
	self-cons. (interior)	-17.6 ±3.8	-49.5 ±3.8	3.61347 ±0.00002	6.24
	Voigt	-19.5 ±4.5	-54 ±4.3	3.6135 ±0.00002	7.16

The values of stress obtained from all models are very similar, however Reuss model leads to a better agreement of experimental data with theoretical one. Factor χ^2 (*characterising quality of fitting*) for Reuss model is smaller then for other models. That is why elastic constants were determined using Reuss model (in Reuss's model the local stress is assumed to be uniform across the sample for all polycrystalline grains, so: $\sigma_{ij}^{g} = \sigma_{ij}^{M}$). The exemplary plots of $\langle a(\psi,\phi)\rangle_{\{hkl\}}$ vs. $\sin^2\psi$ are shown in Figs. 4.2 and 4.3. It is visible that some oscillations appear, which are caused by elastic (texture) or plastic (second order incompatibility stresses) anisotropies. To explain the oscillations appearing on graphs $\langle a(\psi,\phi)\rangle_{\{420\}}$ vs $\sin^2\psi$ the anisotropic elastic properties of crystalites have to be considered. The second order incompatibility stresses in copper (appearing due to anisotropic nature of plastic deformation) are not significant. They do not influence the final results (Wierzbanowski, Wroński et al. 2006d; Wierzbanowski, Wroński et al. 2007a).

The estimated values of the main components of the first order residual stresses (σ_{11}^{M} and σ_{22}^{M}) and their variation with the applied deformation in the cross-rolling (perpendicular) direction are shew in Fig. 4.4a. We see that both components are negative after simple rolling. Then, with increasing value of the deformation in cross-rolling direction, σ^{I}_{11} becomes positive for (Red2=40% and 62%) and next (Red2=80%) it becomes again negative; at Red2=40% this component has a maximum value. The second component σ_{22}^{M} follows roughly the similar behavior, but it stays all the time negative; it reaches the smallest *absolute* value for Red2=40%. On the other hand, the precision of our measurement is confirmed by a constant value of a_0 in the stress free state, estimated by our procedure – Fig. 4.4b.

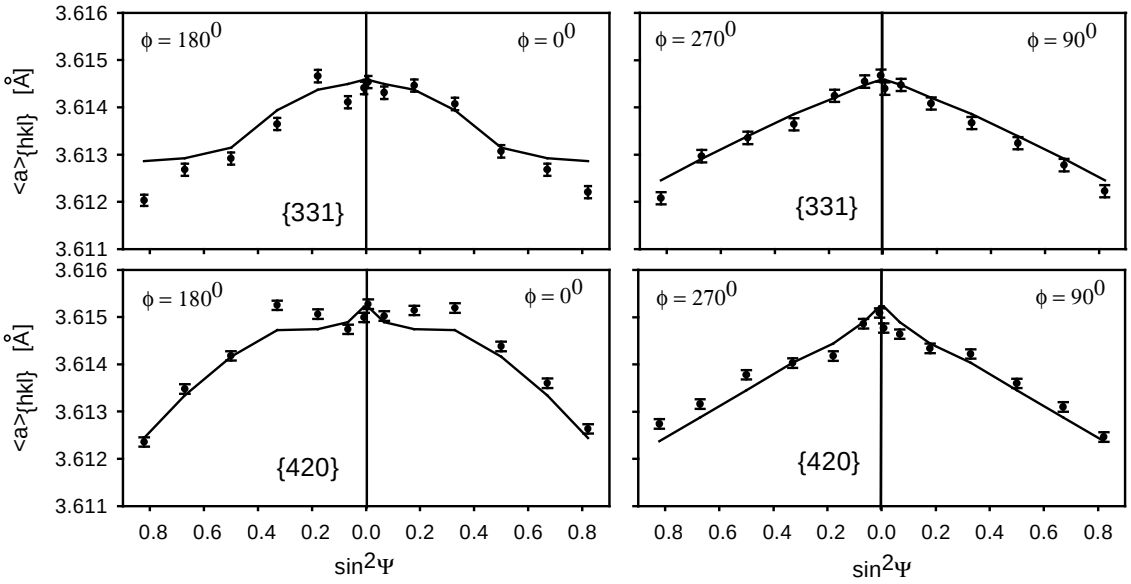

a.

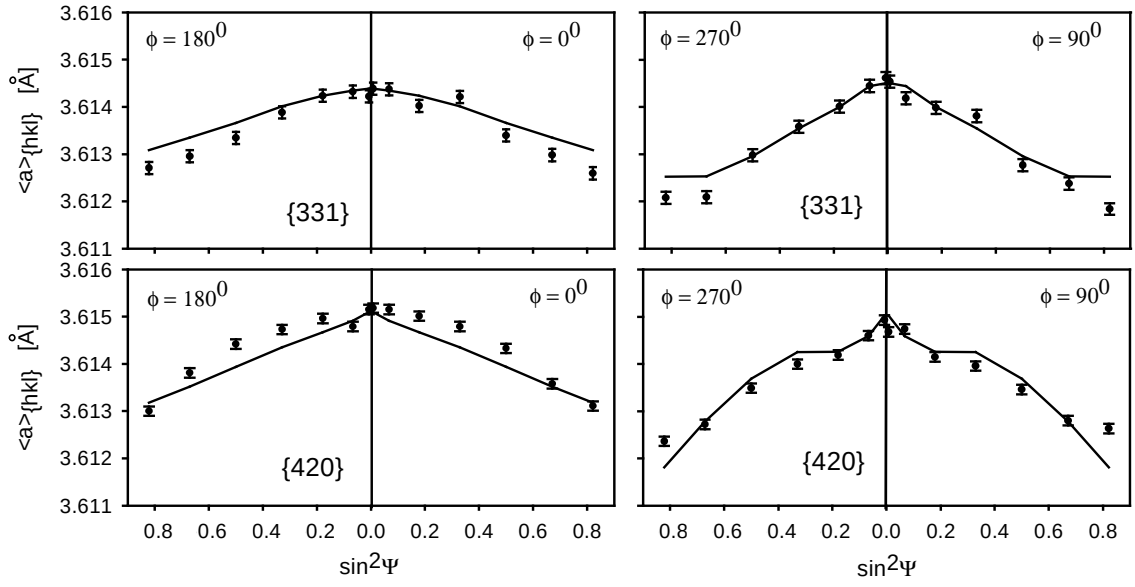
3.616
3.615
3.614
3.613
3.612
3.611
<a>{hkl} [Å]
ϕ = 180⁰
ϕ = 0⁰
ϕ = 270⁰
ϕ = 90⁰
{331}
{420}
0.8 0.6 0.4 0.2 0.0 0.2 0.4 0.6 0.8
sin²Ψ

b.

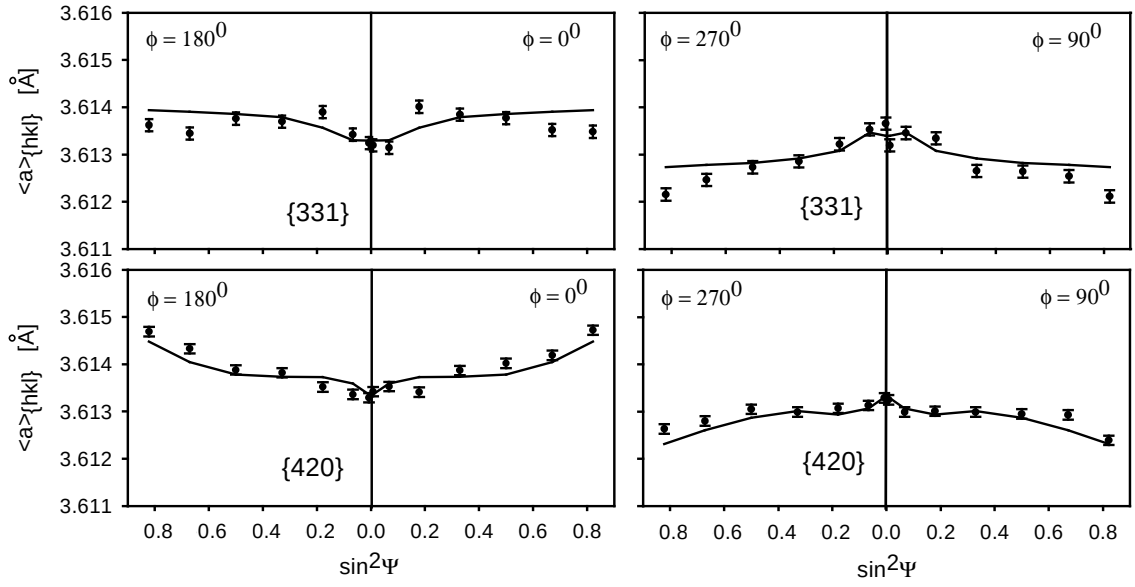
3.616
3.615
3.614
3.613
3.612
3.611
<a>{hkl} [Å]
ϕ = 180⁰
ϕ = 0⁰
ϕ = 270⁰
ϕ = 90⁰
{331}
{420}
0.8 0.6 0.4 0.2 0.0 0.2 0.4 0.6 0.8
sin²Ψ

c.

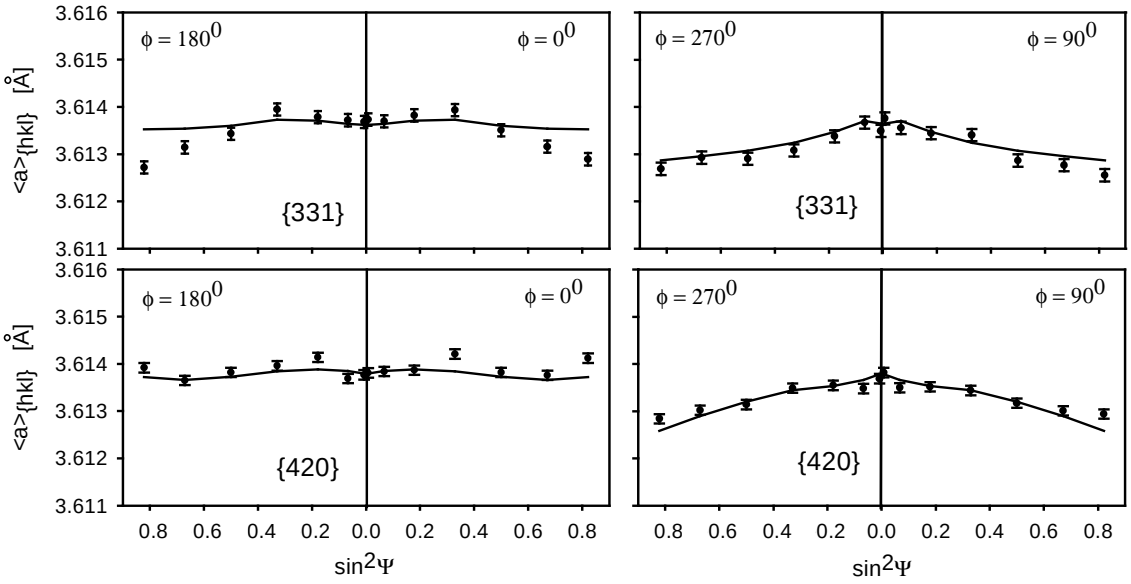

d.

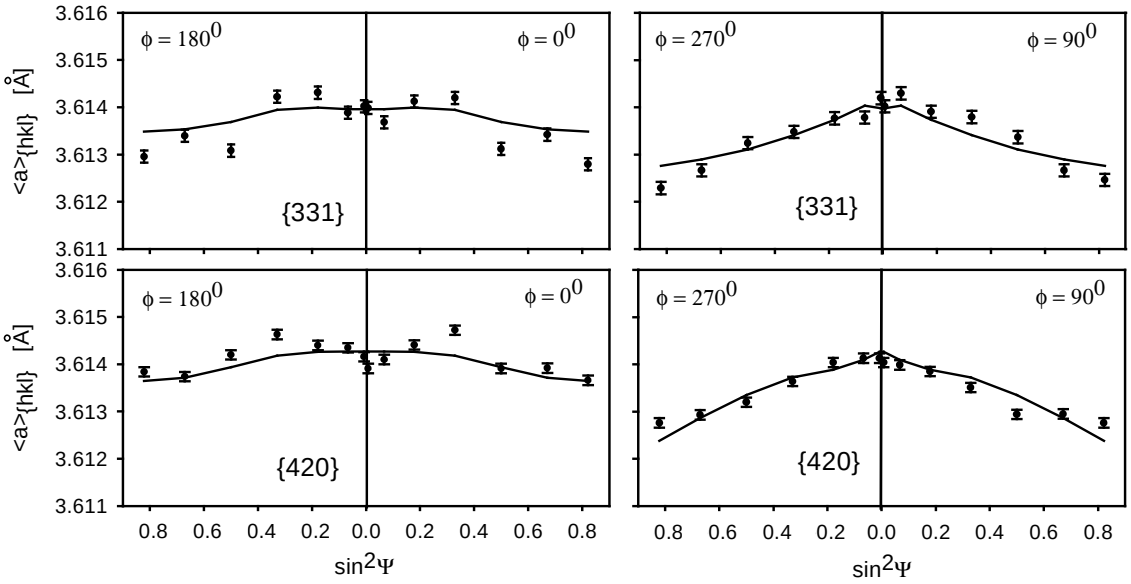

e.

Fig 4.3. *Plots of $<a(\psi,\phi)>_{\{hkl\}}$ vs. $\sin^2\psi$ for polycrystalline copper rolled to*
a) 62% reduction in main direction
b) 62 % reduction in main direction and 10 % in cross direction
c) 62 % reduction in main direction and 40 % in cross direction
d) 62 % reduction in main direction and 62 % in cross direction
e) 62 % reduction in main direction and 80 % in cross direction
(all reflections were fitted simultaneously – multireflection method)

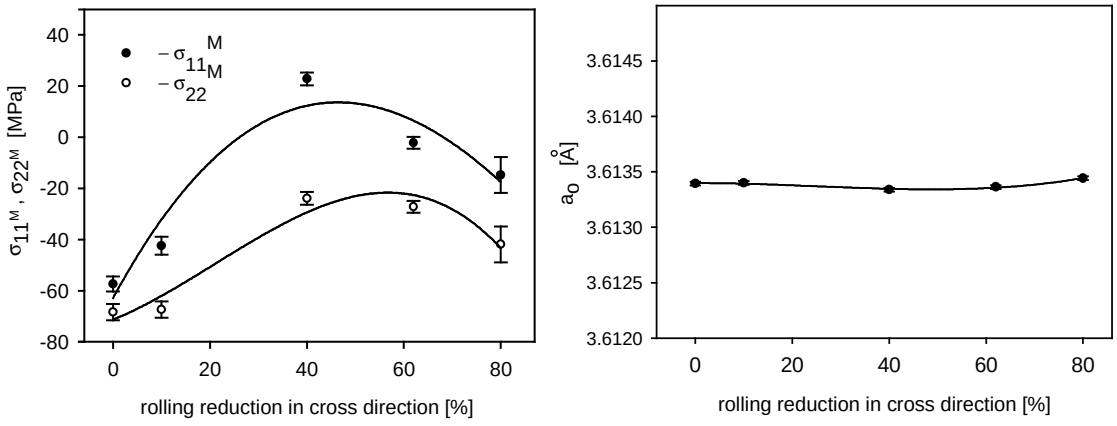

a b

Fig. 4.4. *a). σ_{11}^{M} and σ_{22}^{M} versus deformation in cross-rolling direction (Red2), b). a_0 versus deformation in cross-rolling direction (Red2) for cold rolled polycrystalline copper*

4.2.2. Low carbon steel

Similar experimental procedure as above was used for low carbon steel. The starting sample was rolled to Red1=74%. Next, four samples were cut out and subjected to additional cross-rolling (Red2 of 36%, 49%, 73% and 79%, respectively).
Classical X-ray diffraction (Cr radiation) was used for this measurement. The texture and residual stress (ε_{33} vs. $sin^2\psi$ method) were measured on SET-X diffractometer at the ENSAM Paris, France. The average equivalent inter-planar lattice distances, $< a(\psi,\phi) >_{\{hkl\}}$ were determined for 211 reflection. The exemplary plots of $<a(\psi,\phi)>_{\{211\}}$ vs. $\sin^2\psi$ are shown in Fig. 4.5. We observe strong oscillations in this plot, caused by elastic and plastic anisotropies. To explain such strong oscillations we should take into account a strong anisotropy of the second order stresses. A very good fit is obtained with experimental data, using our approach given by

$$< a(\psi,\phi) >_{\{hkl\}} = [F_{ij}^{M}(\{hkl\},\psi,\phi)\sigma_{ij}^{M} + < a_{3m}a_{3n}s_{mnij}\,\sigma_{ij}^{IIg(ic)} >_{\{hkl\}}]\, a_{\{hkl\}}^{o} + a_{\{hkl\}}^{o} \qquad (4.1)$$

where F_{ij}^{M} are diffraction elastic constants, σ_{ij}^{M} is the first order (macroscopic) stress, tensor, $\sigma_{ij}^{IIg(ic)}$ is the second order incompatibility stress tensor, s_{mnij} are single crystal elastic constants and a_{ij} are direction cosines transforming stress tensor from *X* to *L* coordinate system, $d_{\{hkl\}}^{o}$ are stress free interplanar spacings and <…> denotes averaging over diffracting crystallites.
Assuming that the distribution of the second order incompatibility stresses on crystal orientation (g) is correctly predicted by a deformation model (e.g. the self-consistent elasto-plastic one), one can put:

$$\sigma_{ij}^{IIg(ic)}(g) = q\ \overline{\sigma_{ij}^{IIg(ic)}(g)} \qquad (4.2)$$

where $\overline{\sigma_{ij}^{IIg(ic)}(g)}$ is the model predicted second order stress distribution and *q* is a constant phenomenological factor, of the order of one (it corrects the amplitude of the second order residual stresses, which is not always exactly predicted by the model). Non-linear diffraction elastic constants $F_{ij}(\{hkl\},\psi,\phi)$ were calculated using the self-consistent model, taking into account texture and single crystal elastic constants. The effect of elastic anisotropy is not sufficient to explain the obtained results. For this reason the second order stresses have to be considered to explain the oscillations appearing on graph of $\langle a(\psi,\phi)\rangle_{\{211\}}$ vs. $\sin^2\psi$. It is visible that χ^2 (Table 4.2) is higher in the case when the second order stresses are neglected.

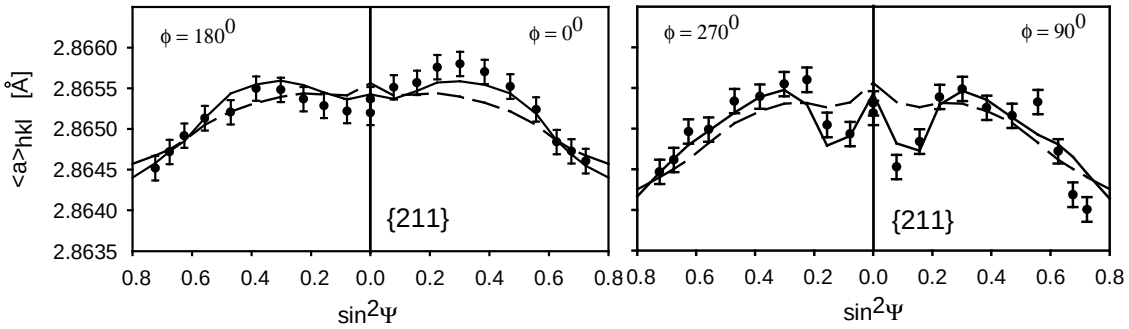

***Fig. 4.5**. Cross-rolled steel sample for the Reuss model. (Red1=74% Red2=73%). Measured lattice parameters (points) and theoretical results of fitting (continuous lines for $q \neq 0$ and dashed lines for $q = 0$)*

Table. 4.2. *Results of fitting procedure for samples after cross-rolling. Calculations were performed taking into account plastic incompatibility stresses. The values of χ^2 parameter obtained neglecting plastic incompatibility stresses are given in brackets.*

Sample	Type of diffraction elastic constants	Macrostresses [MPa]		Scaling factor q	Average equivalent plast. incomp. stress $[\sigma_{eq}^{IIg(ic)}]$ MPa	Stress free interpl. spacing d^o [Å]	χ^2 $q\neq0$ (χ^2) q=0
		σ_{11}^M	σ_{22}^M				
Red1=74%	Reuss	25 ±7.2	96.7 ±7.3	0.75 ±0.16	25.6 ±4.1	2.86475 ±0.00002	1.66 (2.72)
	Self-cons. (free surf.)	25.2 ±8.4	100.1 ±8.7	0.81 ±0.16	24.9 ±3.9	2.8648 ±0.00002	2.18 (2.69)
	Self-cons. (interior.)	25.6 ± 9.1	98 ±9.1	0.79 ±0.16	24.5 ±3.9	2.8646 ±0.00002	2.36 (2.85)
	Voigt	26.1 ±9.2	98.6 ±9.5	0.77 ±0.16	23.8 ±3.8	2.86474 ±0.00002	2.53 (2.98)
Red1=74% Red2=36%	Reuss	-5.2 ± 6.3	54.2 ±6.2	0.69 ±0.12	24.1 ±2.8	2.86487 ±0.00002	1.32 (2.01)
	Self-cons. (free surf.)	-5.3 ±6.3	56.6 ±6.4	0.69 ±0.12	24.2 ±2.9	2.8649 ±0.00002	1.3 (1.99)
	Self-cons. (interior.)	-4.5 ±6.3	57.4 ±6.4	0.59 ±0.12	20.7 ±2.4	2.86486 ±0.00002	1.26 (1.75)
	Voigt	-3.4 ±6.4	59.9 ±6.5	0.51 ±0.1	18.1 ±2.1	2.86486 ±0.00002	1.22 (1.58)
Red1=74% Red2=49%	Reuss	-4.5 ± 5.6	-30.3 ±5.6	0.84 ±0.1	28.9 ±2.9	2.86478 ±0.00002	1.07 (2.52)
	Self-cons. (free surf.)	-4.6 ±5.6	31.8 ±5.6	0.84 ±0.1	28.9 ±2.9	2.8648 ±0.00002	1.05 (2.51)
	Self-cons. (interior.)	-4.2 ±5.7	-43.7 ±5.7	0.79 ±0.1	27 ±2.7	2.86478 ±0.00002	1.06 (2.32)
	Voigt	-3.6 ±5.9	33.3 ±5.9	0.74 ±0.1	25.4 ±2.5	2.86478 ±0.00002	1.06 (2.14)
Red1=74% Red2=73%	Reuss	-68.6 ±6.4	-87.3 ±6.4	0.91 ±0.1	30 ±3	2.86492 ±0.00002	1.42 (3.16)
	Self-cons. (free surf.)	-69.6 ±6.8	-88.5 ±6.7	0.93 ±0.1	30.9 ±3.1	2.8649 ±0.00002	1.47 (3.35)
	Self-cons. (interior.)	-69.1 ±7.3	-89.2 ±7.1	1.13 ±0.1	37.5 ±3.7	2.86494 ±0.00002	1.66 (4.41)
	Voigt	-68.7 ±8	-90.2 ±7.9	1.31 ±0.1	43.2 ±4.3	2.86496 ±0.00002	1.92 (5.53)
Red1=74% Red2=79%	Reuss	-31.2 ±10.8	-116 ±10.6	1.02 ±0.1	32 ±3.2	2.86486 ±0.00002	4.2 (6.18)
	Self-cons. (free surf.)	-29.9 ±11.4	-118 ±11.1	1.05 ±0.1	32.9 ±3.2	2.8649 ±0.00002	4.46 (6.36)
	Self-cons. (interior.)	-28.2 ±11.2	-118 ±11	1.2 ±0.1	40 ±4	2.86487 ±0.00003	4.34 (7.56)
	Voigt	-26.1 ±11.7	-110.1 ±11.5	1.48 ±0.1	46.5 ±4.6	2.86488 ±0.00003	4.53 (8.85)

The values of stress obtained from all models are very similar, however Reuss model gives a better agreement of experimental data with theoretical ones. Factor χ^2 (*characterising quality of fitting*) for Reuss model is smaller then for other models. For this reason elastic constants were determined using Reuss model. (e.g. Fig. 4.7, 4.8)

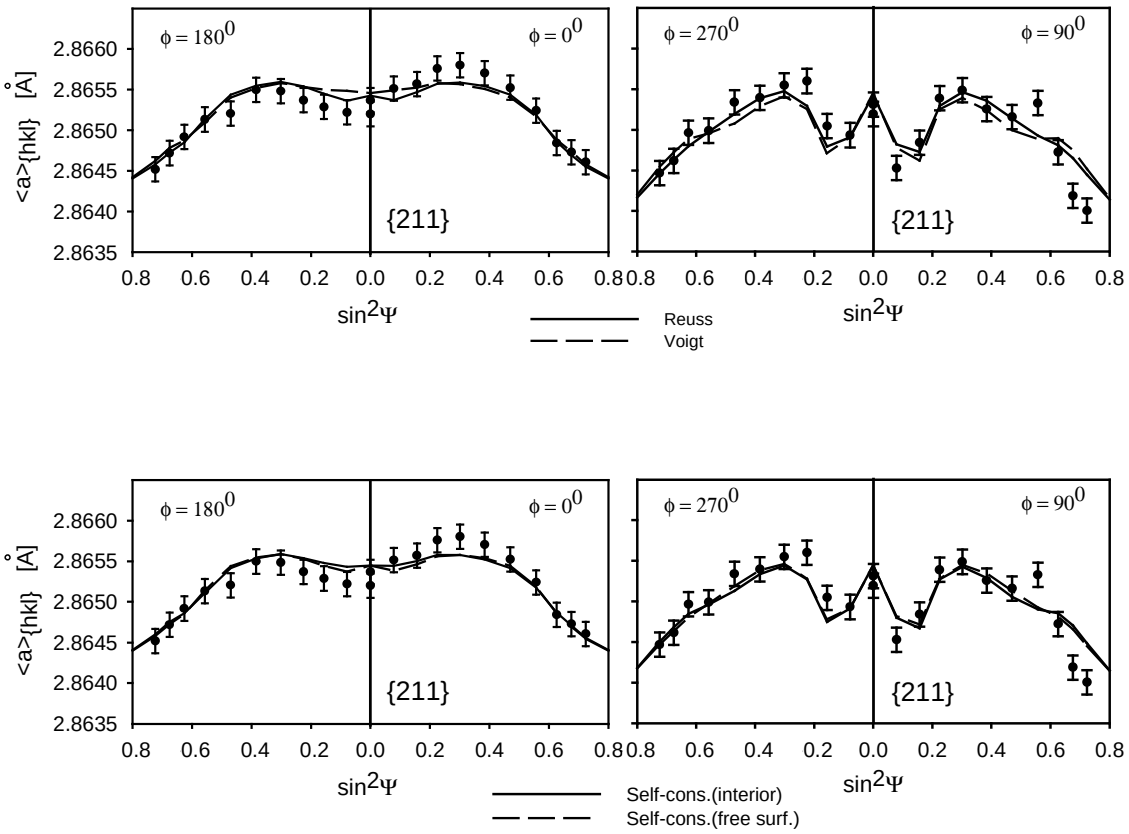

Fig. 4.6. *Plots of $\langle a(\psi,\phi)\rangle_{\{21l\}}$ vs. $\sin^2\psi$ for polycrystalline steel rolled to 74 % reduction in main direction and 49 % in cross direction. Results for Reuss, self-consistent (interior), self-consistent (free surface) and Voigt models are shown.*

The plots of $\langle a(\psi,\phi)\rangle_{\{21l\}}$ vs. $\sin^2\psi$ ({211} reflection) for the steel samples rolled to different deformations in cross rolling are show in Figs. 4.6 and 4.7. Very good fits of model predictions to experimental data is obtained.

The values of main components of the first order residual stresses are listed in Table 4.2. Also *q* parameter, adjusting the amplitude of the predicted second order incompatibility stresses to the real ones (c.f. Eq.4.1), is listed. It varies between 0.7 and 1, hence the real amplitude of the second order stresses is lower than that predicted by the model. This means that the grain-grain interactions are softer than purely elastic ones (some local slip often occurs near grain boundary region and it relaxes partly the incompatibility stresses).

The variation of estimated values of main components of the first order residual stress (σ_{11}^M and σ_{22}^M) in function of the cross-rolling reduction (Red2) is presented in Fig. 4.8. Both components are positive in the simply rolled sample, but with increasing value of Red2 they become negative. Near the value of Red2=73% the two curves intersect.

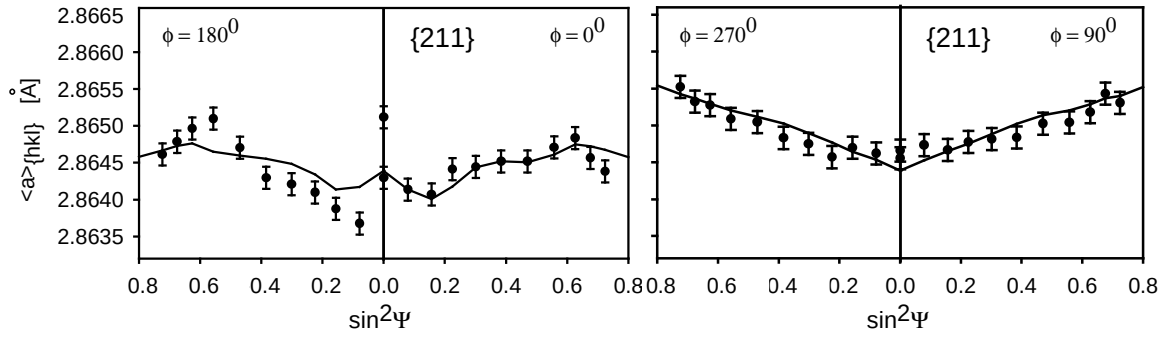
2.8665
2.8660
2.8655
2.8650
2.8645
2.8640
2.8635
<a>{hkl} [Å]
ϕ = 180⁰
{211}
ϕ = 0⁰
ϕ = 270⁰
{211}
ϕ = 90⁰
0.8 0.6 0.4 0.2 0.0 0.2 0.4 0.6 0.8
sin²Ψ

a.

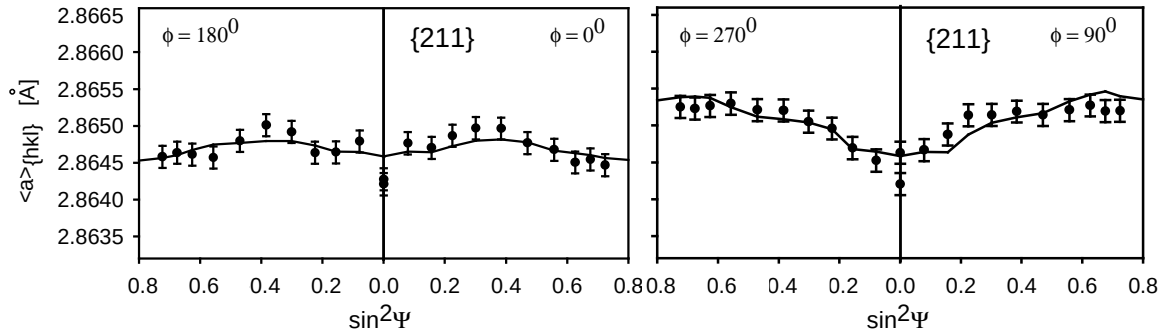
2.8665
2.8660
2.8655
2.8650
2.8645
2.8640
2.8635
<a>{hkl} [Å]
ϕ = 180⁰
{211}
ϕ = 0⁰
ϕ = 270⁰
{211}
ϕ = 90⁰
0.8 0.6 0.4 0.2 0.0 0.2 0.4 0.6 0.8
sin²Ψ

b.

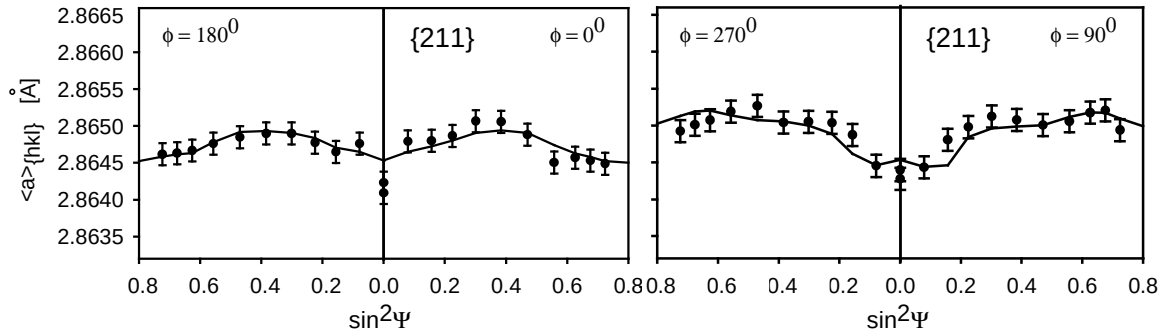
2.8665
2.8660
2.8655
2.8650
2.8645
2.8640
2.8635
<a>{hkl} [Å]
ϕ = 180⁰
{211}
ϕ = 0⁰
ϕ = 270⁰
{211}
ϕ = 90⁰
0.8 0.6 0.4 0.2 0.0 0.2 0.4 0.6 0.8
sin²Ψ

c.

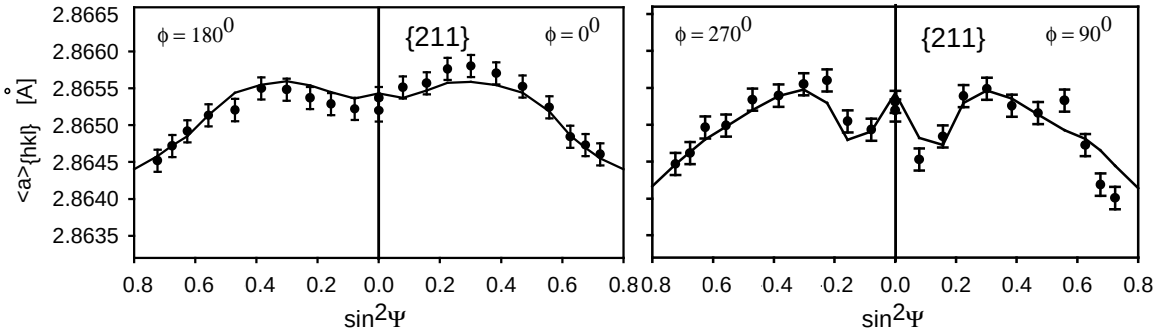

d.

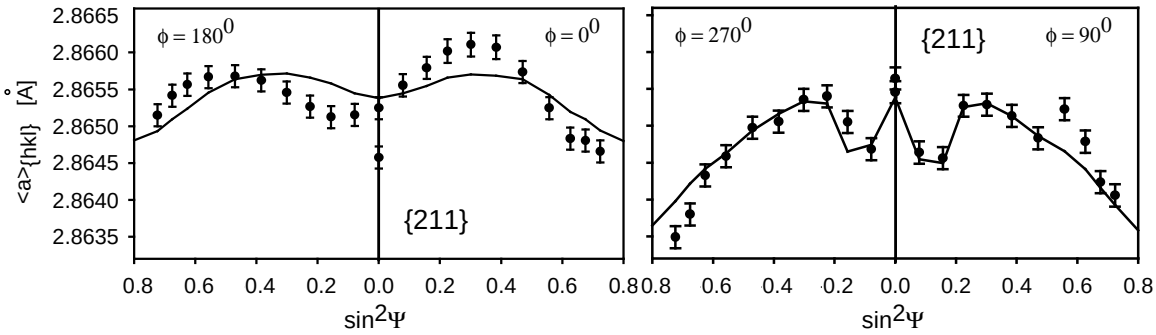

e.

Fig . 4.7. *Plots of $<a(\psi,\phi)>_{\{21l\}}$ vs. $\sin^2\psi$ for polycrystalline steel (Reuss model) rolled to*
a) 74% reduction in main direction
b) 74 % reduction in main direction and 36 % in cross direction
c) 74 % reduction in main direction and 49 % in cross direction
d) 74 % reduction in main direction and 73 % in cross direction
e) 74 % reduction in main direction and 79 % in cross direction

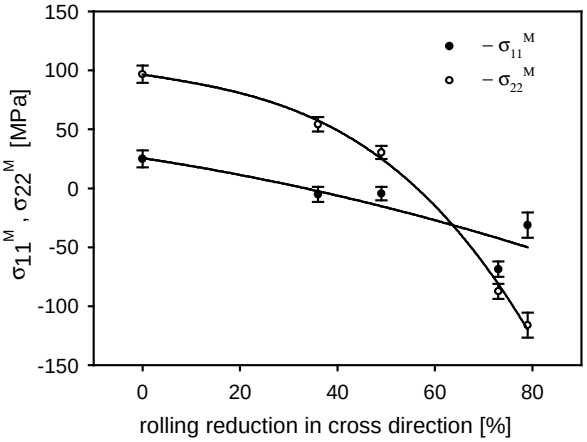

Fig. 4.8. *σ_{11}^M and σ_{22}^M versus deformation in cross rolling direction for cold rolled ferritic steel. Results for Reuss model.*

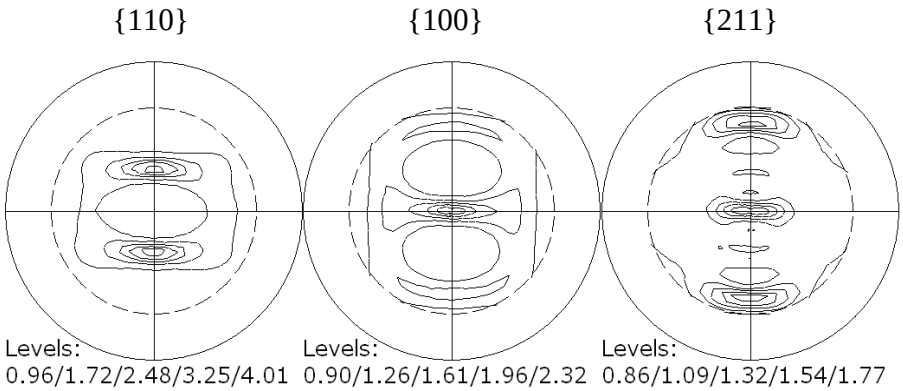
{110}
{100}
{211}
Levels:
0.96/1.72/2.48/3.25/4.01
Levels:
0.90/1.26/1.61/1.96/2.32
Levels:
0.86/1.09/1.32/1.54/1.77
Simple roll. Red=74%

a

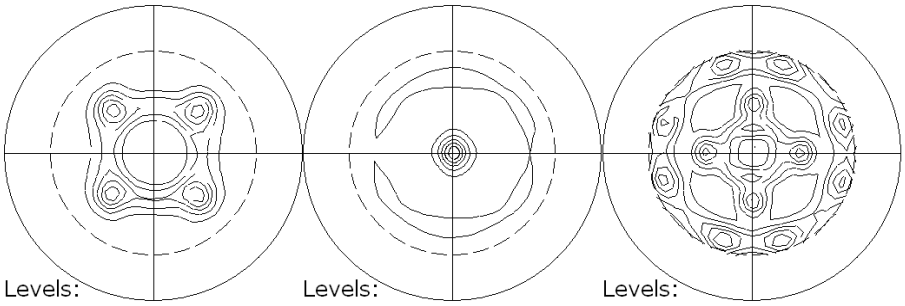
Levels:
0.83/1.46/2.09/2.72/3.35
Levels:
1.24/1.96/2.68/3.41/4.13
Levels:
0.75/0.96/1.16/1.36/1.57
Cross roll. Red1=74% Red2=49%

b

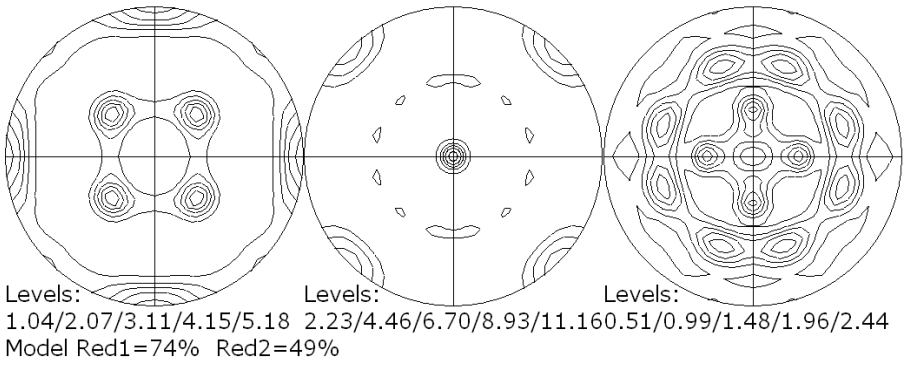
Levels:
1.04/2.07/3.11/4.15/5.18
Levels:
2.23/4.46/6.70/8.93/11.16
Levels:
0.51/0.99/1.48/1.96/2.44
Model Red1=74% Red2=49%

c

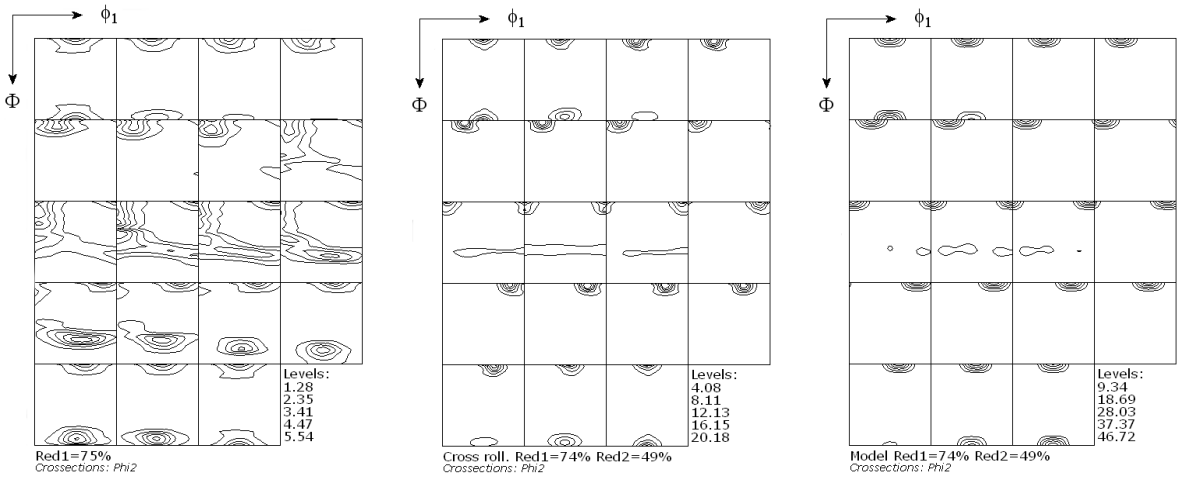

a b c

Fig. 4.9. *(110), (100), (211) pole figures and ODFs for cold rolled steel: a) after simple rolling (Red1=74%), b) cross-rolling (Red1=74% and Red2=49%), c) as above but predicted by the elasto-plastic LW deformation model.*

The crystallographic textures were measured and also predicted by the deformation model (Fig. 4.9). The cross-rolling texture (Fig. 4.9b) is strongly symmetrical compared with the simple rolling one - Fig. 4.9a (two additional symmetry axes inclined ± 45^0 to *x* axis appear) (Wierzbanowski, Wroński et al. 2007a). The model prediction of cross-rolling texture (Fig. 4.9c) gives a perfect agreement with the experimental one.

To show the level of the second order stresses for a statistical grain, the average equivalent residual stress $[\sigma_{eq}^{g(ic)}]$ is calculated (see chapter 1) :

$$[\sigma_{eq}^{IIg(ic)}] = \frac{1}{8\pi^2}\int_E \sigma_{ij}^{IIg(ic)}(\boldsymbol{g})\, f(\boldsymbol{g})\, d\boldsymbol{g} \qquad (4.3)$$

where $\sigma_{eq}^{IIg(ic)} = \left[\frac{1}{2}\left\{(\sigma_{11}^{IIg(ic)} - \sigma_{22}^{IIg(ic)})^2 + (\sigma_{11}^{IIg(ic)} - \sigma_{33}^{IIg(ic)})^2 + (\sigma_{22}^{IIg(ic)} - \sigma_{33}^{IIg(ic)})^2\right\} + 3\left\{(\sigma_{12}^{IIg(ic)})^2 + (\sigma_{13}^{IIg(ic)})^2 + (\sigma_{23}^{IIg(ic)})^2\right\}\right]^{\frac{1}{2}}$ is the equivalent stress calculated according to von Mises formula.

We find that the second order stress level is nearly constant in function of Red2 – Fig. 4.10a. In order to verify the precision of our procedure the stress free inter-planar spacing (a_0) was also plotted in function of Red2. It stays constant, which confirms the precision of our procedure. (within error of $\Delta a_0 = \pm 0.00002$Å) (Wierzbanowski, Wroński et al. 2006d)

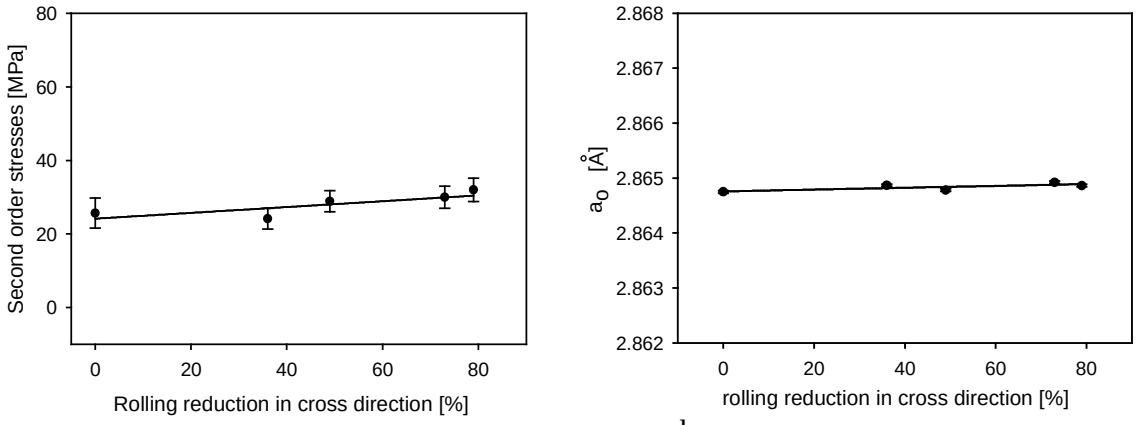

Fig. 4.10. *Equivalent level (Von Misses measure) of the second order stress (a) and a_o versus deformation in cross direction (b) for cold rolled ferritic steel*

4.3. Conclusions

The obtained results show some characteristic tendencies. In the case of rolled polycrystalline copper, the components of residual stresses have a maximum for a defined combination of deformations in both rolling directions. Also in the case of ferritic steel we observe a strong variation of both stress components with the deformation along the second rolling direction. It is worth to point out that oscillations appearing in steel samples cannot be explained only by anisotropy of elastic constants of crystallites, but we should consider also the second order stresses. It is also interesting to note that level of the second order stresses is constant in function of deformation in cross direction for cold rolled ferritic steel.

On the other hand, the operation of cross-rolling involves a strong symmetrization of crystallographic textures, which is easily visible in pole figures. In conclusion, cross-rolling increases the degree of isotropy of physical properties of a material and modifies the level of residual stresses.

Chapter 5

Grazing angle incidence X-ray diffraction geometry used for stress determination

5.1. Introduction

Classical $\sin^2\psi$ method is one of basic methods for measuring the residual stresses and elastic properties of polycrystalline materials. Main disadvantage of this method is a variable penetration depth, which depends on ψ angle. For this reason the classical $\sin^2\psi$ method cannot be used to study materials with a high stress gradient. A stress gradient can be estimated using this method only if the character of stress variation is assumed to be known (e.g., exponential or linear versus with depth). The analysis of stress gradient can also be performed if the standard $\sin^2\psi$ method is repeated for several wavelengths as the X-rays penetrate to different depths or by polishing.

In this chapter, the geometry based on the grazing angle incidence X-ray diffraction (so-called grazing incident diffraction method, GID-$\sin^2\psi$) is discussed and applied for stress measurement. Using this method, it is possible to perform a non-destructive analysis of the heterogeneous stress for different (and well defined) volumes below the surface of the sample. Moreover, the stress can be measured at very small depths, of the order of a few micrometers. The incidence angle is small, consequently it is necessary to take into account additional factors which are not significant in classical geometry. The most important one is refraction. Other factors which are significant for the final result in grazing incidence diffraction method will be also considered.

5.2. Classical and grazing incidence diffraction geometry for stress determination

In symmetric Bragg-Brentano geometry or classical $\sin^2\psi$ geometry, ψ angle (between scattering vector and sample surface normal) is changing during experiment (Noyan and Cohen, 1987). Detector and X-ray source movements are conjugated. This involves that the angle between surface and incident beam equals the angle between surface and diffracted beam. This type of geometry is used in ψ goniometers. The $\sigma(\psi,\phi)$ stress can be measured by determining elastic deformation of lattice parameter - $\varepsilon_{33}^{L}(\psi,\phi)$ - in laboratory system (L). Using Hooke's law and transformation law, the stress is finally expressed in sample coordinates system (S). The main disadvantage of this method is various penetration depth, which depends on mainly 2θ and ψ angles. The penetration depth is defined as the distance from the surface at which the radiation intensity falls to some fraction (e.g., 1/e) of the original value (Cullity, 1956). According to Beer-Lambert law, the intensity of the radiation wave inside a material at the depth z from the surface as:

$$I = I_o \exp(-\mu AB) \qquad (5.1)$$

where $AB=z/\sin\alpha$ is the path of the radiation till a thin layer (dz) situated at the depth z (Fig. 5.1) and μ is the linear coefficient of absorption.

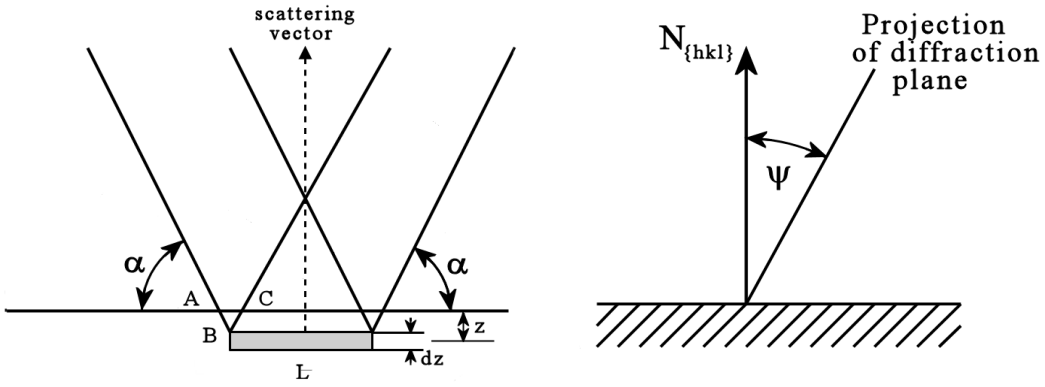

a. b.

Fig. 5.1. *Irradiated thin plate of a material of the thickness dz and length l situated at the depth z. Classical Bragg-Brentano geometry, with scattering vector perpendicular to the sample surface, is shown:*

a). diffraction plane (defined by incident and diffracted beams is perpendicular to the sample surface

b). diffraction plane is inclined of ψ from $N_{\{hkl\}}$.

In this symmetrical geometry, the total beam path x_z=AB+BC inside materials depends on incidence angle α (Fig. 5.1a):

$$x_z = z\left(\frac{1}{\sin\alpha}+\frac{1}{\sin\alpha}\right) \qquad (5.2)$$

If now, the scattering vector (and the diffraction plane, defined by the incident and diffracted beam) is rotated of ψ towards the sample surface, the beam path becomes:

$$x_z = \frac{z}{\cos\psi}\left(\frac{1}{\sin\alpha}+\frac{1}{\sin\alpha}\right) \tag{5.3}$$

Let us calculate the fraction (G_t) of total X-ray intensity absorbed by the layer of thickness t:

$$G_t = \frac{\int_0^t I_0\, exp(-\mu x_z)dz}{\int_0^\infty I_0\, exp(-\mu x_z)dz} \tag{5.4}$$

Substituting x_z from Eq.5.3 and performing the integration, we obtain:

$$G_t = 1-\exp\left[\frac{-\mu t}{\cos\psi}\left(\frac{1}{\sin\alpha}+\frac{1}{\sin\alpha}\right)\right] \tag{5.5}$$

One often defines the penetration depth as a depth t, which corresponds to a particular G_t value (usually for G_t= 1-1/e, i.e., $G_t \cong 0.63$).

For symmetrical geometry (Fig. 5.1): α = θ, and we obtain for the penetration depth:

$$t = \frac{-\ln(1-G_t)}{2\mu}\sin\theta\cos\psi \tag{5.6}$$

The penetration depth t vs. $\sin^2\psi$ for classical geometry (for G_t=0.63) is presented on Fig 5.2.

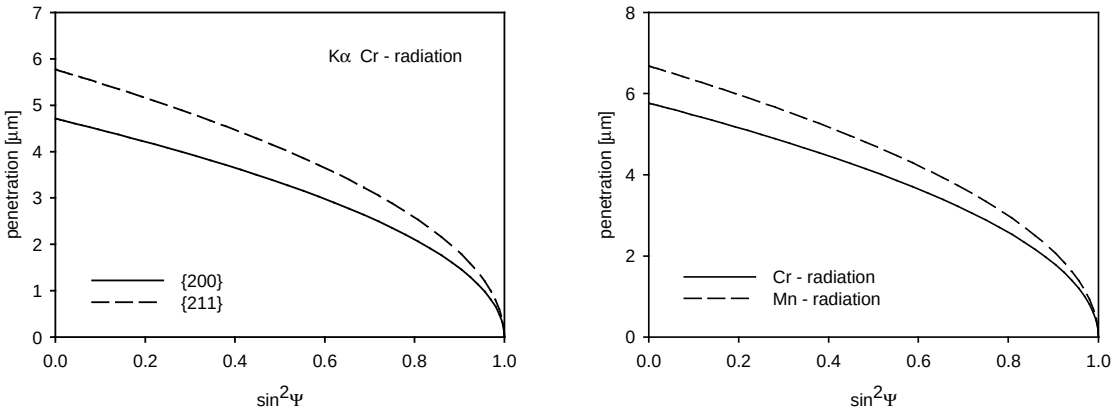

a b

Fig.5.2. *The penetration depth vs. $\sin^2\psi$ calculated from Eq. 5.6. a) for different reflections planes, b) for {211} reflection using different wavelengths for ferrite steel*

Because penetration depth strongly depends on θ and ψ angles, this method cannot be used when large macro-stress gradients are present. The grazing incidence diffraction geometry, so-called GID-sin^{2}ψ method, is characterized by a small and constant incidence angle α (Figs. 5.3 - 5.5) and by different orientations of the scattering vector (changing 2θ angle for a constant wavelength). The parallel beam geometry is used to minimise errors connected with sample misalignment (Skrzypek, 2002). Only detector moves in grazing incidence diffraction geometry and $\psi_{\{hkl\}}$ angle is expressed by equation:

$$\psi_{\{hkl\}} = \theta_{\{hkl\}} - \alpha \qquad (5.7)$$

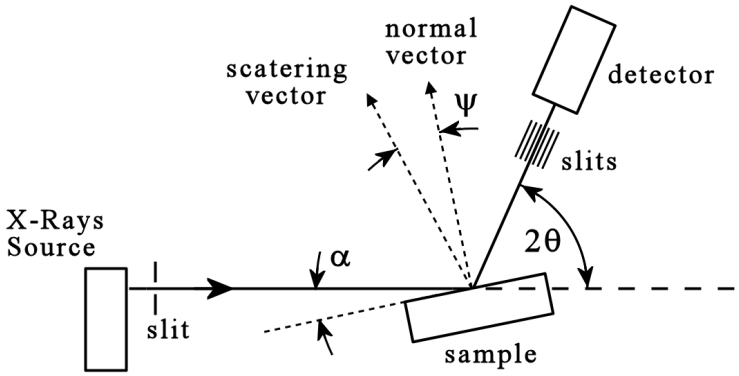

Fig.5.3. *Geometry of GID-sin^{2}ψ method*

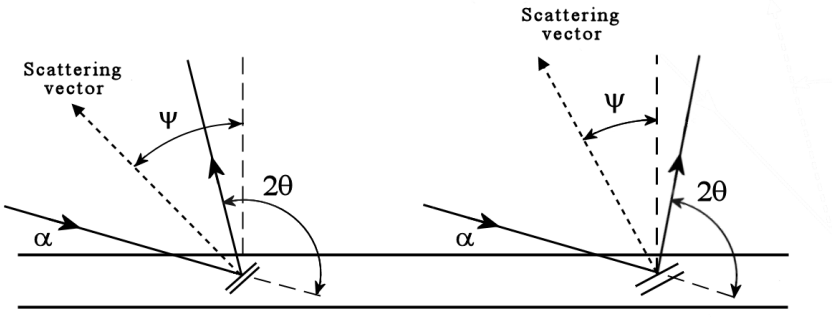

Fig.5.4. *Geometry of GID-sin^{2}ψ method. The incidence angle α is fixed during measurement and the orientation of the scattering vector is characterised by ψ= $\psi_{\{hkl\}}$ angle.*

The $\psi_{\{hkl\}}$ angle depends on incidence angle (α) and type of reflection {*hkl*}. The possible values of $\psi_{\{hkl\}}$ angles are limited to the number of *hkl* reflections used in the experiment.

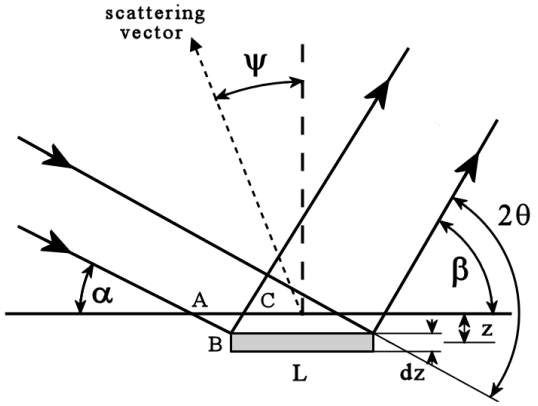

Fig. 5.5. *Irradiated thin plate of a material of the thickness dz and length l situated at the depth z in grazing incidence diffraction geometry.*

The radiation path inside materials depends on incidence angle α and diffracted beam angle β (Fig.5.5).

$$x_z = z\left(\frac{1}{\sin\alpha}+\frac{1}{\sin\beta}\right) \tag{5.8}$$

Similarly as it was done in Eq. 5.4, let us calculate the fraction (G_t) of X-ray intensity absorbed by the layer of thickness t:

$$G_t = \frac{\int_0^t I_0\, exp(-\mu x_z)dz}{\int_0^\infty I_0\, exp(-\mu x_z)dz} \tag{5.9}$$

Substituting x_z from Eq.5.8 and performing the integration, we obtain:

$$G_t = 1-\exp\left[-\mu t\left(\frac{1}{\sin\alpha}+\frac{1}{\sin\beta}\right)\right] \tag{5.10}$$

where: $\beta = 2\theta - \alpha$.
The corresponding penetration depth is:

$$t = \frac{-ln(1-G_t)}{\mu\left[\frac{1}{sin\alpha}+\frac{1}{sin(2\theta-\alpha)}\right]} \tag{5.11}$$

This relation versus $\sin^2\psi$ where $\psi_{\{hkl\}} = \theta_{\{hkl\}}-\alpha$ (for G_t=0.63) is shown in Fig.5.6.

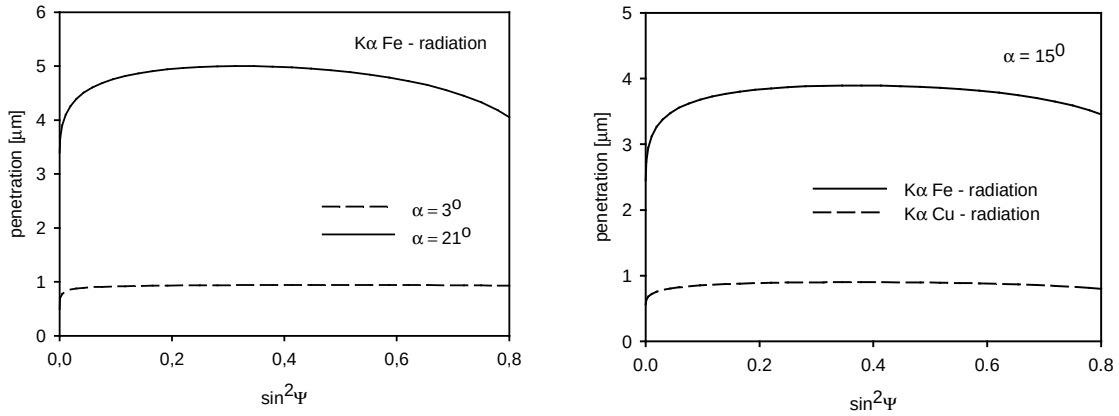

a b

Fig. 5.6. *Penetration depth in function of $sin^2\psi$ for 211 reflection for ferrite($\psi_{\{hkl\}}=\theta_{\{hkl\}}-\alpha$): a) for two different incidence angles, b) for two different wavelengths at* $\alpha=15^0$.

The main advantage of the g-$sin^2\psi$ method is constant or almost constant penetration depth for a fixed α value and for a radiation of given type. However, the penetration depth can be changed by selection of the incidence angle. This gives a possibility to investigate materials with a stress gradient. Choosing appropriate α values and type of radiation it is possible to measure stresses from different volumes below the surface.

Exemplary values of penetration depths were calculated for steel sample (Table 5.1). Using GID-$sin^2\psi$ technique (incidence angles from 3^0 to 21^0) and two types of radiations (Cu and Fe radiation) it is possible to investigate variation of stresses on the depth ranging from 0.2 to 4.4 μm below the surface. For comparison, the *average* penetration depth in the standard method for Mn radiation was also calculated (about 6.13 μm). In the latter case, however, it is not possible to analyse the stress gradient across a sample.

Table. 5.1. *Penetration depth of X-ray radiation in steel.*

Radiation /absorption coeff. [cm^{-1}]/	Incidence angle α[^{0}] and penetration depth t [μm] – grazing incidence diffraction method:						
	3^0	6^0	9^0	12^0	15^0	18^0	21^0
Cu /μ_l = 2395/	0.21	0.39	0.55	0.69	0.82	0.93	1.02
Fe /μ_l = 554/	0.89	1.67	2.36	2.97	3.53	4.01	4.42
Average penetration depth for standard $sin^2\psi$ method [μm]:							
Mn /μ_l = 700/	6.13						
Fe /μ_l = 554/	7.8						
Cu /μ_l = 2395/	1.75						

In *GID-$sin^2\psi$* method, the $<d(\psi,\phi)>_{\{hkl\}}$ interplanar spacing is measured in directions defined by the ϕ and ψ angles for different *hkl* reflections. These experimental data can be easily analysed by the multi-reflection method and residual stresses can be determined for every incidence angle α (Skrzypek and Baczmański 2001a and 2001b, Baczmański 2003a, 2003b and

2004). The interplanar spacing measured in the L_3 direction (Fig. 1.3) is given by the well known relation, which can be rewritten for equivalent lattice parameters a_{hkl}:

$$< a(\psi,\phi) >_{\{hkl\}} = \left[s_1\{hkl\}\,(\sigma_{11}^M + \sigma_{22}^M + \sigma_{33}^M) + \frac{1}{2} s_2\{hkl\}(\sigma_{11}^M \cos^2\phi + \sigma_{22}^M \sin^2\phi + \sigma_{12}^M \sin 2\phi)\sin^2\psi_{\{hkl\}} + \frac{1}{2} s_2\{hkl\}\,\sigma_{33}^M \cos^2\psi_{\{hkl\}} + \frac{1}{2} s_2\{hkl\}\,(\sigma_{13}^M \cos\phi + \sigma_{23}^M \sin\phi)\sin 2\psi_{\{hkl\}} \right] a^o + a^o \tag{5.12}$$

where: $a_{\{hkl\}} = d_{\{hkl\}} / \sqrt{h^2 + k^2 + l^2}$ are equivalent lattice parameters, σ_{ij}^M is the average macrostress for the penetration depth t corresponding to a given incidence angle α (see Eq. 5.11), while $s_1\{hkl\}$ and $1/2\, s_2\{hkl\}$ are the diffraction elastic constants for the studied quasi-isotropic sample, calculated for different *hkl* reflections related to $\psi_{\{hkl\}}$ angles defined by Eq. 5.7.
The $<a(\psi,\phi)>_{\{hkl\}}$ parameters can be fitted applying the least square procedure and, consequently, the values of a^0 and the macrostress σ_{ij}^M can be found. For presentation of the results of *GID-sin*$^2\psi$ method, the $<a(\psi,\phi)>_{\{hkl\}}$ values instead of $<d(\psi,\phi)>_{\{hkl\}}$ are shown versus $sin^2\psi_{\{hkl\}}$, where $\psi_{\{hkl\}} = \theta_{\{hkl\}} - \alpha$ angles correspond to various *hkl* reflections. The $<a(\psi,\phi)>_{\{hkl\}}$ versus $sin^2\psi_{\{hkl\}}$ plot is linear in the case of quasi-isotropic sample.

5.3. Corrections in grazing incidence diffraction geometry

Similarly as in symmetrical Bragg-Brentano geometry, to estimate stresses it is necessary to consider all factors which influence the final result and to apply accurate corrections. The intensity of diffraction peak for a given diffraction pattern depends on several parameters (Cullity, 1956, Guinier, 1964):

- multiplicity
- temperature factor
- absorption factor
- Lorentz-polarization factor
- structure factor
- refraction factor

Residual stress measurement is based on the peak position analysis. The first two factors (multiplicity and temperature factor) do not change the peak position but they modify intensity of the peak and FWHM (Full Width at Half Maximum). For these reasons they can be neglected in elastic stress analysis. Next factors from the list above are significant in stress analysis and they should be considered in diffraction data analysis.

5.3.1 Absorption Factor

The intensity of diffracted beam is affected by absorption, which is directly related to the path length which is traversed by the beam in a specimen. Consider the case where a beam of intensity I_O and of unit area in cross-section, is incident on a flat plate at the angle α (Fig. 5.7). The beam intensity reaching a layer of length L and thickness dz located at depth z below the surface is proportional to $I_o e^{-\mu AB}$ (μ is the linear absorption coefficient of the sample). The beam intensity diffracted by the layer is:

$$abLI_O e^{-\mu AB} dz \tag{5.13}$$

where *a* is the volume fraction of crystallites that can diffract at this angle and *b* is the fraction of incident energy diffracted by unit volume.

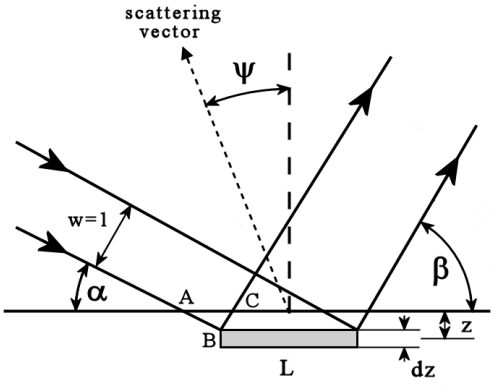

Fig. 5.7. *Diffraction form a flat plate at the depth z.*

This diffracted intensity is also attenuated by the absorption along BC by a factor $e^{-\mu BC}$ until it exits the material, thus the total diffracted intensity outside the specimen is given by:

$$dI_D = aLbI_O e^{-\mu(AB+BC)} dz \tag{5.14}$$

where:

$$AB = \frac{z}{\sin\alpha} \qquad BC = \frac{z}{\sin\beta} \tag{5.15}$$

The illuminated length l of the layer for a beam of unit cross-section (and of unit width), is:

$$L = \frac{1}{\sin\alpha} \tag{5.16}$$

Finally, Eq. 5.14 becomes:

$$dI_D = \frac{I_O ab}{\sin\alpha} exp\left\{-\mu z\left[\frac{1}{\sin\alpha} + \frac{1}{\sin\beta}\right]\right\} dz \tag{5.17}$$

In the case of grazing incident diffraction geometry:

$$\beta = 2\theta - \alpha \tag{5.18}$$

Hence:

$$dI_D = \frac{I_O ab}{\sin\alpha} exp\left\{-\mu z\left[\frac{1}{\sin\alpha} + \frac{1}{\sin 2\theta - \alpha}\right]\right\} dz \tag{5.19}$$

The total diffracted intensity, for a fixed α angle, is obtained by integrating for an infinitely thick specimen:

$$I_D = \int_{z=0}^{\infty} dI_D \tag{5.20}$$

After performing the integration:

$$I_D = const \frac{1}{1 + \frac{\sin\alpha}{\sin(2\theta - \alpha)}} \tag{5.21}$$

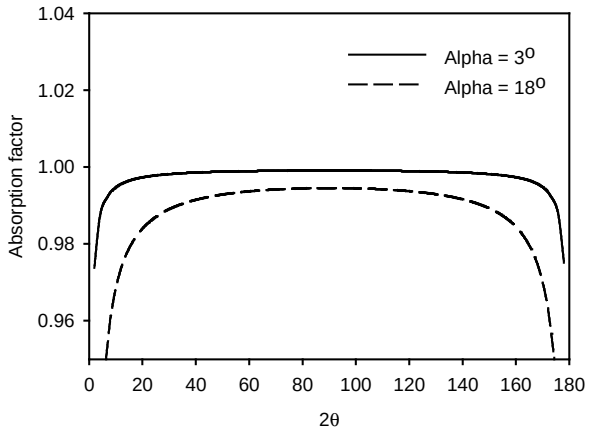

Fig. 5.8. *Absorption factor versus 2θ for ferrite steel.*

The absorption factor (Eq. 5.21) for two different incidence angles is presented in Fig. 5.8. It is easy to observe that absorption factor depends on incidence angle; on the other hand, for the 2θ range between 40^0 and 140^0 it is practically constant. For small and big 2θ angles the absorption factor changes quickly and this changes a peak position. This effect has to be taken into account in data correction.

5.3.2 Lorentz-Polarization Factor

The Lorentz factor is a collection of trigonometric terms that describes the dependence of the diffracted intensity on the diffraction angle. There are three factors that contribute to Lorentz factor (Cullity, 1956, Senczyk, 1974):

- The number of grains which are oriented such that they can diffract at a given angle 2θ.
- The diffracted intensity per unit length of the diffraction cone.
- The dependence of diffracted intensity from any one crystalline 2θ.

The results for the above terms can be combined to form a single factor which describes the variation of intensity with angle θ. This factor is so-called the Lorentz factor, and is given by (see Appendix A):

$$L.F = K\frac{1}{\sin^2\theta} \tag{5.22}$$

where K is constant.
Moreover, the polarization factor has to be taken into account. The Lorentz factor and the polarization factor are usually combined together to form the L-P (Lorentz-Polarization) factor:

$$(L.P.) = \frac{1+\cos^2\theta}{\sin^2\theta} \tag{5.23}$$

The Lorentz – polarization factor is shown in Fig. 5.9. Like for absorption this correction is significant for small and big angles 2θ.

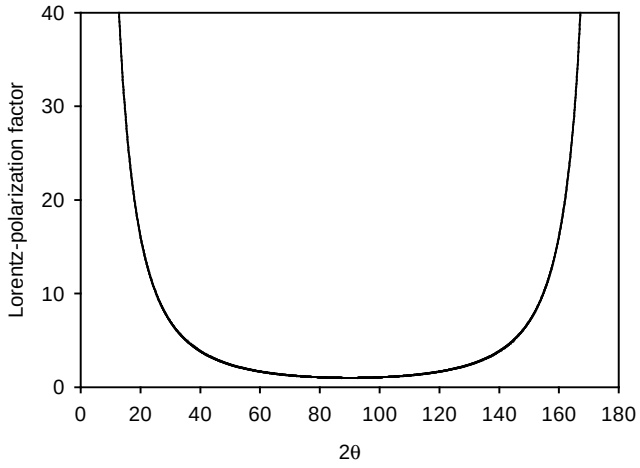

Fig. 5.9. *Lorentz-Polarization factor versus 2θ for ferrite steel.*

5.3.3. Structure factor

When an X-ray beam encounters an atom, each electron in it scatters a part of the radiation coherently in accordance with the Thomson equation. One might also expect the nucleus to take part in the coherent scattering, since it also bears a charge and should be capable of oscillating under the influence of the incident beam. But the nucleus has an extremely big mass relative to that of the electron and cannot oscillate. Finally the coherent scattering by an atom is due only to the electrons contained in that atom. The wave scattered by a single atom is not the sum of the waves scattered by its component electrons. It is sum only if the scattering is in the forward direction ($2\theta = 0$), because the waves scattered by all the electrons of the atom are then in phase and the amplitudes of all the scattered waves can be added directly. This is not true for other directions of scattering. The fact that the electrons of an atom are situated at different points in space introduces differences in phase between the waves scatted by different electrons.

A quantity f, the atomic scattering factor, is used to describe the "efficiency" of scattering of a given atom in given direction. It is defined as a ratio of amplitudes:

$$f = \frac{\text{amplitude of the wave scattered by an atom}}{\text{amplitude of the wave scattered by one electron}} \qquad (5.24)$$

From what has been said already, it is clear that $f=Z$ for any atom scattering in forward direction. As θ increases, however, the waves scattered by individual electrons become more and more out of phase and f decreases. The atomic scattering factor also depends on the wavelength of the incident beam. The actual calculation of f involves $\sin\theta$ rather than θ, because f decreases as the quantity ($\sin\theta/\lambda$) increases (Fig. 5.12).

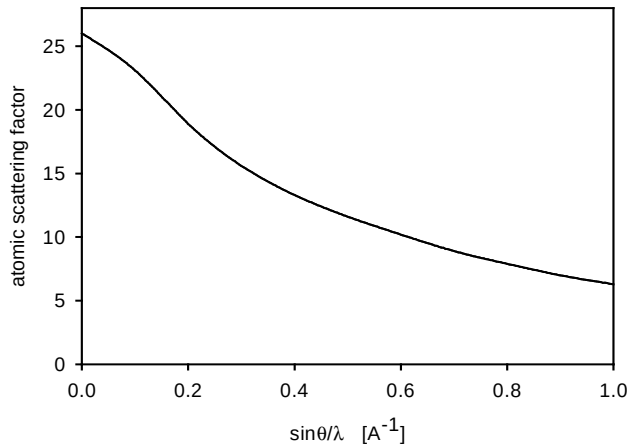

Fig. 5.12. *The atomic scattering factor for iron.*

Direct calculation of atomic factor is quite complicated. Values of this factor are collected in crystallography tables.

5.3.4. Refraction factor

The next factor, which has strong influences on peak position, is refraction index. Refraction index for X-ray radiation in metals is slightly less than unit (Hart, 1988, Parratt, 1954 and Ely, 1997). For this reason velocity in material of EM (electro-magnetic) wave is different than velocity outside material.
The quantum-mechanical theory for the complex refractive index, gives

$$n = 1 - \delta + i\beta \tag{5.25}$$

where complex part of n factor depends on damping factor. The δ and β factors are described by Kramers-Kronig relations.
If anomalous dispersion is ignored, the refraction index factor for X-ray range is given by

$$n = 1 - \delta \tag{5.26}$$

with:

$$\delta = A' \lambda^2 \frac{\rho Z}{M} \tag{5.27}$$

where:

$$A' = {N_A e^2}/{2\pi m_e c^2} = 2.7019 \cdot 10^{10} \qquad \left[{\text{cm}}/{\text{mol}}\right] \tag{5.28}$$

and: N_A – Avogadro's number; e – electron charge, m_e – electron mass, c – velocity of light, M – molecular weight, ρ – density, Z – atomic number and λ wavelength in cm^{-1}.
The index of refraction n of X-rays is slightly less than unity. For wavelengths below 2Å, δ is of the order of 10^{-4} to 10^{-5}, depending on the density of the material. Refraction index depends on frequency of EM wave. For some frequency ranges it is higher than one and for other lower than one. Variation of refraction index is shown on Fig. 5.13.

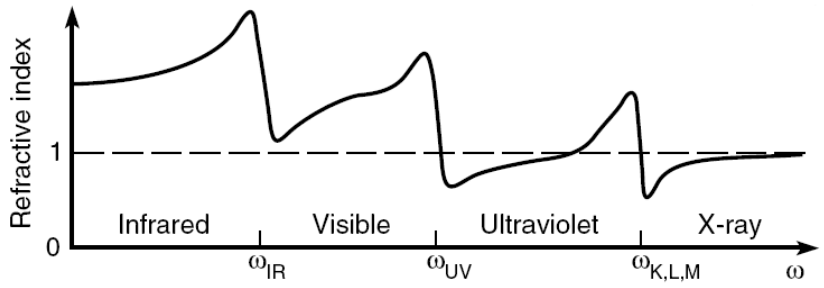

Fig. 5.13. *Refraction index versus* ω.

Propagation direction of EM wave changes during passing by boundary of two media. This change depends on refraction index of a material and is described by Snell's law. Refraction causes a change in 2θ angle and a shift of peak position. For this reason Bragg's law should be modified.

The total correction consist of two factors:

- the first one takes into account a different wavelength in a material (change of so-called optical path),
- the second one takes into account the refraction on a boundary between two media.

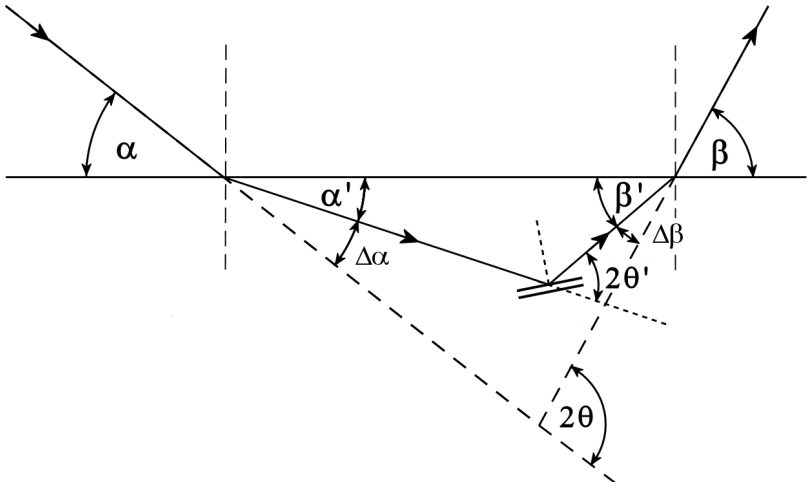

Fig. 5.14. *Effect of refraction in grazing incidence diffraction geometry.*

Bragg's law in a basic form (without refraction) is described by equation (for the first order reflection):

$$\lambda = 2d\sin\theta_0 \tag{5.29}$$

Let us consider the first effect. The refraction index has different value in a material (n=1-δ) than outside it (n=1). Hence, the optical path of the beam inside a material is changed and Bragg's law has a form:

$$\lambda' = 2d\sin\theta' = \frac{\lambda}{1-\delta} \tag{5.30}$$

Combining the last two equations, we obtain:

$$1-\delta = \frac{\sin\theta_0}{\sin\theta'} \tag{5.31}$$

The change of Bragg's angle is:

$$\Delta\theta_1 = \theta' - \theta_0 \tag{5.32}$$

From Eq. 5.31 one obtains:

$$1-\delta = \frac{\sin\theta_0}{\sin\theta'} = \frac{\sin(\theta'-\Delta\theta_1)}{\sin\theta'} \tag{5.33}$$

Taking into account that $\Delta\theta_1$ has a small value and using obvious trigonometric relations , one obtains from the above:

$$\Delta\theta_1 = \delta\,\mathrm{tg}\theta' \tag{5.34}$$

Now, let us consider the second effect. The incident beam refracts on the boundary of two media according to Snell's law (Fig. 5.14). We obtain:

$$\frac{\sin(90-\alpha)}{\sin(90-\alpha')} = 1-\delta \tag{5.35}$$

The relative refraction index has a value smaller than one and accordingly:

$$\alpha > \alpha' \;\Rightarrow\; \alpha = \alpha' + \Delta\alpha \tag{5.36 a}$$
$$\beta > \beta' \;\Rightarrow\; \beta = \beta' + \Delta\beta \tag{5.36 b}$$

After substituting Eq. 5.36a into Snell's law, assuming that $\Delta\alpha$ has small value and using obvious trigonometric relations, one obtains:

$$\Delta\alpha = \delta\,\mathrm{ctg}\alpha' \tag{5.37}$$

Similarly, one finds:

$$\Delta\beta = \delta\,\mathrm{ctg}\beta' \tag{5.38}$$

Let us define:

$$(\Delta\theta)_2 = 2\theta - 2\theta' \tag{5.39}$$

It is seen from Fig. 5.15 that $(\Delta\theta)_2 = \Delta\alpha + \Delta\beta$, hence:

$$(\Delta\theta)_2 = \delta(ctg\,\alpha' + ctg\,\beta') \tag{5.40}$$

The total correction:

$$\Delta 2\theta = 2\theta - 2\theta_0 \tag{5.41}$$

where 2θ is measured Bragg angle and $2\theta_0$ – its corrected value.
Substituting Eq. 5.32 to Eq.5.39, one obtains:

$$\Delta 2\theta = (\Delta\theta)_2 + 2\Delta\theta_1 \tag{5.42}$$

and equals to:

$$\Delta 2\theta = \delta(\mathrm{ctg}\alpha' + \mathrm{ctg}\beta' + 2\mathrm{tg}\theta') \tag{5.43}$$

In general the corrections are small, hence: $\alpha \cong \alpha'$, $\beta \cong \beta'$, $\theta \cong \theta'$, and:

$$\Delta 2\theta = \delta(ctg\,\alpha + ctg\,\beta + 2tg\,\theta) \tag{5.44}$$

Moreover, in the case of grazing incidence diffraction geometry: $\beta = 2\theta - \alpha$, and we obtain finally:

$$\Delta 2\theta = \delta[ctg\alpha + ctg(2\theta - \alpha) + 2tg\theta] \qquad (5.45)$$

Total correction for X-ray radiation depends on the incident beam angle α, the Bragg angle 2θ and on the material constant (δ). The variation of the total correction versus incidence angle and Bragg angle is shown in Fig.5.15.

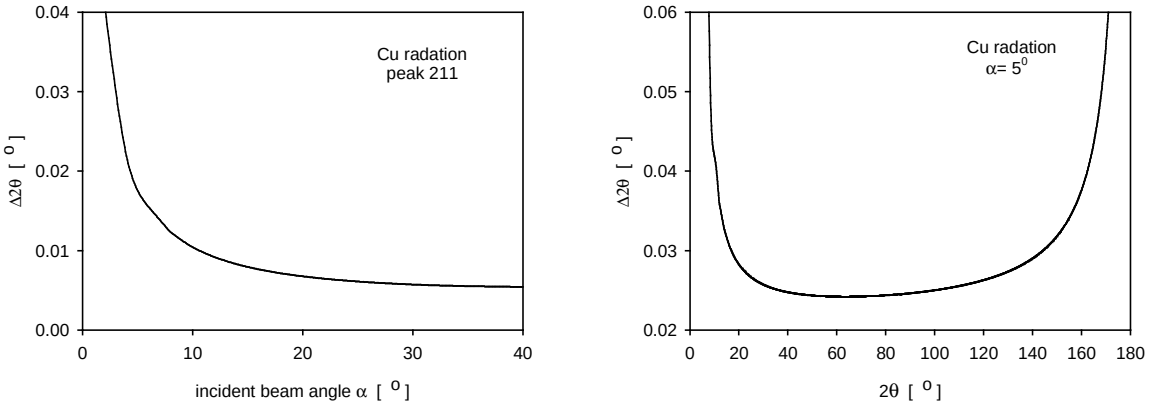

a. b.

Fig. 5.15. *a) Correction $\Delta 2\theta$ versus α for 211 peak in steel,*
b) Correction $\Delta 2\theta$ versus 2θ for the constant incidence angle $\alpha = 5^0$.
The graphs were calculated for Cu radiation.

The correction for refraction strongly depends on the incidence angle α. For small α the shift can easily exceed 0.01^0, than with growing α angle the shift decreases.

5.4. Experimental results

Ferrite powder sample

The next step was to find the influence of the corrections described above on results obtained with the grazing incidence diffraction method. The simple and standard sample is the powder one. The reference ferrite powder sample was prepared. The powder sample was obtained from mechanically deformed material. The grazing incidence diffraction measurements were performed on the Brücker D8 X-ray diffractometer using the Co radiation. The grazing incidence diffraction measurements were done for $\phi=0^0$ and $<a(\psi,\phi)>_{\{hkl\}}$ versus $sin^2\psi_{\{hkl\}}$ relation was determined. The experimental data was analysed applying the multi-reflection method. The experiment was repeated for various incidence angles α, corresponding to different penetration depths *z* given in Table 5.1.

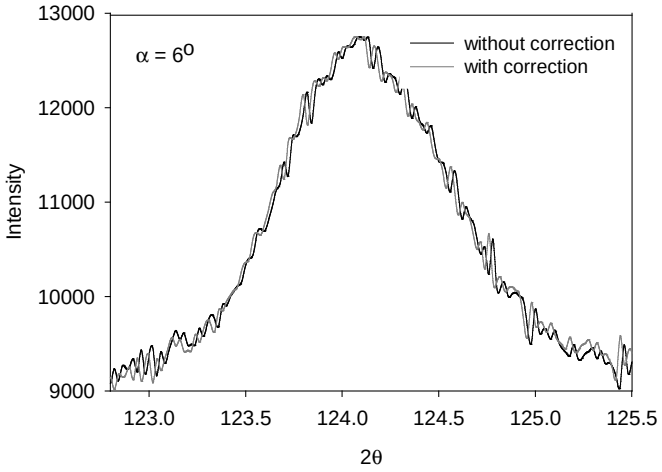

Fig. 5.16. *Position of 220 peak for steel powder sample with and without corrections.*

Figure 5.16 shows exemplary 220 peak for steel powder sample and the shift of its position due to the applied correction. The determined peak position without corrections is 2θ = 123.9788 deg. Applying corrections for absorption, atomic structure factor and Lorentz-polarization factor we find the peak position at 2θ = 123.979 deg. If, moreover, the correction for refraction is added – the determined peak position is 2θ = 123.9674 deg. It is clear that the correction for refraction factor has the main influence on the peak position and the corresponding shift can be even of 0.05 deg.

In order to calculate the diffraction elastic constants, the Reuss, Voigt and the self-consistent (for interior and for surface) models were used. The correction effect on residual stresses, determined in the powder sample, is presented in Table 5.2. Taking into account the isotropic properties of this sample, the relation: $\sigma_{11}^{M} = \sigma_{22}^{M}$ and $\sigma_{33}^{M} = 0$ was assumed. The stress components and stress-free lattice parameter for the powder sample versus penetration depth are presented in Figs. 5.17 and 5.18.

Table 5.2 *Comparison of macrostresses for powder sample using different models for calculation of the diffraction elastic constants. (LP – Lorentz-polarization, A – absorption, f-atomic structure factor).*

Penetration depth, incidence angle	Type of correction	Determined $\sigma^{M}_{11}=\sigma^{M}_{22}$ [MPa]			
		Voigt	self-cons. (interior)	self-cons. (free surface)	Reuss
2 μm $\alpha=6^0$ (Co – rad.)	No corr.	88.9±17.1	73.2±14.2	61±12.1	57.9±11.4
	LP, A, f	86±17.1	70.7±14.2	58.8±12.1	55.8±11.4
	Refraction	-0.8±17.1	-0.7±14.2	-0.6±12.1	-0.5±11.4
3.7 μm $\alpha=12^0$ (Co – rad.)	No corr.	59.9±15.9	49.8±13.5	40.3±11.3	39.7±11.1
	LP, A, f	57.1±15.2	47.6±13.5	38.8±11.3	37.9±11.1
	Refraction	28±15.9	22.9±13.5	18.3±11.3	17.9±11.1
5 μm $\alpha=18^0$ (Co – rad.)	No corr.	49.2±15.5	42±13.5	33.5±11.2	33.9±11.3
	LP, A, f	47.7±15.5	40.9±13.5	32.7±11.2	33.3±11.3
	Refraction	21±15.5	17.5±13.5	13.7±11.2	13.8±11.3

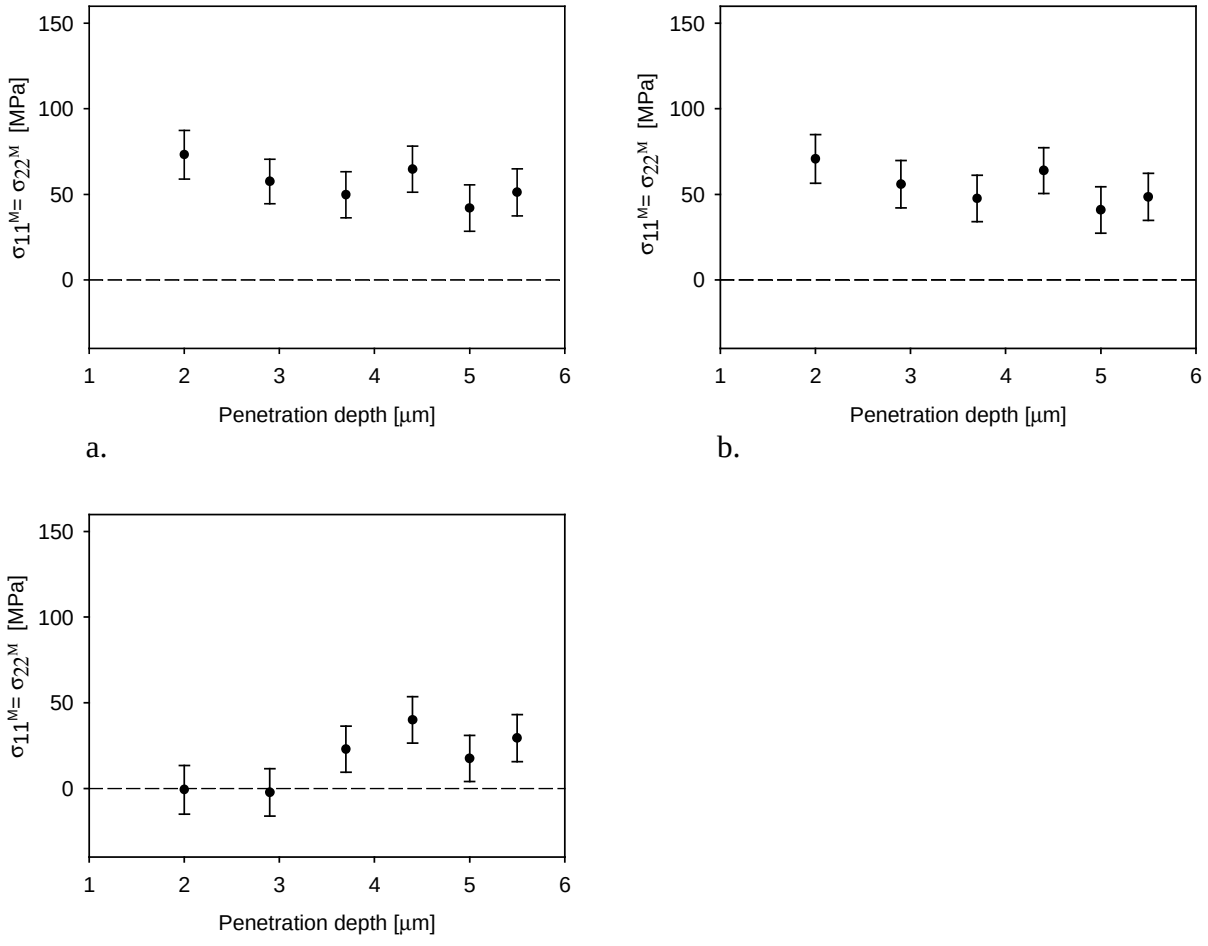

Fig.5.17. *Stress components* $\sigma_{11}^{M} = \sigma_{22}^{M}$ *(multi-reflection method, Co radiation) versus penetration depth z for the ferrite powder sample:*
a) without corrections, b) with absorption, Lorentz-polarization and atomic structure factor corrections, c) taking into account above corrections and refraction.

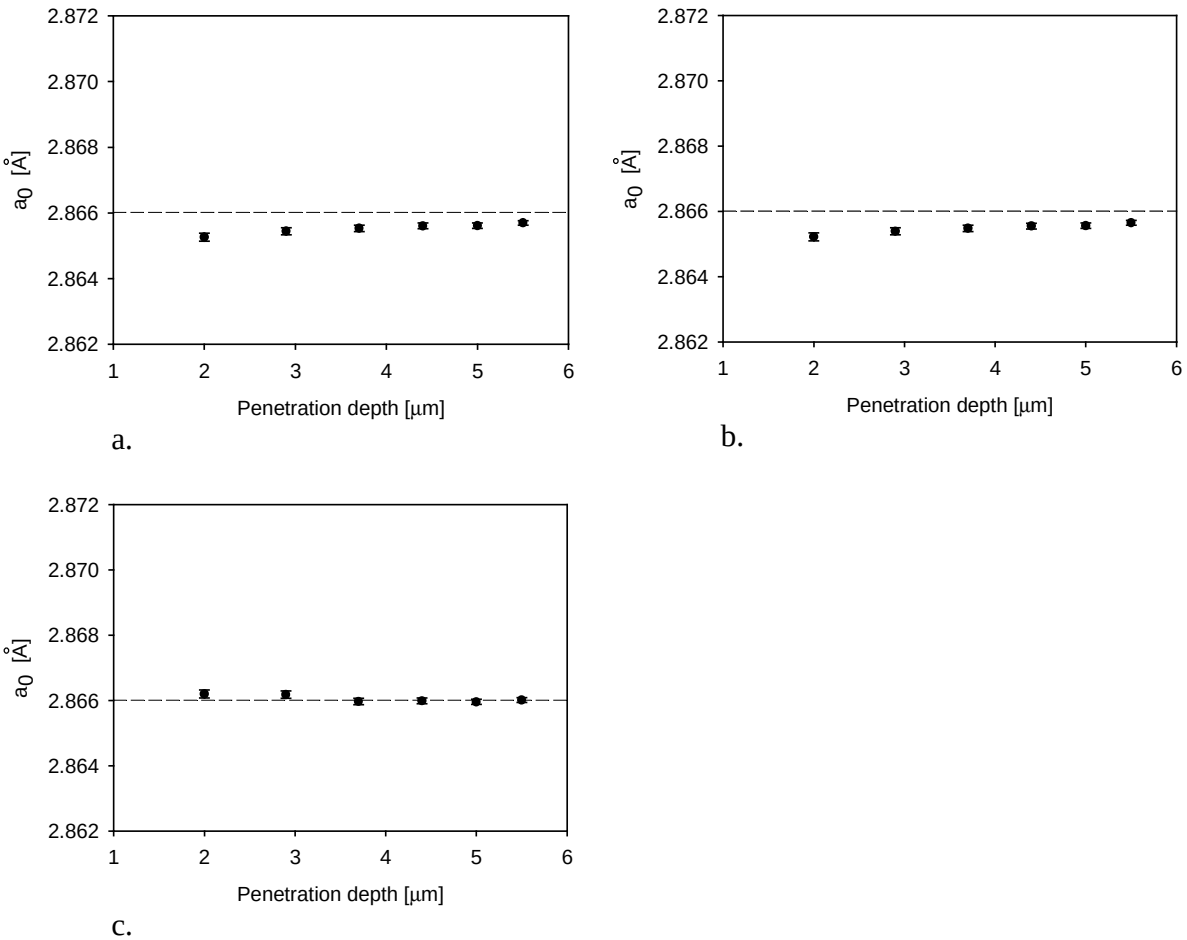

Fig. 5.18. *Stress-free equivalent lattice parameter a_0 (multi-reflection method, Co radiation) versus penetration depth z for the ferrite powder sample:*
a) without corrections,
b) with absorption, Lorentz-polarization and atomic structure factor corrections,
c) taking into account above corrections and refraction.

It is worth to notice that all corrections decrease the value of stresses (Table 5.2). Corrections for absorption, structure and Lorentz-polarization factor change only slightly the stress values (about 2 MPa). However, when refraction correction is introduced, a significant change of stress values is observed. In powder samples this stress reduction reached even the value of about 90 MPa. In a typical case the refraction correction lowered the stress of about 20 MPa. The resulting final stress value for the powder sample – between 20 and 30 MPa - can be treated as a possible systematic error for all measurements and, in fact, it determines the accuracy of the method.

The applied corrections have also influence on stress-free lattice parameter a_0. For data without corrections a slight change of a_0 is observed - the value of lattice parameter increases with penetration depth (Fig. 5.18a). On the other hand, when corrections are considered, the lattice parameter a_0 is practically constant in the whole range of penetration depth (Fig. 5.18c).

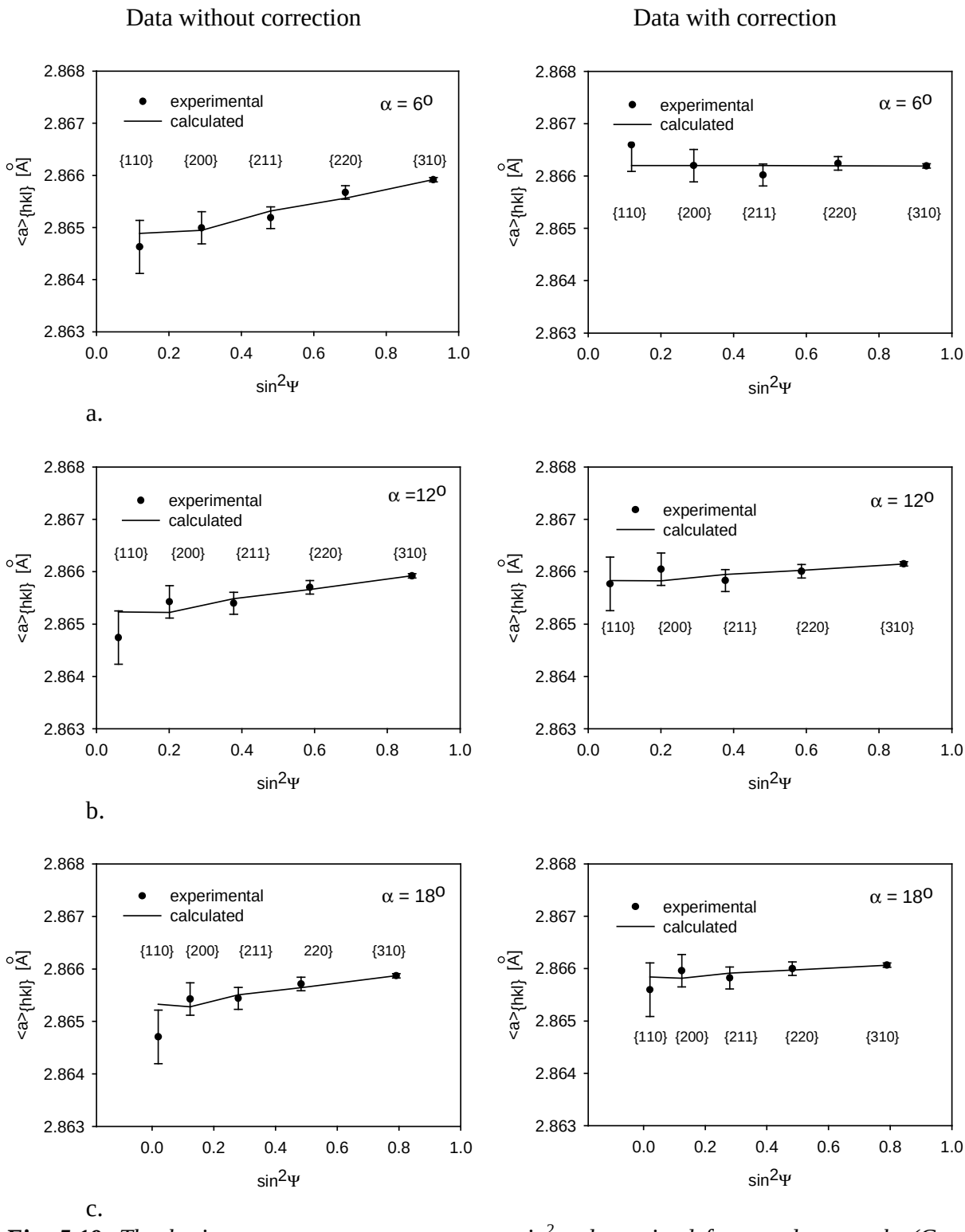

Fig. 5.19. *The lattice parameter $<a>_{\{hkl\}}$ versus $\sin^2\psi$ determined for powder sample (Co radiation). Results for a) $\alpha=6^0$ b) $\alpha=12^0$ and c) $\alpha=18^0$ are shown. Diffraction elastic constants were calculated using the self-consistent model for the interior. On the left - results without corrections, on the right – results with all corrections are shown.*

The dependence of the equivalent lattice parameter $<a>_{\{hkl\}}$ versus $\sin^2\psi$ is shown in Fig. 5.19. The cases with and without corrections are presented. It is easy to observe that graphs after correction are more linear and have lower slope; this results in lower residual stresses, which is a correct tendency for a powder sample.
In conclusion, the applied corrections improve the results; they reduce the value of stresses in powder sample (in theory their value should approach zero). They also give a constant value of a_0 parameter (with a better precision), independently of the penetration depth.

316L stainless steel after grinding treatment

The discussed corrections were applied next to austenite steel samples after grinding. Chemical composition and mechanical properties of the material used for sample preparation are listed in Table 5.3 and Table 5.4. The surface of the sample, produced from the 316L stainless steel, was ground:
in SAMPLE No 1: at the workpiece speed of $v_w = 4$ *m/min*, and the depth of cut equal to $d_c = 4$ μm was applied,
in SAMPLE No 2: at the workpiece speed of $v_w = 1$ *m/min*, and the depth of cut equal to $d_c = 1$ μm was applied.

Table 5.3. *Chemical composition of the studied steels (mass %)*

	C	Si	Mn	P	S	Cu	Ni	Cr	Mo
316L	0.02	0.56	1.67	0.041	0.041	0.35	11.14	17.24	1.96

Table 5.4. *Mechanical properties of the as received materials*

Specimen	0.2% proof stress [MPa]	Ultimate tensile strength [MPa]	E [GPa] Young modulus
316L	200	535	196

The grazing incidence diffraction measurements were performed with X-pert Philips and Seifert X-ray diffractometer using Cu and Fe radiations, respectively. The interplanar spacings were determined for different reflections *hkl* (see Eq. 5.11) and analysed using multi-reflection method. The experiment was repeated for various incidence angles α corresponding to different penetration depths *t* (Table 5.1). To verify the results of the grazing incidence diffraction measurements, also the standard $sin^2\psi$ method was applied using the *311* reflection (Mn radiation). Due to the varying penetration depth with ψ angle in the latter experiment, an approximate average value of penetration depth was estimated (see Table. 5.1).

The alignment of experimental set-up for grazing incidence diffraction geometry was first checked (on the used diffractometer) on a powder sample of ferrite iron. In this case, zero stress should be obtained for each incidence angle α, i.e., for different penetration depths *t*. Application of the corrections leads to a good agreement between two series of measurements (with Cu-radiation and Fe-radiations) – Fig. 5.20. A relatively low value of the measured pseudo-stress in the powder sample ($\sigma_{11}^M = \sigma_{22}^M \approx -25$ MPa) was found independently of the α angle. (Fig.5.20). This value should be treated as a possible systematic error for other measurements.

The variation of the lattice parameter a_0 obtained by the multi-reflection analysis was studied as a function of the penetration depth t (or α), with and without corrections (Fig. 5.20). As expected, after correction the a_0 value does not depend on the depth and it is equal to *2.8663 ± 0.0002 Å*. Like in the case of stress, corrections improve the agreement between results obtained with different radiations.

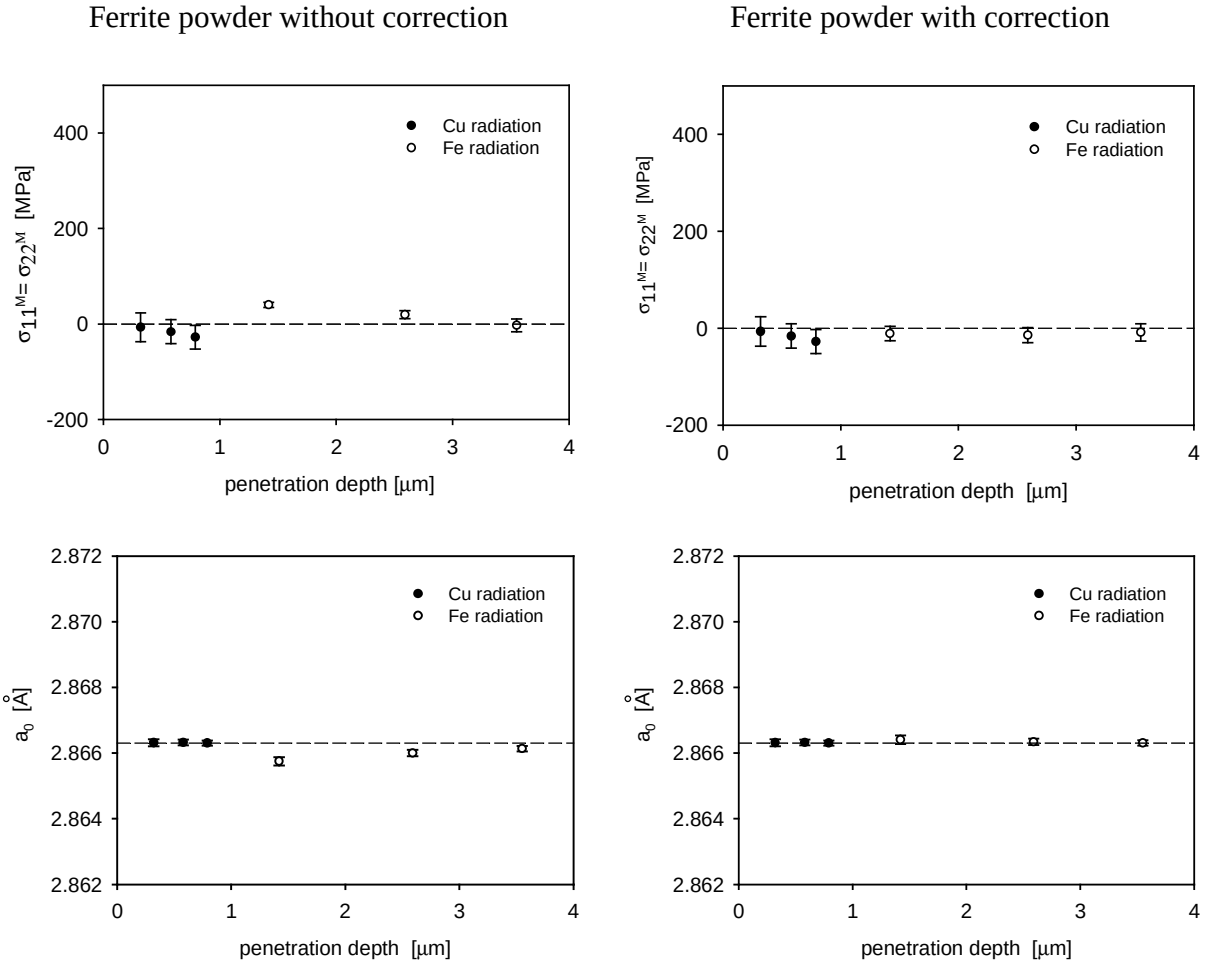

Fig. 5.20. *$\sigma_{11}^{M} = \sigma_{22}^{M}$ and a_0 versus penetration depth for the ferrite powder sample. Cu and Fe radiations and multi-reflection method were used. On the left - results without corrections, on the right- results with corrections are shown.*

For the 316L stainless steel samples studied in the present work two independent diffraction elastic constants ($s_1\{hkl\}$ and $1/2\, s_2\{hkl\}$) were calculated using Voigt, Reuss and the self-consistent models for sample surface and interior (see chapter 1). The calculations were performed using single crystal elastic constants. The surface of the 316L stainless steel was subjected to grinding treatment in one direction. Consequently, the asymmetry of planar stresses (i.e., $\sigma_{11}^{M} \neq \sigma_{22}^{M}$) is expected. The grazing incidence diffraction method was applied using Cu and Fe radiations. Exemplary results of analysis for the ground steel are shown in Table 5.5 and in Figs. 5.21-5.25. The best quality of fitting (small value of χ^2) was found for the self-consistent approach of free surface, and slightly worse results were obtained for the Reuss and self-consistent (interior) models. The worst fitting quality appears for the Voigt model.

Table. 5.5. Components of macroscopic residual stress σ^{M}_{11} and σ^{M}_{22} (MPa) for 316L samples. Reuss, Voigt and self-consistent models were used for calculation of diffraction elastic constants. χ^2 is also listed.

Penetration depth, incidence angle	Analysis with correction	Stress σ^{M}_{ij} [MPa], χ^2	Results of fitting assuming $\sigma^{M}_{33}=0$			
			Voigt	self-cons. (interior)	self-cons. (free surface)	Reuss
0.32 μm $\alpha=5^0$ (Cu - radiation)	Yes	σ^{M}_{11} σ^{M}_{22} χ^2	1341±154 322±151 96.07	1159±63 263±62 23.36	999±36 167±35 11.34	912±45 181±43 19.79
	No	σ^{M}_{11} σ^{M}_{22} χ^2	1368±149 356±146 90.51	1180±59 289±58 20.51	1014±36 187±35 11.04	926±45 200±44 20.37
0.79 μm $\alpha=15^0$ (Cu – radiation)	Yes	σ^{M}_{11} σ^{M}_{22} χ^2	1357±210 480±206 148.18	1175±126 402±123 74.7	1044±67 316±66 29.21	932±80 299±78 48.78
	No	σ^{M}_{11} σ^{M}_{22} χ^2	1359±208 487±203 144.32	1177±124 407±121 71.95	1045±65 320±64 27.93	933±79 303±77 47.1
0.88 μm $\alpha=3^0$ (Fe – radiation)	Yes	σ^{M}_{11} σ^{M}_{22} χ^2	1191±241 378±240 139.97	1128±107 300±107 34.93	980±67 152±67 20.41	931±93 159±91 40.29
	No	σ^{M}_{11} σ^{M}_{22} χ^2	1290±240 480±239 138.68	1213±109 387±109 36	1041±81 217±80 29.09	990±104 221±103 50.91
1.42 μm $\alpha=5^0$ (Fe - radiation)	Yes	σ^{M}_{11} σ^{M}_{22} χ^2	1219±235 466±232 133.9	1147±109 376±108 37.21	991±65 216±65 19.77	941±83 218±82 34.22
	No	σ^{M}_{11} σ^{M}_{22} χ^2	1287±234 538±231 132.73	1206±109 438±108 36.97	1034±73 263±72 24.62	983±90 263±89 39.9
2.59 μm $\alpha=10^0$ (Fe – radiation)	Yes	σ^{M}_{11} σ^{M}_{22} χ^2	1155±231 582±230 128.1	1064±128 465±127 53.53	915±73 299±72 26.25	855±77 278±76 32.67
	No	σ^{M}_{11} σ^{M}_{22} χ^2	1197±230 627±229 127.49	1097±128 502±127 53.73	939±76.8 327±76.3 29.31	878±81 304±81 36.5
4.32 μm $\alpha=20^0$ (Fe - radiation)	Yes	σ^{M}_{11} σ^{M}_{22} χ^2	1205±190 813±190 71.75	1031±79 616±78 19.46	849±52 414±52 13.21	759±58 349±58 20.32
	No	σ^{M}_{11} σ^{M}_{22} χ^2	1201±190 814±189 71.63	1026±82 616±82 21.03	845±54 415±54 14.36	753±62 348±62 22.83

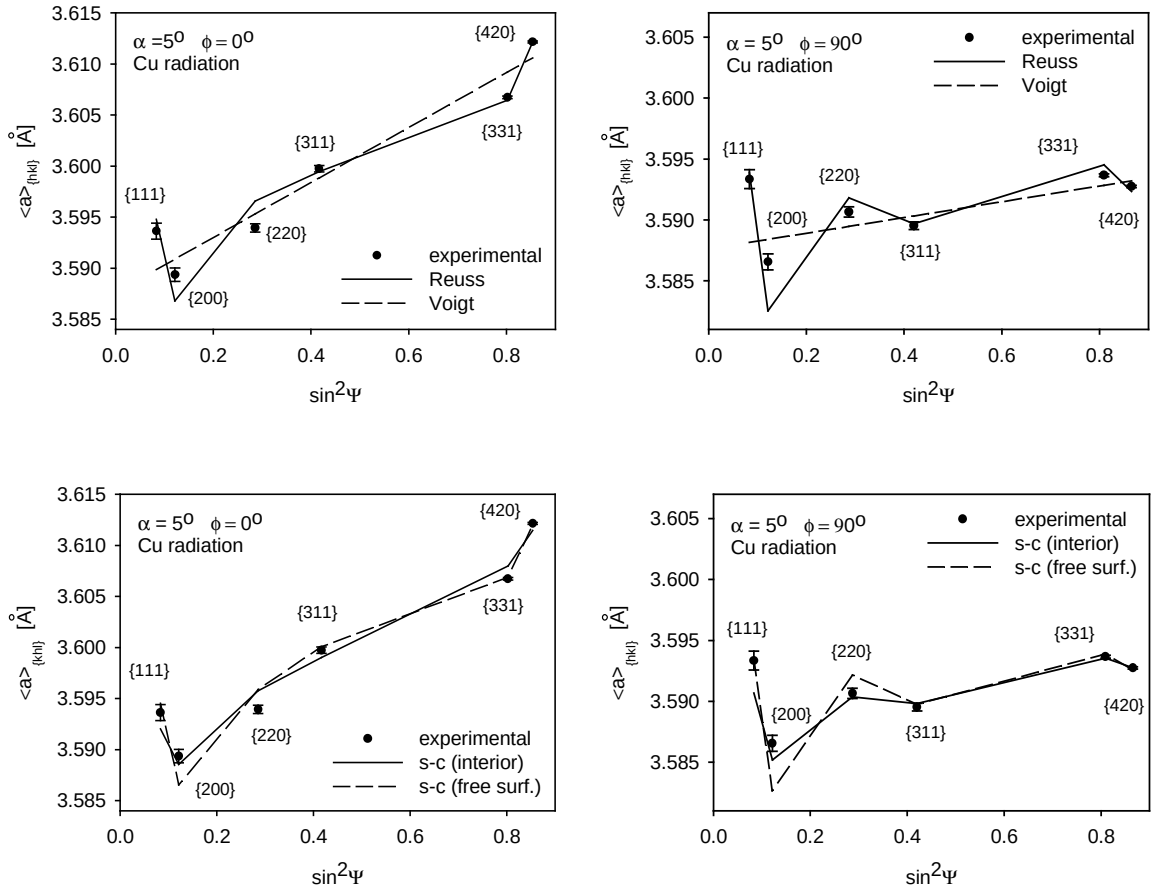

Fig. 5.21. *Measured $\langle a(\psi,\phi)\rangle_{\{hkl\}}$ lattice parameters and fitted theoretical curves for the 316L sample after grinding (Cu radiation and $\alpha=5^0$). Corrections were applied to all experimental points. Different models were used for the calculation of diffraction elastic constants.*

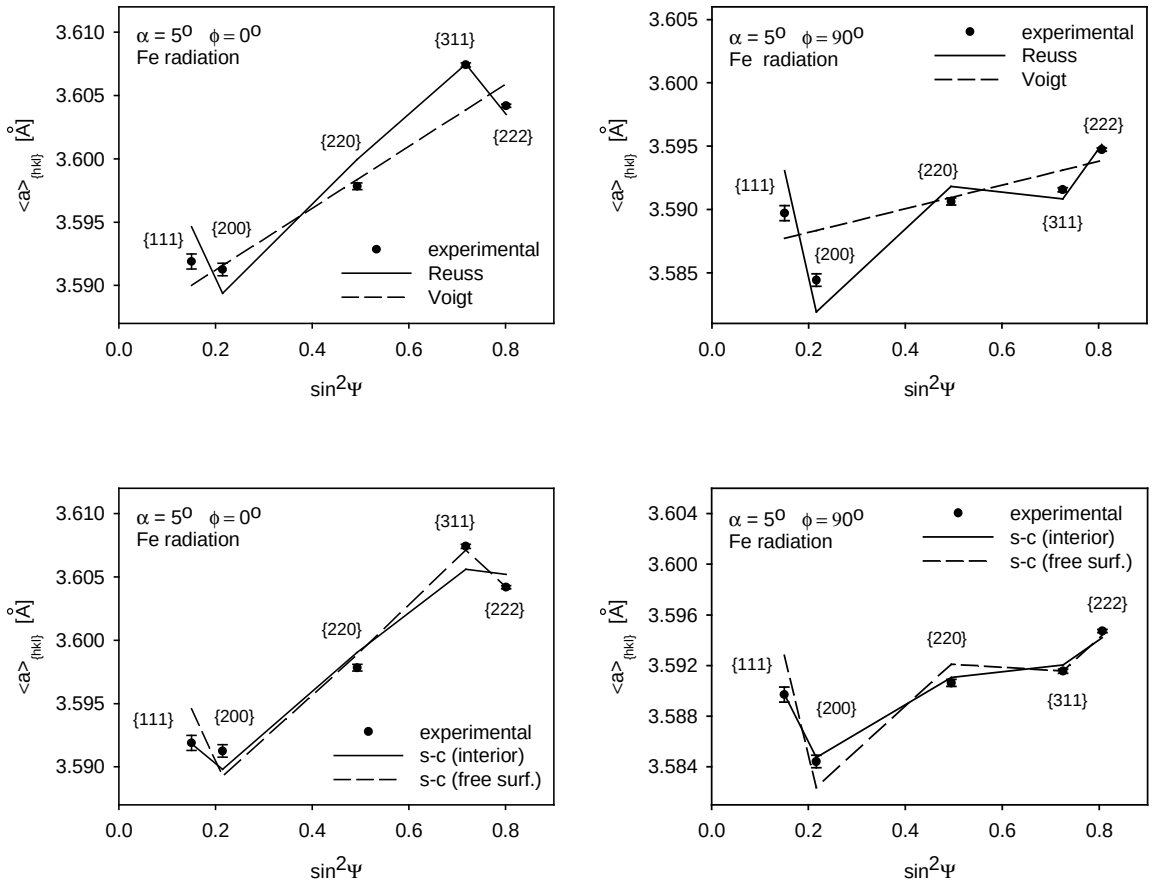

Fig. 5.22. *Measured <a(ψ,ϕ)>{hkl} lattice parameters and theoretical curves fitted to them for the 316L sample after grinding (Fe radiation and α=5⁰). Corrections were applied to all experimental points. Different models were used for the calculation of diffraction elastic constants.*

Generally, we can conclude that reasonably good fits to experimental data are obtained with Reuss and self-consistent models (especially free surface version). In contrast to them, Voigt model predictions do not describe sufficiently well a character of the observed relations.

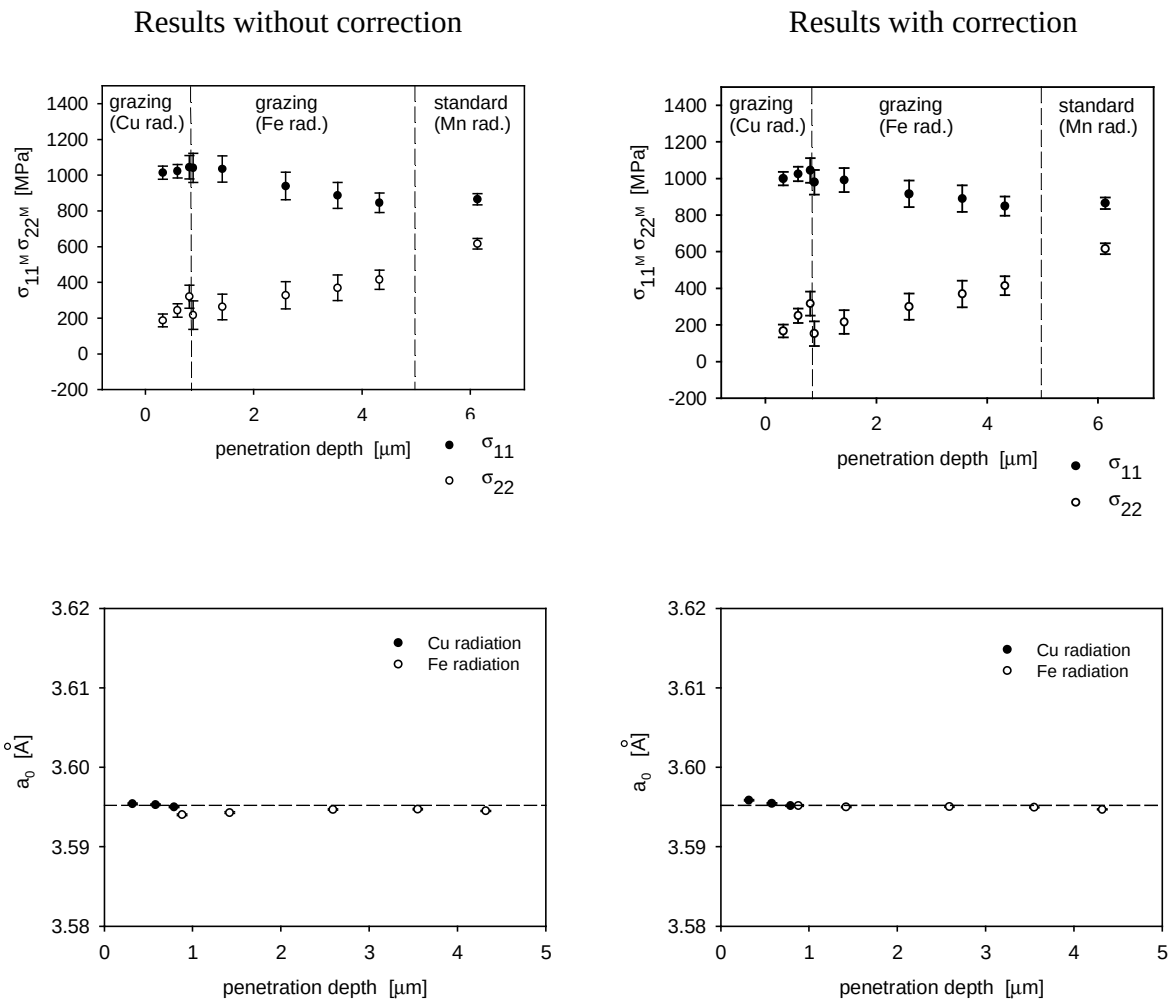

Fig.5.23. *Stress components (σ_{11}^M and σ_{22}^M) and stress-free equivalent lattice parameter a_0 versus penetration depth for the ground sample (SAMPLE 1). The self-consistent model for free surface was used to calculate the diffraction elastic constants. On the left - results without corrections, on the right – with corrections.*

The values of σ_{11}^M and σ_{22}^M stress components in function of penetration depth are shown for SAMPLE 1 in Fig. 5.23. A very good quality of fitting and small uncertainty of the determined stresses suggest that the self-consistent approach for sample surface gives the best estimation of residual stresses (quite similar values were obtained with the Reuss model). It should be noted that good continuity of the measured stresses versus depth was obtained using the grazing incidence diffraction with Cu and Fe radiations. The experiment by means of standard diffraction method (using Mn radiation and *311* reflection) confirmed change of stresses in function depth. As for the previously studied samples, the stress- free parameter a_0 is almost constant versus penetration depth ($a_0 = 3.5951 \pm 0.0009$ *Å*, see Fig. 5.23).

Figure 5.24 shows the results for the sample similar to the previous one, but with different technological parameters (SAMPLE 2). Just like previously, when corrections are applied - a better agreement between three experiments with different radiations is observed (Fig. 5.24)

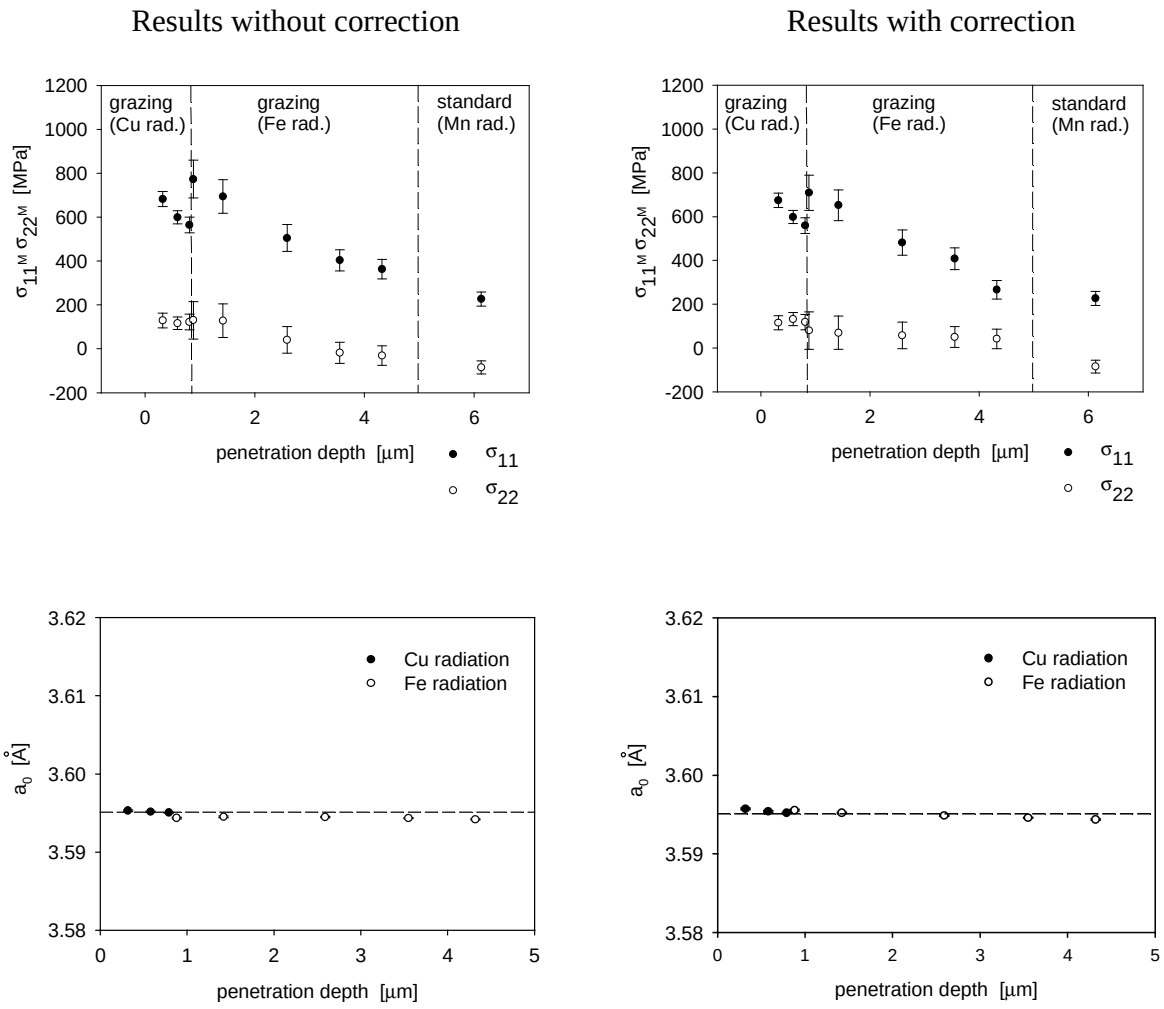

Fig.5.24. *Stress components (σ_{11}^{M} and σ_{22}^{M}) and stress-free equivalent lattice parameter a_0 versus penetration depth for the ground sample (SAMPLE 2). The self-consistent model for free surface was used to calculate the diffraction elastic constants. On the left - results without corrections, on the right - with corrections.*

5.5. Conclusions

Asymmetric geometry is applied in the grazing incidence diffraction method. Penetration depth of radiation is almost constant during experiment and it can be easily changed by an appropriate selection of incidence angle or by using different type of radiation. Variation of penetration depth enables investigation of materials with stress gradient. Classical $\sin^2\psi$ method cannot be applied for this purpose, because penetration depth is not constant during experiment.

Refraction of EM-wave (with refraction coefficient smaller than one) causes two effects: it changes the wavelength and the direction of the beam inside a sample. The two effects change the 2θ angle and shift the pick position. This shift has to be considered in data treatment. For small incidence angles ($\alpha \leq 10^0$) the corrections are significant and can modify the resulting stress even of 70 MPa. The refraction correction decreases with growing incidence angle. Other corrections (absorption, atomic factor, Lorentz-polarization factor) are less important for final stress values.

General conclusions

The stress field in polycrystalline materials was examined and described. The first and second residual stresses were studied in polycrystalline single and multi-phase materials. Strict formulae describing effects of the first and the second order stresses on interplanar spacings (or equivalent lattice parameter) were derived. The aim of this work is to propose a methodology of residual stress study using diffraction methods, theoretical approaches and modelling. This enables to analyse and better understand the mechanical behaviour of polycrystalline materials. Two methods of internal stresses determination were described and used (classical method and multi-reflection one).

A new grazing angle incident diffraction X-ray diffraction technique was developed in order to analyse the residual stress gradient. Using this method, it is possible to perform a non-destructive analysis of the heterogeneous stress for different (and well defined) volumes below the sample surface. Moreover, the stress can be measured at very small depths, of the order of a few micrometers. Uncertainty of measurement was considered; the influence of absorption, Lorentz-polarization, atomic scattering factor and refractive index was studied. By means of powder references sample the importance of all factors responsible for the peak position was examined and taken into account. The performed analysis confirmed a small influence of absorption, Lorentz-polarization and atomic scattering factor on the results of stress determination. Contrary to them, the refraction index was found very significant, especially for small incident angles. For the incidence angles $\alpha \leq 10^0$ the corrections are important and they can modify the resulting stress significantly (even of 70 MPa in powder). The refraction correction decreases with growing incidence angle.

The self-consistent and Lefers-Wierzbanowski models of elasto-plastic deformation were developed and used for the study of sample properties and the stress evolution. The presented models of elasto-plastic deformation (LW and SC) are useful tools for the study of mechanical properties of polycrystalline materials. They enable the prediction of macroscopic material properties (e.g., texture, stress-strain curves, plastic flow surfaces, dislocation density, final state of residual stress, etc.), basing on the micro-structural characteristics (crystallography of slip systems, hardening law, initial texture, initial residual stress state, etc.). The presented models predict mechanical properties of materials in particular, rolling textures were correctly predicted for materials with cubic and hexagonal crystal structure. Such models are convenient tools for technologists searching for optimal material properties.

The residual stresses were examined in corss-rolled polycrystalline copper and steel. The stress variation in function of deromation in corss rolling direction as well as resulting textures were explained using LW and SC models.

The new multi-reflection method for stress determination was applied to analyse the experimental data for duplex stainless steel. The main advantage of this method is that experimental data obtained for various *hkl* reflections are treated simultaneously. The significant values of the phase stresses were found in both phases of duplex steel. During elasto-plastic deformation the evolution of phase stresses and generation of the second order incompatibility stresses were observed. The influence of elastic anisotropy and crystallographic texture on the creation of the second order incompatibility stresses was also studied. Using the methodology developed in this work, the first and the second order stresses were quantitatively determined for each phase. It has been shown that experimentally determined lattice strains could be successfully correlated with the theoretical results only when the influence of the second order stresses is taken into account. Moreover, our results confirm that the best quality of fit between experimentally determined lattice strains and theoretical predictions is obtained when anisotropic elastic constants and real initial sample texture are taken into account.

The described experimental methods combined with deformation models present useful tools for evaluation of the stress fields in polycrystalline materials, hence for the investigation of new materials for technology.

APPENDIX A

Lorentz-Polarization Factor

The Lorentz factor is a collection of trigonometric terms that describes the dependence of the diffracted intensity on the diffraction angle. There are three factors that contribute to Lorentz factor:

- The number of grains, which are, oriented such that they can diffract at a given angle 2θ.
- The diffracted intensity per unit length of the diffraction cone.
- The dependence of diffracted intensity from any one crystalline 2θ.

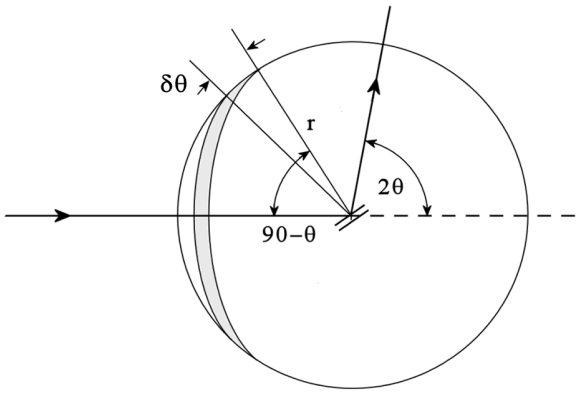

Fig. A.1. *Cone of reflected rays.*

The first factor is dependent on the volume fraction of grains oriented such that they can diffract at very near the particular Bragg angle. Even if a completely random distribution of grain orientations is assumed, this volume fraction is not the same for all orientations of the incident beam. Assume that a sphere of radius r is drawn around a powder sample (Fig. A.1). If the angular range around the Bragg angle into which appreciable intensity is diffracted is δθ, then the normals to the planes that can diffract will intersect the sphere within a band of width r·δθ, with an area of δθ·2π·r·[sin(90-θ].

The fraction of the crystallites is the ratio of this area to the total area of the sphere $4\pi r^2$:

$$\frac{\Delta N}{N} = \frac{r\delta\theta 2\pi r \sin(90-\theta)}{4\pi r^2} \cong \frac{\delta\theta \cos\theta}{2} \qquad \text{(A.1)}$$

Thus the fraction of diffracting particles is proportional to

$$c_1 = \cos\theta \qquad \text{(A.2)}$$

and is small for large θ.

The second factor, intensity per unit length of the diffraction cone, is important because, as discussed before, in normal X-ray work only small segment of the intersection of the diffraction cone with the detection plane is used in measuring intensities. However, since the radius of each cone is different, the diffracted intensity into each unit length of the cone circumference is different. If the radius of the diffractometer is R, the radius of the circumference of any diffraction cone is $2\pi R\sin 2\theta$. Thus, the diffracted intensity per unit length is proportional to:

$$c_2 = \frac{1}{\sin 2\theta} \qquad \text{(A.3)}$$

The third factor describes the variation of intensity with 2θ, when all other factor are constant. It was previously shown that, when deviations from ideality occur in the wavelength distribution of the X-ray beam, or in the degree of perfection of the crystal, appreciable X-ray intensity is observed at angles $\delta\theta$ away from the Bragg angle θ_B, resulting in the broadening of the X-ray peak. Maximum intensity on the other hand, occurs at θ_B. Thus, diffracted intensity is a function of θ.

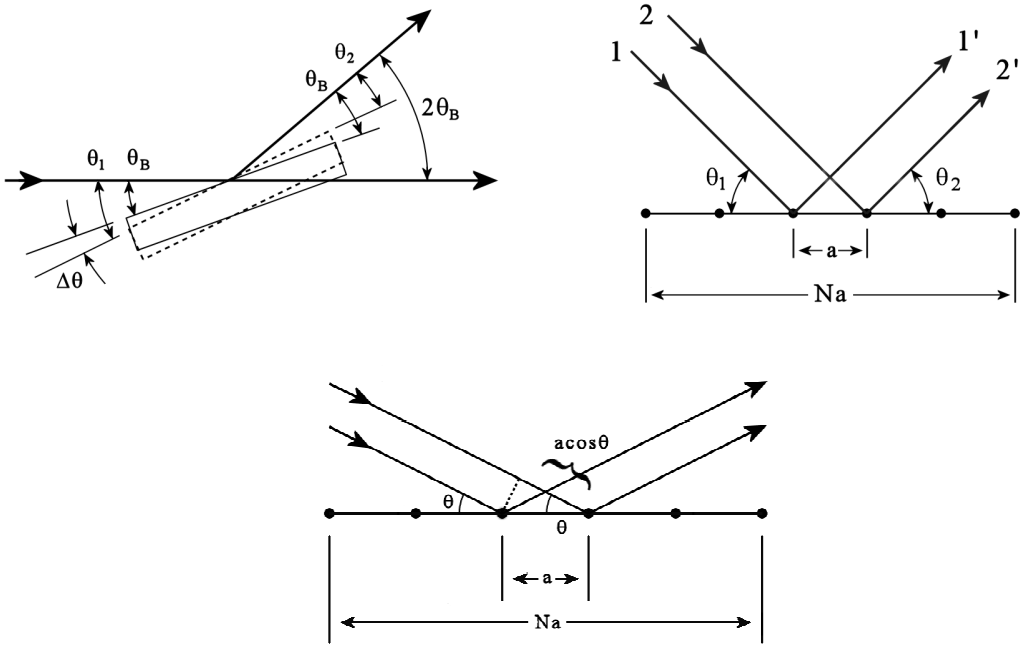

Fig. A.2. *Scattering in fixed direction during crystal rotation.*

Consider a plane containing N atoms which is rotated an angle δθ for θ (Fig. A.2). In this case the angles that the incident and diffracted beams make with the plane are θ_1 and θ_2. The path difference between the rays scattered by the two atoms on the plane is:

$$\Delta = a\cos\theta_2 - a\cos\theta_1 = a\left[\cos\left(\theta_B - \Delta\theta\right) - \cos\left(\theta_B + \Delta\theta\right)\right] \tag{A.4}$$

which can be expressed as:

$$\Delta = 2a\delta\theta\sin\theta_B \tag{A.5}$$

where, since δθ is small, sinδθ≅δθ. The path difference between the rays diffracted from the first and the N-th atom on the plane is

$$N\cdot\delta\theta = N\cdot 2a\cdot\delta\theta\cdot\sin\theta_B \tag{A.6}$$

If this difference is equal to an integral multiple of the wavelength, the diffracted intensity is zero. Thus, the maximum rotation of any crystallite from the Bragg position is

$$\begin{aligned} N\cdot 2a\cdot\delta\theta\cdot\sin\theta_B &= \lambda \\ \delta\theta &= \frac{\lambda}{2Na\sin\theta} \end{aligned} \tag{A.7}$$

Finally the diffracted intensity varies as a function of 1/sinθ:

$$c_3 = \frac{1}{\sin\theta} \tag{A.8}$$

All the trigonometric terms discussed above (Eqs. A.2, A.3, A.8) can be combined to form a single factor, which describes the variation of intensity with angle θ. This factor is so-called the Lorentz factor, and is given by:

$$L.F = K\frac{1}{\sin^2\theta} \tag{A.9}$$

where K is constant.

Although x-rays are scattered in all directions by an electron, the intensity of scattered beam depends on the angle of scattering. According J. J. Thomson theory the intensity I of the beam scattered by single electron of charge e and mass m, at the distance r from the electron is given by

$$I = I_0\frac{e^4}{r^2m^2c^4}\sin^2\alpha \tag{A.10}$$

where α is the angle between electric field of the incident wave and OP direction (Fig. A.3.) Suppose the incident beam is travelling in the direction Ox (Fig. A.3.) and encounters an election in O. We want know the scattered intensity at P in the xz plane where OP is inclined at scattering angle of 2θ to the incident beam.

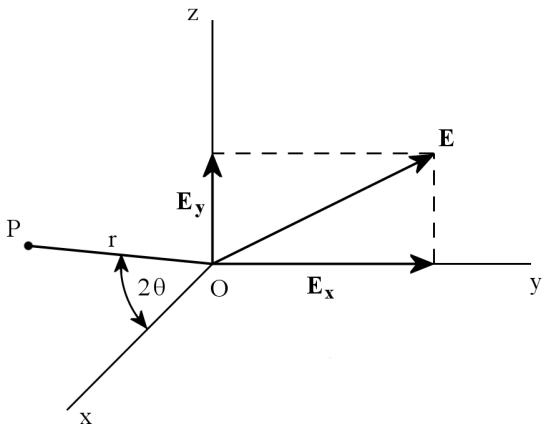

Fig. A.3*. Scattering of X-rays by a single electron.*

An unpolarized incident beam has electric vector E in a random direction in *yz* plane:

$$E_y^{\ 2} = E_z^{\ 2} = \frac{1}{2}E^2 \qquad \text{(A.11)}$$

The ratio of incident intensity at O to the scattered intensity at P is equal to the ration of the squares of the amplitude of the electric field ($I \sim E^2$).

$$I_{0y} = I_{0z} = \frac{1}{2}I_0 \qquad \text{(A.12)}$$

The *y* component of the incident beam accelerates the electron in the direction Oy. It therefore gives rise to a scattered beam whose intensity at P is found from equation A.10.:

$$I_{Py} = I_{0y}\frac{e^4}{r^2m^2c^4} \qquad \text{(A.13)}$$

It should by noted that angle α (*yOP)* equals $\pi/2$

Similarly, the intensity of the scattered *z* component is given by:

$$I_{Pz} = I_{0z}\frac{e^4}{r^2m^2c^4}\cos^2 2\theta \qquad \text{(A.14)}$$

since $\alpha = \pi/2 - 2\theta$.

The total scattered intensity at P is obtain by summing the intensities of two components:

$$I_P = I_{Py} + I_{Pz} \tag{A.15}$$

Finally we obtain:

$$I_P = I_0 \frac{e^4}{r^2 m^2 c^4} \left(\frac{1 + \cos^2 2\theta}{2} \right) \tag{A.16}$$

The Lorentz factor and the polarization factor are usually combined together to form the L-P (Lorentz-Polarization) factor:

$$(L.P.) = \frac{1 + \cos^2 \theta}{\sin^2 \theta} \tag{A.17}$$

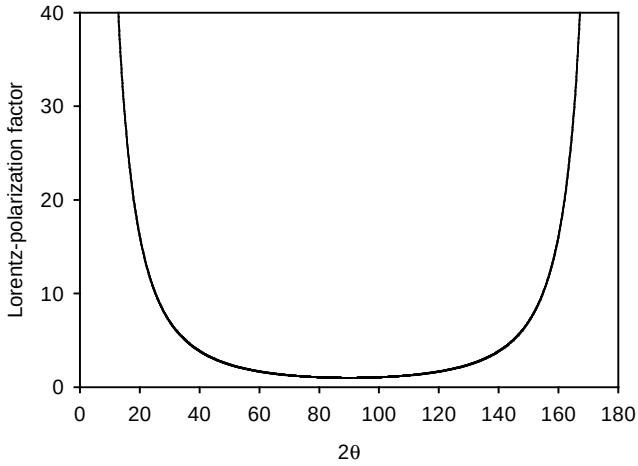

Fig. A.4. Lorentz-Polarization factor versus 2θ for ferrite steel.

The Lorentz – polarization factor is shown in Fig. A.4. Like for absorption this correction is significant for small and high angles 2θ.

List of author's publication

Wierzbanowski, K., **Wroński, S.**, Baczmański, A., Wróbel, M., Fitzpatrick, M., Braham, C. and Lodini, A., 2007a, Variation of Residual Stresses during Cross-Rolling, Journal of Neutron Research, **15**, – in print

Dakhlaoui, R., **Wroński, S.**, Braham, C., Baczmański A. and Wierzbanowski, K., 2007b, Influence of nitrogen content and residual stresses on mechanical properties of duplex stainless steels studied by X-ray and neutron diffraction, Journal of Neutron Research, **15**, – in print

Wroński, S., Baczmański, A., Dakhlaoui, R., Braham, C., Wierzbanowski K. and Oliver, E.C., 2006a, Determination of Stress Field in Textured Duplex Steel Using TOF Neutron Diffraction Method, Acta Materialia, doi:10.1016/j.actamat2007.07.044.

Wroński, **S.**, Baczmański, A., Wierzbanowski, K., Braham, C., Dakhlaoui, R. and Oliver, E.C., 2006b, Quantitative Estimation of the Second Order Plastic Incompatibility Stresses in Textured Duplex Steel, Materials Science Forum, **524-525**, 841-846

Dakhlaoui, R., Baczmański, A., Braham, C., **Wroński, S.**, Wierzbanowski, K. and Oliver, E.C., 2006c, Effect of residual stresses on individual phase mechanical properties of austeno-ferritic duplex stainless steel, Acta Materialia, **54**, 5027-5039

Wierzbanowski, K., **Wroński, S.**, Baczmański, A., Wróbel, M., Braham, C., Fitzpatrick, M. and Lodini, A., 2006d, Residual Stresses Induced by Cross-Rolling, Materials Science Forum, **524-525**, 63-68

Dakhlaoui, R., Braham, C., Baczmański, A., **Wroński, S.**, Wierzbanowski, K. and Oliver, E.C., 2006e, Effect of residual stresses on mechanical properties of duplex stainless steel studied by diffraction and self-consistent modelling, Materials Science Forum, **524-525**, 185-190

Wierzbanowski, K., Baczmański, A., **Wroński, S.**, Braham, C. and Lodini, A., 2005, "Tuning" of deformation models by residual stress measurements, Archives of Metallurgy and Materials, **50**, 457-464

Wroński, **S.**, Wierzbanowski, K., Baczmański, A., Braham, C. and Lodini, A., 2004, Verification of Inter-Granular Interaction in Deformation Models by Residual Stress Measurements, Journal of Neutron Research, **12**, 9-14

Participation in conferences

Wroński, S., Baczmański, A., Wierzbanowski, K., Braham, C., Dakhlaoui, R. and Oliver, E.C., 2006, Quantitative Estimation of the Second Order Plastic Incompatibility Stresses in Textured Duplex Steel, 7-th European Conf. on Residual Stresses (ECRS7), Berlin (2006); published in: Materials Science Forum, **524-525**, 841-846

Wierzbanowski, K., **Wroński, S.**, Baczmański, A., Wróbel, M., Braham, C., Fitzpatrick, M., and Lodini, A., 2006, Residual Stresses Induced by Cross-Rolling, 7-th European Conf. on Residual Stresses (ECRS7), Berlin; published in: Materials Science Forum, **524-525**, 63-68

Dakhlaoui, R., Braham, C., Baczmanski, A., **Wronski, S.**, Wierzbanowski, K. and Oliver, E.C., 2006, Effect of residual stresses on mechanical properties of duplex stainless steel studied by diffraction and self-consistent modelling, 7-th European Conf. on Residual Stresses (ECRS7), Berlin; published in: Materials Science Forum, **524-525**, 185-190

Wierzbanowski, K., **Wroński, S.**, Baczmański, A., Wróbel, M., Fitzpatrick, M., Braham, C. and Lodini, A., 2005, Variation of Residual Stresses during Cross-Rolling, Abstracts of the Conference on Stress Evaluation MECA SENS III, p.104, Los Alamos National Laboratory, Santa Fe, New Mexico, USA

Dakhlaoui, R., **Wroński, S.**, Braham, C., Baczmański, A. and Wierzbanowski, K., 2005, Influence of nitrogen content and residual stresses on mechanical properties of duplex stainless steels studied by X-ray and neutron diffraction, Abstracts of the Conference on Stress Evaluation MECA SENS III, p.17, Los Alamos National Laboratory, Santa Fe, New Mexico, USA

Wierzbanowski, K., Baczmański, A., **Wroński, S.**, Braham, C. and Lodini, A., 2004, "Tuning" of deformation models by residual stress measurements, Abstracts of Symp. on Texture and Microstructure Analysis of Functionally Graded Materials (SOTAMA-FGM), p. 61, Kraków, Poland

Wroński, S., Wierzbanowski, K., Baczmański, A. and Braham, C., 2003, Estimation of interaction level in deformation models by residual stress measurements, Abstracts of the 2-nd Int. Conf. on Stress Evaluation MECA SENS II, p. 76, Manchester, U.K.

References

Allen, A.J., Hutchings, M.T.,Windsor, C.G and Andreani,C., 1985, Adv. Phisics, **34**, 445.

Baczmański, A., Wierzbanowski, K., Haije, W.G., Helmholdt, R.B., Ekambaranathan, G. and Pathiraj, B., 1993, Cryst. Res. Technol., **28**, 229.

Baczmański, A., Wierzbanowski, K., Lipiński, P., 1994a, Materials Science Forum, **157-162**, 2051- 2058.

Baczmański, A., Wierzbanowski, K., Lipiński, P., Helmholdt, R.B., Ekambaranathan, G., Pathiraj, B., 1994b, Examination of the residual stress field in plastically deformed polycrystalline material, Phil. Mag., A, **69**, 437- 449

Baczmański, A., Wierzbanowski, K., Tarasiuk, J., 1995, Models of Plastic Deformation Used for Internal Stress Measurements, Zeit. Metallk., **86**, 507-511

Baczmański, A., Wierzbanowski, K., Tarasiuk, J., and Lodini, A., 1997a, *Arch. Metall.*, **42**, 173.

Baczmański, A., Wierzbanowski, K., Tarasiuk, J., Ceretti, M. and Lodini, A., 1997b, Rev. de Metall., **42**, 1467.

Baczmański, A., Zattarin P., Lipiński P. and Wierzbanowski K., 2000, Different methods of slip system selection used in plastic deformation models, In: Proc. of Int. Conf. JSTMM 2000, Tunis, Tunisie 2000. pp. 33.1-33.7.

Baczmański, A., Skrzypek, S.J., Braham, C., Seiler, W. and Wierzbanowski, K., 2003a, *Arch. Metall.*,**48,** 137.

Baczmański, A., Skrzypek, S.J., Braham, C., Wierzbanowski, K. and Seiler, W. 2003b, *Rev. de Metall.*, **99** , 843.

Baczmański, A., Braham, C., and Seiller, W., 2003c, Microstresses in textured polycrystals studied by the multireflection diffraction method and self-consistent model, Phil. Mag., **83**, 3225-3246

Baczmański, A., Braham, C., Seiler, W. and Shiraki, N. 2004, *Surface and Coat. Technology*, **182** , 43.

Baczmański, A,. 2005, Habilitation Thesis, Faculty of Physics and Applied Computer Sciences, AGH UST, Kraków, Poland.

Baczmański,A., Wierzbanowski,K., Benmarouane,A., Lodini,A., Lipiński,P. and Bacroix, B., 2007, Stored energy and recrystallization process, Materials Science Forum **539-534**, 3335

Barral, M., Lebrum, J.L., Sprauel, J.M. and Maeder,G., 1987, *X-ray Macrostress Determination on Textured Matarial; Use of ODF for Calculating the X-Ray Compliances*, Met. Trans., **18A**, 1229-1238.

Berveiller, M. and Zaoui, A., 1979, J. Mech. Phys. Solids, **26**, 325.

Bochnowski, W., Leitner H., Major, Ł., Ebner R. and Major B., 2003, Mat. Chem. and Phys., **81**, 503.

Bojarski, Z., Bołd, T., 1970, *Rentgenograficzne metody wyznaczania zniekształceń sieciowych i wielkości bloków materiałów polikrystalicznych*, Prace Inst. Hut., **22**, 115-127

Bojarski, Z., Łągiewka, E., 1995, *Rentgenowska analiza strukturalna*, Skrypt UŚ 510, Wydawnictwo Uniwersytetu Ślaskiego, Katowice, Poland.

Brakman, C.M., 1987 . Phil. Mag. *A*, **55,** 39.

Bunge, J., H., 1982, Texture analysis in materials science: Mathematical Methods. Butterworths, London.

Ceretti, M., 1993, *Ph.D. Thesis*, Universite de Reims Champagne-Ardenne, France

Clyne, T.W. and Withers, P.J., 1993, *An introduction to Metal Matrix Composites*. Cambridge Solid State Science Series. Cambridge: Cambridge University Press.

Cullity, B. D. 1956, *Elements of X-ray Diffraction*, Addison-Wesley, Massachusetts.

Cullity, B.D., 1978, *Elements of X-ray Diffraction*, 2rd ed. Massachussetts: Addison-Wesley.

Dakhlaoui, R., Baczmański, A., Braham, C., Wroński, S., Wierzbanowski, K. and Oliver, EC., 2006, *Effect of residual stresses on individual phase mechanical properties of austeno-ferritic duplex stainless steel*, **54**, 5027. Acta Mater.

Dakhlaoui, R., Baczmański, A., Braham, C., Wroński, S., Wierzbanowski, K. and Oliver, EC., 2007, *Influence of nitrogen content and residual stresses on mechanical properties of duplex stainless steels studied by X-ray and neutron diffraction*, Journal of Neutron Research, **15**,

Daymond M.R. and Priesmeyer H.G., 2002, *Acta Mater.* **50**, 1613.

Dann, JA., Daymond, MR., James, JAJ., Santisteban, JR., Edwards, L., 2003, *ENGIN-X: a new diffractometer optimised for stress measurement*, in Proc. ICANS XVI, vol. 1, ISSN 1433-559X, pp. 231.

Dölle, H. 1979, *The influence of multiaxial stress states, stress gradients and elastic anisotrophy on the evaluation of residual stresses by X-ray*, Appl. Cryst., **12**, 489-501.

Ely, T., Predecki, P., K., Zhu, X., Etaough, M., Goehner, R., 1997, *Advance in X-Ray Analysis*, **39**, 381-389.

Eshelby, J.D., 1957, *The Determination of the Elastic Field of an Ellipsoidal Inclusion and Related Problems*, Proc. Roy. Soc. London, **A241**, 376.

Fitzpatrick, M.E., 1995, *Ph.D. Thesis*, University of Cambridge, UK.

Fitzpatrick, M.E., Lodini, A., 2003, *Analysis of Residual Stress Using Neutron and Synchrotron Radiation.* Taylor & Francis, London.

Franciosi, P., Berveiller, M, and Zaoui, A., 1980, *Latent Hardening in Copper and Aluminium Single Crystals*, Acta Met., **28**, 273.

Gloaugen, D., 2001, *Ph.D. Thesis*, Universite de Nantes, France.

Guinier, A., 1964, *Theorie et Technique de la Radiocrystallographie*, DUNOD, Paris

Hart, M., Bellotto, M. and Lim, G.S., 1988, *The refractive index correction in powder diffraction.* Acta Cryst., A44m 193-197.

Hauk,V., 1986, Adv. X-ray Anal., **29,** 1.

Hill, R., 1965, *Continuum Micro-Mechanics of Elastoplastic Polycrystals*, J. Mech. Phys. Solids, **13**, 89.

Hill, R., 1952, Proc. Phys. Soc., **A65**, 349

Hutchinson, J.W. 1964a, J. Mech. Phys. Solids, **12**, 25.

Hutchinson, J.W., 1964b, J. Mech. Phys. Solids, **12**, 11.

James, R.W., 1962, *The Optical Principles of the Diffraction of X-Rays*, G. Bell and Son, London.

Kraus, I., Ganev, N., 1998, *X-ray Diffraction Analysis of Non-uniform Stress Fields*, Acta Politechnica, **38**, 25.

Kröner, E., 1961, *Zur plastischen Verformung des Vielkristalls*, Acta Met., **9**, 155.

Kröner, E., 1958, Zeit. Phys., **151**, 504

Larson, A., Von Dreele, RB., 1994, *GSAS – general structure analysis system. Technical Report LA-UR-86-748*, Los Alamos National Laboratory.

Leffers, T., 1968a, *Phys. Stat. Sol.*, **25**, 337.

Leffers, T., 1968b, Scripta Met., **1**, 1121.

Leffers, T., 1975, Risö Report No **302**, Danish Atomic Energy Comission, Risö.

Lin, T.H., 1957, *Analysis of Elastic and Plastic Strains of a FCC Crystal*, J. Mech. Phys.

Lipiński, P. and Berveiller, M., 1989, *Elastoplasticity of micro-inhomogeneous metals at large strains*, *Int. J. of Plasticity*, **5**, 149.

Lipiński, P., 1993, *Modélisation du comportement des métaux, en transformations élasto-plastiques finies, à partir des méthodes de transition d'échelles*. Habilitation, University of Metz.

Meader, G., Lebrun, J.L. and Sprauel, J.M., 1981, *Non Dest. Testing Int*.,**10**, 235.

Mura, T., 1993, *Micromechanics of defects in Solids*, Kluwer Academic Publicher, Dordrecht, Boston, London.

Noyan, I.C., Cohen, J.B. 1987, *Residual Streess - Measurement by Diffraction and Interpretation*, Springer-Verlag, Berlin.

Oleś, A., 1998, *Metody Experymentalne fizyki ciała stałego*, WNT, Warszawa

Parratt, L.G., 1954, *Surface studies of solids by total reflection of X-Rays*. *Phys. Review*, **95**, 2, 359-369.

Pathiraj, B., 1994, Phil. Mag. A, **69**, 437

Pintschovius, L., Hauk, V. and Krug, W.K., 1987, *Mater. Sci. and Eng.* **92**, 1.

Piękoś, K., 2006, *Ph.D. Thesis*, University of Science ant Technology and L'Universite Paris XVIII, Poland.

Philippe, M., J., 1983, *Thèse de doctorat*, Metz.

Philippe, M., J., Serghat, M., Van Houtte, P., and Esling, C., 1995, *Acta metall. Mater*. **43**, pp. 1619-1630. Elsevier Science Ltd.

Rickerby, D.S., Bellamy, B.A. and Jones, A.M. 1987**,** *Surf. Eng*., **3**, 138.

Reid, C. N., 1973, Deformation Geometry for Material Scientists, Pergamon Press, Oxford.

Reuss, A., 1929, *Berechnung der Fliessgrenze von Mischkristallen auf Grund der Plastizitätsbedingung für Einkristalle*, Z. Angew. Math. Mech., **9**, 49.

Reuss, A., Angew, Z., 1929, Math. Mech., **9**, 49

Sachs, G., 1928, *On the Derivation of a Condition of Flow*, Z. Verein. Deutsch. Ing., **72,** 734.

Senczyk, D., 1974, *Laboratorium z rentgenografii strukturalnej*, Wydawnictwo Uczelniane Politechniki Poznańskiej, Poznań.

Senczyk, D., 1995, *Dyfraktometria rentgenowska w badaniach stanów naprężenia i własności sprężystych materiałówpolikrystalicznych,* Wydawnictwo Politechniki Poznańskiej, Poznań.

Senczyk, D., 1998, *Proc. of 17th Conf. Applied Crystallography*, eds: H.Morawiec and D.Stróż, Word Scientific-Singapore-London-Hong Kong, 427.

Simoms, G., and Wang, H., 1971, *Single Crystal Elastic Constants and Calculated Aggregate Properties: A Handbook*, 2nd edition, The M.I.T. Press, Cambridge, Massachusetts and London.

Skrzypek, S.J. 1998a, *Inżynieria Materiałowa*, **4**, 1035.

Skrzypek, S.,J. 1998b, *Proc. of the XVII Conference on Applied Crystallography*, eds: H.Morawiec, D. Stróż, Word Scientific, Singapoure-London-Honkong, 417.

Skrzypek, S.J. Baczmański, A., 2001a, *Adv. X-Ray Anal.*, **44**, 124.

Skrzypek, S.J., Baczmański, A., Ratuszek, W. and Kusior, E. 2001b, *J. Appl. Cryst.*, 34, 427.

Skrzypek, S.J., Ratuszek, W. and Baczmański, A., 2002a, *Acta Cryst.*, A58 Supplement, C24.

Skrzypek, S.J. 2002b, *Nowe możliwości pomiaru makronaprężeń własnych materiałów przy zastosowaniu dyfrakcji promieniowania X w geometrii stałego kąta padania.* Rozprawy Monografie, Uczelniane Wydawnictwo Naukowo- Dydaktyczne AGH, Kraków

Taylor, G.I., 1938, *Plastic Strain of Metals*, J. Inst. Met., **62**, 307.

Van Leeuwen, M., Kamminga, J.-D. and Mittemeijer, E. J. 1999, J. *Appl. Phys*. **86**, 1904.

Van Acker, K., De Bayser,L., Celis,J.P. and Van Houtte, P. 1994, J. *Apll. Cryst*, **27**, 56.

Voigt, W., 1928, *Lehrbuch der Kristallphysik, Leipzig*, BG Teubner Verlag.

Wang,Y.N. and Huang, J.C., 2003, *Texture analysis in hexagonal materials*, Materials Chemistry and Physics **81,** 11-26.

Welzel, U., Leoni, M. and Mittemeijer, 2003, *Phil. Mag.*, **83**, 603.

Wierzbanowski, K., 1978, PhD Thesis, AGH University of Science and Technology, Kraków, Poland

Wierzbanowski, K., 1979, Numerical Prediction of Cross- Rolling and Compression Textures, Scripta Metall., **13**, 1117- 1120

Wierzbanowski, K., 1982, *Generalized Computer Program for Texture Simulation*, Arch. Hutn., **27**, 189.

Wierzbanowski, K., 1987, *Some results of a theoretical study of plastic deformation and texture formation in polycrystals*, Scientific Bulletins of St. Staszic Acad. if Mining and Met., **1132**, Phys. Bull. 12.

Wierzbanowski, K., Jura, J., Haije, W.G., Helmholdt, R.B., 1992, FCC Rolling Texture Transitions in Relation to Constraint Relaxation, Cryst. Res. Technol., **27**, 513- 522

Wolfstieg, U., 1976, *ψ-Goniometer*, HTM 31, 19-21

Zattarin, P., Baczmanski, A., Lipinski P., and Wierzbanowski, K., 2000, Modified Self-Consistent Model for Time Independent Plasticity of Polycrystalline Material, Arch. of Metall., **45**, 163-184

Quaeyhaegens,C. and Knuyt,G., 1995, *Surface and Coat. Technology*, **74/75**,104.